Towards the characterisation of automotive specific woven composite laminates at intermediate strain rates

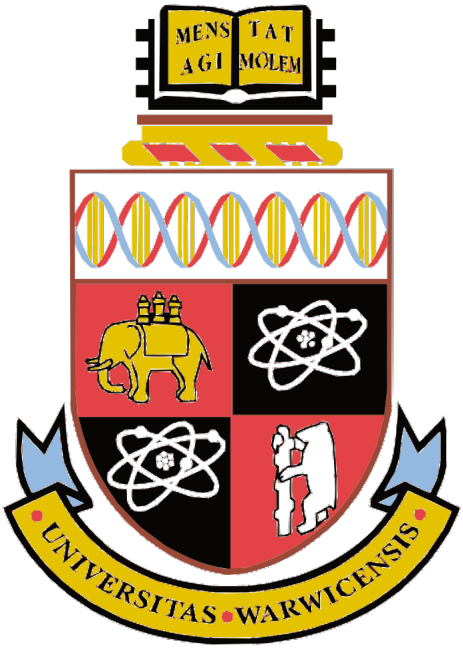

by

Richard Andrew Warman Powe

This thesis submitted in partial fulfilment of the requirements for the degree of

Doctor of Philosophy

WMG

University of Warwick

14th September 2018

Abstract

This thesis examines the sensitivity of an automotive specific T700 12K 2 x 2 twill carbon fibre epoxy composite to intermediate strain rate loads. Literature to date has focused on characterising uni-directional laminates at intermediate strain rates with few individual studies on aerospace 1K and 3K woven fabrics, however, there is a dearth of information on the strain rate effect of large tow woven fabrics at intermediate strain rates.

Preliminary ASTM standard quasi-static experiments highlighted the heterogeneity of the surface strains in both tension and in-plane shear through the application of 3D digital image correlation full field measurements. Experimental studies in literature conventionally use small specimens to induce elevated strain rates however, this thesis demonstrates that due to the heterogeneous strain field, small specimens induce erroneous failure mechanisms in a material with such a large reciprocating tow structure. To overcome this, a new specimen sizing methodology was employed based on determining the representative surface element of the specimen through quadrangular windowing of the measured surface strains. Experimental correlation showed no statistical difference in comparison to the ASTM standard results. Since the specimens induced failure loads of ~ 50 kN, a new high capacity slack adaptor was designed and commissioned as composite materials with this failure load had previously not been explored at intermediate strain rates.

The experimental response of the representative tensile and shear specimens was investigated at discrete intervals between nominal longitudinal strain rates of 2.2×10^{-4} s^{-1} and 1.0×10^{2} s^{-1}. Surface strain analysis at all strain rates using 3D DIC enabled review of the damage mechanisms occurring over the specimen. Woven tensile specimens were shown to be more sensitive to strain rate than UD laminates with T700 carbon fibres that have previously investigated in literature with large increases in strength and modulus observed. This is thought to be a result of the large resin rich regions created by the interstitial sites of the 400 gsm - 12K fabric and the large elliptical tow boundaries. Ultimate tensile strain was also shown to increase significantly at low strain rates prior to stabilising, this was hypothesised to be the due to the rate effect of damage coalescence whilst the fibres remain insensitive to strain rate. Shear specimens showed statistically significant increases in modulus, yield shear strain, yield shear strength and ultimate shear strength whilst ultimate shear strain was shown to be truncated with increasing strain rate.

It was shown that the currently available finite element material cards for modelling strain rate sensitivity within LS-DYNA lack accuracy to model the strain rate effect

of longitudinal tensile, shear and quasi-isotropic specimens. The modelled tensile response was shown to be more ductile than the experiment at fracture. This inaccuracy was compounded when attempting to model the tensile strain rate sensitivity due to the inability replicate the stiffness increase with rate. In comparison shear modelling was capable of predicting the bi-linear response with rate, however, it was unable to terminate the element, inducing high inaccurate virtual strain energies. This thesis highlights the critical importance of strain rate modelling of automotive specific woven composite materials for CAE vehicle development through extensive experimental studies, and it recommends that the current material cards and appropriate phenomenological models require further research and development.

Acknowledgements

I would like to express my sincerest appreciation for all of the support that I have received over the course of this project. First and foremost I would like to express my gratitude to WMG, EPSRC, Jaguar Land Rover and Penso Consulting for sponsoring the project. My academic and industrial supervisors; Dr Darren Hughes, Professor Ken Kendall, Dr Mark Blagdon, Dr Mark Arnold, Paul Bristo and Colin Chung, your technical insight, thoughtful discussion and assistance has been essential to the projects progression.

Thank you to everyone within WMG who has willingly given up their time in order to help over the course of this project. Particular mention must be given to Neil Reynolds, Dr Sumit Hazra, Corentin Pasco, Dr Rich Woodward, Dr Elspeth Keating and Chris Micallef, thank you all for constantly answering my persistent questions with patience; it has been a pleasure to work alongside each of you for the past few years. To the technical team at WMG and in particular Zac, Luke, Daz and Martyn, thank you for producing parts, often at short notice, this research would not have been possible without you.

I would also like to extend my gratitude to Instron and in particular Andrew Pierce; your loan of prototype equipment as well as many thought provoking discussions on dynamic characterisation has proven invaluable. Thank you also to John Hackett from Solvay for providing the composite materials used within this project.

To Mum, Dad, Kit and KP, thank you for your unwavering support, it has been a lifeline as you have so often been the voice of reason.

Most importantly; Lettie. Your perpetual enthusiasm and acceptance of me disappearing for long periods of time in order to follow up on my ideas has been invaluable. I am looking forward to making up for the time I have spent working on, and writing this thesis over the coming months and years with you. I love you.

Declaration

This thesis is submitted in partial fulfilment of the requirements for the degree of Doctor of Philosophy and describes work carried out from September 2014 to September 2018. Unless otherwise indicated, the research described is my own and not the product of collaboration. No part of this thesis has been submitted to any other University, or as any part of any other submission to the University of Warwick.

Table of Contents

List of Figures

List of Tables

Abbreviations

$\bar{\epsilon}_{global}$ Average localised strains

$\bar{\epsilon}_{local}$ Average localised strains

$\dot{\epsilon}_{exp}(SHEAR)$ average experimental longitudinal shear strain rate

$\dot{\epsilon}_{exp}(TENSION)$ average experimenta tensile strain rate

$\dot{\epsilon}_{max}$ average experimental strain rate

$\dot{\epsilon}_{nom}$ Nominal strain rate

α Quasi-static value of arbitary mechanical property

ϵ_{yy} Longitudinal strain

ϵ_{yy} Longitudinal strain

ϵ_{eng} Engineering strain

ϵ_{error} strain error

ϵ_h Hooke's law driven failure strain

ϵ_q Failure strain prescribed in *MAT$_0$58

ϵ_{True} True stress

γ_{xy} Shear strain

λ length to width ratio

ω_{ij} *MAT$_0$58$damageparameterinijorientation$

ω_l longitudinal stress wave frequency

ϕ Strain rate scaling constant

ρ density

ρ_f fibre density

σ_{eng} Engineering stress

σ_{True} True stress

δ Unit cell width

ϑ_{image} DIC imaging angle

Beta Fibre orientation relative to element direction

BIW Body-in-white refers to the vehicle structure to which all sub-assemblies are mounted to.

C Strain rate scaling value

CAD Computer aided design

CAE Computer Aided Engineering

CCD Charged coupled device

CFRP Carbon fibre reinforced polymer composites

CMOS Complementary metal-oxide semiconductor

CoV Coefficient of variation

CPT Cured ply thickness

DAQ Data acquistion

DIC Digital image correlation

DOF Degree of freedom

E_{ij} Modulus in ij orientation

ERODS Definition of strain at element erosion

EXPD External ply drop off

FE finite element

FoV Field of view

G Shear modulus

GAMMA1 Shear strain at yield

GMS Shear strain at failure

HP-RTM High pressure resin transfer moulding

IPD Internal ply drop off

ISSS Intermediate speed shear specimen

ISTS Intermediate speed tensile specimen

ISTS-QI Quasi-isotropic variant of ISTS specimen

L_0 un-deformed length

L_{free} Specimen free length

L_t deformed length at time t

LMD lost motion device

M Arbitary mechanical property

m *MAT_058 damage constant

M_{fabric} Ariel fabric weight

N_t Number of fabric layers

N_{uc} Number of unit cells

NCF Non-crimp fabrics

OEM Original equipment manufacturer, in this instance the automotive manufacturer (i.e. Jaguar Land Rover)

PCM Pre-impregnated fabric compression moulding

PLW Plain weave

PMC Polymer matrix composites

R RoI width for the analysis of unit cell quantity in RSE

RoI Region of interest

RSE Representative surface element

SC Shear strength at failure

SD Standard deviation

SH Servo-hydraulic

SHTB Split Hopkinson tensile bar

SLIMxx Post strength stress, T - tension, S - shear and C - compression

STW	Satin weave
t	total thickness
$t_{F_{max}}$	Time at peak force
t_{yield}	Time at yield
TAU1	Shear strength at yield
TTL	Transistor-transistor logic
TW	Twill weave
UD	Uni-directional fibres
V_0	Test velocity
Vf	Fibre volume fraction, ratio of fibres to matrix within the composite laminate.
VHS	Instron Very High Speed 8800 160/100-20 test frame
XT	Warp tensile strength
YT	Weft tensile strength

Chapter 1

Introduction

Increasing awareness of the impact of greenhouse gases on the developing climate change crisis has put pressure on the transport industry as it currently accounts for 26 % (as of 2014) of global greenhouse gas emissions per annum [1]. Within the UK, the automotive industry accounts for 17 % of the total CO_2 emissions from transport [2]. As a result, automotive manufacturers (OEMs) are under intensive scrutiny to reduce fleet average tail pipe emissions of CO_2 to below 95 g/km in 2020, with further restrictions to be put in place in the future [3]. Two primary methods have been identified by the UK Automotive Council in order to achieve these reductions, the electrification or hybridisation of power trains and vehicle light-weighting [4]. The integration of electrified powertrains will further increase the sprung mass of the vehicle, which has been shown to have a negative effect on the range of battery powered electric and hybrid vehicles as well as having a detrimental effect on the handling characteristics of the vehicle [5]. The UK Automotive Council predicts that in order to achieve the CO_2 emissions targets of 95 g/km a vehicle's mass must be reduced by 170 kg ($\sim$10 %) from the 2013 average for executive saloon cars (typical Jaguar vehicle) [4, 6].

The structure of automotive vehicles has evolved over time from the Model T cab on a ladder frame platform to the modern uni-body body-in-white (BIW), an example of which is shown in Figure 1.1. The BIW forms the armature to which all other components (closures, interior trim, drive line etc) are mounted to, as well as the survival cell for its occupants during a crash. Typically this uni-body structure is made of thin metallic sheets that are stamped to the correct profile before being joined together to obtain the optimum combination of stiffness, weight, crashworthiness and cost [7]. The metallic BIW currently accounts for at least 20 % of the total vehicle mass, consisting of over 400 parts, and as a result it is a suitable candidate for light-weighting [8].

A number of solutions can be implemented to reduce the weight of the BIW. The most common solutions are down gauging of the material through the introduction of high performance ultra high strength steels and design optimisation, including

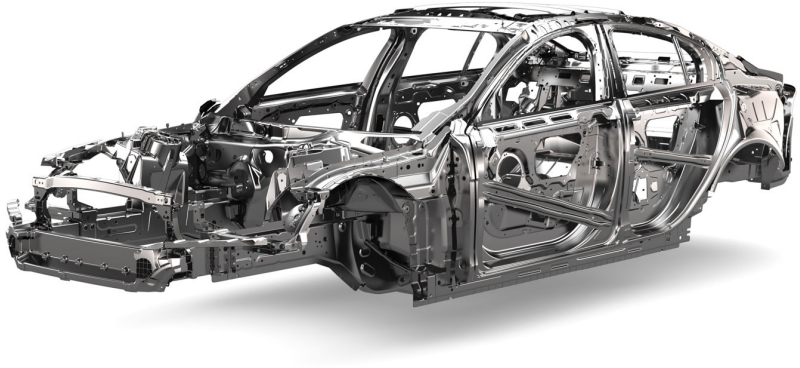

Figure 1.1: Jaguar XE aluminium uni-body BIW [9].

the introduction of tailor-welded blanks, where multiple materials of differing gauge and grade are joined prior to the final pressing [8]. Lightweight material substitution such as aluminium has been adopted by Jaguar Land Rover and enables the designers to reduce mass by up to 40 % [10], the substitution for composite materials and in particular carbon fibre reinforced polymer composites (CFRP) offers the potential to significantly further reduce vehicle mass by 60-70 % in comparison to conventional steels [11, 12]. However, this comes at a large cost, suggested to be approximately 570 % the price of standard steel (as of 2012) [10]. As a result, the use of CFRP for full BIW structures has been limited to use within motorsport or on high performance super cars that are produced at very low volumes by manufacturers such as Ferrari, McLaren or Koenigsegg (Figure 1.2).

Although no mass produced vehicles are currently manufactured with CFRP as the primary BIW material, many vehicles are starting to incorporate CFRP into their multi-material vehicle structures. Nissan have utilised CFRP within the boot of the GT-R, producing components from carbon fabrics pre-impregnated with polymer matrix (pre-preg) cured by compression moulding to achieve a 3 to 5 minute cure time [14]. In 2013, BMW released their *i-series* whose platform consists of a CFRP cabin (life module) mounted onto a aluminium frame (Drive module) to keep mass to a minimum [15]. The aluminium frame carries the drive line, battery and chassis components whereas the composite cabin contains all interior trim fittings and occupant controls. The directional nature of CFRP mechanical properties allows for the optimisation of the design dependent on the localised loading

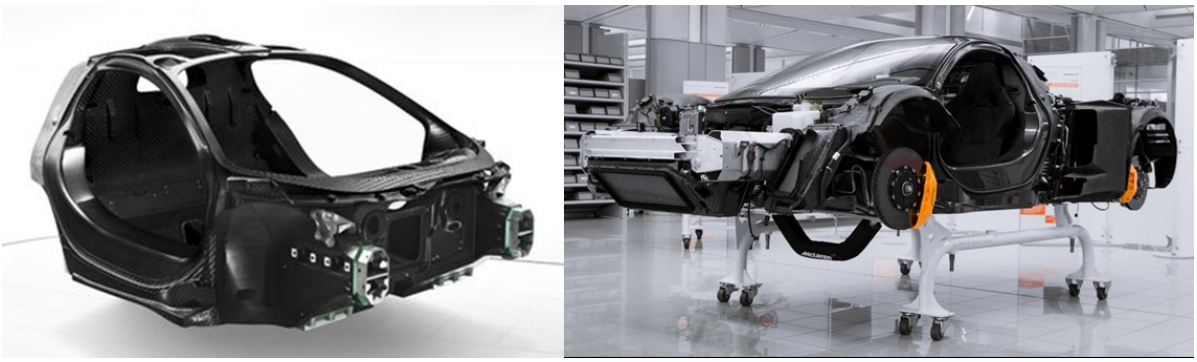

Figure 1.2: McLaren Monocage vehicle structure with aluminium sub-frames used on the McLaren P1. [13]

directions. For example, the left and right hand side of the BMW *i3* life module is a single resin transfer moulded part produced from nine preforms with different layups [16]. Laminates surrounding the front bulkhead are quasi-isotropic due to the complex multi-directional load cases, in comparison fibres are organised in a more anisotropic manner through the A, B and C pillars. BMW have since introduced CFRP into their multi-material chassis structures, producing components such as the central tunnel, B/C pillars and door sills on the 2016 *7-series* [6]. It is claimed that *the application of the correct material for each component* has achieved a vehicle structure which is 130 kg lighter than the previous model.

The use of composites as efficient energy absorbing structures has been shown in Formula 1 and motorsport since McLaren unveiled the MP4-1 chassis in 1981 [17]. As result carbon fibre composite axial impact structures have been explored within production models produced by Aston Martin [18], McLaren and Lexus [19]. The response of composite materials to axial loading has been the topic of an extensive range of experimental tests and the disintegration of the laminate has been found to provide a specific energy absorption at least four times greater than that produced by monolithic steel and aluminium structures [20–32]. The experimental studies have reviewed the effect of different fibre and matrix materials, fibre orientation, fabric architecture and loading rates on the energy absorbing response of the structures. Since there is no standardised test method and all the authors tested different geometries the responses cannot truly be compared, however, all studies highlighted a strain rate sensitivity with increasing energy absorbed during dynamic experiments compared to those conducted at quasi-static impact velocities.

1.1 Composite materials for automotive applications

Composites are a physical combination of two or more constituents, combined they produce a material with higher specific mechanical properties than those possessed by either of the individual constituents [33]. The most common composites are composed of reinforcements mounted within a metal, ceramic or polymer matrix. The matrix serves the purpose of binding the reinforcement together, transferring loads from external influences to the reinforcements and dictating the working environment of the final material. Within structural automotive BIW applications, polymer matrix composites (PMC) are most commonly applied [34]. The final performance of the PMC will be dependent upon; the mechanical properties of the individual fibre and matrix constituents, the volume of fibre relative to that of the matrix (fibre volume fraction), the quality of adhesion between the constituents and the orientation of the fibres.

Two types of polymer matrix are common; thermoset (e.g. epoxy, polyester) and thermoplastic (e.g. poly-amide, polypropylene). Thermoset polymers are the more commonly applied matrix in automotive PMC body structures [35]. This is due to the lower viscosity of the thermoset resins before cross-linking improving fabric impregnation, they also have lower cost specific mechanical properties in comparison to thermoplastic polymers. Epoxy's have increased modulus and strength in comparison to polyester and vinyl esters and are therefore commonly the desired matrix despite their elevated cost [35], modern epoxy polymers have cure cycles of a minute or less making them suitable for high volume manufacturing [36].

Fibres are ideal reinforcement agents due to their high specific properties and are classified according to their length as continuous (long) or dis-continuous (short) as well as their stiffness (modulus) and strength. Discontinuous materials reduce the anisotropic nature of the material, however, continuous fibres offer increased mechanical properties in the fibre direction. A wide range of fibre materials are available, carbon fibres offer a good combination of high specific strength and modulus making them highly desirable for use within lightweight components [33]. Continuous fibres offer high strength and stiffness characteristics and are available in a range of fabric architectures. The simplest 2D fabric is uni-directional tape (UD) with all fibres laid in the same direction, UD laminates offer very good mechanical behaviour in the fibre direction, however, the transverse properties are significantly reduced. Due to the weak transverse properties UD lamina are prone to splitting when being formed (draped) over complex shapes. The introduction of bi-axial fabrics provide similar characteristics in the longitudinal (warp) and transverse (weft) fibre orientations.

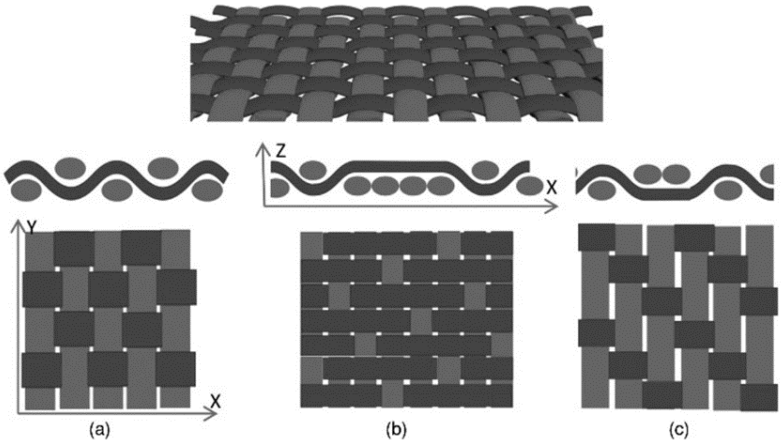

Figure 1.3: 2D woven composites: (a) 2D plain weave composite, (b) five harness satin weave composite, (c) 2D twill weave composite [40].

Bi-axial fabrics are available in a number of architectures, woven fabrics offer more balanced properties in the warp and weft orientations. However, due to the weaving process they are subject to crimp (undulation in the fibres) which reduces mechanical performance due to deforming the fibres, as well as introducing increased resin rich areas at the weaves interstitial sites. The most common weaves are; plain, twill and satin (Figure 1.3). Plain weaves are the most heavily crimped, however, are also the most stable during draping. In comparison, satin weaves are the least crimped but also are less stable often splitting when being formed over complex shapes. Twill weaves are often chosen as a compromise between the two. Non-crimp fabrics (NCF) are composed of multiple UD lamina supported with a non structural through thickness binder, this provides the material with improved drapability compared to UD laminates and less crimp than woven structures. Within the automotive industry, twill weave or NCF's are primarily chosen by OEM's due to their improved drapability. Due to the high cost of composite structures that was previously identified, OEM's favour the use of *heavy* fabrics (400 g/m^2 and above) with large tow counts (12K and above) as this enables the cost to be kept to a minimum by reducing the amount of labour and time required to weave the fabrics [37, 38]. The large tow counts can also introduce larger and more common defects such as void and resin rich regions into the laminate which can reduce the mechanical properties of the final laminate [39].

The final fibre volume fraction (V_f) of the component is dependent upon the manufacturing process employed. For manufacturing techniques such as wet lay up the V_f can be as low as 30 %, whilst in comparison the use of precise manufacturing

techniques in aerospace enables the user to generate a maximum V_f of 70 % [41]. Above this V_f the quality of adhesion between the fibres and matrix could be reduced potentially reducing the mechanical properties of the material system.

As previously mentioned, the isotropy of a continuously reinforced composite component is based on the design requirements. It is achieved by producing laminates composed of multiple lamina with varied fibre orientation [42]. To eliminate residual stresses within the laminate, the lay-up must be balanced around the neutral axis of the material. The lay-up is presented as the smallest replicating ply sequence that is symmetrical through thickness, for example the shorthand laminate notion of $[0/90]_{2S}$ refers to a [0/90] sequence repeated twice and symmetrical, thus has a complete laminate lay up of [0/90/0/90/90/0/90/0]. The laminate notion and co-ordinate system employed throughout this thesis is provided in Figure 1.4. Common stacking sequences include quasi-isotropic lay-ups $[0/\pm45/90]_{ns}$ and cross-ply $[0/90]_{ns}$; although within components the lay-up will be optimised based on the applied loading conditions.

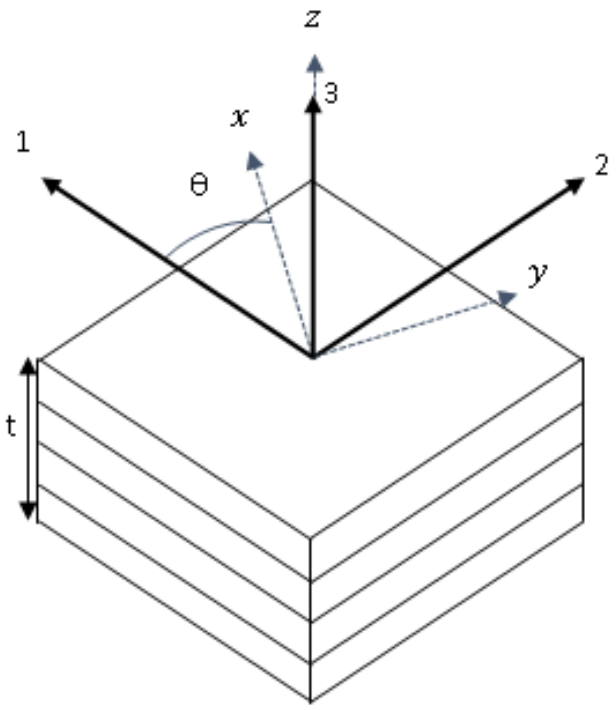

Figure 1.4: Laminate notation and co-ordinate system used throughout this thesis.

1.2 Automotive composite design using finite element tools

In an attempt to reduce the cost, development time and optimise the design of new vehicles that meet strict regulatory requirements, automotive OEM's have become increasingly reliant on the use of computer aided design (CAD) and engineering (CAE) tools such as finite element numerical modelling (FE). For example, the Nissan V3P design process reduced the time between styling freeze and start of production by 9.5 months through the replacement of early physical prototype vehicles with digital vehicles rigorously evaluated using CAD and CAE [43]. The loss of early prototype vehicles has resulted in the use of crash tests to validate the CAE models, rather than to develop the crashworthiness of the vehicle.

FE techniques discretise a continuum medium into a finite number of elements to form a mesh, the boundary conditions and external loads are introduced to the elements though direct loading of the element nodes or contact analysis. Material cards apply mechanical properties to these elements to predict the transfer of stresses and strains through the part based on the applied loads and boundary conditions [44].

Solid and shell elements are both suitable architectures for modelling the response of composite materials. Solid element modelling typically conducts analysis of composites at a fibre/resin/interface length scale [45]. Each of the individual constituents are modelled as solid elements with contact laws defining their interaction. Various studies have demonstrated their potential for accurately modelling the development and transfer of stress concentrations; particularly at free-edges [46]. However, due to the high computational requirements of this modelling method, it is often limited to microscopic modelling and used for the development of a material system and is unsuitable for full vehicle or component level modelling [47]. To reduce computational expense a composite material can be modelled as a single or series of 2D shell elements. Multiple through-thickness integration points represent the laminates stacking sequence; which is not possible when using solid elements [48]. Single shells are capable of simulating the in-plane response of composites, however, they struggle to model the out-of plane stresses and failure mechanisms, largely due to the inability to split 2D shell elements. Multiple stacked shells tied together represent a meso-level model, where each shell represents an individually orientated lamina. Modelling the ply-to-ply interface improves the ability to predict inter-laminar stresses and damage development.

As each element within the mesh is loaded it undergoes a life-cycle that is dictated by

the material card [49]. Initially, the element behaves in an elastic manner calculated using classical laminate theory, a continuum damage law can be integrated to account for the loss of stiffness experience by the material as microcracks and other damage mechanisms propagate through the laminate [50, 51]. The element will continue to behave in this way until a failure criterion is reached. Most commonly these define maximum stresses or strains that can be reached before the element begins to be eroded, however, they can incorporate more complicated fracture mechanics including fracture energies [52, 53]. Post failure properties are dictated by a damage criterion, before the element is finally deleted or eroded.

1.3 Background and motivation

This chapter has demonstrated how continuous carbon fibre composites are suitable for producing lightweight structural body components for the automotive industry, in order to assist OEMs in achieving the legislative emission directives for greenhouse gases. In order to reduce the prohibitively high cost of the materials OEM's have employed fabrics with large tow sizes and fabric weights.

The homologation of vehicle crash performance was shown to be essential in order to deliver the vehicle to multiple markets across the globe. Increased adoption of CAD and CAE has seen the number of prototype vehicles manufactured reduced, with increased design and testing be conducted in the virtual domain. Due to the high cost in delaying the start of production, the employed CAE tools must be capable of replicating the true behaviour of the vehicle as accurately as possible.

Material cards used within CAE are populated with composite material datasets that are obtained at quasi-static test speeds, within this strain rate realm their experimental response is well understood. However, impact studies on composites has shown that the response of composite materials can be highly affected by the rate at which they are loaded. Furthermore, there is clear lack of quality material data when single stress states are isolated in elevated strain rate regimes, this is highlighted in review papers by different authors delivering different verdicts on the rate sensitivity of similar constituents loaded at similar loading regimes [54, 55].

The objective of this thesis was to undertake fundamental research into the performance of carbon fibre reinforced polymer composites that are appropriate to the automotive industry. This is achieved through experimentally reviewing the affect of strain rate on the macroscopic tensile and tensile shear mechanical behaviour of the

laminate in order to improve the CAE development process of their design. The following section will detail a state of the art review in composite tensile experimental mechanics and in particular the strain rate sensitivity of the loading mechanisms.

Chapter 2

Developments towards the standardisation of dynamic composite material characterisation

A brief introduction to composite materials was provided in Section 1.1, this discussed the different types of composite materials and their suitability for application in automotive structural components. Strain rate sensitivity was highlighted due to the effect on the specific energy absorption capabilities of different materials at loading rates above quasi-static. The aim of this chapter is to review the current understanding of the mechanical response of composites exposed to elevated strain-rate regimes. This is achieved through an initial detailed discussion of the damage and failure mechanisms of laminates under quasi-static loading conditions. The failure mechanisms of different fabric architectures are discussed, however, an emphasis is placed on the response of twill weave fabrics as this is the material system considered in this thesis. The advantages and limitations of different methods of characterising materials at elevated strain rates are discussed. The current understanding of composite strain rate sensitivity is presented in relation to each of the test methods used to generate the data. The chapter then concludes with a short summary and the identification of potential novel research topics as well as the objectives researched in this thesis.

2.1 Composite experimental mechanics

The experimental response of composites has been well documented at quasi-static speeds, due to their anisotropic and inhomogeneous nature the damage and failure mechanisms differ from those of isotropic metallic materials. When reviewing composite materials on a macroscopic scale, the term *failure* refers to the final disintegration of the laminate, whilst *damage* relates to the loss of stiffness due to the coalescence of microscopic failures. Due to their heterogeneity, ultimate failure

is highly dependent upon the response of the brittle fibre and viscoelastic matrix constituents, the loading orientation relative to the fibre direction, the V_f and the architecture of the reinforcement. Typical failure mechanisms include fibre fracture, matrix cracking, failure of fibre-matrix interface, inter and intra lamina delamination. The following sections will discuss; the effect of longitudinal tensile loading of the warp fibres in both UD and woven fabrics as well as the response as the loading angle is increased relative to the warp fibres.

2.1.1 Response of UD laminates to tensile loading

The in-plane mechanical response of a continuously reinforced CFRP in the fibre direction under a tensile stress is dominated by the response of the fibres [33]. As a result on a macro scale the composite appear to behave in a brittle manner with almost constant modulus to failure. Figure 2.1 shows how the failure is driven by the constituent that is strain sensitive, typically in CFRP this is the fibres, as the strain increases random fibre failures occur due to the variation in fibre strength introduced by defects (e.g. contamination, voids, resin rich areas or poor adhesion at the fibre-matrix interface) [42]. Fibre fracture leads to highly localised stress concentrations forming within the matrix at the point of fracture. Considering a perfect adhesion at the fibre-matrix interface, these stress concentrations are transferred to nearby fibres, leading to adjacent fibre fractures. Simultaneously, considering the lower yield strength of the polymer matrix and that it is under greater stress than before the fibre fracture, it will likely undergo plastic deformation introducing microscopic shear cracks that can lead to fibre pull-out. As the load continues to rise, the density of fibre fractures, matrix cracks and interface failures increases, reducing the stiffness of the laminate response until the cracks coalesce to form a non-linear macroscopic fracture plane [56]. As the specimen strains, longitudinal splitting may occur as a result of the transverse strains being induced in the longitudinal fibres as a result of the Poissons contraction of the material or due to external influences such as the boundary conditions of the system [57].

In comparison, when the load is applied perpendicular to the fibre direction, the reinforcing fibres are not able to distribute the stress as efficiently, as a result the transverse modulus and strength of the material is typically lower than that of the longitudinal direction [58]. The distribution pattern of the reinforcing fibres constrains the matrix with variable volume of resin between each tow, as shown in Figure 2.2. The fibres restrict the strain of the matrix, this results in the formation of localised stress concentrations within the matrix local to the fibres and fibre-matrix interface. If the interfacial strength is weak, then cracks initiate at the interface and

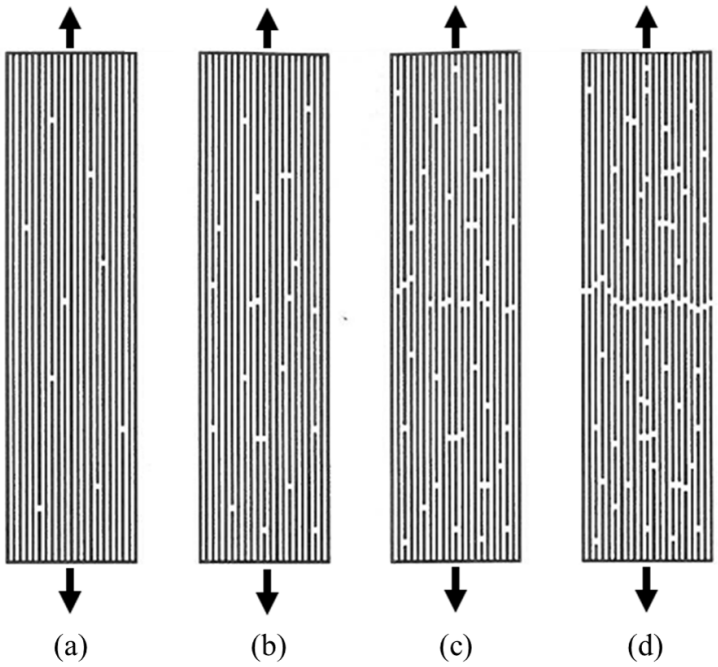

Figure 2.1: Damage initiation and crack propagation in a UD lamina loading in longitudinal tension. Initial failure occurs as random localised fibre fractures (a), these fractures introduce stress concentrations overloading nearby failures increasing density of fibre failures (b), these cracks coalesce to form cracks (c) before finally leading to the macroscopic transverse failure of the lamina in tension (d) [33].

propagate through the highly stressed areas of the matrix. If the interface is strong and fibre de-bonding does not occur, then matrix cracks form in the immediate vicinity of the interface region due to the high stress concentrations [33] . The global transverse failure is a result of the coalescence of the individual failures to form a single crack propagating through the matrix and the interface [59].

As the loading angle transitions from being aligned to the warp fibres, the global damage mechanism changes from fibre fracture to shear cracking of the matrix, a result of the principal tensile stress created in the off-axis fibres. This transition occurs once the loading angle has increased such that $\vartheta \succcurlyeq 5^{o}$ [59]. Shear cracks develop within the matrix at inclines to fibre direction, as the cracks propagate towards the fibre-matrix interface they rotate to form axial cracks running parallel to the fibres causing intra-lamina delamination [60, 61]. Off-axis shear places large stresses through the fibre-matrix interface, if the interface is weak then cracks initiate

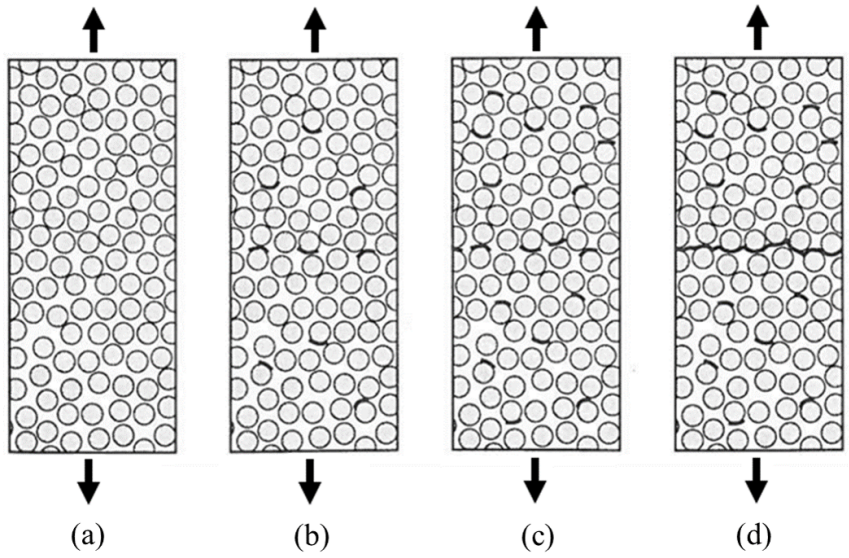

Figure 2.2: Damage initiation and crack propogation in a UD lamina loading in transverse tension. Initial lamina state highlighting variation in the volume of resin rich regions (a), localised crack initiation occurs in the matrix between fibres or at the fibre-matrix interface (b), as the load continues to rise the crack density increases (c) finally the coalescene of these cracks forms a transverse tensile matrix crack failing the lamina (d) [33].

within it as well as in the matrix [62]. Localised interface failures propagate along the fibre, resulting in fibre-matrix de-bonding and ultimately fibre pull-out. Pure shear failure of the matrix is observed when $\theta = 45°$, above this loading angle the tow begins to behave as a transversely loaded UD ply . Due to failure being dominated by the matrix, the global response is elastic until initial matrix or interface failure, at this point the material yields and non-linear plastic shearing occurs until the matrix fails.

2.1.2 Response of multi-axial laminates to tensile loading

As previously discussed, the use of UD materials will provide desirable weight specific properties in the fibre direction, however, the transverse properties are often lower. As a result the stacking sequence of composite automotive components is rarely composed of UD plies in oriented to a single direction as the applied load cases are complicated. Biaxial fabric and stacking sequences improves the orthotropic

nature of the laminate providing balanced properties in both the warp and weft fibre directions, however, due to the simultaneous loading of longitudinal and transverse plies, this leads to a more complicated damage and failure sequence [63].

The origin of damage within multiaxial laminates is within the lamina that has the highest stress normal to the fibre direction [56]. Within cross-ply $[0/90]_{ns}$ laminates, both the axial and transverse plies initial strain in a constant linear manner, macroscopic damage typically becomes evident as the material exceeds 0.65 % longitudinal strain for cross ply UD laminates [64]. The macroscopic damage is a result of the applied load exceeding the transverse tensile strength, as a result matrix microcracks propagate within the weft lamina. As well as transverse matrix cracking, quasi-isotropic laminates induce shear stresses within the $[\pm 45]$ lamina, creating microscopic shear strains within the matrix [65]. The combination of these microscopic failures leads to damage propagation on a macroscopic scale. As the load continues to rise matrix cracks propagate through the off-axis laminae and along the fibre-matrix interface with interlaminar delamination occurring just before catastrophic brittle failure of the laminate

The opposing Poissons contractions of each lamina within a multi-axial laminate creates through thickness shear stress concentrations at the boundary of different fibre orientations. The resultant shear stresses are dictated by the lamina orientations of the final laminate, peak interlaminar shear stresses are observed in laminates with a $[15/-15]_s$ stacking sequence [66, 67]. Within the centre of the specimen these through thickness stresses can lead to splitting of the warp and weft fibres, however, their effect is more prominent at the free-edges of specimens [68]. Large interlaminar shear stresses have been observed to form within a specimen thickness of the edge, these stress concentrations form cracks that propagate through the material and can lead to premature ultimate failure of the laminate.

2.1.3 Response of woven laminates to tensile loading

The elastic response of a biaxial woven fabrics is dictated by the properties of the fibre and matrix constituent as well as the fibre-matrix interface, with damage propagation containing similar trends to those observed in UD and biaxial UD laminates based on the consistent warp and weft orientations. However, the final fracture properties are typically governed by the structural organisation of the woven fabric [64]. Depending on the architecture, fabric weight and tow count of the woven fabric the amount of induced crimp will vary [69]. The greater the induced crimp and elliptical shape of the tows (increases with greater tow counts) the larger the

resin rich regions found at the interstitial sites as well as the tow boundaries. Stress concentrations form at these localised regions and the cracks propagate into inter-ply delaminations as well as intra-ply delaminations between the orthogonal tows.

The propagation of damage follows similar trends to those produced in UD and biaxial UD laminates based on the consistent warp and weft orientations, however, other damage mechanisms are also introduced based on the structure of the woven fabric [70]. A schematic highlighting the various damage mechanisms introduced in woven laminates is shown in Figure 2.3. Damage initially forms as highly localised transverse tensile cracks within the weft tows due to the stress concentrations created within the matrix and fibre to matrix interface [71]. The density of cracks increases and propagates through the resin rich interstitial sites and tow boundary regions to form cracks multiple tow widths in length [72]. Following the saturation of transverse cracks, the transverse tensile stresses induced by weft fibres leads to the transverse splitting of the warp fibres and the formation of longitudinal cracks. The mismatch in Poissons ratio also introduces highly localised through thickness shear stresses that propagate to form intra-lamina delaminations at the tow boundary [68]. Within woven laminates the delaminations are highly localised as the tow crimping arrests the global propagation of intra-lamina cracks between warp and weft fibres [73]. As with UD laminates loaded in the fibre direction, the ultimate failure of the laminate is due to fibres exceeding their ultimate strain, however, this is restricted due to the crimp of the fabric along with the quantity of inter-laminar delaminations.

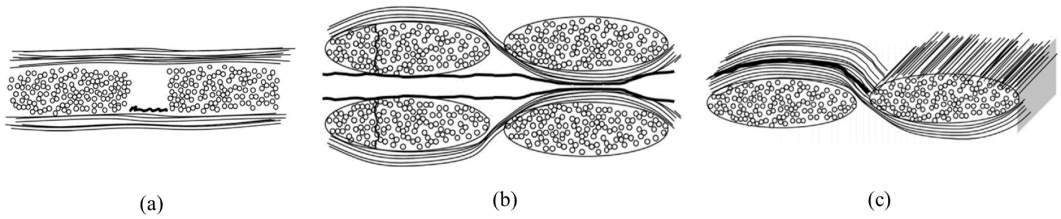

Figure 2.3: Schematic of the damage mechanisms developing within a composite laminate within a woven subjected to longitudinal tensile loads, (a) matrix cracks initiating and propagating within matrix rich regions at tow boundaries and weave interstitial sites, (b) transverse cracks forming in tows before propagating to form interlaminar delaminations and (c) splitting of tows leading to the splaying of transverse and longitudinal tows [Adapted from [64]].

The initiation and propagation of damage reduces the stiffness in the longitudinal direction, this *knee* point is highlighted on Figure 2.4 as the commencement of matrix cracking. Due to the materials ability to redistribute the load around these damaged

areas, this premature damage does not result in the ultimate failure of the laminate. However, its stiffness as it strains beyond the knee point is variable, fluctuations in stiffness are caused by the localised propagation of damage. Kissat et al. reviewed the effect of tow count on plain and twill weave carbon epoxy composites [74]. The author observed that 3K fabrics undergo limited damage appearing to strain with almost constant stiffness to fracture in both plain and twill fabrics. In comparison the 12K fabrics underwent a transition with greater non-linear damage, the plain weave fabric kneed after 0.4 % strain, whilst the reduced crimp of the twill kneed at 0.8 % strain. Optical measurement on the surface of the material highlighted that the knee was caused by extensive splaying of the transverse tows, since this does not occur in the 3K fabric it is assumed to have propagated from the resin rich regions at the tow boundary.

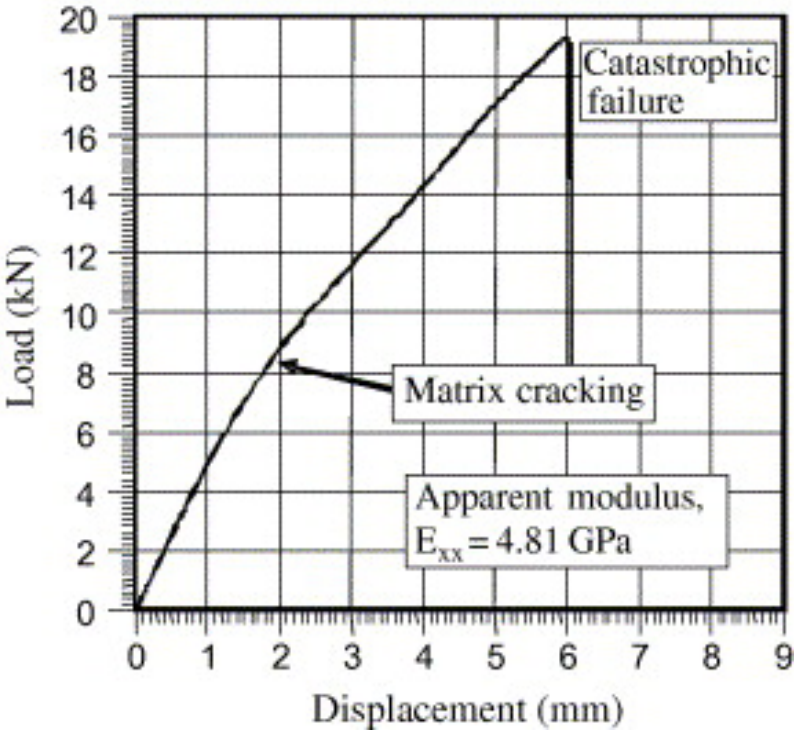

Figure 2.4: Engineering stress-strain plot for a woven laminate loaded in the fibre orientation. [65].

The phase shift on the mechanical behaviour of a 12K 2 x 2 twill weave CFRP laminate was reviewed by Matveev et al. [75]. Surface strain maps recorded the same phenomenon as Kissat et al. with extensive splaying of the transverse tows observed in laminates with zero phase shift of the fabric. In comparison, less transverse tow damage was observed in the specimens evaluated with a random phase shift, instead

experiencing greater interlaminar damage. The potential cause of these delaminations is the through thickness shear stresses generated by the mismatched Poissons contractions of the perpendicular tows (also discussed in Section 2.1.2). Matveev et al. observed that damage was introduced to the random shift specimens earlier, kneeing at 0.7 % longitudinal strain, in comparison the zero phase shift specimens transitioned above 1 % strain, however, the zero phase specimens experienced a greater reduction in stiffness beyond this point.

Increased crimp in woven fabrics offers improved handling and draping characteristics as the fabric is less susceptible to splaying when being handled or formed into complex shapes. However, this improved stability is compensated with a performance reduction. Due to the crimp angles introduced to the fibres, the modulus and ultimate strength of the laminate are reduced. Abot et al. observed that a heavily crimped plain weave composite has a modulus and tensile strength of approximately 80 % that of a UD fabric with a common warp fibre volume fraction [76, 77]. In comparison a five harness satin weave that has five times less crimp only has an approximate 10 % reduction in tensile modulus and strength. This was supported by Tang et al. who demonstrated that the saturation of damage within the more heavily crimped plain weave laminate lead to its reduced stiffness and earlier knee transition [78].

Similarly to the response of UD laminates to off-axis loading, as the orientation of the warp tows with respect to the loading orientation is increased, woven laminates behave in an increasingly elastic-plastic manner. When the loading angle is small ($\theta \leq 20°$) the matrix undergoes shear damage, however, the stress is successfully transferred to the warp tows which remain loaded in tension. As shown in Figure 2.5 this causes a slight reduction in modulus through the linear elastic response of the material in comparison to on-axis loading. The premature knee is caused by the extensive microscopic matrix and fibre-matrix interface damage as a result of the high load, thus reducing the stiffens of the material, the properties of the matrix and interface define the plastic response prior to ultimate failure, which occurs along the fibre plane [79].

A laminate loaded closer to *pure shear* [1] $\theta = 45°$ has initial elastic behaviour dictated by the characteristics of the shearing of the matrix as very little tensile stress is sustained by the warp and weft fibres. The position of the fibres within the matrix arrests the natural Poissons contraction of the matrix leading to further stress concentrations and localised failures created at the fibre-matrix interface in

[1] The loading of a ±45 laminate will not induce *pure shear* since the fibres will always be loaded under tension [81], therefore pure shear in this context refers to the shear response of an orthotropic laminate.

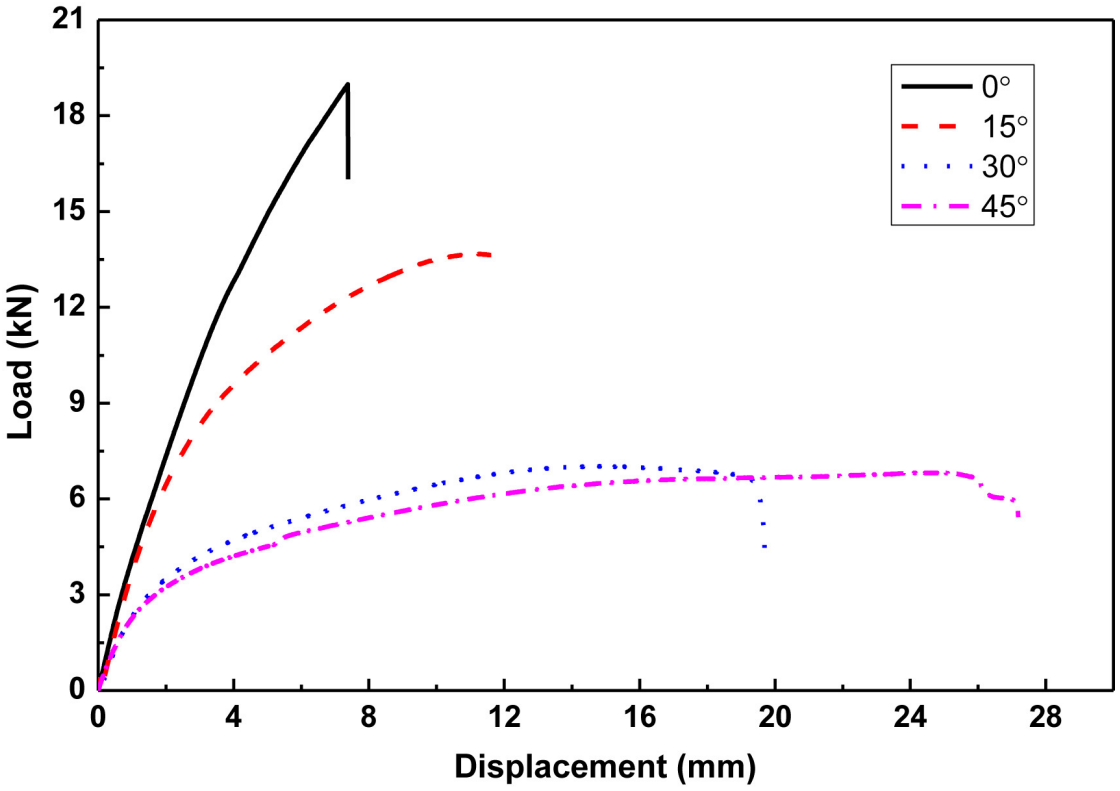

Figure 2.5: Load-displacement curves for a 2 x 2 twill woven laminate subject to off-axis loading up to pure shear [80].

the form of shear cusps [82]. The coalescence of these localised failures results in the cracks forming and the laminate yielding; and plastically straining to failure [83]. During plastic straining the crack density increases, forming intra and inter-lamina delamination. Depending on the weave architecture this can either result in the strain hardening of strain softening of the plastic deformation as the fabric locks. Wang et al. observed that a 3K 2 x 2 twill CFRP laminate underwent strain hardening to fracture [84]. Liang et al. studied both 3K 2 x 2 twill and 5 HS CFRP laminates, observing a reduced strain hardening in the looser satin weave. [85] The final fracture occurs in the plane of the warp and weft fibres forming a complex saw tooth surface once the crack density has saturated, analysis of the final surfaces demonstrated extensive fibre-matrix interface damage as well as fibre fracture [81].

Few studies have been conducted that review the effect of tow count on the damage mechanisms of woven laminates under off-axis tensile loading with the majority of in-plane shear experiments focusing on the application of 3K woven fabrics. Karahan utilised optical measurements to measure the surface strains of 6K 2 x 2 twill CFRP

specimens under in-plane shear loads [86]. The author observed that as the specimen was loaded, longitudinal strains were most intensive at the interstitial sites of the weave along the tow boundaries (Figure 2.6). Temporal synchronization of the strain vector growth at these locations with acoustic emission data enabled the author to determine that the crimp of the interstitial sites were inducing transverse matrix cracks that propagated rapidly through the structure. This suggests that the increased crimp of fabrics with higher tow counts will increase the transverse crack density earlier in the tensile life cycle of the laminate.

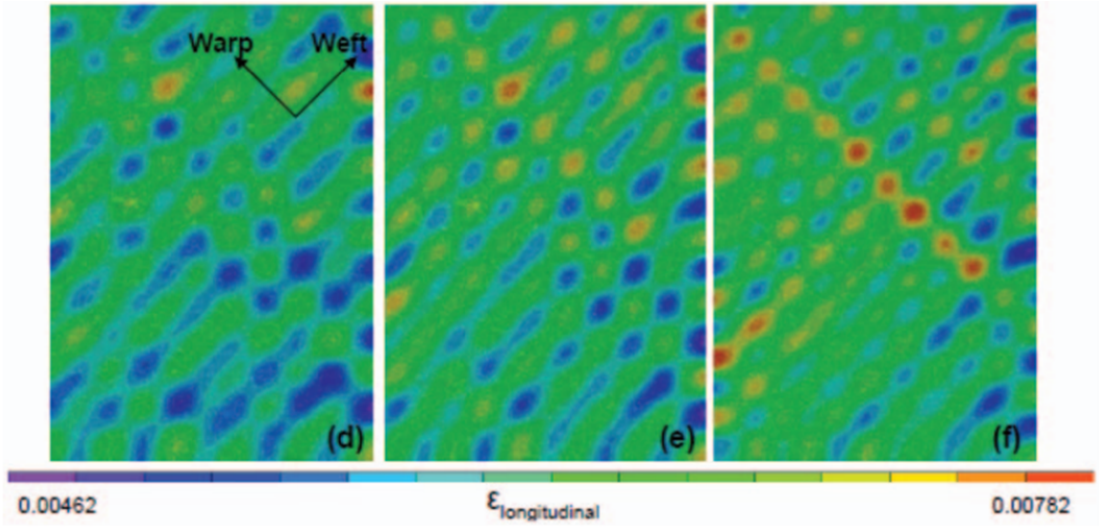

Figure 2.6: Surface strain maps of a 6K 2 x 2 twill CFRP laminate under a ±45° tensile load highlighting longitudinal strain growth at the interstitial sites of the weave at (d) 0.6 %, (e) 4 % and (f) 8 % longitudinal strain (imaging region is 25 x 40 mm^2) [86].

2.2 Experimental characterisation of composite tensile mechanical properties

As previously mentioned in Chapter 1 the sensitivity of composite components to loading speed has been well documented in relation to automotive and aerospace crash testing. In order to improve the understanding of the sensitivity of each constituent and each stress state, dynamic characterisation tests are conducted. The strain rate induced within a structure is related to the velocity of the impactor and the length scale of the object. Due to the large length of vehicle structures and impact velocities of 32 km/h and 64 km/h used for side pole and front impact NCAP tests [87] average strain rates in automotive impacts are within the intermediate regime between 30 s^{-1} and 100 s^{-1} [88, 89]. As a result strain rates up to 100 s^{-1} will be the focus of this research.

The characterisation of any material at any speed must consider a number attributes that can affect the outcome of the test, such as specimen geometry and alignment within the fixturing, as well as the effect of any fixturing on the boundary conditions of the system. Hamouda et al. [90] identified that the following additional factors must also be considered when conducting dynamic experiments;

1. The development of a launch mechanism that is capable of reducing the inertial loading period and ensures that the specimen deforms at the desired strain rates.
2. The period of inertial loading must be short relative to the total test duration.
3. The compliance and resonance introduced through the introduction of the launch mechanism must be considered in relation to the total mass and stiffness of the load path.
4. The specimen geometry evaluated must induce the correct stress state and represent the global response of the material system and not the response of a localised defect.
5. The instrumentation employed must be capable of recording the transient deformation characteristics of the material system accurately.

A number of solutions have been developed that meet these criteria, and have subsequently been used for the characterisation of different types of materials under dynamic loading. In order to test materials at multiple strain rate magnitudes, an

array of test machines must be used (Figure 2.7). The standardised technique for the dynamic characterisation of metallic materials has two proposed standards that are dependent upon the target strain rates. BSI ISO 26203-1:2018 [91] explores the use of Split Hopkinson Bar systems (SHB) to characterise specimens between 100 and 10,000 s^{-1} , whilst for strain rates from 0.1 to 1000 s^{-1} a high speed servo-hydraulic machine (SH) is preferred (BSI ISO 26203-2:2011 [92]). BSI ISO 18872:2007 [93] is the polymer adaption of these metallic standards.

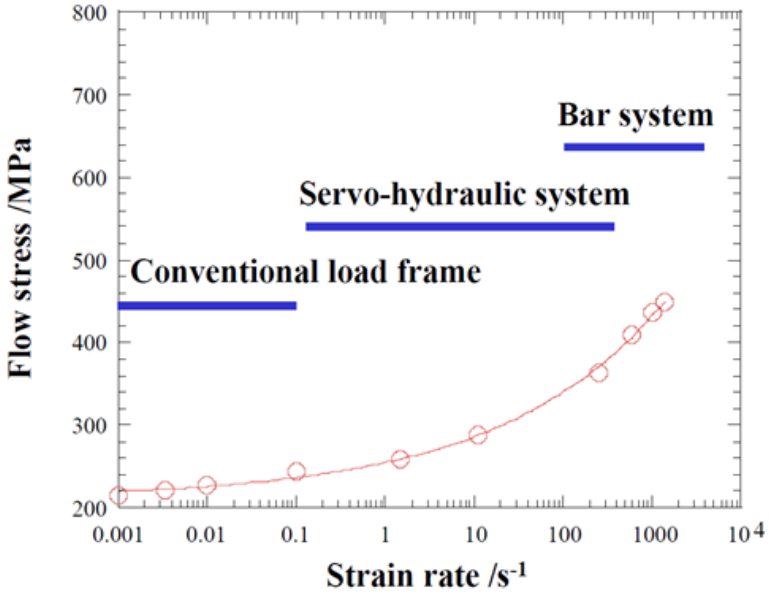

Figure 2.7: Standardised test methods and their appropriate strain rates for the characterisation of metallic and polymer materials. Conventional testing machines are typically suitable for the determination of material properties at strain rates up to 0.1 s^{-1}, Servo-hydraulic systems are capable of loading specimens to strain rates between 0.1 s^{-1} and 1000 s^{-1} whilst elastic bar (Split Hopkinson Bar) systems are capable of achieving very high deformation rates ($>$ 1000 s^{-1}) using wave propagation theory [94].

ISO 26203-2:2011 [92] outlines the requirements for determining a valid experimental result when reviewing the stress and strain behaviour for metallic specimens using a SH machine. The primary requirement of any high speed test methodology is the production of a stable strain rate. A non-linear strain rate is unavoidable due to the inertial effects of the specimen and the load path. To compensate for this inertial period the average experimental strain rate ($\dot{\varepsilon}_{exp}$) is typically determined during the the plastic deformation of the specimen between the time at yield (t_{yield}) and peak force ($t_{F_{max}}$) using Equation 2.1. This is suitable for metallic specimens due to the

large plastic strain region, however, this method will be unuitable for composites due to the brittle fracture during elastic loading.

$$\dot{\varepsilon}_{exp} = F\{\dot{\varepsilon}(t_{yield})...\dot{\varepsilon}(t_{F_{max}})\} \tag{2.1}$$

Figure 2.8 shows an example of a valid result for a metallic specimen reviewed at 250 s^{-1} using a SH machine. It is evident that neither the stress-strain nor the strain rate plot is stable due to the sudden excitation of the system this is common. This oscillation is dependent upon many factors including; the compliance of the frame and load path, potential variations in actuator velocity experienced on engagement of the load path, as well as the material properties such as stiffness, yield strength and strain hardening behaviour. ISO 26203-2:2011 dictates that an allowable variation in experimental strain rate during an experiment is ± 30 % [91].

No standard currently exists for the characterisation of continuously reinforced composite materials at elevated strain rates using either the elastic bar or servo-hydraulic

Figure 2.8: Example of an engineering stress-strain plot (1) for a metallic specimen at an average experimental strain rate of 250 s^{-1}. The engineering strain rate of the experiment (3) is shown on the secondary axis, due to the reduced stress as the specimen undergoes necking which increases the heterogeneity of the strain field within the specimen the experimental strain rate is determined between the yield point and the engineering tensile strain at peak force (2). (Adapted from [92])

frames. Based on the discussion of composite experimental mechanics in Section 2.1 the primary challenge with characterising composites at elevated strain rate regimes is the ability to produce a stable strain rate within the specimen prior to fracture. Due to the highly brittle elastic response in the fibre direction, the period for determining a stable strain rate regime is short, typically 1 - 2 % longitudinal strain. The increased ductility of composite laminates exposed to off-axis shear loading results in a similar yield and strain hardening and softening response as observed within metallic components, however, they also behave in a brittle response when compared to the ductile behaviour of metallic specimens. Due to the lack of standards and the challenge in inducing a stable strain rate many different systems and specimen configurations have been employed to review their behaviour. Therefore, prior to discussing the current understanding of composite strain rate sensitivity the different experimental methodologies are introduced, including the advantages and disadvantages of each system.

2.2.1 Drop weight testing

Drop weight testing is used to review material behaviour at low to intermediate strain rates (<100 s^{-1}). A typical drop weight test apparatus is shown in Figure 2.9, it consists of a weighted trolley that is lifted to a pre-determined height thus providing the velocity and energy at the point of impact. The direction of the trolley is controlled by a set of guides. A clearance fit is required on the guides to reduce the friction of the test system, however, this introduces compliance to the system. The impactor will typically make contact with an impactor platen that transfers the load to the specimen. Finally, different specimen fixturing can be employed in order to produce compressive, tensile and shear stress states in the specimen [95]. Drop towers allow specimens to be tested at close to quasi-static geometries, however, they are also prone to ringing in the load measurements induced due to inertial ringing and wave propagation [96]. It has also been observed that the input energy can vary between specimens inducing inconsistent strain rates between samples. As a result they are considered better suited for determining the crash worthiness of sub-system components rather than material characterisation.

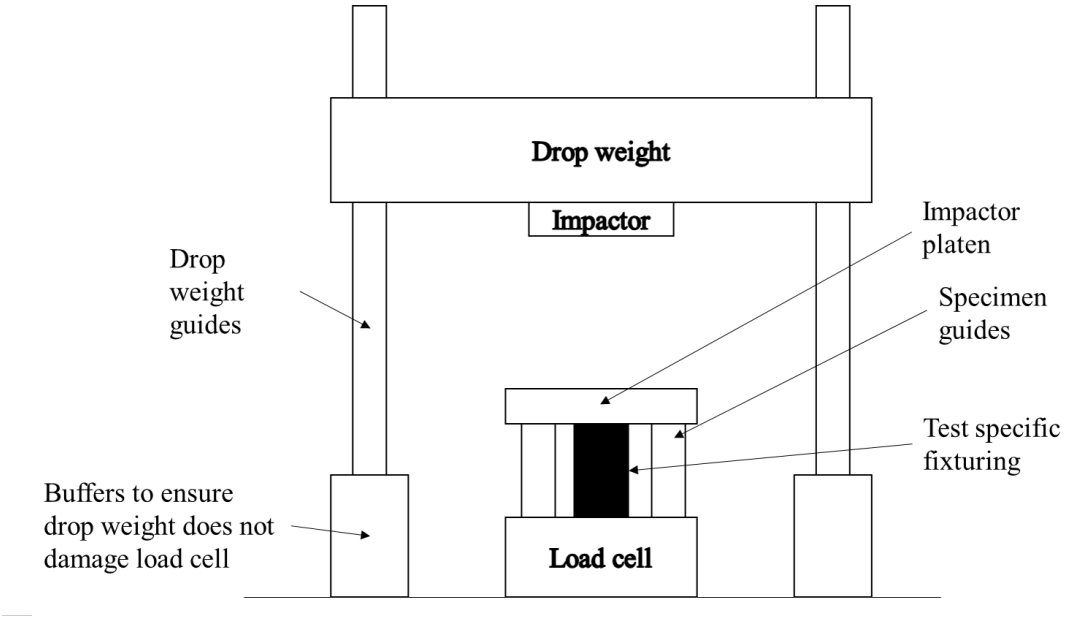

Figure 2.9: Schematic of typical drop weight tower for dynamic material characterisation

2.2.2 Split Hopkinson Tensile Bar

The SHB elastic bar experimental method was originally developed for characterisation of materials under compressive stress states [97]. It has since been adapted for use in tensile characterisation, Harding et al. [98] have been accredited with developing one of the first Split Hopkinson Tensile Bar (SHTB) test apparatus. Since its inception it has been widely adopted throughout literature at a range of strain rates. For example Staab and Gilat [99] used a SHTB to characterise a UD glass-epoxy laminate at strain rates between 933 - 1613 s^{-1}, whilst Paul et al. used one to characterise the off-axis response of a carbon-epoxy material at 140 s^{-1} [100]. A schematic of a conventional SHTB experiment is shown in Figure 2.10.

The tensile stress state is introduced through a striker making contact with a loading block at speeds of up to 20 ms^{-1}. This impact generates a tensile stress state through the loading bar. As the tensile wave reaches the input/loading bar interface the stress wave is transmitted into the input bar and reflected back through the loading bar. This same transmission and reflection also occurs at the interface between the input bar and specimen as well as the specimen and the output bar. The homogeneous

stress state of the specimen is dependent upon the superposition of the stress waves reflecting within the specimen. All of the bars used within the load path must be produced from a material and of a geometry such that only elastic deformation occurs. Provided that the output bar is of sufficient length that the stress wave reflection at the end of the load path does not occur before the specimen has failed then strain gauges bonded to the input and output bar can be used to determine the load and the axial displacement of the system. However, additional strain gauges or measurement methods must be used to identify the behaviour of the specimen itself.

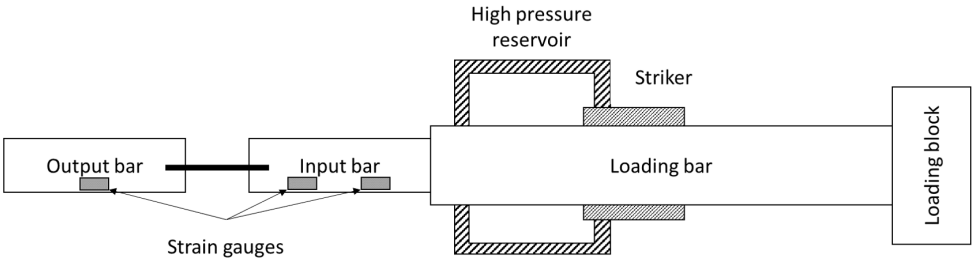

Figure 2.10: Schematic of a typical Split Hopkinson Bar configured for high rate tensile testing, the specimen is mounted between the input and output bars. The striker is propelled horizontally at the loading block at a preset velocity controlled by the high pressure reservoir, upon contact with the loading block a tensile stress wave is generated within the loading and latterly the input bar and specimen. At each interface the stress wave is reflected, therefore to avoid the introduction of compressive stress states within the specimen, failure must occur prior to the reflection of stress waves at the end of the output bar.

Selection of the appropriate specimen geometry is essential in order to produce a uniform stress field. The ISO standards for the characterisation of metals and plastics using elastic bar systems deems that this state is established upon the reflection of 12 and 10 stress waves respectively within the elastic response of the material [91, 93]. The stress wave speed is determined based upon the modulus and density of the material system and when combined with the quasi-statically obtained yield strain can be used to determine the minimum length of the specimen based upon the length of output bar available. As with testing of metals and plastics, composite specimens are often machined into dog bone shapes (an example of which is provided in Fig-

ure 2.11). The specimens have a reduced width in the prescribed gauge region in order to isolate a region with a stable uniform stress state, away from any stress concentrations introduced by boundary conditions at the grips. The compliance of the gripped regions reduces the strain rate slightly from the nominal values estimated using Equations 2.2 to 2.4 whereby strain rate ($\dot{\varepsilon}_{nom}$) is proportional to the test velocity (V_0) and the un-deformed length (L_0) of the specimen according to equations 2.2 to 2.4. L_t is the deformed length at time t

$$\dot{\varepsilon}_{nom} = \frac{d\varepsilon}{dt} \tag{2.2}$$

$$\frac{d\varepsilon}{dt} = \frac{d}{dt}\left(\frac{L_t - L_0}{L_0}\right) \tag{2.3}$$

$$\dot{\varepsilon} = \frac{V_0}{L_0} \tag{2.4}$$

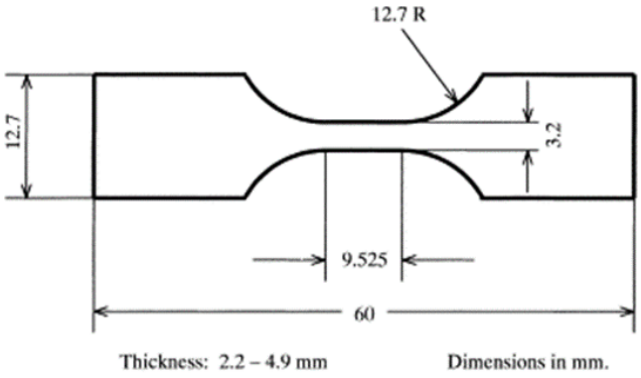

Figure 2.11: Example of dog bone shaped specimens used by Gilat et al. for the characterisation of unidirectional IM7/977-2 carbon fibre epoxy composite laminate using a Split Hopkinson Tensile Bar to achieve nominal strain rates of 400 s^{-1} [101].

The small specimens that allow high strain rates to be achieved also reduce the volume of material with which to represent a global material system. Typically gauge areas between 3 x 3 mm^2 and 20 x 20 mm^2 are common depending on the available equipment and the desired nominal strain rates. The effect of fabric heterogeneity has been shown to have an impact on the response of the fabric, Lang et al. [102] demonstrated that the use of strain gauges below the unit cell of the fabric essentially rendered the obtained results useless. Koohbar et al. [103] utilised optical

measurements of the surface of a plain weave fabric to determine that the minimum area capable of representing the global mechanical properties of the laminate was 3.4 unit cells squared (unit cell is defined as the smallest self replicating pattern of the fabric). The experimental response of a specimen volume that is below the minimum representative surface element (RSE) is likely to be a function of the localised stresses of a particular constituent or architectural effect. The damage is induced and propagates based on the heterogeneous stress field, ultimately this can lead to a change in the global failure mechanisms of the specimen in comparison to those of a large scale composite components. Smaller specimen volumes also result in increased sensitivity to defects, potentially introduced during manufacture (such as resin rich regions, voids and fibre misalignments) or based on poor fibre alignment within the test fixturing [63]. Paul et al. [100] evaluated the response of a straight sided UD laminate with stacking sequence $[45/-45/90]_S$ at strain rates up to 140 s^{-1}. In comparison to the 25 mm x 250 mm standardised test, experiments with reduced free lengths (distance between grips), 10 x 10 mm^2, 10 x 10 mm^2 and 15 x 15 mm^2 were observed to have a reduced mean strength and increased variance. The damage mechanism was observed to change, increased interlaminar delamination and matrix cracks propagating from the specimen free edges were observed. As a result the controlled reduction of specimen geometries is critical in order to evaluate the true global response of the composite laminate when high heterogeneous heavy woven fabrics are employed, as is the case in this thesis.

2.2.3 High speed servo-hydraulic loading frames

The volume of literature surrounding the use of SH is less compared to that of SHTB experiments. This is attributed to the high initial cost of purchasing the equipment. SH test frames are composed of six primary parts, a schematic highlighting these is shown in Section 2.12. The primary difference between a standard SH machine used in low speed or fatigue testing and a high speed one is the employment of a lost motion device (LMD) (5). LMD's allow the acceleration of the cross head prior to the engagement of the specimen, thereby reducing the inertial loading period and allowing specimen response to be evaluated at higher test speeds.

The base of the specimen is mounted to the very stiff frame via a static grip (2), this grip also typically contains the piezoelectric load cell (1). Any compliance of the frame and gripping mechanism will be observed as inertial damping, increasing the period of specimen deformation at a non-linear strain rate. As a result, the stiffest frame possible must be produced [104]. The dynamic jaw (4) is mounted to both the specimen (3) and the LMD. The LMD is also connected to a hydraulic

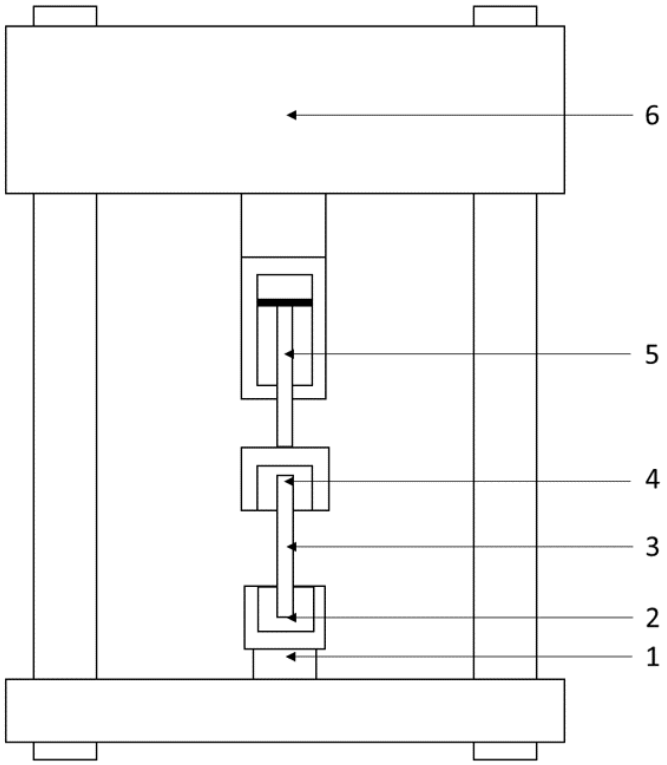

Figure 2.12: Schematic of the layout of a high speed servo-hydraulic test machine; (1) piezoelectric load cell, (2) static lower grip, (3) specimen, (4) dynamic upper grip, (5) lost motion device and (6) servo-hydrualic actuator.

actuator (6) that provides the uni-axial cross-head displacement. The velocity and acceleration profile of the LMD is based on the flow rate of high pressure oil through a servo-valve running in velocity control.

The piezoelectric load cell mounted at the base of SH machines are the most widely used due to their combination of high stiffness and small volume providing a high frequency response that can easily be packaged within the test machine [105]. The inertial loading of conventional strain gauged load cells renders them unsuitable above quasi-static test speeds. Piezoelectric load cells are prone to ringing, the sudden engagement of the LMD generates a longitudinal stress wave within the load path at the systems natural frequency, the frequency of this stress wave is superimposed within the instrumentation signals and therefore the subsequently generated stress strain plots and mechanical data potentially rendering them unusable [106]. The frequency of the longitudinal stress wave (ω_l) can be determined using Equation

2.5 based on the specimen free length of the material tested (L_{free}), its modulus (E_{ij}) and density (ρ).

$$\omega_l = \frac{1}{2L}\sqrt{\frac{E_{ij}}{\rho}} \tag{2.5}$$

A qualitative assessment to the magnitude of the ringing observed during the dynamic characterisation is shown in Figure 2.13. The initial response is unacceptable due to the large signal to noise ratio rendering the true stress-time undetectable. This noise can be reduced by introducing damping or by redesigning the load path to reduce the mass between the specimen and load cell thus increasing the natural frequency. Positioning a damping agent (e.g. 1 mm polyethylene [107] and 1.5 mm rubber nitrile [108]) within the load path, has been shown to limit the noise of the experiment and enable to authors to extract a valid response of a material as it undergoes yield and strain hardening [108]. However, over damping the system will increase the strain rate rising period, reducing the duration of loading that the specimen is deforming at the desired rate. As a result Borsutzki et al. recommends that for the characterisation of sheet steel damping should not be employed if the failure strain is below 10 % [94]. When characterising the response of a metallic component the specimen itself can be used to measure load by bonding a strain gauge below the necked gauge length onto a portion of the specimen that will be deforming linearly to fracture [88]. Since the natural frequency is dependent upon the mass, positioning the load cell on the specimen minimises the mass and increases the natural frequency of the load measurement device thus extracting a load measurement with reduced ringing relative to that of the piezoelectric load cell. However, since dog boned continuous fibre composites specimens are prone to premature failure and a straight sided specimen does not have a region of purely elastic deformation, this method is unsuitable and the machine mounted load cell must be used, therefore. Post processing data filtering can be applied to remove the effect of noise on the mechanical properties of the laminate, however, this must be done carefully so as to not remove any artefacts of the test. As a result the preferred method is the development of the load path to enable the user to obtain the correct level of damping through structural design.

A number of LMD solutions have been employed throughout literature. A schematic highlighting the various types of LMD's is shown in Figure 2.14. All of the LMD's shown in Figure 2.14 assume that the static jaw and load cell is positioned at the base of the machine and the hydraulic accumulators at the top. This layout provides the stiffest frame and load cell configuration (this is the configuration used for this

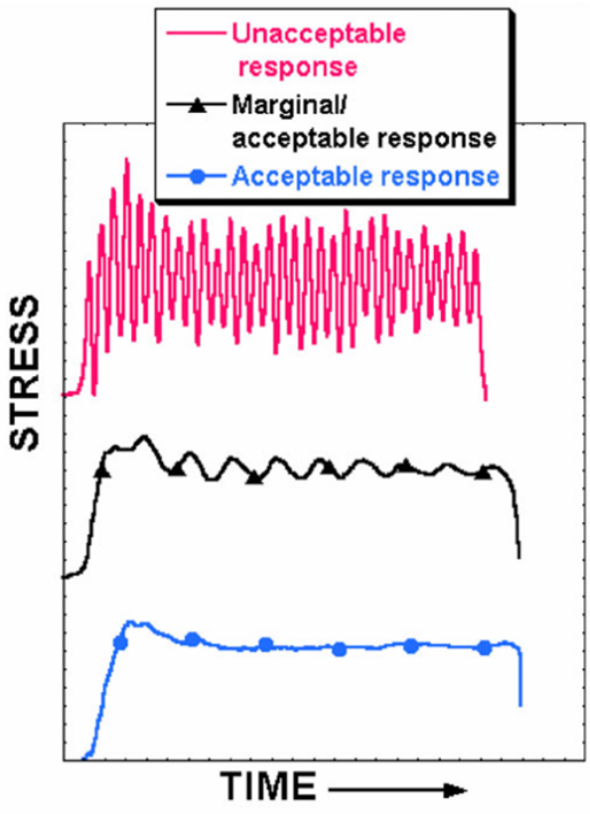

Figure 2.13: Qualitative examples of unacceptable and acceptable ringing observed through a piezoelectric load cells [109].

work). High speed servo-hydraulic machines can also be designed the other way up, however, these have a reduced load capacity due to their lower stiffness.

LMD style (a) (Figure 2.14) has been employed by Longana [110], Battams [107] and Fitoussi [108] for the characterisation of straight sided composite laminates. Due to the load path between the slack adaptor and load cell containing multiple parts with varying stiffness's and mass it is likely that this fixture will induce out-of plane motions of the specimen at the upper jaw. The amplitude of these measurements may induce additional ringing within the load measurement. Since the acceleration distance is prescribed by the slack rod, dog boned specimens do not need to be employed enabling the characterisation of straight sided specimens. Positioning of polymer dampers between the slack rod and slack adaptor allows the damping of the system to be controlled and reduces some of the observed system ringing, at the expense of the strain rate rising period of the system. In contrast, both LMD (b) and LMD (c) require the use of long specimens that are machined into dog bone shapes to

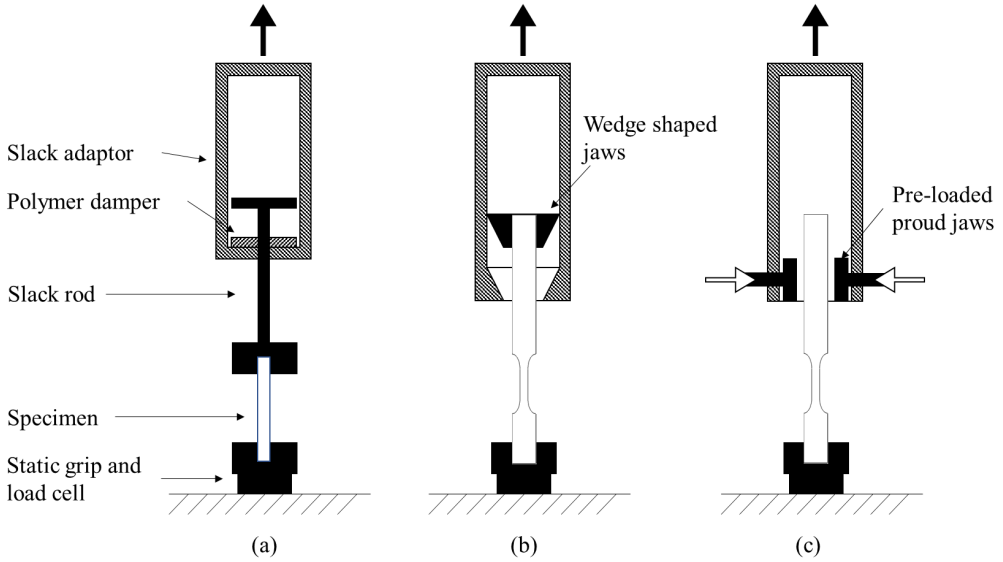

Figure 2.14: Schematic of lost motion devices employed on high speed servo-hydraulic machines to reduce inertial loading effects (Adapted from [92]).

provide sufficient distance to accelerate the actuator and remove the inertial loading period. LMD (b) integrates the specimen and the upper jaw to provide a load train that is significantly shorter and thus stiffer than LMD (a) loading mechanism, this potentially helps to reduce the noise of the system. A lightweight solution is offered by LMD (c) which is a patented solution by Instron (from this point is referred to as the fast jaw system). The minimum acceleration distance of LMD (c) is determined by the specimen length, however, the use of dog bone specimens with short gauge lengths enables the user to extract high strain rates ($\sim$1000 s^{-1}) and a secondary load instrumentation below the gauge in a elastic region. Two jaw faces are mounted within the fast jaws, these are held proud of the specimen surface via knock out wedges, as the fast jaw is accelerated at a pre-determined height the wedges are removed and the specimen loaded at the desired speed. Due to the lower inertial mass between jaws and the specimen, the gripping mechanism is capable of achieving the lowest load rising time of the three configurations displayed. Further information on the Instron fast jaw system in Section 3.3.3.

The primary advantage of SH test frames is the ability to conduct experiments with specimen at an increased length scale, for composite laminates this enables the user to capture material data at the RSE of the global material system rather than characterising the response of an individual constituent. Servo-hydraulic sys-

tems are capable of testing significantly larger specimens (in comparison to a SHTB setup) up to a capacity of 100 kN [111]. The increased failure loads of large length scale composite specimens challenges the ability to induce stable strain rates over the test period. Large inertial loads increases the retardation of the cross-head at the onset of loading introducing non-linear effects within the experimental strain rate. According to metallic SH standard ISO 26203-2:2011 (previously discussed in Section 2.2) the strain rate is determined based on the deformation rate of the plastic straining period of the experiment between yield and peak force [92, 104]. Due to the experimental noise induced in the experiment the experimental strain rate between yield and peak force must be within ± 30 % of the average experimental strain rate. Predominantly authors of composite dynamic characterisation studies report the determined mechanical properties as a function of the nominal strain rate. Longana [110] reviewed the elastic modulus of UD glass epoxy composite laminates at nominal strain rates of 20 $s^{-1}$and 80 s^{-1}using digital image correlation (DIC) and grid method optical strain measurement techniques. Based upon the 100 mm gauge length and desired test velocities of 2 ms^{-1} and 8 ms^{-1}. Figure 2.15 shows the experimental engineering strain rates and engineering stress-strain plots for tests conducted at 2 ms^{-1} (a & b) and 8 ms^{-1} (c & d) respectively. The experimental strain rate in Figure 2.15 (b) is slightly reduced, peaking at 16 s^{-1} from the 20 s^{-1}nominal rate before settling at approximately 8 s^{-1}, this could be due to the respective compliance and dynamic response of the custom built slack adaptor or the inability of the servo-valve within the SH frame to adjust the velocity profile to overcome the inertial load of the specimen. In comparison when the experiment is conducted at 8 ms^{-1} the inertia of the slack adaptor is sufficient in order to overcome the inertial load of the specimen and the strain rate can be observed to converge to an average greater than 70 s^{-1} beyond 1 % strain. Figure 2.15 (a) and Figure 2.15 (c) show that the specimens initially behaved in a linear elastic manner, however, once the specimen exceeds 1 % - 1.5 % longitudinal engineering strain the stiffness of the specimen visibly reduces. The inability for the strain rate to converge to a constant value will induce transient loads in the specimen due to its acceleration profile, as the specimen undergoes damage this may be introducing alternative damage mechanisms. A further challenge is presented when attempting to characterise the modulus of CFRP materials at elevated strain rates, due to failure occurring at approximately 1 % - 1.5 % tensile strain and stiffness reduction appearing to occur from 0.2 % tensile strain in woven fabrics. No literature has been identified that discusses the period of strain rate rising with an emphasis on its effect on the modulus and failure properties of woven CFRP materials. Therefore careful assessment of the mechanical properties must be determined based on the strain rate profile during the test period, and particularly during periods of localised damage.

In summary the use of SHTB's allow for the characterisation of composite materials at very high strain rates. However, the equipment is not suitable for use in low to intermediate rates due to the large output bar lengths required to remove stress wave superposition at these test speeds. Composite characterisation on a SHTB is further limited due to the stress heterogeneity observed in small specimen sizes. In comparison high speed servo-hydraulic machines have been proven capable of characterising a material at strain rates between 0.1 and 1000 s^{-1}. Due to their design they are capable of testing significantly larger specimens with geometries closely aligned to those used in standardised quasi-static characterisation tests (Section 3.3) which reduce the risk of size effects, however, care must be taken when defining the strain rate profile of the experiment since transient loads during damage coalescing may potentially vary the damage mechanisms observed during the experiment.

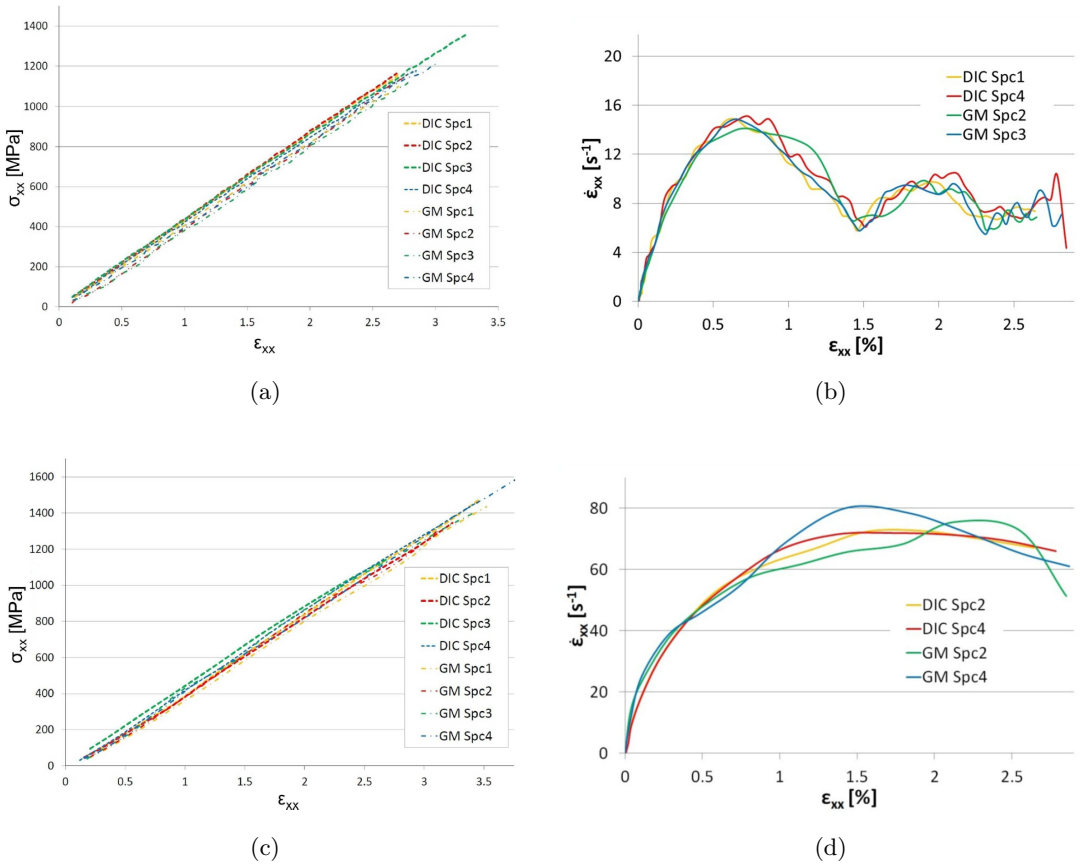

Figure 2.15: Longitudinal engineering stress-strain response of glass-fibre epoxy UD composite specimens evaluated at nominal strain rates of 20 s^{-1}(a) and 80 s^{-1} (c), the respective experimental strain rate plots are determined based on the temporal strain measurements recorded using optical digital image correlation (DIC) and grid method (GM) techniques (Adapted from [110]).

2.3 Current understanding of the strain rate sensitivity of CFRP laminates

Section 2.2 has discussed the two most common types of test machines used in the dynamic characterisation of composite strain rate sensitivity under tensile loads. This section will present the current understanding of strain rate sensitivity of both UD and woven GFRP and CFRP laminates making reference to the different test methods employed. The starting point for this study was an early review in the strain rate sensitivity of composites presented by Jacob et al. [112], this has since been updated by Ray et al. [113]. Both papers highlight how the majority of data collected has been conducted using a SHTB to characterise UD laminates composed of glass fibres not aligned to the loading direction. The following review aims to establish the current knowledge regarding the tensile behaviour of automotive specific large tow woven carbon epoxy laminates. However, due to the lack of data regarding this precise material system, the review starts by considering the effect on glass and carbon UD fabrics before turning to the impact of fabric weaving on the laminates strain rate sensitivity.

Experiments evaluating the characteristics of individual fibre tows without the supporting matrices are challenging even at quasi-static speeds and therefore have not been conducted at elevated strain rates. As a result the strain rate sensitivity of the fibres must be based upon the results observed during laminate testing. In comparison, experiments have been conducted to review the strain rate sensitivity of the polymer matrix. Gilat et al. [101] evaluated the response of a epoxy polymer to loading rate and observed that they behave in a highly viscoelastic manner. Experiments were conducted on dog bone specimens mounted within a servo hydraulic machine without a LMD for testing at strain rates of 1 s^{-1} and a SHTB was used for characterising materials at strain rates of 360 s^{-1} . The lack of a LMD results in a long inertial loading period significantly reducing the strain rate at the start of the test, this may explain why the measured modulus at 1.3 s^{-1} was equal to the the quasi-static value. In contrast to the linear material response, the post yield behaviour of the material highlighted a classical viscoelastic response, experiencing an increase in strength and a reduction in ultimate strain (Figure 2.16). Specimens loaded at 360 s^{-1} using a SHTB did not require the use of a LMD due to the experimental arrangement, these specimens also experienced increasing strength and truncating strain, whilst also observed a large increase in modulus. Although the response has required estimating due to the inability to record the true material response due to ringing and premature specimen failure induced by the employed strain gauges. A similar response was observed by both Xiao [114]and Al-Zubaidy [115] when they

isolated the behaviour of the polymer matrix systems.

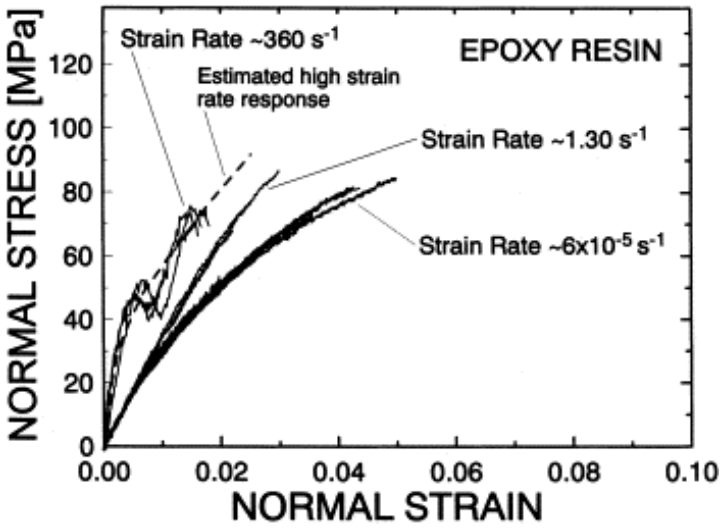

Figure 2.16: Stress strain plot of a pure epoxy dog bone specimen evaluated using a SHTB at intermediate strain rates [101] .

As well as testing pure epoxy, Gilat et al. also used the SHTB to review the effect of changing loading angle on UD IM-7/977-2 CFRP laminates [101]. The warp fibre angle was positioned such that loading angles of 10°/ 90°/45°/ ±45°were achieved within dog bone samples with a gauge region of 3.2 x 9.5 x 2.5 mm^3. The authors observations of increasing transverse modulus and strength were supported by Shokreigh et al. [116] who investigated the transverse behaviour of glass epoxy UD using a SH machine, the continuity across different fibre materials and test systems highlights that this matrix dominated failure is highly sensitive to loading rate.

As previously discussed the cross ply laminate loaded at 45° undergoes shear damage mechanisms that are dependent upon the matrix properties. Since it has been observed that the viscoelastic nature of the matrix is highly sensitive to strain rate, it can be assumed that the off-axis loading will be the most sensitive to strain rate than that in the fibre direction. However, although all authors suggest the same trends; increasing modulus, delayed yield and increased strength, most authors differ on the observed ultimate strain to failure. For similar T700 UD carbon epoxy material system Gilat et al. [101] and Berthe et al. [117] observed different responses for specimens loaded in in-plane shear ($[\pm 45]_s$). Gilat observed that as strain rate increased, the ultimate strain remained approximately constant (Figure 2.17 (a)), whilst in comparison a more highly viscoelastic response was observed by Berthe with heavily truncated ultimate strain (Figure 2.17 (b)). Further investigation by Cui et

al. [118] on the response of $[\pm 45]_{4S}$ UD carbon fibre epoxy at strain rates between 0.0005 and 1300 s^{-1} using a SHTB, found that the laminate underwent increasing modulus, yield and ultimate shear strength with strain rate whilst the ultimate shear strain was reduced, although not as severely noted by Berthe. This variation in failure response can also be observed by differences in failure mechanisms in the loaded specimens. Cui et al. used SEM micrographs to show evidence of matrix damage earlier in the damage sequence due to the higher tensile stresses leading to the failure of the matrix, whilst the final ultimate failure of the laminate was due to the inter-lamina delamination of the specimen. In comparison Shokreigh et al. evaluated a glass-epoxy UD laminate under [±45] loading, however, unlike the work conducted on the SHTB, the authors used a SH machine with specimens geometries of 20 x 12.7 x 2.3 mm^3 in order to achieve the high desired strain rates yet attempt to alleviate free-edge stresses [119]. However, since the length to width ratio is less than one, continuous fibres are rigidly gripped within the upper and lower jaw. As a result the fibre rotation is restricted, loading the fibres in tension and thus increases in modulus and shear strength are observed.

Due to the challenge of characterising the individual fibre strain rate sensitivity, they must be estimated based upon the response of warp aligned UD specimens. The early work suggested an insensitivity to strain rate of composites tested in the warp direction [120]. This was supported in part by research conducted by Shokrieh et al., who utilised a SH machine to apply tensile loads at 85 s^{-1} to small UD GFRP samples [121]. The modulus appeared to be rate insensitive until 0.6 % strain, at which point the material appeared to increasingly strain hardening with rate until tensile fracture of the laminate occurred at a constant ultimate strain, resulting in an increase of tensile strength with increasing strain rate. The final fracture surfaces were found to show no signs of highly localised damage as suggested by other authors and instead the fibre cracks that lead to the ultimate failure were observed in both tab regions and the gauge length leading to a very uneven fracture surface. Wang et al. [122] used the fast jaw system on an Instron SH machine in order to characterise the response of large CFRP UD laminates under warp tension. Between 14 and 42 s^{-1}, the tensile strength was found to increase by 7.2 %, however, the modulus was found to remain approximately constant. In comparison Longana [123], who characterised the longitudinal, transverse and shear modulus of carbon and glass epoxy UD laminates of large scale specimens (15 mm x 100 mm x 2 mm) using a SH machine complete with an LMD (Type (a) Figure 2.14) fixture, saw an increase in modulus. Longana observed that as the strain rate increased nominally from 0.001 s^{-1} to 62.5 s^{-1} the elastic modulus increased by 4.5 % for the carbon-epoxy material, whilst a glass-epoxy increased by 8.7 % at 35 s^{-1}. In contrast to these small increases in modulus and strength with strain rate Al-Zubaidy et al. [115] utilised

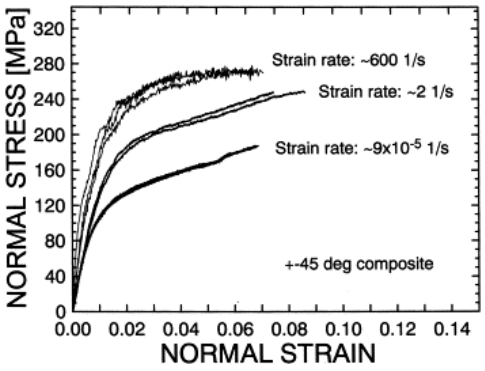

(a)

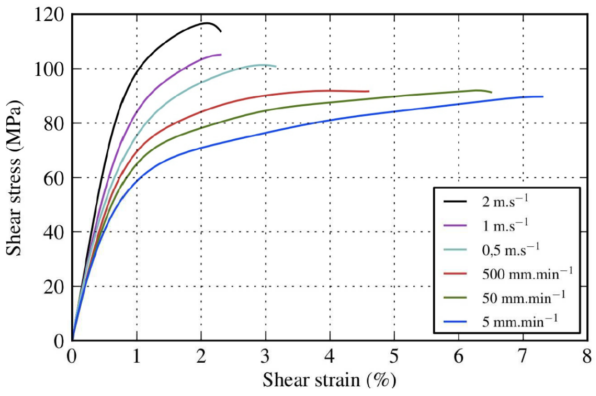

(b)

Figure 2.17: Differences in observed engineering shear stress vs shear strain plots for tests conducted at multiple strain rates on carbon epoxy lamiantes. [101, 117]

a drop weight tower to characterise the longitudinal tensile properties of a CFRP laminate and observed a 43 % and 20 % increase in tensile strength and modulus respectively between quasi-static and 87.4 s^{-1}. This is substantially larger than any other strain rate sensitivity observed in literature and is thought to be due in part to the inertial ringing of the drop weight methodology.

As previously mentioned determining the strain rate sensitivity of a laminates mechanical properties in the warp direction is challenging and therefore has not been attempted as much as off-axis material characterisation. Other attempts at extracting the longitudinal and transverse modulus using compression testing have been conducted [124–126]. However, since the material response is substantially different with fracture dominated by fibre kinking they have not been detailed in this section, however, lessons based on dynamic strain measurement are detailed in Chapter 3.

Early research into the effect of strain rate on different woven fabric architectures was conducted by Welsh and Harding [127]. The authors reviewed the strength

and stiffness sensitivity of 3K T300 five harness satin carbon polyester subject to strain rates up to 700 s^{-1} using a SHTB. The large unit cell of the fabric combined with the small (5 mm x 6 mm) gauge area required for use with a SHTB resulted in the tested specimen volumes containing with few interstitial sites and providing a representative volume with more similarity to that of a cross-ply UD laminate rather than the woven fabric. Tensile modulus and strength was found to increase only slightly between quasi-static strain rates and 0.1 s^{-1}, however, at the strain rates of 700 s^{-1} both the modulus and strength increased significantly. Kawata et al. supported their findings of both increasing strength and modulus, and the introduction of premature yielding as the specimens approached failure [128]. The increase in mechanical properties challenged Welsh and Hardings [127] previous work on UD laminates, that had highlighted the rate independence of carbon fibres to axial loads. This suggests that localised stiffening of the matrix between/within tows as the strain rate increases improves the load distribution through the laminate. Despite the large experimental scatter in the experiments conducted by Welsh and Harding the localised stiffening of the matrix is supported by Gerlach et al. who investigated the effect of rising strain rate on the tensile response of heavily crimped 3D woven laminate and saw an increase in failure stress with damage isolated to localised regions [129]. This all suggests that as the strain rate is increased the onset of damage is delayed in comparison to quasi-static experiments.

Foroutan led one of the few studies to provide direct comparison between different carbon fabric architectures and their effect on failure strengths in the warp fibre direction [130]. Using a SHTB with a common dog bone specimen geometry with a gauge region of 5 x 10 mm^2 the author was capable of achieving strain rates of 500 s^{-1}. Three carbon fibre fabrics were considered, carbon fibre epoxy laminates with a plain weave (material A) and twill (material B) weave carbon composites were reviewed alongside a five harness satin bis-maleimide laminate (material C). Figure 2.18 shows the tensile stress strain response of the three fabrics. The strain at peak force of each of the material systems was seen to be lower under dynamic loading whilst the modulus and failure strengths (A - 10%, B - 11.6 % and C - 33 %) are significantly increased. Post peak strength, the specimens appear to undergo an extensive strain softening to ultimate fracture. The quasi-static tensile behaviour of the twill fabric compared to that of the plain and satin fabrics appears to challenge the consensus that twill fabrics offer improved mechanical properties (discussed in Section 2.1.3). Potential reasoning for this is the lack of experimental evaluation for size effects, comparing standardised specimen geometries with those of the SHTB specimen under quasi-static conditions, which could introduce damage mechanisms that lead to the premature failure of the laminate [131]. Chen et al. also used a SHTB to investigated small plain weave T300 1K carbon epoxy laminates subject

to [0°] tensile loads at 130 s^{-1} [132]. The authors noted an increase in modulus with delayed yield leading to the failure strength increasing by 41 % to 833 MPa. However, as the strain rate increased, so too did the non-linear strain softening post yield, resulting in ultimate strains 85 % larger than their quasi-static counterparts. The strain softening highlighted in Figure 2.18 is a result of the open loop nature of SHTB whereby the laminate is fully disintegrated rather than the test being terminated due to a drop in load. Chen in comparison observed definitive yielding and strain softening, which could be a result of the size effect of the small specimens employed. Due to the balanced nature of woven fabrics Naik et al. [133] demonstrated that the strain rate sensitivity is independent of whether the mechanical properties are reviewed in the warp and weft fabric directions.

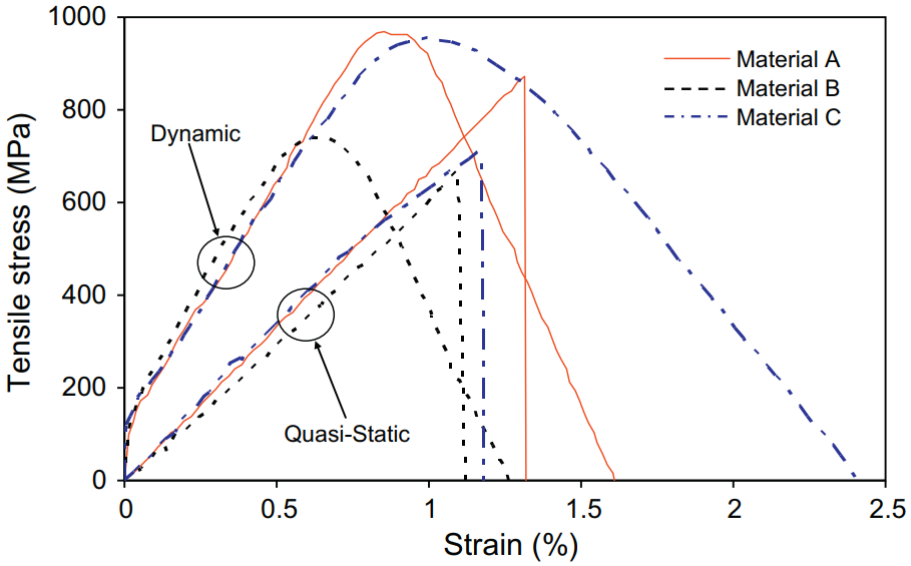

Figure 2.18: Comparison of T700 plain (material A) and twill (material B) weave carbon epoxy composites with a T700 five harness satin weave carbon bis-maleimide (material C) composite under quasi-static load conditions and 500 s^{-1} [130].

Bergmann et al. used a SH machine to review the effect of strain rate on 1K and 3K, plain and twill weave fabrics under $[\pm 45]_s$ bias tension loads [134]. The use of a SH machine enabled the author to employ large scale specimens with a gauge area of 25 x 130 mm^2. Figure 2.19 shows the engineering stress-strain plots for each of the fabrics at strain rates between quasi static (0.001 s^{-1}) and 80 s^{-1}. The 3K plain weave fabric (Figure 2.19 (a)) has quasi-static stiffness of 11.3 GPa, 7.6 % greater than that of the 1K plain weave fabric ((Figure 2.19 (b)). However, as the strain

rate is increased to 20 s^{-1} the increased tow count induces an increase in the shear modulus of 47 % to 16.7 GPa, this is 27.4 % greater than the 1K fabric at the same rate. The ultimate strength increases by 17.5 % in comparison to the 3.5 % by the 1K fabric at 20 s^{-1}. In comparison the 1K fabric appears more sensitive to ultimate strain, between 0.001 and 20 s^{-1} the failure strain reduces by 24.1 %, in comparison the 3K fabric reduces by just 5.9 %. This reduction in ultimate strain of the 1K fabric may be due to external factors since it is observed as a sudden truncation at 20 s^{-1} which remains approximately stable at 80 s^{-1} in comparison to that observed at 0.001 and 0.1 s^{-1}, and is unexplained by the authors. The effect of strain rate on weave architecture is observed through the comparison of the 3K plain weave with the 3K twill weave fabric (Figure 2.19 (c)) with consistent FVF (51 %). Unlike the plain weave, the twill weave experiences a 6.7 % increase in stiffness and a 4.2 % increase in failure strain whilst the failure strength was comparable with an 18.3 % increase up to 20 s^{-1}.

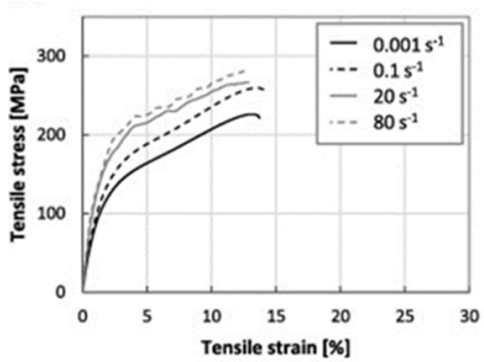

(a)

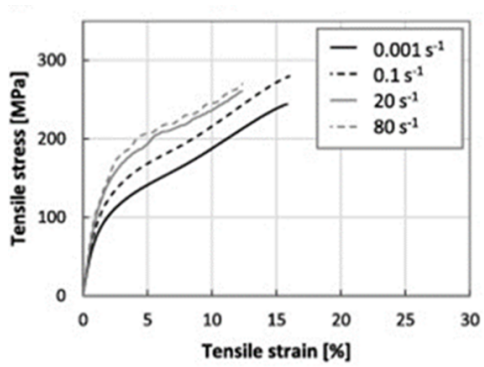

(b)

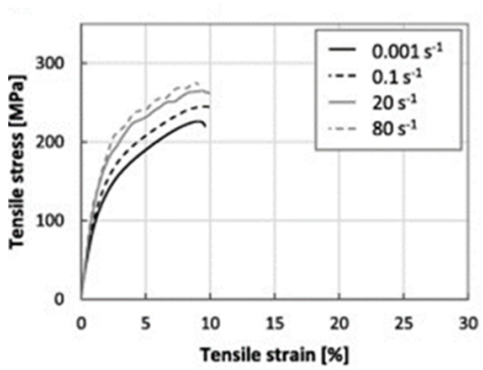

(c)

Figure 2.19: Comparison of the engineering tensile stress - strain plots of (a) 200 gsm plain weave 3K carbon epoxy, (b) 93 gsm 1K plain weave carbon epoxy and (c) 200 gsm 3K 2 x 2 twill carbon epoxy between nominal strain rates of 0.001 s^{-1} and 80 s^{-1} [134].

Li et al. [135] investigated the response of quasi-isotropic $[-45/0/45/90]_{6S}$ T700 3K plain woven carbon epoxy composites between 0.5 and 2300 s^{-1} using a SHTB. The dog bone samples had a gauge volume of 3 x 6 x 2 mm^3. Li observed significant axial strength increases from 374 MPa at 0.5 s^{-1} to 791 MPa to 1290 MPa as the strain rate was increased between 1281 and 2310 s^{-1} respectively. The increase in strength is attributed to the stiffening of the matrix within the [±45] tows, however, they still prove to be the weakest constituent as the global fracture of the laminate occurred along the [±45] tows with the dynamic and quasi-static response being very similar.

All of the research presented so far discusses how the global macro-mechanical behaviour of the laminate appears to be improved with strain rate derived from the stiffening of the viscoelastic matrix. The challenge with determining the damage sequence of dynamic tests on a microscopic scale is that as mentioned previously, both SHTB and SH machines operate in open loop removing the ability to remove the specimen loading at the point of fracture, this results in the total disintegration of the laminate. As a result, the inspection of fracture surfaces that could have been created either during the test or during the laminate disintegrating. In comparison the closed loop quasi-static frames allow for partial loading and controlled unloading of the specimen at fracture. This allows for detailed assessment of the damage mechanisms to be assessed using SEM and optical microscopic techniques. Despite the issue of reviewing specimens produced by open loop experiments Naresh et al. [136] observed that the fibre-matrix interface for a [0/90] plain weave carbon epoxy laminate appeared to weaken with increasing strain rate. The authors noted that despite increased tensile strength of 6.3 % and a modulus increase of 1.3 % at a nominal strain rate of 542 s^{-1} , SEM micrographs showed that the fibre-matrix interface appears to be weakened with strain rate due to the reduced matrix residue at fibre pull out sites in the dynamic specimens. Fitoussi et al. [108] used a poly methyl meth acrylate fuse running in series with the specimen (Figure 2.20) to run an interrupted test on a dog boned five harness carbon epoxy with the warp at 45º to the loading direction at 15 s^{-1}. Although the use of a fuse enabled the author to run an interrupted test, the specimens experienced spring-back loads induced by the relaxation of the specimen and the mass of the fixturing potentially affecting the observed damage. The macro damage was determined as the loss in modulus during repeated cyclic loading of the specimen at each of the desired strain rates. As the strain rate was increased, the threshold for damage development occurs at higher tensile strain, delaying the material yield allowing the component to undergo a higher global stress. The author also observed that although the initial onset of macroscopic damage was delayed, once the damage begins to propagate through the specimen it appears to do so in a rate independent manner. The isolation of microscopic damage is done more qualitatively using SEM, which as previously discussed

may be affected by the spring-back of the specimen. Irrespective of strain rate the specimens were found to undergo matrix cracking as the initial onset of damage, however, the damage appeared to be highly localised in comparison to the diffusive damage that occurs of the sample at quasi-static speeds. This has been suggested to be related to the viscoelastic nature of the matrix. Battams [107] utilised a similar loading methodology applied by Fitoussi in order to review the damage development in partially loaded cross ply UD glass-epoxy laminates. The author introduced a anti-buckling feature to eliminate the spring-back of the specimen, although this required straining the specimen to ε_{yy}= 0.35 % prior to the test commencing. Battams observed that although the damage sequence remained constant irrespective of strain rate, specimens loaded at 32 s^{-1} exhibited highly localised damage with much larger transverse crack propagation.

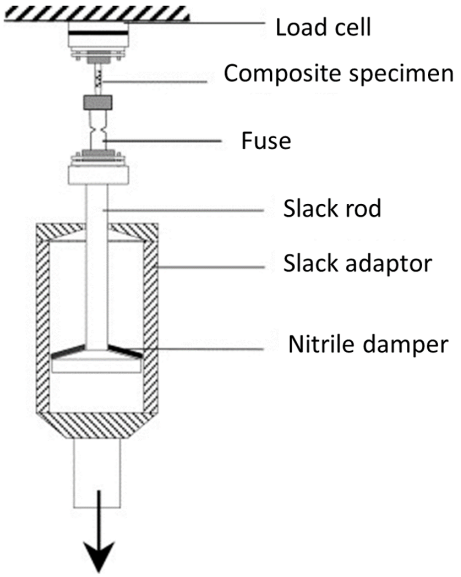

Figure 2.20: Schematic of fuse design for interrupted tensile testing on a open loop servo-hydraulic test machine developed by Fitoussi et al. [108].

In order to simplify the comparison of different materials and test systems, the results discussed throughout Chapter 2 have been summarised in Tables[2] 2.1 and 2.2.

[2]Table Key; E_{11T} - Elastic modulus in the warp fibre direction, E_{22T} - Elastic modulus in the weft fibre direction, G - shear modulus, XT - Tensile strength in warp direction, YT - Tensile strength in the weft direction , $TAU1$ - shear strength at yield, SC - shear strength at failure, PLW - plain weave, TW - twill weave, STW - satin weave.

Table 2.1: Summary of strain rate sensitivity of composite materials subject to tensile loads using a servo hydraulic test machine.

Author [Reference]	Material Fibre/matrix	Material Architecture	Layup	Strain rate (s^{-1})	Strain rate effect on modulus	Strain rate effect on strength
Lee [137]	GFRP	PLW	$[0/90]_{18}$	0.1 - 20	-	17 % increase fracture energy
Okoli [138]	GFRP	PLW	$[0/90]_{18}$	0.1 - 20	Increase E_{11}/E_{22}	Increase XT
Fitousii [108]	CFRP	5HS SW	$[\pm 45]_{4S}$	0.5 - 60	No effect on G_{12}	Increase SC/TAU1
Longana [123]	GFRP	UD	$[0]_4$	QS - 80	Increase in E_{11}	-
Longana [123]	CFRP	UD	$[0]_4$	QS - 80	Increase in E_{11}/E_{22}	-
Wang [122]	CFRP	UD	$[0]_4$	14 - 42	No effect on E_{11}	Increase XT
Shokreigh [119]	GFRP	UD	$[\pm 45]_{3S}$	1.1^{-3}- 84	No effect on G_{12}	Increase SC/TAU1
Shokreigh [116]	GFRP	UD	$[90]_9$	1.7^{-3}- 85	Slight increase E_{22}	Slight increase YT
Shokreigh [121]	GFRP	UD	$[0]_5$	1.7^{-3}- 85	No effect on E_{11}	Increase XT
Bergmann [134]	CFRP	3K PL	$[\pm 45]_{2S}$	20 - 80	Increase in G_{12}	Increase SC/TAU1
	CFRP	1K PLW	$[\pm 45]_{2S}$	20 - 80	Increase in G_{12}	Increase SC/TAU1
	CFRP	3K 2x2 TW	$[\pm 45]_{2S}$	20 - 80	Increase in G_{12}	Increase SC/TAU1
Berthe [117]	CFRP	T700 UD	$[\pm 45]_{2S}$	1.1^{-3}- 50	Increase in G_{12}	-
	CFRP	T700 UD	$[90]_8$	1.1^{-3}- 21	No effect on E_{22}	-

Table 2.2: Summary of strain rate sensitivity of composite materials subject to tensile loads using a Split Hopkinson Tensile Bar.

Author [Reference]	Material Fibre/matrix	Material Architecture	Layup	Strain rate (s^{-1})	Strain rate effect on modulus	Strain rate effect on strength
Gilat [101]	CFRP	UD	[10]	5^{-5}- 400	No effect up to 1 s^{-1} then increase $E_{11}/E_{22}/G_{12}$	Increase in XT
	CFRP	UD	$[\pm 45]_S$	5^{-5}- 400		Increase SC/TAU1
	CFRP	UD	[90]	5^{-5}- 400		Increase in YT
Foroutan [130, 131]	CFRP	PLW	$[0/90]_8$	1^{-4}- 500	Increase in E_{11}	Increase XT
	CFRP	5HS SW	$[0/90]_6$	1^{-4}- 500	Increase in E_{11}	Increase XT
	CFRP	2 x 2 TW	$[0/90]_6$	1^{-4}- 500	Increase in E_{11}	No effect XT
Al-Zubaidy [115]	CFRP	UD	[0]	2.4^{-4}- 87	Slight increase in E_{11}	Increase XT
Cui [118]	CFRP	UD	$[\pm 45]_S$	5^{-4}- 1300	Slight increase in G_{12}	Increase SC/TAU1
Naik [133]	GFRP	PLW	$[0]_7/[90]_7$	180 - 380	Increase in E_{11}/E_{22}	Increase in YT / XT
Staab [99]	GFRP	UD	$[\pm 45]_{4S}$	10^{-4}- 1000	No effect on G_{12}	Increase SC/TAU1
Gowtham [139]	GFRP	UD	$[\pm 45]_{4S}$	QS - 180	Reduction in G_{12}	Increase SC/TAU1
Taniguchi [140]	CFRP	UD	[90]	QS - 100	Increase in E_{22}	Slight increase YT
	CFRP	UD	[10]	QS - 100	Increase in E_{11}	Increase XT
	CFRP	UD	[45]	QS - 100	Reduction in G_{12}	Increase SC/TAU1
Welsh [127]	CFRP	5HS SW	$[0/90]_7$	0.017 - 1000	Slight increase in E_{11}	Slight increase in XT

2.4 Summary

This chapter presents the state of the art for the characterisation of tensile carbon fibre composites with a focus on the effect of testing at elevated strain rates. Composite tensile failure is the result of the culmination of microscopic failures, this damage is driven by the heterogeneity of the material system and the loading position relative to the each constituent. When the loading angle is aligned to the fibres, due to their brittle nature and low ultimate strain the fibres are the limiting constituent, resulting in fibre fracture as the part continues to be loaded. In comparison as the loading angle is increased the failure becomes more dependent upon the shear behaviour of the fibre-matrix interface and the matrix, which behave in a more ductile manner. Woven fabrics offer balanced mechanical properties in the warp and weft directions and improved draping characteristics in comparison to UD materials. However, as a result of the weaving process, crimp is induced into the fibres along with resin rich regions at the interstitial points within the weave. Both of these features of woven fabrics have been shown to reduce the mechanical properties of the laminate. In order for woven composites to be applied to the automotive industry they must be cost effective, as a result the fabrics chosen are often heavy (400 gsm and above) and have a large tow count (12K and above). There is little literature reviewing these specific material systems, commonly woven fabrics up to 6K have been the subject of experimental studies. These tow sizes have demonstrated increased susceptibility to matrix damage due to the increased volume of resin rich regions surrounding the ovular fibre cross section and the interstitial sites. This damage has been observed to occur much earlier within woven laminates in comparison to their UD and cross-ply counterparts. As a result it is thought that the application of larger tow counts will further increase the heterogeneity of the laminate, and the rate of damage propagation due to extensive matrix cracking in particular.

Based on the prescribed automotive legislative crash test velocities previous researchers have identified that the average strain rates expeienced by automotive structures are within the intermediate regime between 10 and 100 s^{-1}. The review of dynamic material characterisation clearly highlighted how the lack of standardised composite methodologies has resulted in different experimental techniques and specimen geometries being applied in order to review the laminate response at intermediate and high strain rates. The strain rate sensitivity of continuous reinforced composites (Section 2.3) highlighted that the largest increase in stiffness and strength are seen in off-axis matrix dominated failure mechanisms. This is primarily thought to be a result of the viscoelastic nature of the polymer matrix. Increases in modulus and

strength are also observed within warp loaded laminates, this is thought to be due to the stiffening of the polymer matrix in the region surrounding the fibre failure improving the transfer of load to the adjacent fibres. However, although literature points to a common trend, the extent of the strain rate sensitivity has been disputed and is dependent on the specimen geometry employed, which is a result of the constraints of the employed experimental setup. The most commonly employed methodology is an elastic bar system that requires a small specimen mounted between an incident and transmission bar. The experimental response of size effects has been studied and small specimens have been shown to have failure mechanisms that are dictated by the free-edge interlaminar shear stress concentrations in cross-ply UD fabrics and architectural features in woven fabrics. It was shown that authors had attempted to characterise the global response of woven materials at elevated strain rates using specimens with width below the unit cell of the fabric and closer to the geometry of a single tow. Characterisation on this length scale is unable to capture the heterogeneity of the laminate and therefore invalidates the data obtained, furthermore, characterisation of off-axis properties can also lead to tensile loading of fibres distorting the experimental stress state from that desired. In comparison, high speed servo-hydraulic machines are unable to load materials within the strain rate regime of multiple 1000's s^{-1}, which is achievable with a SHTB. However, they offer the ability to evaluate the behaviour of significantly larger specimens, and within isotropic metallic research have demonstrated to be capable of loading specimens up to 1000 s^{-1}. Although these strain rates are unachievable with composites (due to the requirement to have longer straight sided gauge lengths than that of metallic dog boned specimens) the larger specimen size enables the user to evaluate a geometry that provides a true representation of the global mechanical properties of the material system. Thus eliminating the global failure of the laminate being dominated by is large scale heterogeneity, which is thought to be particularly prevalent when characterising large tow count woven fabrics.

2.4.1 Research opportunities

The use of continuous carbon fibre reinforcement in polymer matrices has been identified as a solution to achieve extensive automotive vehicle light-weighting. However, the response of automotive length scale materials is less understood based on the interest of available published experimental studies primarily having concentrated on UD, cross-ply and aerospace specific fibre architectures (~ 3K). This presents an opportunity to review the response of a previously scarcely considered material system. Previous dynamic characterisation studies have presented a common trend of matrix dominated properties being highly sensitive to the applied strain rates.

However, due to the large scale heterogeneity and large resin rich regions induced by the architecture of the structure it is thought that the response of such coarse woven fabrics will be dependent on strain rate when loaded in both the longitudinal (fibre dominated) and off-axis (matrix dominated) axis. Therefore it is the purpose of this research to identify the effect of intermediate strain rates up to 100 s^{-1} on the mechanical properties of longitudinal and off-axis tension in order to populate material cards suitable for vehicle length scale automotive crash simulations.

In order to target these research opportunities the following specific objectives were established;

1. Develop a robust and efficient experimental methodology capable of characterising a woven composite laminate at multiple strain rates within the intermediate regime that is applicable to automotive crash ($2 \times :10^{-4}$ s^{-1} to 100 s^{-1}):
    - Assessment of the patented Instron Fast Jaw system for its suitability to characterise continuously reinforced composite materials.
    - Development of a LMD that is a combination of LMD (a) and (b) (Figure 2.14) to increase the stiffness of the load path and limit the resonance amplitude; whilst being capable of loading high capacity composite specimens (100 kN) at strain rates of up to longitudinal strain rates of 100 s^{-1}.
    - Development of a robust instrumentation methodology to review the strain of a specimen on a specimen length scale over the course of a dynamic experiment in order to provide data that is devoid of potential errors based on experimental and material architectural effects.
    - Establishment of a coupon geometry capable of representing the global macro mechanical response of the heterogeneous material system yet minimise the cross section in order to reduce the resistive loads of the specimen and therefore the strain rate rising period.
    - Establishment of a working criteria for establishing the validity of a dynamic test based on the experimental strain rate recorded on the surface of the specimen.
2. Characterisation of the elastic and damage response of an automotive specific woven carbon fibre composite up to 100 s^{-1} in order to define the effect of strain rate on;
    - The elastic modulus (E_{11}), tensile strength (XT) and ultimate strain (E_{11T}) of longitudinal $[0]_{ns}$ specimens .

- The shear modulus (G_{12}), shear strain (GAMMA1) and shear strength (TAU1) at yield and shear strain (GMS) and shear strength (SC) at failure respectively using off-axis $[45]_{ns}$ specimens.

3. Review the capability of LS-DYNA material card library to model the strain rate behaviour of the material system.
    - Review the suitability of LS-DYNA material cards to model the non-linear behaviour that occurs during automotive crash events.
    - Experimental validation of the rate sensitive material card using a building block approach in order to review the model accuracy at a single element and coupon ($[0]_{ns}$, $[45]_{ns}$ and $[0/45]_{ns}$) level scale.

2.4.2 Thesis structure

This thesis has a total of seven chapters. Chapter 1 provided the background of the project in order to provide context to many of the choices made during the latter parts of this thesis. Chapter 2 built upon the basic introduction to composite loading under tensile in-plane loads and highlighted the current understanding of strain rate sensitivity of composite laminates. It concluded by outlining the aims and objectives of this project. In order to achieve these objectives the research conducted has been split across the following chapters;

Chapter 3 Chapter 3 introduces the automotive relevant 12K 2 x 2 twill woven fabric and how it is manufactured to produce composite laminates that are evaluated throughout this thesis. Detailed descriptions of the quasi-static and dynamic Instron equipment used at WMG are provided along with an introduction to the use of the GOM ARAMIS digital image correlation equipment for the measurement of surface strains. A preliminary investigation into the Instron VHS fast jaw system is conducted to review its suitability for characterising continuously reinforced composite laminates.

Chapter 4 Chapter 4 commences with a benchmarking study that defines the capabilities of the composite material system chosen for this research at quasi-static strain rates according to ASTM standard test procedures. The mechanical behaviour extracted from these experiments is utilised to define the requirements of the high capacity slack rod fixturing developed for the VHS 8800 system. An optical measurement study is conducted on the standard specimens in order to define the

minimum representative surface elements, this represents a novel specimen reduction methodology capable of establishing coupon geometries that are not affected based on the heterogeneity of the woven fabric. However, since the plane stress condition is assumed through the development of the specimen the chapter concludes with the experimental validation of the coupons using the quasi-static frame, statistical analysis is employed to demonstrate that there is not a statistical difference between them and the standard geometries.

Chapter 5 Chapter 5 utilises the dynamic characterisation technique developed over the course of Chapters 3 and 4 to characterise the automotive specific 12K 2 x 2 twill weave composite laminate at discrete strain rate intervals between nominal longitudinal strain rates of 6.7×10^{-2} s^{-1} to 1.0×10^{2} s^{-1}. Initially the tensile behaviour is presented, the effect of the specimens inertial load is presented along with the derivation of the experimental strain rates prior to the statistical analysis of the results using F-test's and Tukey HSD tests. Following this, the results of the in-plane shear experiments are provided and analysed using the same statistical tools along with an analysis of the experimental strain rates experienced as a result of the bi-linear behaviour of the laminate. The chapter concludes with a discussion of the results as well as the experimental technique.

Chapter 6 Chapter 6 presents the findings of a review of the application of the gathered strain rate sensitive data and its application to LS-DYNA composite material models. experimental data. The challenges of modelling the tensile behaviour of brittle laminates and the bi-linear shear response within *MAT_058 are identified using single element models. The building block modelling approach is then applied to review the effect of strain rate modelling on the tensile, shear and quasi-isotropic response of the automotive specific 12K 2 x 2 twill weave composite laminate on a coupon model length scale.

Chapter 7 Chapter 7 presents a summary of the work conducted throughout this thesis before identifying the key findings. The chapter concludes by identifying the limitations of the work and areas of potential future research.

Chapter 3

Experimental materials and methods

This chapter introduces the materials and methodologies used during the experimental portion of the project. Initially the automotive grade woven carbon fibre composite material and its respective manufacturing processes are presented. The experimental test frames capable of evaluating the material at both quasi-static and dynamic strain rates are introduced. An introduction to the optical measurement technique; digital image correlation is provided. The Chapter includes an initial experimental investigation into the experimental repeatability of the Instron patented fast-jaw LMD for testing continuous composites, including an experimental study on the choice of tabbing material.

3.1 Carbon fibre reinforced polymer composite

The composite material chosen for this project was an automotive specific 400 gsm 12K T700SC60E 2 x 2 twill pre-impregnated with Solvalite 710-1 at 38 % resin weight (henceforth referred to as 12K 2 x 2 twill CFRP) the fundamental characteristics are provided in Table 3.1. The combination of 400 gsm aerial fabric weight and the large 12K tow size reduces cost and therefore makes the material system suitable for use in potential future lightweight vehicle programs. The Solvalite range of thermoset epoxy matrix systems have been specifically developed for the manufacture of high volume automotive components with fast cure cycles and good mechanical properties. Pre-impregnation of the epoxy resin at 38 % weight results in components with a fibre volume fraction of 53 $\pm$ 1 %. This volume fraction is targetted by OEM's since the large resin content will ensure large scale fabric wet out, thereby reducing the risk of defects during complex part manufacture [141].

Throughout the weaving and matrix pre-impregnation phase, the carbon fibre fabric can be deformed. As the warp fibres are constantly under tension these remain true, however, the weft fibres experience bowing or angular distortion. In order to limit the effect of variability created by this distortion all tested parts have been produced from the same material batch. Material positioned within 50 mm of the edges of the 1250 mm roll was discarded, as this is the most highly distorted region. In order to control the production of preforms, a ZUND CNC cutting table was employed. Whilst the impregnated fabric was positioned on the table, the weft tow distortion was measured by recording the displacement of a single weft tow every 0.5 metres over the central 1150 mm of pre-preg used. The roll of material employed for this project had a linear angular distortion of 1.26° (average weft fibre misalignment of 25.3 mm). This nominally created a fabric with a warp fibre orientation of 0° and a weft orientation of 91.26°. As this is within the Solvay tolerance of 0°/90° (± 2.86°), the material system used throughout this project is considered to be representative of that used in automotive structures [142]. As this project only employs a single batch of material it is unlikely that the weft fibre distortion would be consistent with other batches. Therefore, experimental investigation of multiple batches should be conducted in order to characterise the variation in weft fibre distortion on the mechanical properties of the system prior to the data sets being employed within automotive CAE material cards. This is outside the scope of this Ph.D as only a single batch was investigated.

Table 3.1: Nominal 400 gsm 12K T700SC60E 2 X 2 twill Solvalite 710-1 material specification [143].

Pre-preg material parameters	value
Fibre density (g/cm^3)	1.80
Fabric weight (g/m^2)	398
Resin density (g/cm^3)	1.22
cured ply thickness (mm)	0.42
fibre volume fraction (%)	53.0

3.2 Composite manufacturing

High volume automotive parts are generally produced using either pre-preg compression moulding (PCM) or resin infusion processes such as liquid compression moulding and high pressure resin transfer moulding (HP-RTM) [144]. Both moulding solutions offer cycle times significantly below those of the autoclave process used

to produce motorsport and aerospace components. The WMG 1700 tonne Engel press is capable of producing parts using both PCM and HP-RTM techniques. The high injection pressures of HP-RTM can induce distortion in both the warp and weft fibre orientations as a result of fibre wash. In comparison, PCM is proven to produce repeatable results with little deformation recorded between preform and cured laminate. PCM was conducted according to the moulding specifications outlined in Table 3.2, which were developed in conjunction with Solvay.

Prior to moulding the pre-forms were stacked using hand layup within a constrained fixture with stacking sequences of $[0]_4$, $[0]_6$ and $[45]_8$.

Table 3.2: Pre-preg compression moulding specification for Solvalite 710-1

Compression moulding parameter	value
Cure temperature	150 ^{o}C
Dwell time	12 s
Dwell height	8 mm
Clamping force	2750 kN
Cure time	180 s
Cycle time	300 s

Prior to preparing the cured plaques for testing, the fibre volume fraction (V_f) was calculated using Equation 3.1 [86]. Calculation of the V_f enables the normalisation of the subsequent mechanical properties to a nominal value, removing plaque variability from the statistical comparison of test data. Finally, composite specimens were cut from the plaques using a single axis CNC diamond bladed precision saw and the thickness and width of the samples were recorded to two decimal places using a micrometer and vernier respectively in order to accurately determine the cross-sectional area.

$$V_f = \frac{N_t M_{fabric}}{\rho_f t} \tag{3.1}$$

Where; N_t - total number of fabric layers, M_{fabric} - ariel fabric weight, ρ_f - fibre density, t - total thickness.

3.3 Quasi-static material characterisation

3.3.1 Test frames

Quasi-static testing was conducted on a uniaxial Instron 5980 electromechanical universal testing machine (Figure 3.1) with a strain gauged load cell with capacity of 250 kN (±0.25 kN) [145]. The frame has the capability to be fitted with a variety of fixtures in order to isolate the required stress states, and due to its high stiffness it is suitable for testing high strength materials.

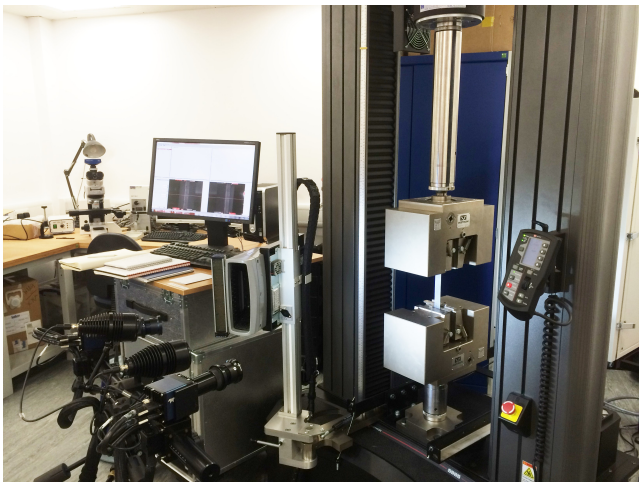

Figure 3.1: 250 kN Instron 5980 electromechanical uni axial test machine used throughout this project, GOM 12M DIC equipment is setup in the foreground to measure the surface strains of the specimens.

Load and cross-head extension measurements were recorded via a data acquisition system sampling at a maximum frequency of 2.5 kHz. Figure 3.2 shows the tensile engineering stress-strain response of a CFRP specimen loaded in longitudinal tension. Strain was instrumented based on the displacement of the specimen as well as on the surface of the specimen using non-contact DIC (Section 3.5). It is evident that the cross-head displacement measurement is not suitable for establishing the strain behaviour of the specimen as the compliance of the load path exaggerates the displacement of the specimen leading to an over-prediction of the ultimate strain by 158 % in comparison to measurements taken directly from the specimen. Therefore, an accurate methodology for determining the strain on the specimen must be employed, consequently the DIC technique is discussed in more detail in Section 3.5.

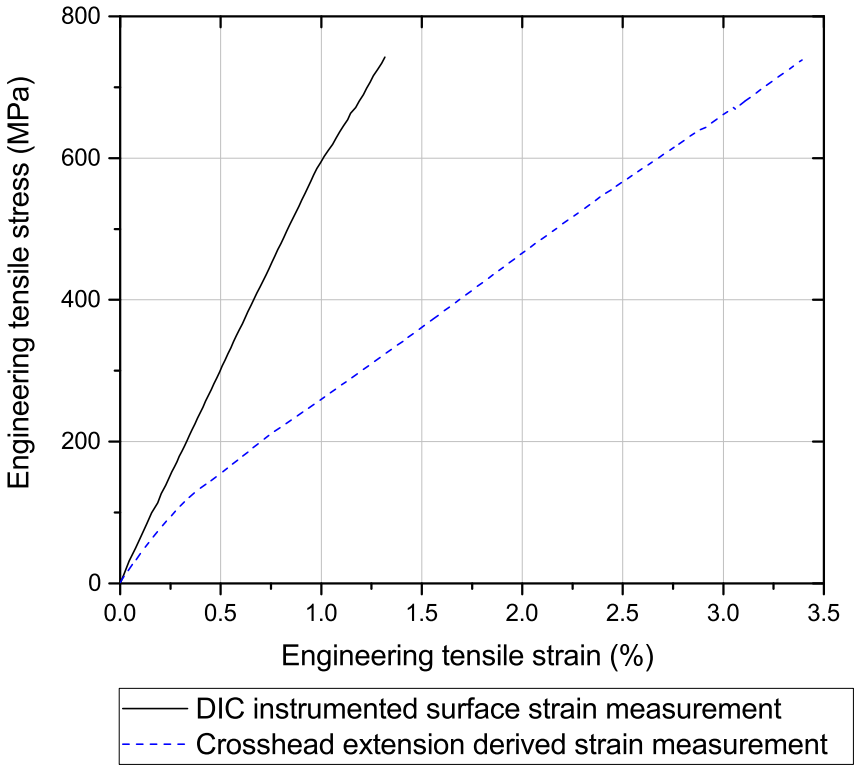

Figure 3.2: Engineering tensile stress-strain plot for 0° composite laminate with strain measured on the specimen using DIC and using the crosshead of the test frame.

3.3.2 Standardised quasi-static specimen geometries

Evolution in the understanding of composite behaviour has led to the development of standardised test methods that induce isolated stress states such as fibre orientated tension, in-plane and out of plane shear, inter-laminar tension and in-plane compression. The following sections will discuss the existing standards applicable to the two stress states isolated for this project, longitudinal tension and in-plane shear.

3.3.2.1 Tension

Two standards are predominately used for the characterisation of composites in in-plane tension. ISO 527-1:2012 [146] recommends the use of a *dog bone* shaped specimen that has been developed from a polymer standard. Due to the necked

geometry, continuous axial fibres are cut outside of the gauge region when the specimens are machined. When the specimen is placed under a tensile load, the stress is transmitted to the end of these truncated fibres, at which point localised stress concentrations arise. Cracks are initiated as a result of these stress concentrations and propogate, resulting in the premature transverse failure of the laminate either end of the gauge length, as shown in Figure 3.3. Due to the specimen failing prematurely the resultant mechanical properties are under-estimated.

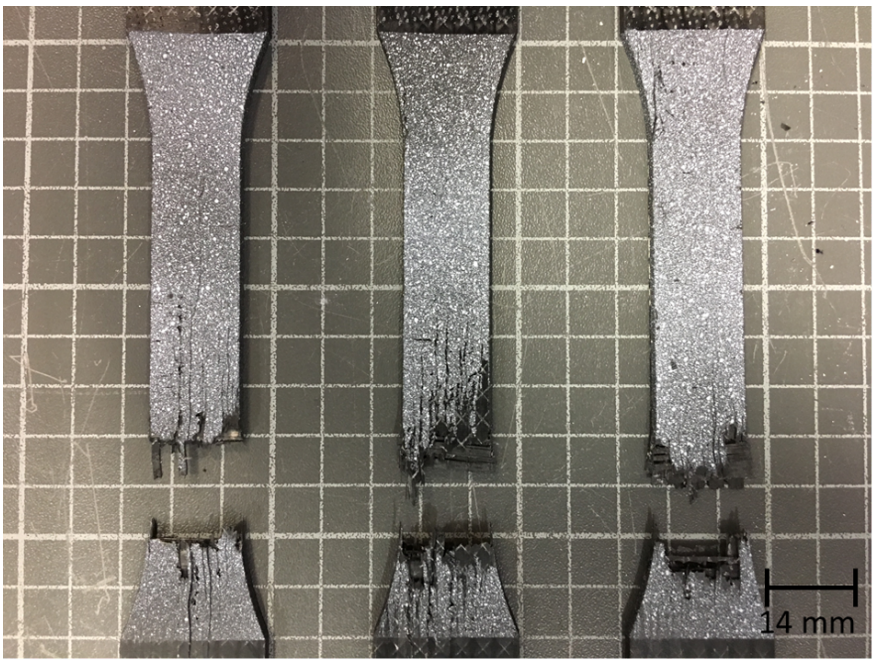

Figure 3.3: Examples of the premature geometry induced tensile failure mode of cross-ply laminates that have been machined into dog bones (18 mm gauge width), transverse fracture occurs at base of the gauge length as a result of axial splitting of the truncated longitudinal fibres.

Straight sided ASTM D3039-14 [147] specimens are frequently employed as an alternative to a necked design, these specimens consist of a free length, total length between the jaws, and a gauge length, region used for measurements. A schematic of the nominal dimensions is shown in Figure 3.4. Due to the straight sides, the specimens do not suffer from premature failure as there are no geometric stress raisers. However, removal of the necked region results in localised shear stresses generated at the grip-specimen interface due to the rigid constraints of the grips opposing the Poissons contraction of the specimen. This too can lead to the premature failure of the specimen, either within or in the immediate vicinity of the grips. To alleviate the effect of the shear stress and promote failure within the central 100 mm gauge

length of the specimen, tabbing can be used to alleviate shear strains and promote failure within the centre of the specimen.

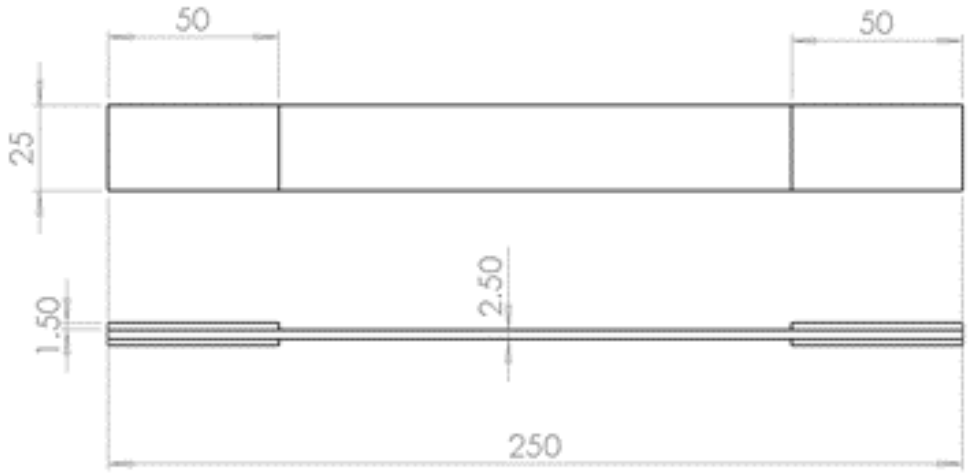

Figure 3.4: Nominal dimensions (mm) of ASTM D3039-14 straight sided in-plane tension continuous composite specimen extracted from the standard [147].

The aim of the tabbing configuration is to create an interface that has greater compliance than the specimen itself, whereby its Poissons contraction relives the shear stresses away from the specimen. As a result the employed tabbing solution is dependent upon the material system being characterised. It is recommended to use to either the same material (either bonded on or co-cured), GFRP or aluminium for the tabbing, and an adhesive that is softer than the matrix [148].

The tabbing material used in this project was 1.5 mm plain weave glass-epoxy sourced from Croylek Ltd. The VTA 260 adhesive was sourced from Solvay in film form with a mesh that provides a nominal bondline thickness of 0.3 mm. It was cured under vacuum well below the transition temperature of the matrix (the cure cycle is provided in Table 3.3), as a result the mechanical properties of the cured laminate are not affected by the tabbing process.

The nominal dimensions recommended by ASTM are sufficient to produce global homogeneous stress states when characterising most woven composite architectures. However, fabrics that have large unit cells; induced either as a result of their weave or large tow counts, can demonstrate large scale heterogeneity. If the representative volume of the specimen is too small then this can lead to the damage initiation and

Table 3.3: Cure parameters of VTA260 adhesive film [149].

Parameter	value
Cure temperature	65 $°C$
Cure time	16 hours
Vacuum pressure	14.2 psi

propagation that causes ultimate failure being related to the heterogeneity of the weave architecture rather than the global properties of the material system itself. In the context of a woven fabric, a unit cell is defined as the smallest self replicating component of the weave architecture in three dimensions. Composite textile standard ASTM D6856-03 [150] specifies that the laminate used within characterisation tests must have a unit cell to width ratio of at least 2 : 1. For the chosen 400 gsm 12K T700SC60E 2 x 2 twill fabric which has a tow width of 4 mm, the unit cell is 16 mm x 16 mm as shown in Figure 3.5. Considering the 16 mm^2 unit cell and a stacking sequence of $[0]_6$ (0.42 mm CPT), the final tensile coupon geometry used throughout this project for quasi-static testing is provided in Figure 3.6.

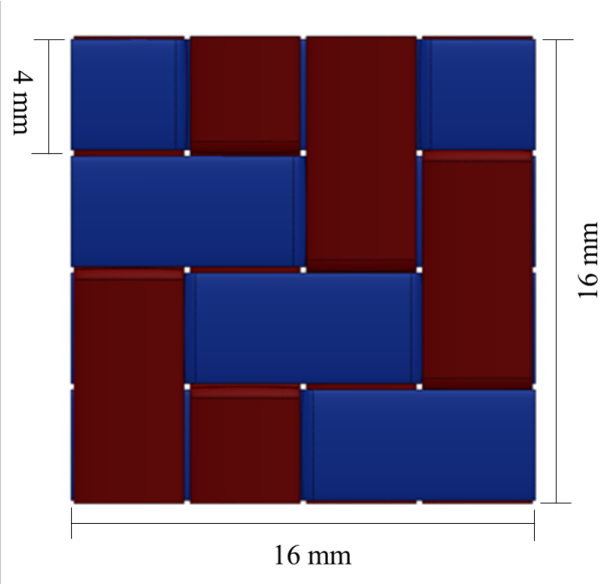

Figure 3.5: Representative unit cell of the 400 gsm 12K T700SC60E 2x2 twill fabric

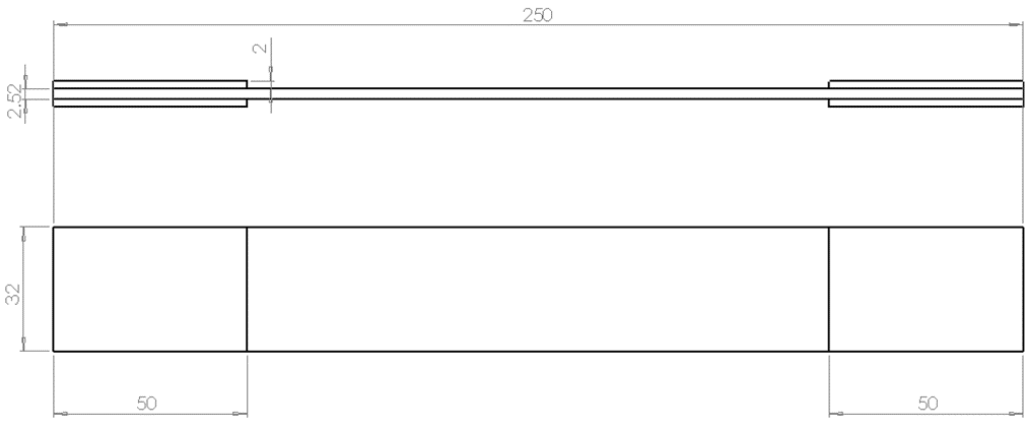

Figure 3.6: ASTM D3039-14 composite tensile coupon used to determine the tensile characteristics throughout this thesis (dimensions in mm).

3.3.2.2 In-plane shear

A variety of test methodologies can replicate the in-plane shear deformation of a composite laminate in a lab environment in order to characterise the shear strength and shear modulus of a composite material system. The Iosipescu double V-Notched method can accurately predict shear strength and shear modulus, however, requires a complex fixture and since the specimen is loaded in edge-wise compression the specimens can undergo localised crushing at the fixture contact sites [151]. Rail shear methods can also be employed however, the specimens are expensive due to requirement of large volumes of materials and detailed machining; the complex gripping method also causes stress concentrations at the grip-specimen interface [152]. A V-Notched sample can be employed with a rail shear fixture, thus producing an ideal shear stress state, however, these specimens too are prone to stress concentrations leading to premature failure [153]. A [±45] specimen placed under tensile stress state can also be used for calculating the shear response of a woven laminate [154]. Due to its uni-axial lightweight design this specimen geometry is easier to employ on the dynamic test facility at WMG (discussed in Section 3.3.3), therefore this research focuses on the ASTM D3518-13 standard [155].

ASTM 3518-13 employs the same coupon geometry as ASTM D3039-14 for in-plane shear tests (Figure 3.7), although the stacking sequence is changed to $[45]_8$ in order to induce a shear state. As with specimens loaded in the warp direction, failure

can initiate as a result of the boundary conditions of the grips. To limit this risk, GFRP tabs are bonded onto the specimen using VTA 260 adhesive film as on tensile specimens.

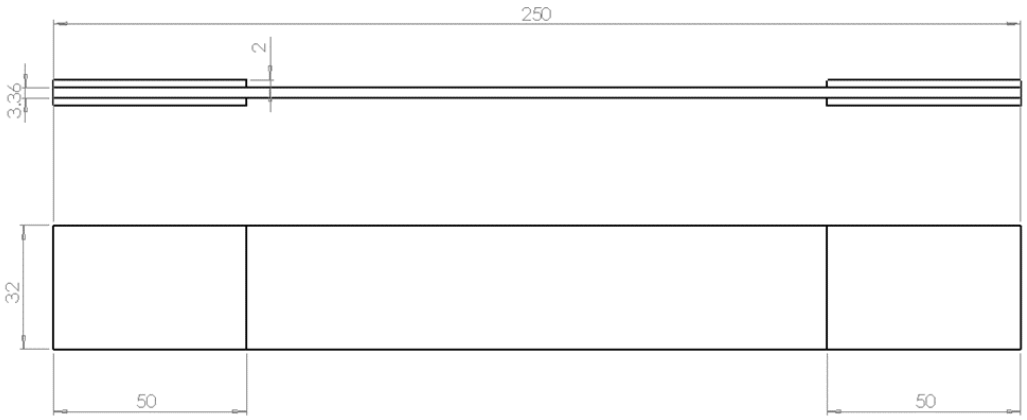

Figure 3.7: ASTM D3518-13 composite tensile shear coupon used to determine the in-plane shear characteristics throughout this thesis (dimensions in mm).

3.3.3 Instron 8800 100-20 VHS high speed test system

The Instron Very High Speed 8800 160/100-20 (VHS) is a high rate servo-hydraulic test machine that was specifically designed for testing materials at intermediate to high strain rates (Figure 3.8). The actuator mounted within the VHS is capable of achieving a maximum cross head velocity of 20 ms^{-1} and apply a load of 100 kN in both tension and compression [111]. Two proportional valves are used to control the flow rate of oil and therefore the crosshead speed. Closed loop control of the VHS employs a feedback loop to ensure that the actuator velocity remains constant, this drive control can be conducted up to a maximum velocity of 1 ms^{-1}. Above this speed the frame must operate in open loop whereby the actuator velocity is based on on a constant valve drive that is calibrated to the frame by Instron. The ramp period of the flow rate is passed onto to the crosshead as an inertial period, whereby the crosshead is not travelling at a constant velocity. This inertial period increases with increasing nominal test velocities up to 20 ms^{-1}, at which point the inertial period lasts a total of 165 mm. As a result the VHS requires the use of an LMD (introduced in Section 2.2.3), the WMG VHS frame is equipped with the

Instron fast jaw system. As well as the inertial ramp period, Chen et al. [156] also observed that as the actuator approached maximum displacement it was unable to maintain a constant velocity. However, unlike the authors research into expanded polystyrene the composite material chosen for this project has a maximum axial strain of approximately 11 %. Considering a quasi-static specimen with a deforming length of 150 mm this corresponds to a maximum displacement of 16.5 mm. As a result, the reduced operating window due to deceleration at the end of the actuator travel will not have an effect on results.

Figure 3.8: Instron VHS 8800 servo-hydraulic test machine

Two data acquisition channels with a maximum sampling frequency of 5 MHz are used on the VHS in order to record the observed load and displacement. A dynamic load cell is integrated into the lower static grip of the VHS in the form of a Kistler 9071A piezoelectric load cell washer. The VHS is also instrumented with a displacement transducer to record the position of the actuator in order to provide test velocity readings. As with the quasi-static frames these measurements are not suitable for establishing strain due to the compliance of the load path, therefore additional specimen instrumented strain measurement is required.

Unlike the SHPB discussed in Chapter 2, the tensile fast jaw system is capable of

testing larger specimens. The equipment at WMG is capable of testing samples up to 30 mm wide and 5 mm thick. The 5 mm maximum thickness is a result of the maximum cavity created between the jaw faces without contact with the specimen surface. The implementation of a fast jaw mechanism allows the two serrated gripping faces to be held clear of the specimen surface whilst the actuator accelerates reducing the inertial region to a minimum. Figure 3.9 shows a straight sided composite specimen with aluminium tabbing mounted within the fast jaw system. The base of the specimen is held within a set of static self aligning jaws ensuring vertical alignment through the centre of actuator. The dynamic jaw faces are activated by four pre-tensioned bolts (torqued to 15 Nm). Initially the jaw faces are held ~ 100 μm proud of the specimen surface by a set of angled knock out wedges. Once the crossshead has travelled a preset distance the travel of the knock out wedges is restricted by a pre-set spacer rod. At this instance, the pre-tensioned

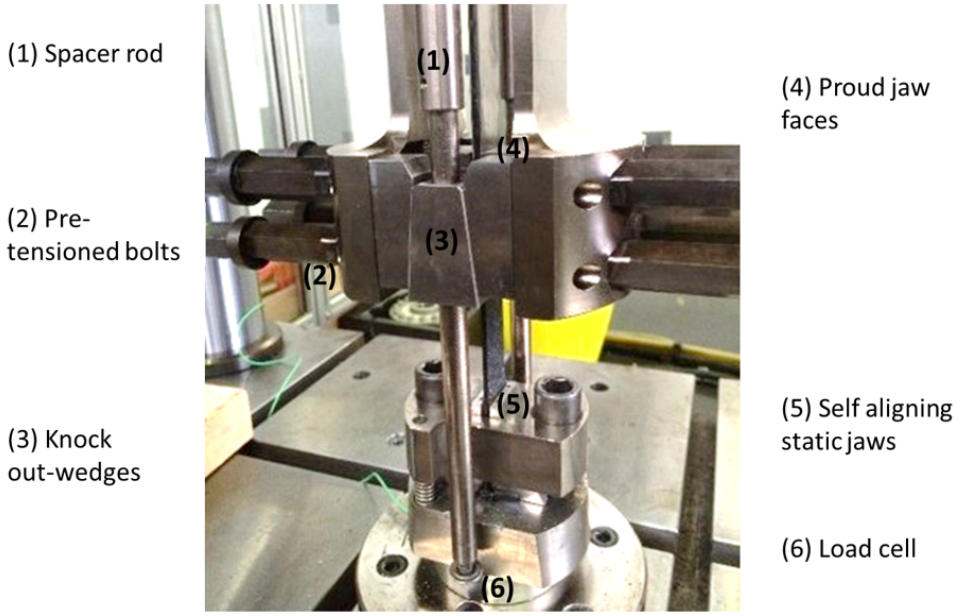

Figure 3.9: Instron VHS 8800 fast jaw system showing the static self aligning lower jaw mounted directly above the Kistler 9071A piezoelectric load cell washer. The serrated jaw faces of the fast jaw LMD are pre-tensioned to provide the required gripping load, however, they are held proud by a set of knock out-wedges. The wedges are removed upon impact with the spacer rod at a pre-determined height inducing a tensile load at an intermediate to high strain rate.

bolts apply the serrated jaw faces to the specimen surface in under 5 μs and the specimen is dynamically strained until fracture.

3.4 Preliminary experiments utilising the VHS fast jaw gripping System

In order to investigate the use of the Instron VHS fast jaw system for testing composite specimens loaded in tension a preliminary experiment was conducted. Specimens with three different tabbing configurations (untabbed, GFRP tabbing and aluminium tabbing) were loaded at 0.1 ms^{-1}, in order to review the repeatability of the results five repeats of each experiment were conducted. The specimen geometry employed is shown in Figure 3.10, it was a modified form of ASTM D3039 adjusted for use in the VHS. The free length was reduced from 150 mm to 100 mm in an attempt to replicate the specimen geometries used by Longana [110] and Brown et al. [95]. The upper tab length was extended to allow the fast jaws to accelerate prior to gripping the sample once it had reached the pre-determined speed. Due to the packaging constraints of the fast jaw system (maximum 5 mm thickness), tabbing thickness was limited to 0.9 mm on either side of the specimen. Longana [157] observed tab de-bonding when using the fast jaw system to test UD glass epoxy laminates. As a result a high performance structural adhesive (3M DP490) was used, the increased shear strength will reduce the risk of delamination at the specimen-tab interface. The ramped cure cycle for 3M DP490 is provided in Table 3.4. The dwell temperature is below the glass-transition temperature of the matrix system, therefore, the cure cycle is not expected to have an effect on the mechanical behaviour of the laminate. Unlike the VTA 260 adhesive film used during quasi-static characterisation, the 3M DP490 does not contain a mesh that ensures the bondline is a constant thickness. Therefore, 0.3 mm glass beads where mixed with the adhesive prior to bonding the specimen and tabs to provide this stable thickness.

Table 3.4: Cure parameters of 3M DP490 adhesive. [149]

Parameter	Step 1	Step 2
Cure temperature	23 $°C$	80 $°C$
Cure time	24 hours	1 hour
Vacuum pressure	14.2 psi	14.2 psi

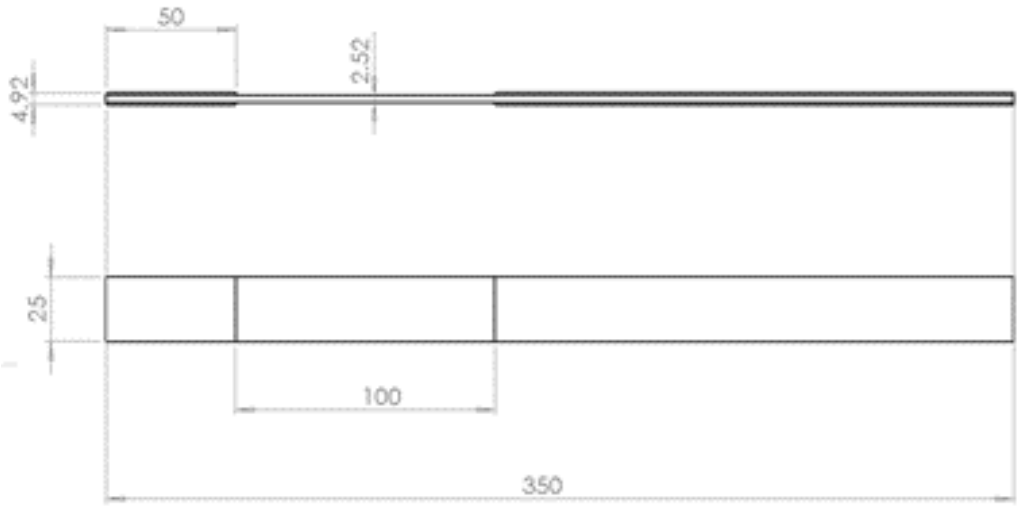

Figure 3.10: Tensile coupon for initial VHS testing with the fast-jaw system, the short tab region is mounted within the stationary jaw, whilst the extended upper tab allows for the fast jaw system to accelerate prior to gripping the specimen (dimension in mm).

Assessment of the tabbing material Figure 3.11 shows the load - time response of the tensile tests conducted using the three different tab configurations at 0.1 ms^{-1}, since the trends observed for each tab configuration were repeatable a single plot of each is presented. Specimens with no tabbing were unable to be loaded to failure of the material system due to slipping of the jaw faces. Initial slipping, was evident from the start, hence the reduced stiffness of the initial response. However, once the load reaches approximately 16 kN the specimen is unable to be loaded further, the force exceeds the dynamic friction between the serrated teeth and the specimen. This causes extensive damage within the surface plies as the serrated jaw moves through the material leaving deep grooves. As a result the load-time trace continues at this load, until the jaws reached the end of the specimen. The GFRP and aluminium tabs behave very similarly at the onset of loading with load cell ringing visible early in the load-time plot, this ringing is damped out as specimen strains and is caused by the oscillation of the load path. The GFRP tabbed specimens experienced slipping as the load reached 45 kN, however, unlike the untabbed specimens the jaws manage to re-engage with the specimen surface and the load was able to continue to rise. However, the specimen slips again prior to specimen failure and is unable to induce fracture of the specimen. In comparison the aluminium tabs were capable of transferring the load to the specimen resulting in the linear loading until fracture. Figure 3.12 shows the specimens post test. The aluminium tabbed specimen is the

only one to show failure of the laminate. The GFRP tabbed specimen exhibits signs of slipping on both the upper and lower tabs and the untabbed specimen shows signs of fast jaw slipping along its free length.

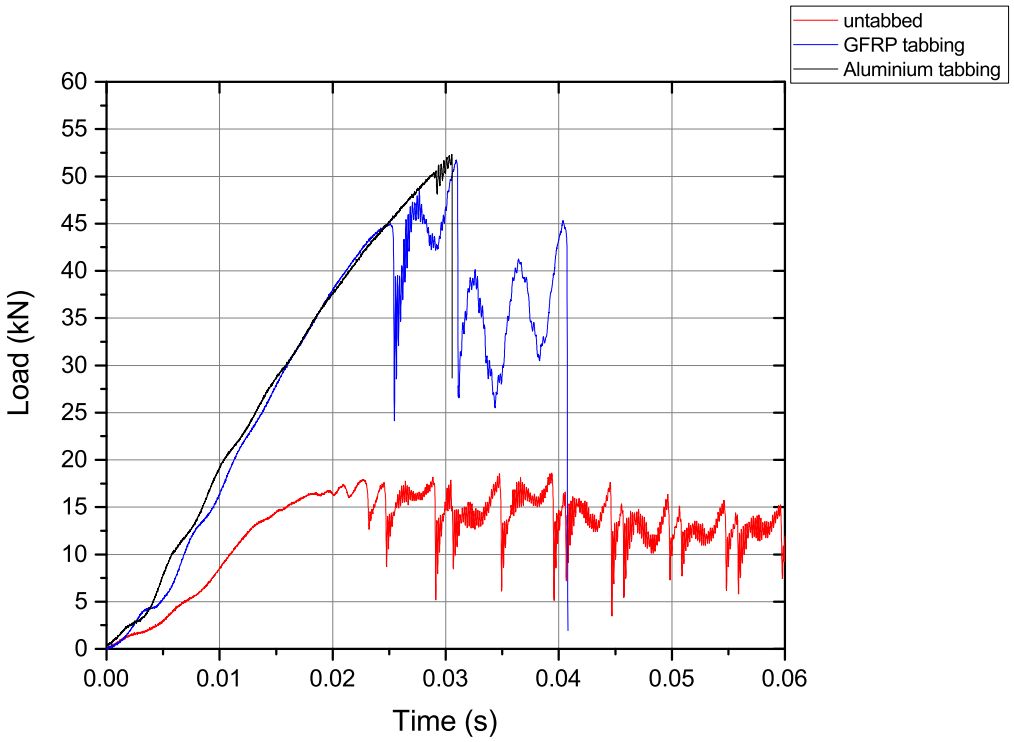

Figure 3.11: Load - time plots for 0.1 ms^{-1} tensile tests using VHS fast jaw for different tabbing materials.

Figure 3.12: Modified ASTM D3039-14 specimens (width 25 mm) tested at 0.1 ms^{-1}using the fast jaw system. The untabbed specimen (top) shows signs of jaw slip along its full length, GFRP tabbed specimen (centre) has slip marks on both the upper and lower jaws, the aluminium tabbed specimen shown no signs of slipping and successfully loaded the specimen to fracture.

Experimental observations Figure 3.13 shows a sequence of images captured as the fast jaw system impacts with the spacer bars removing the knock out wedges. The images were captured by a Photron SA-X2 high speed camera (sampling at 12.5 kHz) positioned perpendicular to the front face of the specimen. As the sequence progresses the knock out wedge on the right hand side of the specimen can be seen to be removed prior to the left hand wedge. This delayed release of a single wedge results in a non-uniform gripping pressure being applied to the specimen, thus inducing slipping as the jaws initially make contact as well as in-plane bending strains. This was evident with initial slipping observed in two out of the five aluminium tabbed experiments. The inability to release both wedges simultaneously is considered to be a result of the height of the knock out wedges varying. The height had to be adjusted for each experiment due to the variation in specimen thickness (which is dependent

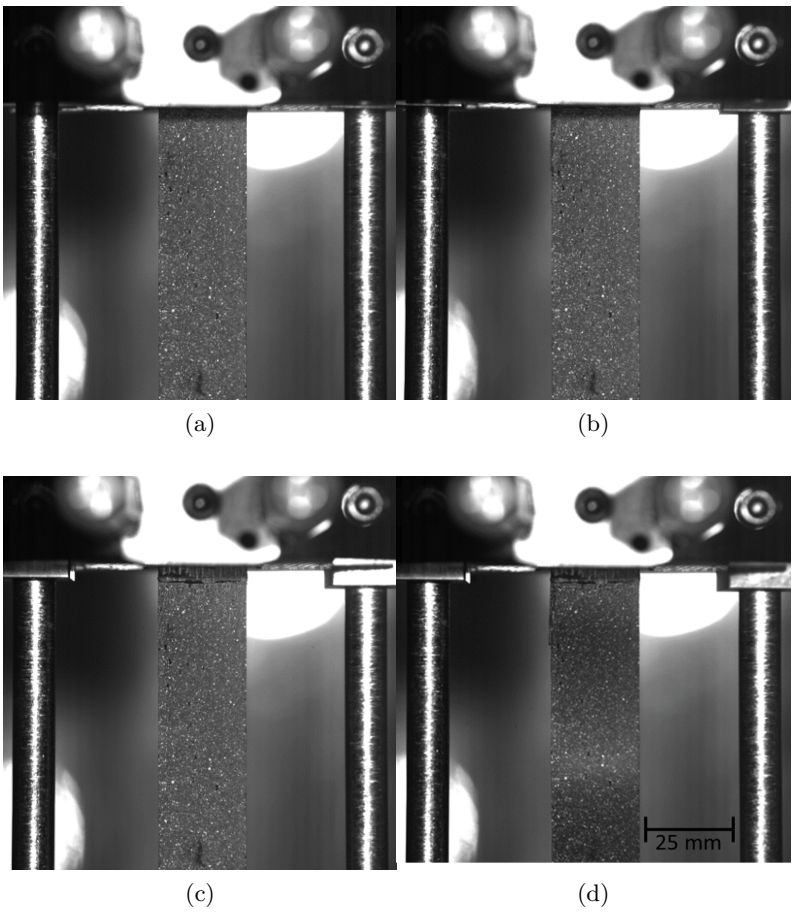

Figure 3.13: Surface images captured at (a) t = 0 ms, (b) t = 6.5 ms, (c) t = 13 ms and (d) t = 19.5 ms showing the unequal release of the knock out wedges of the fast jaw system, this caused poor experimental repeatability.

upon the variation in laminate, tab and bondline thicknesses) being greater than the desired 100 μm cavity between the jaws. Slip gauges were used to set both the knock out wedge heights to provide a constant jaw cavity, however, despite this time consuming process the experimental repeatability was poor.

Reviewing the images recorded by the high speed camera prior to engagement the fast jaw system it is possible to observe the fast jaw system is fluttering in the Z plane. Longana [157] used strain gauges mounted to the front and back of a UD composite specimen to calculate the bending strains and thus the through thickness displacement of the fast jaw system. Since the instrumentation was applied to the specimen the author was only able to determine the out-of plane displacement once the system is closed and the jaws have engaged. Longana measured that the fast jaw system was found to oscillate by 1 mm through thickness. The combination of in-plane and out-of plane bending will in induce a rotational moment, these bending strains modify the boundary conditions of the test and thus distort the specimens stress field and potentially the obtained mechanical data.

The flutter of the fast jaw system also creates challenges regarding the gripping of the specimen. Prior to the engagement of the fast jaws with the specimen, the fast jaws are not constrained, as a result they are oscillating at their natural frequency with an amplitude greater than 1 mm when a specimen is loaded. Due to this large oscillation the position of the fast jaws prior to being accelerated to the test velocity cannot be below the base of the upper tab. If the test is commenced from below the tabbing, the jaw face could impact with the tab during the crosshead acceleration phase, which would invalidate the test.

Since the fast jaw crosshead must be accelerated from above the upper tab it is incapable of loading materials to high rates of strain. The fast jaw system was developed for the characterisation of metallic specimens, the extended tail of dog boned metallic specimens is 2.4 times wider than the gauge region (29 mm vs 12 mm). As a result, the tail is elastically loaded whilst the necked gauge length deforms, thus the tail introduces negligible strain rate damping allowing the specimens to be loaded up to 1000 s^{-1}. In comparison, due to the straight sided design of composite specimens, an increase in gripping height will be inversely proportional to the strain rate of the test according to Equation 2.4 (repeated below).

$$\dot{\varepsilon}_{nom} = \frac{V_0}{L_0}$$

Considering the specimens used for this study (100 mm gauge length) and that the maximum test velocity of the VHS is 20 ms^{-1} (which requires an acceleration

distance of 165 mm) the maximum strain rate achievable with the fast jaw system is 55 s^{-1}(Equation 3.2).

$$\dot{\varepsilon}_{nom} = \frac{20 \times 10^3}{265} = 55 s^{-1} \tag{3.2}$$

This effect was also observed by Wang, who despite running experiments on a high speed servo-hydraulic machine at 20 ms^{-1} was only capable of inducing a maximum strain rate of 43 s^{-1} due to using straight sided specimens with a gauge length of 150 mm [122]. As a result the fast jaw system is rendered incapable of testing the composite laminates at the strain rates desired for this project (100 s^{-1}).

Conclusions This preliminary study has determined that the dynamic friction created between the untabbed or GFRP tabbed laminate and the fast jaw dynamic gripping system is not sufficient to load the specimen to failure. However, the use of more ductile aluminium tabbing with 3M DP490 adhesive was capable of loading the specimen to failure and will therefore be used throughout the rest of this project.

The VHS fast jaw itself was shown to be inappropriate for use in testing of composite fabrics at automotive specific strain rates. Metallic specimens that have been evaluated using fast jaw LMD on a servo-hydraulic frame have had dog boned geometries, therefore testing at increased velocities results in gripping higher on the tail of the specimen. As a result the gauge region is capable of being loaded at strain rates up to 1000 s^{-1}, in comparison the maximum strain rate of a composite material with a 100 mm gauge length is 55 s^{-1} due to the straight sided coupon resulting in the gauge region possessing equal properties as the elongated specimen tail. Chapter 4 details the development of a coupon geometry and an appropriate LMD that is capable of loading CFRP at the desired strain rates.

3.5 Digital Image Correlation

Previously in Section 3.3.1 it was shown that in order to accurately determine the deformation of the specimen and not incorporate losses in the load path, strain must be recorded locally to the specimen. Strain can successfully be instrumented at quasi-static speeds using contact (i.e. extensometers and strain gauges) or non-contact optical techniques. Non-contact optical techniques offer advantages as they do not interact with the specimen during a test. The knife edges of contact extensometers can create localised stress concentrations within the material and are prone to slipping as damage develops in the material, as shown in the stress-strain response of a CFRP laminate in Figure 3.14. The initial modulus values are consistent, however, as the material strains the contact extensometer stress strain curves undergo sudden compressive or tensile strains post 0.6 % strain. Contact extensometers should also be removed prior to specimen failure, since the shock waves induced in the material at failure can damage them. This produces accurate modulus properties however, the ultimate strain measurement (measured by the cross-head displacement) has reduced accuracy due to the compliance of the test machine which is undesirable for automotive FE simulations [158]. In comparison full field optical techniques offer the ability to analyse the different strain components at any point over a specimen with high accuracy, the measurement resolution is also maintained irrespective of the strain scale. This results in accurate determination of mechanical properties within the elastic portion of an experiment as well as high levels of plastic strain at fracture. This makes them extremely useful when analysing the accuracy of failure criterion's developed for FE of highly heterogeneous composite laminates. [159].

Optical techniques can be classified into two main types. Interferometric and non-interferometric. Interferometric techniques track the phase difference of the scattered light wave from the measurement surface, this phase difference creates fringe patterns that determine the deformation of the surface, they are capable of achieving very high spatial resolutions. In comparison non-interferometric techniques measure surface deformation by the displacement of patterns [160]. These techniques achieve a lower spatial resolution, however, as interferometric techniques require the use of vibration isolated laboratory equipment, experimental measurements are easier to obtain using non-interferometric techniques. Of these techniques, Digital Image Correlation (DIC) is the most widely adopted optical measurement method due to its flexibility and desirable measurement accuracy.

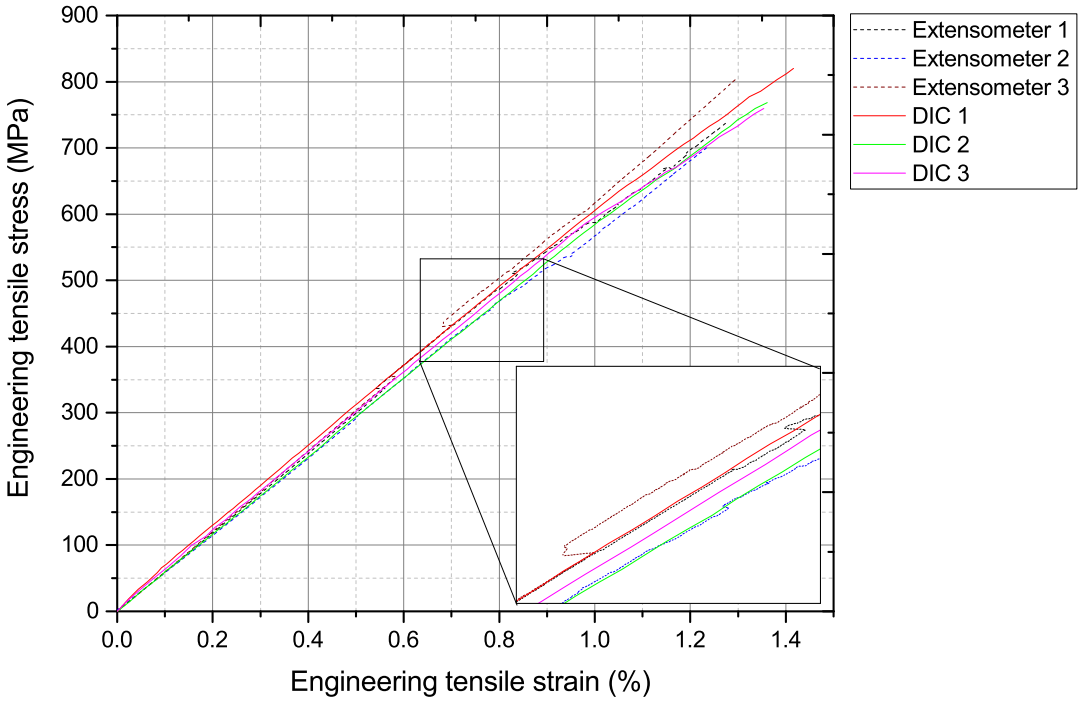

Figure 3.14: Three repetitions of a CFRP laminate undergoing a tensile experiment with strain measured using a 50 mm contact extensometer (Extensometer) and GOM 12M 3D DIC system (DIC). The inset shows the slipping of the extensometer knife edges mounted to the specimen as the load rises this is undesirable when attempting to characterise the stiffness and damage propagation of the specimen.

The DIC technique has been developed over the past two decades and can be summarised under two main categories. Two dimensional (2D) DIC uses a single camera set perpendicular to the measurement surface to capture the images (Figure 3.15(a)), this constrains the obtained measurements to the in-plane deformation of the surface as out of plane movement adjusts the speckle magnification inducing artificial 2D surface strains. To overcome this limitation of the 2D system, three dimensional (3D) DIC can be conducted using the stereo vision principle. 3D DIC is conducted upon a corrected image which is generated based on the two intersecting measurement points from each sensors angle of view and is capable of measuring through

thickness displacements [161]. The two cameras can be offset from one-another to produce the required measurement field as shown in Figure 3.15 (b). The field of view (FoV) is dictated by the assembly of the two cameras. An imaging angle (ϑ_{image}) of 12.5° from perpendicular to the imaged surface has been found to be optimum. Narrower angles reduce the accuracy of the camera triangulation whilst wider angles significantly reduce the FoV. Therefore the desirable method of adjusting the FoV is the selection of appropriate camera spacing (distance between sensor

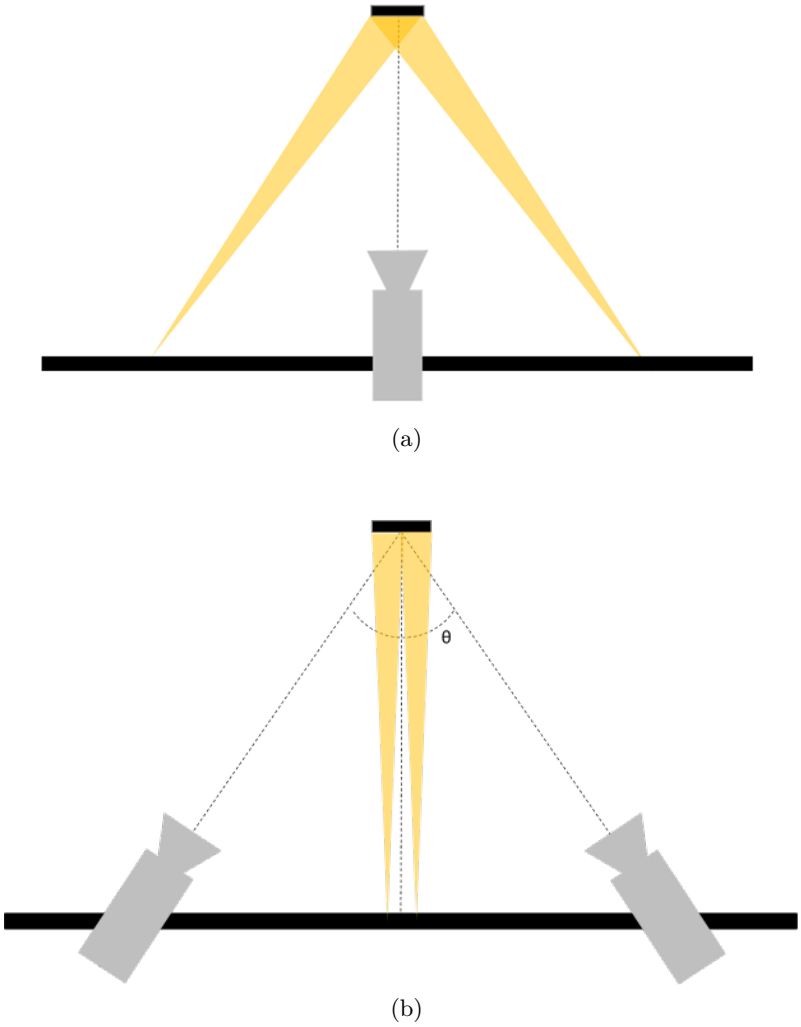

(a)

(b)

Figure 3.15: Schematic of camera set ups for 2D (a) and 3D DIC experiments (b), the optimal position of the illumination is shown by the yellow beams. 3D DIC requires illumination from the centre, whilst 2D DIC must be illuminated from either side of the sensor.

centres) and the camera stand off distance (distance of the sensor to the specimen surface) for a given lens system.

Both 2D and 3D techniques employ the same principles whereby an image of a speckle pattern is reduced to an array of quadrangular facets (Figure 3.16). Each facet contains a unique greyscale intensity due to the random combination of speckle artefacts within it. After deformation has been applied to the component, the speckle patten will have moved, however, the greyscale intensity will have remained the same. Therefore, comparison of the facet intensities between those in the reference image and the deformed images enables the computation of the displacement vectors and strains across the surface. This is achieved through use of a cross-correlation matching algorithm which is dependent upon the chosen DIC software (an extensive review is available in literature [161]). Improvement in displacement calculation is possible through sub-pixel interpolation, the GOM ARAMIS software employed in this thesis is capable of matching facets to an accuracy magnitude of 0.01 pixels [162]. In order to identify the position and shape of the deformed facet a shape function is used. A variety of different order shape functions are available. Zero-order shape functions assume that the facet has moved under rigid body motion, i.e. all pixels are displacing equally. Increased order functions are capable of defining the translation, rotation, scaling and shearing of the deformed facet, however, these functions require increased computational resource. ARAMIS uses a first order shape function which defines the bilinear transformation of the facet

The described correlation procedure is sufficient to map the displacement of a single facet, in order to produce a full field measurement, the process is completed for each image within the sequence producing a full-field displacement map. If the speckle pattern applied to the material has a low uniqueness and repeats itself over the measurement field then the matching algorithm will find multiple match locations increasing the chances of decorrelation and poor measurement accuracy.

A 3D measurement system requires calibration of the two cameras in order to ensure dimensional consistency of the measuring system, it determines the relative position and orientation of the cameras as well as the imaging characteristics of the lens systems and must be completed under the test conditions; illumination, shutter speed, etc.. GOM ARAMIS V6.1 uses a calibration plate of various sizes depending on the desired FoV, the calibration plate has highly accurate and precisely positioned markers that determine the orientation and position of the plate as it is moved throughout the measurement volume during a series of images. The position of the calibration markers is calculated by ARAMIS to determine their position in the 3D measurement volume and they are then computed back into their 2D positions to provide the

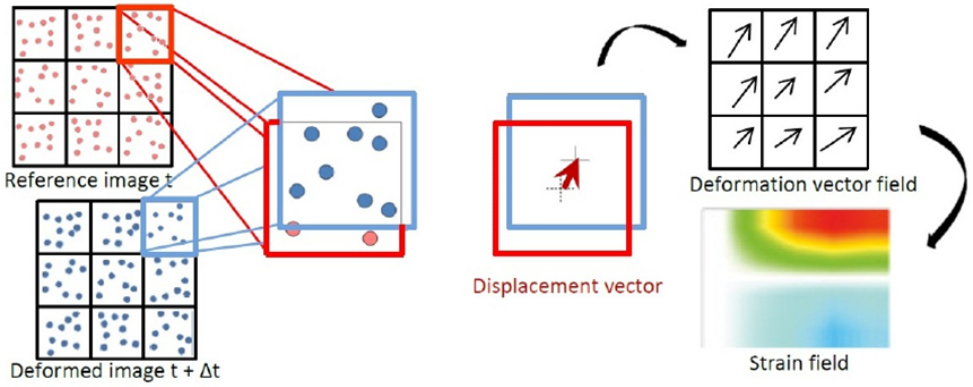

Figure 3.16: Schematic of the DIC analysis process, initial displacement of the greyscale intensity, calculation of the displacement vectors and ultimately the computation of the strain field [163].

intersection error. A calibration is deemed to be successful if the obtained calibration deviation, the discrepancy between reference point location throughout the image series is between 0.01 and 0.04 pixels. A guide to the positioning of the calibration plate throughout the calibration process used throughout this thesis is available in the ARAMIS manual [164]. In all experiments calibration is only completed after the sensor has had 25 minutes to warm up in order to reduce the drift distortion that can occur prior to the sensor achieving thermal equilibrium. Multiple calibration plates are required depending on the desired measurement volume, therefore the calibration plates used to define the volume of interest are defined where appropriate throughout this thesis.

3.5.1 Digital camera systems for full-field measurements

The quality of the acquired images can have a significant impact on the quality of observed results, the following section will outline each step of the process of obtaining images suitable for full field measurements. Two types of sensors are typically used within DIC measurement systems, Charge-Coupled Devices (CCD) and Complementary Metal-Oxide Semiconductor (CMOS). Although both operate on the same principle of converting photons to electrons via the photoelectric effect, they do so using different technologies.

CCD sensors have a large fill-factor (portion of the pixel capable of reading photons) and are the most light sensitive sensor composition available. However, the imaging

frequency is limited by the slow shift rate of the pixel charge across the sensor prior to voltage conversion. As a result they are not suitable for high frequency imaging solutions. In comparison CMOS sensors have reduced light sensitivity as result of the reduced fill factor of the photodiode (region of the pixel sensitive to light), however, the integration of the circuits at the pixel allows for parallel processing of pixels in order to reduce the potential exposure time of the sensor [165].

The primary challenge with conducting DIC over dynamic events is the ability to achieve an image series that has a sufficiently low exposure time to provide an adequate sampling frequency whilst allowing the photodiodes to observe sufficient light in order to fill the dynamic range of the sensor. The use of high powered external light sources can limit the impedance of the sensor and significantly reduce the exposure time, however, care must be taken to employ cold lighting so as to not change the thermal properties of the surrounding air over the course of the experiment (thus creating a virtual lens). The development of high speed digital camera technology has followed two philosophies. Ultra high speed imaging divides the image sequence across multiple sensors providing frame rates at multiple millions of frames per second (fps). However, these cameras have a low record length and can increase the distortion of full-field strain maps during post processing of DIC data since each image is recorded on a separate sensor [166]. Therefore they are not considered for this work. The development of single sensor CMOS cameras has attempted to increase the sensitivity of the photodiode and reduce the delay in data transfer. This has enabled cameras to achieve frame rates around 10,000 fps with a recording length of 30,000 frames.

Throughout this thesis two sets of digital cameras with CMOS sensors were employed; GOM 12M cameras for quasi-static experiments with an imaging frequency below 58 Hz and Photron SA-X2 cameras for imaging frequencies above 58 Hz. The SA-X2 cameras can achieve a frame rate of 12,500 fps operating at 1024 $\times$ 1024 pixels. The sampling frequency of the camera can be further increased by cropping or *windowing* the sensor which reduces the number of active pixels. Reduction in pixel volume results in a reduced period for digitisation of the pixel readings in order for the pixel to be able to re-set Thus reducing the exposure time of the camera. Windowing the sensor allows frames rates of up to 1 MHz to be achieved with a sensor size 8 x 128 pixel^2 [167]. However, considering that this sensor configuration is less than half the width of a recommended GOM facet, it is not suitable to consider that the strains sampled at 1 MHz would provide sufficient resolution to draw accurate measurements. Therefore a balance must be reached between achieving a high temporal resolution and sampling at a sufficient spatial resolution.

Naresh et al. [136] utilised a single Phantom V611 high speed camera to image the

drop weight tensile tests at 542 $s^{-1}$of plain weave GFRP, CFRP and carbon and glass hybrid composites. To achieve an imaging frequency of 100 kHz the authors cropped the sensor to a size of 128 x 128 $pixel^2$, a small region of interest (RoI) (10 x 3 mm^2) was established within this imaged area across the gauge region of the dog boned specimen, as shown in Figure 3.17. Although the highly cropped sensor size allowed the authors to reach the required temporal distribution of the images during the test, the small pixel density across the RoI reduced the spatial resolution (defined as the distance between two unique data points) of the generated strain fields thus causing extensive smoothing. The extent of the smoothing can be observed to eliminate the expected heterogeneity of a woven fabric and it is expected that the true longitudinal strain response of the laminate has been damped.

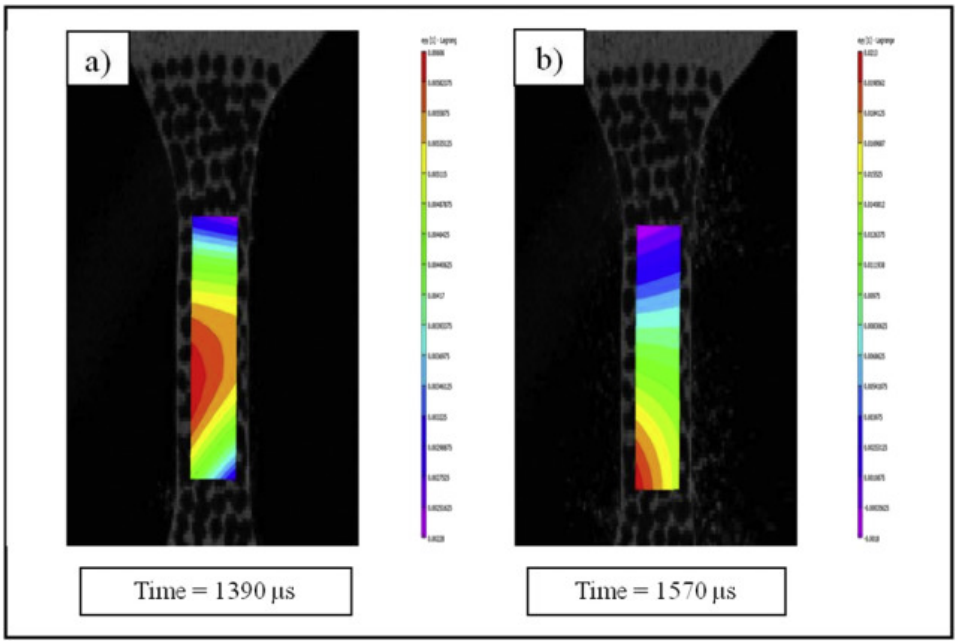

Figure 3.17: Longitudinal strain progression of a carbon fibre epoxy composite specimen (3 mm gauge width) at (a) 0.6 % and (b) 2.0 % longitudinal engineering strain [136]. Due to the highly cropped Phantom V611 sensor that enabled the authors to achieve a sampling frequency of 100 kHz the recorded strains presented are highly smoothed and not representative of the strain field populated based on the hetrogenity of the matieral structure.

In comparison, Lee [168, 169] conducted quasi-static and dynamic fracture tests on notched UD CFRP laminates using a 1 mega pixel Cordin-550 ultra high speed rotating mirror camera sampling at 250 kHz, and recording a total of 32 images. The high pixel density across the 30 x 30 mm^2 RoI enabled the author to review

the rate and orientation of crack propagation during the dynamic fracture toughness experiments with high spatial and strain resolution.

Koerber et al. used a SHPB and a Photron SA5 camera positioned for 2D DIC to review the response of a IM7-8552 UD CFRP composite to longitudinal [170] and transverse [126] compressive loads; the same experimental technique was also used to analyse the compressive response of a CFRP five harness satin weave composite [171]. Compressive characterisation at 350 s^{-1} involved the authors photographing the specimen deformation over a RoI of 20 x 10 mm^2 at 100 kHz with a sensor window of 320 x 192 $pixel^2$. Due to the increased pixel density across the RoI in comparison to the research presented by Naresh, the author achieved a high spatial resolution of 0.74 mm, thus achieving low smoothing of the appropriate strain map. The strain resolution of 0.04 % was calculated based on the average longitudinal engineering strain provided a random error of 0.6 % in relation to the ultimate failure strain of the specimen.

The use of 3D DIC in dynamic events has been utilised to validate the experimental conditions of impact plate tests. Flores et al. [172] utilised 3D DIC to measure the out-of plane displacement of a UD composite plate subjected to a 10 J impact. Imaging on the back surface of the plate allowed the authors to validate the residual damage of the plate as well as consider its true morphology based upon the strain maps. Pankow et al. [173] also employed 3D DIC to measure the out-of plane displacement of glass fibre 3D composite panels on the rear surface of the specimen during the a 250 μs pressure test. Longana also utilised 3D DIC to remove the effect of parasitic strains on the dynamic characterisation of the elastic Young's modulus and shear modulus of UD GFRP and CFRP laminates using an Instron VHS test machine. The authors 3D DIC strain measurements were validated through the use of a single camera conducting strain analysis using the grid method simultaneously at strain rates up to 83 s^{-1} [110]. In order to achieve the temporal resolution required, the author cropped the sensor and decreased the spatial resolution from 1.1 mm to 3.4 mm as the strain rate was increased from quasi-static to 83 s^{-1}. The Photron SA1.1 cameras employed by the author are capable of imaging at 5.4 kHz at full frame, the sensor was cropped in order to increase the frame rate. At 10 kHz, the empty space around the specimen (100 x 15 mm^2) was removed, providing a sensor size of 512 x 1024 $pixel^2$. Since the spatial resolution of the measurement was not changed, the accuracy of the computed strains was unaffected with the author capable of achieving a strain resolution of 33 με. In order to achieve sampling rates of 25 kHz and 40 kHz the author had to reduce the spatial resolution of the recorded images and was only capable of achieving a strain resolution of 470 με and 510 με respectively. Due to the highly elastic brittle nature of UD CFRP, the specimen

fractured below 1 % tensile strain, as a result the author only managed to record a total of eight images over the deformation sequence.

Coussa et al. [174] demonstrated how optimisation of the specimen free length can achieve a higher temporal resolution whilst maintaining the desired spatial resolution and thus not result in the extensive smoothing observed by other authors at elevated frame rates. Coussa et al. reduced the free length of a $[\pm 45]_3$ 2 x 2 twill glass PA66 thermoplastic specimen to 60 x 25 mm^2. The reduced specimen was experimentally validated to ensure that elastic and plastic damage propagation was unaffected by the reduced gauge period and in particular the grip induced shear loading regions. The result of the optimisation was such that the entire free length was sampled with a similar image resolution as that achieved by Longana (8.5 pixel/mm and 8.9 pixel/mm respectively), despite the frame rate being increased to 62.5 kHz (+56 %) with an identical Photron SA1.1 high speed camera.

The presented literature highlights that there is no formal technique for the use of DIC within high speed imaging environments. Due to the lower resolution cameras typically employed in high speed DIC in comparison to quasi-static analysis, many researchers appear to prefer to reduce the RoI in order to achieve a suitable measurement resolutions. However, for this research the full-field approach of Longana and Coussa et al. is preferred to the small RoI computing the strain fields for the entire specimen free length will enable the author to review the global damage and fracture response of the laminate since failure can occur at any point of the specimen free length. The use of 3D DIC, as explored by Flores et al., Pankow et al. and Longana was demonstrated to be capable of recording the out-of plane displacement of the specimen and provide longitudinal strains of the specimen without the false tension and compressive strains induced by out-of plane motion. Therefore 3D DIC with full field analysis will enable the author to generate an understanding of the material, the effect of the boundary conditions and selected specimen geometries on the extracted mechanical properties. The effect of reduced specimen length was previously expressed as a benefit when conducting dynamic experiments due to the lower input velocity required to achieve a higher uniform strain rate. This was reinforced by Coussa et al., whom demonstrated how the optimisation of a specimens free length resulted in the ability to achieve a higher imaging frequency, at a constant spatial resolution, thus improving the temporal distribution of the collected measurements. However, as recognised in Chapter 2 it is important to reduce a specimens geometry in a controlled manner so as to maintain the global representative response of composite architecture and not induce size effects.

3.5.2 Image acquisition

The previous sections has detailed the importance of establishing a robust imaging methodology, the first step is to chapter high quality images. The accuracy of the produced results depends on the variation in pixel intensity across the image, GOM ARAMIS uses 8 bit .tif images capable of providing a dynamic range of 256 grey scale levels. This refers to the bit depth of a sensor and is the smallest change in intensity

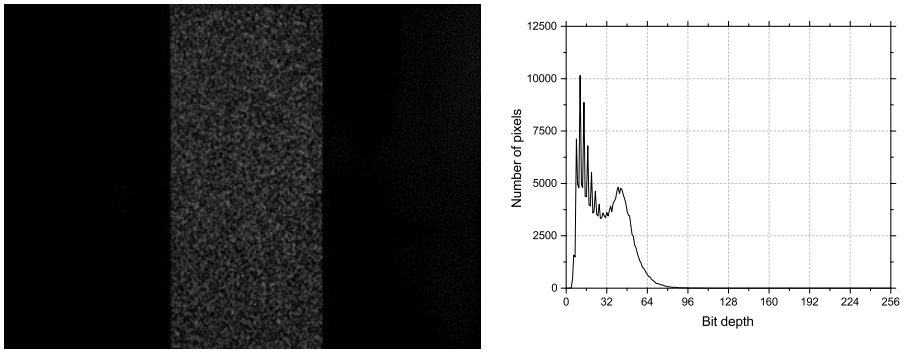

(a)

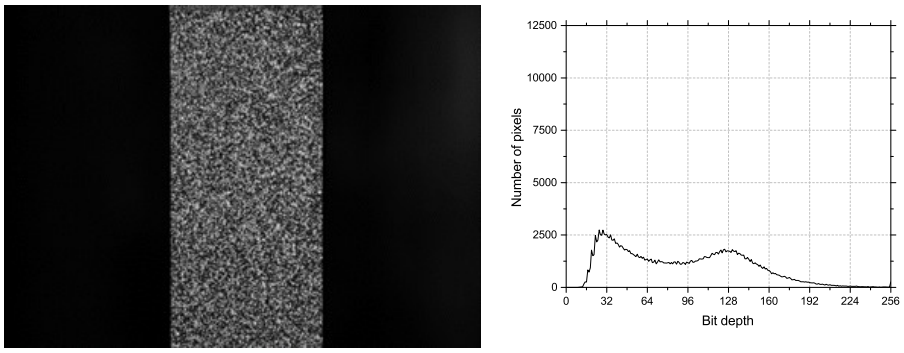

(b)

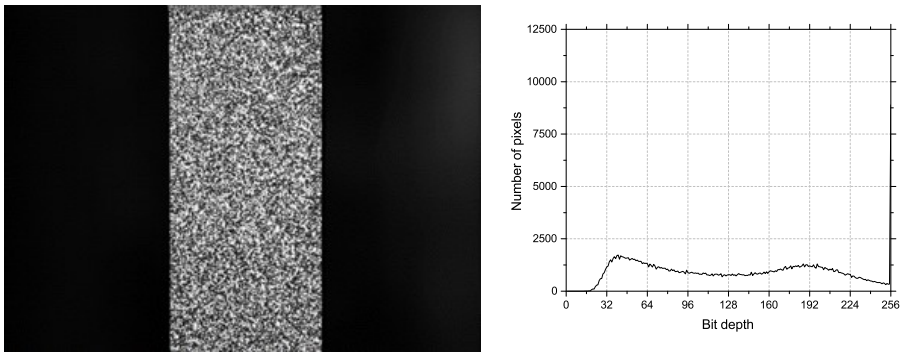

(c)

Figure 3.18: Dynamic range of a under-exposed (a), standard (b) and saturated (c) speckle patterns imaged using an 8 bit Photron SA-X2 CMOS camera

that a pixel can resolve. Figure 3.18 shows the dynamic range of a under-exposed image (a) which uses only the lower values, whilst a saturated image (c) will use the upper values and exceed the maximum intensity measurable. The inability of both the dark and saturated image to fill the dynamic range of the sensor reduces the pixel intensity resolution, reducing the ability of unique facets to be created. In order to maximise the dynamic range (Figure 3.18 (b)) a high quality speckle pattern must be applied to a surface of the specimen as well as adjusting the cameras aperture, focal length and exposure values.

The aperture controls the depth of field in the captured images, an open aperture provides maximum light to the sensor but has the smallest depth of field. This is useful for focusing the cameras and ensuring that the depth of field and pixel intensity is equal across both cameras. However, considering the non-perpendicular positioning of the specimen relative to each of the cameras when using a 3D DIC setup, the depth of field is critical to achieving sharp focused images. Figure 3.19 provides an example of an image with a depth of field suitable for 3D DIC and one which due to the lack of depth of field lacks focus at the top and bottom of the specimens gauge length. For the GOM 12M system GOM ARAMIS provides a range of sensor configurations that are capable of providing the appropriate measurement volume [162]. The compromise of closing the aperture to capture images with a sufficient depth of field is that it limits the light available to the sensor potentially

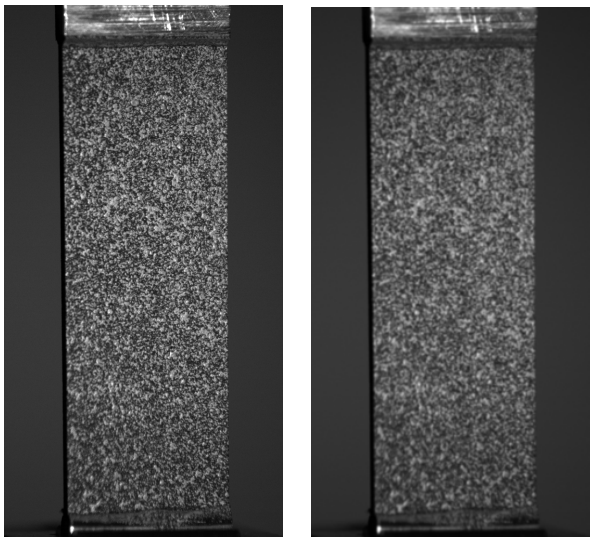

(a) (b)

Figure 3.19: Left camera images of a specimen with (a) a depth of field suitable for 3D DIC and (b) a too shallow a depth of field with a lack of focus top and bottom of the specimens gauge length (50 mm).

reducing the dynamic range of the collected images, as a result the measurement surface must be illuminated using artificial light sources.

The external lighting sources used must evenly distribute the light across the specimen, uneven specimen illumination induces fringe patterns, reflections or shadows. Over a series of images this fringe pattern is measured as displacement and increases the systematic error of the measurement [175]. Two light positions are commonly employed as show in Figure 3.15; for 2D DIC lights are positioned either side of the camera, whilst for 3D DIC the lights must be positioned perpendicular to the imaged surface central to the two cameras. The projection of false colour is useful for determining the quality of specimen illumination, both cameras should demonstrate a similar pattern with matching intensity; the pixel intensity is displayed as a random distribution indicating that lighting is not affecting the measurement. An example of a well illuminated specimen can be seen in Figure 3.20.

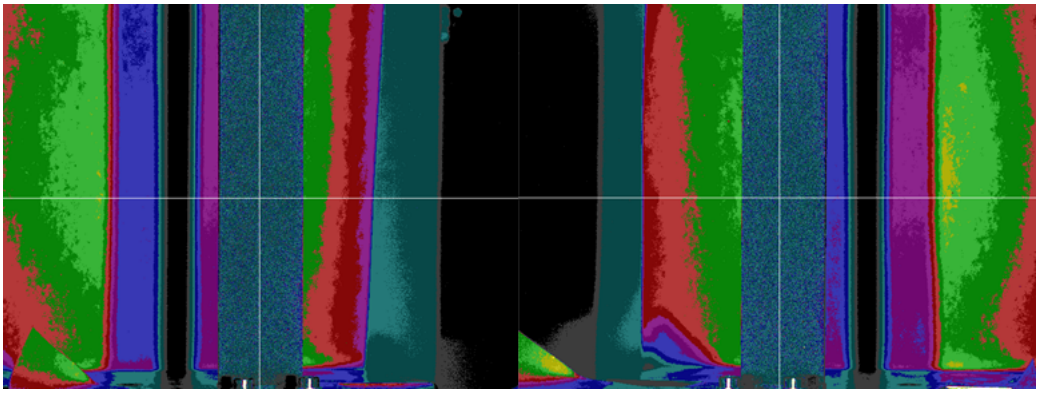

Figure 3.20: Example of the balanced false colour projection between left and right camera images indicating an evenly illuminated ASTM D3039-14 specimen (25×250 mm^2) using the GOM 12M LED lights.

Specimen illumination is often provided by halogen lamps or LED lights. LED lighting solutions are preferred as they are a cold light source, reducing potential noise due to thermal convection [175]. The GOM 12M system uses dual high power LED light solution suitable for measuring areas up to 500×400 mm^2. For dynamic experiments where more illumination is required due to the lower exposure time, two 10,000 lumen LED Sigmatech ICARUS lights were used. These enabled the images to be captured with a reduced aperture increasing the depth of field and enabling the use of 3D DIC up to 90 kHz.

The exposure time must be set such that no pixels are over exposed which leads to the saturation of the dynamic range and that no blurring of the image occurs due to rapid

movement of the subject. A minimum sampling frequency for temporal resolution of the data set is often prescribed in material characterisation test standards along with strain rate. For example the ASTM D3039-14 standard for determining the tensile characteristics of a continuous composite requires at least 100 data points to succinctly quantify the modulus, strength and ultimate strain of the material system [176]. Considering the approximate tensile strain of 1 % and test speed of 2 mm/min, a sampling frequency of 2 Hz with an exposure time of approximately 85 ms is appropriate. For images captured utilising the high speed camera system, Photron Fastcam automatically selects the maximum exposure time for a given imaging frequency.

3.5.3 Temporal synchronisation of DIC and frame data

Temporal synchronisation of the load measurements and optical measurement equipment is essential. Without this it is very challenging to match the data sets and generate an accurate understanding of the material performance. The GOM 12M system incorporates a data acquisition system that is capable of temporally syncing the frame and imaging data. In comparison the use of Photron high speed cameras and the VHS requires the use of a separate data acquisition system.

The Instron VHS test machine has an internal trigger system to record the load measurements of the piezoelectric load cell, this same transistor-transistor logic (TTL) pulse can be used to trigger the high speed cameras as well as a National instruments data acquisition (DAQ) board in order to provide temporal matching of the data [177]. A schematic of the BNC cable layout and triggering method used for 3D DIC is shown in Figure 3.21.

The displacement of the actuator is used to generate the TTL pulse that triggers the high speed cameras and provides synchronisation. Throughout this project the TTL pulse was controlled based on the actuator drive, at the moment the actuator accelerates the pulse voltage changed from 3.5 V to 0 V. This voltage change triggers the master camera, which in turn triggers the slave camera. At the same instant a pulse is sent to the DAQ board via channel *General out 1* in order to trigger the recording of data. A positive synchronisation pulse is output from the master camera using the camera I/O channel *General out 2* to both the slave camera and the DAQ. This temporally synchronises the analogue load and displacement signals with the images recorded [167]. The analogue signals can then be read into Photron Fastcam Viewer using the DAQ plugin. The image series and temporally matched load and displacement data can then be trimmed in Photron Fastcam Viewer before

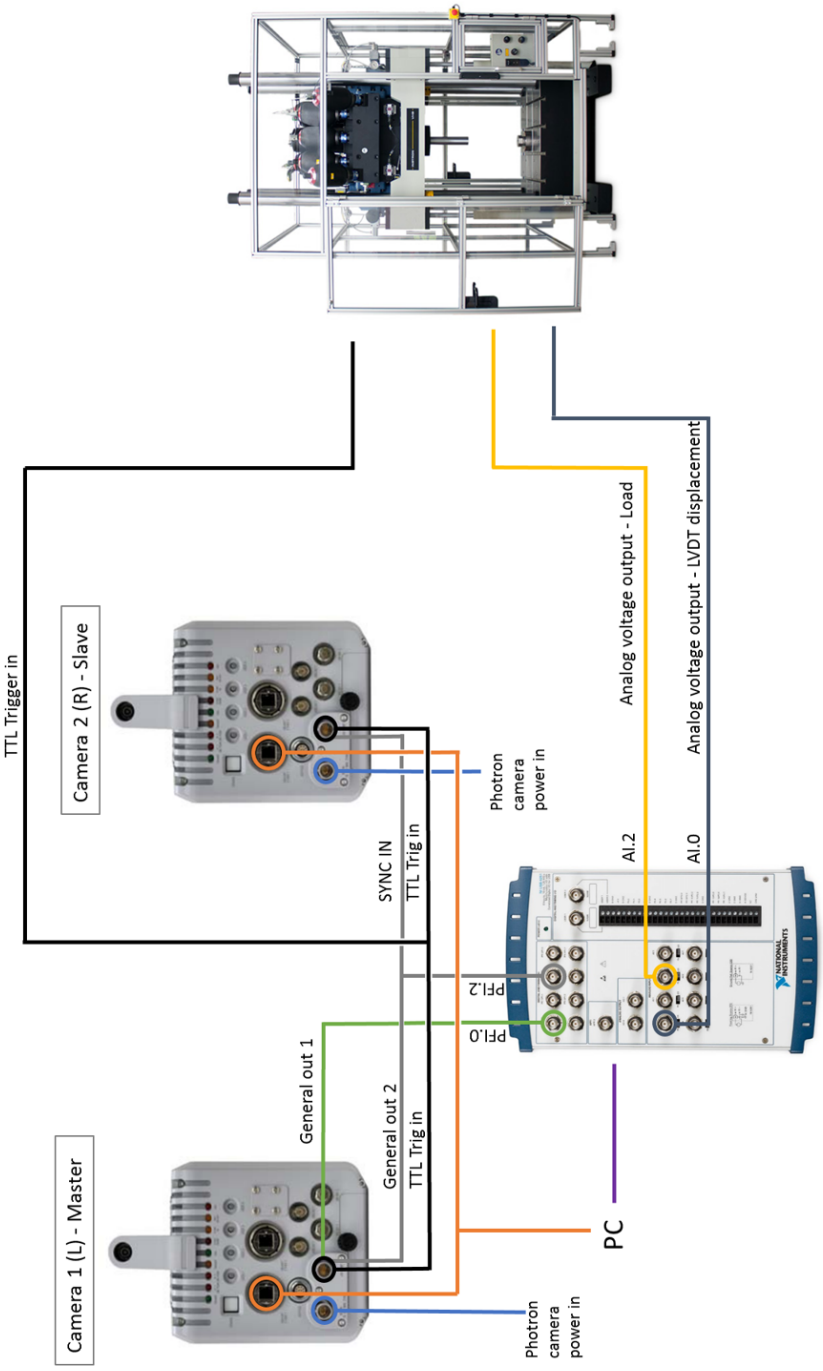

Figure 3.21: Schematic of triggering method used for 3D DIC

being exported as 8 bit .tif files for use in GOM ARAMIS. Figure 3.22 provides an example of the temporally matched tensile stress and tensile strain data, the consistent strain and stress rising time point denotes that the data is synchronised to within less than a frames error.

The equal imaging frequency of the two identical cameras simplifies the triggering method and enables the *Manual* trigger mode to be employed. In this triggering method, the data acquisition system constantly buffers 5 % of whole buffer size and then records the remaining 95 % once the trigger pulse has been received.

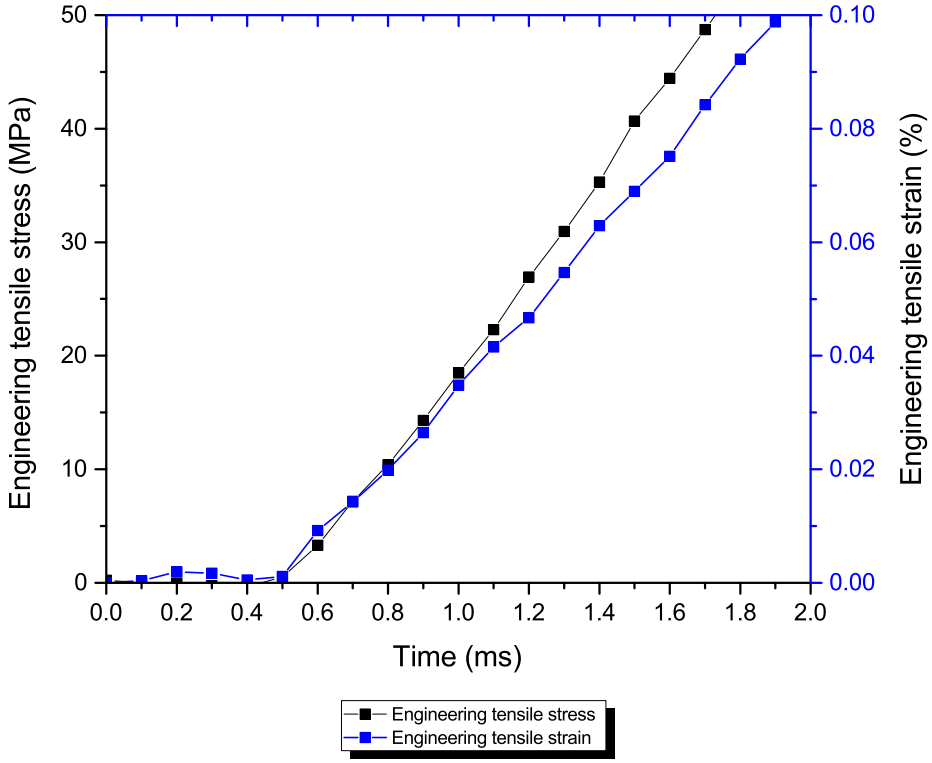

Figure 3.22: Example results of syncronised stress and strain measurements during tensile characterisation at 0.05 ms^{-1} with strain sampled at 10 kHz.

3.5.4 Specimen preparation

The objective of the specimen preparation phase is to provide a good quality contrasting pattern on the measurement surface in order to maximise the dynamic range of the sensor yet provide a unique pattern. The increased random nature of a speckle pattern will provide better results in comparison to a coarser and more structured

patterns [178]. In this thesis a matt black surface was applied using *Plastikote Matt Black Primer* prior to the application of the speckle pattern on the specimen surface. It is important that the matt black paint is allowed to dry sufficiently such that it loses all gloss, however, it must still have a low enough viscosity that it will deform with the specimen and not crack as this would be interpreted as a material failure by the DIC solver. As a result all experiments in this thesis were conducted within an hour of spraying the specimens.

Defining the quality of a speckle pattern has been the subject of research in literature [179–181]. The quality of the pattern is dependent upon the measurement scale, when the RoI is very small and the spatial resolution of the image is in the order of 3 μm per pixel then speckles must have a diameter no less than 9 μm , giving a minimum speckle size of 9 pixels. As the pixel quantity per speckle is reduced below this value it will become subject to pixel locking whereby the resultant displacement values become biased towards integer pixel grey scale values. This ratio can be upscaled for larger RoI's giving speckles that have a magnitude greater than 10 mm. In order to maximise the dynamic range of the cameras employed throughout this thesis speckle patterns were applied in two methods. In order to maximise the range of the 12 megapixel sensors speckles with a minimum diameter of 100 μm were applied using diluted white emulsion paint and an air brush. In comparison the 1 megapixel sensors within the Photron SA-X2 cameras required a minimum speckle size of 260 μm, these were applied using variable pressure acrylic *Montana Gold Shock White* spray paint.

3.5.5 Establishment of the DIC processing parameters

Prior to running a test a series of static images must be collected and analysed in order to review the measurement accuracy and to ensure the system is set up correctly. Throughout the setup of the imaging equipment it can be easy to introduce errors into the system. As previously commented on these errors are represented as false strains in the final measurements. The measured average strain across the strain map over a sequence of stages provides the bias of the measurement system whilst the variance of the average strain and displacement maps for the specimen provides the minimum measurement resolution. The appearance of large highly localised strains or appearance of a fringe pattern represents the incorrect set up of the imaging equipment, instead the error measurement should appear as white noise (as shown in Figure 3.23).

The selection of facet and step sizes has a direct relationship with the observed measurement resolutions as well as the spatial resolution. If a facet size is small then

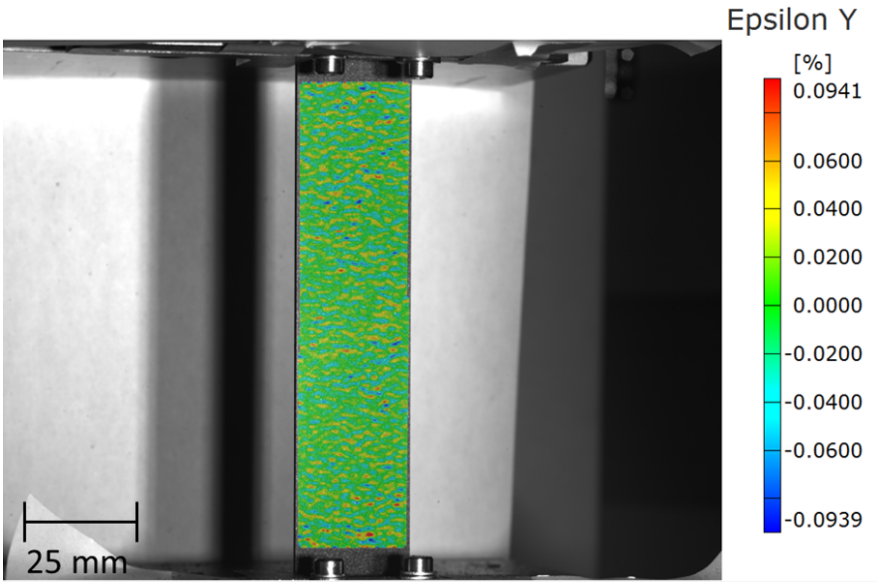

Figure 3.23: Example of random distribution of longitudinal strain (ε_{YY}) errors within the processed image due to the experimental set up of the DIC measurement system.

the calculated displacement vector will be dependent upon the local deformation of the speckle pattern within the facet, this can lead to the computation of large amounts of noise. In comparison if the facet size is set to a very large value in relation to the specimen size then the produced displacement vector will be highly smoothed and the low spatial resolution will result in the inability of the captured displacements to represent the heterogeneity of the material system.

The effect of varying facet and step sizes on the strain resolution captured over a series of stationary images is shown in Figures 3.24 and 3.25. A specimen prepared with a speckle pattern was imaged by both the GOM 12M and Photron SA-X2 camera systems with a FoV of 200 x 150 mm^2 and 150 mm^2 respectively. With no rigid body motion applied the strain fields for each of the five stationary images were computed with facet sizes from 8 $pixels^2$ to 64 $pixels^2$ whilst the step size was reduced from 100 % of the facet size to 25 % (facet overlap of 75 %). In order to assess the noise the longitudinal strain and displacement were output for each measurement point along ten sections distributed evenly along the specimens length. As expected when considering the GOM 12M camera system (Figure 3.24) the strain resolution improves with increasing facet size, whilst the reduction in step size induces a small increase in noise, yet yields a large increase in the density of data points. The greater the number of data points, the better the ability to detect damage as a result of the

heterogeneity of the laminate. The same effect is also observed with the Photron SA-X2 camera system (Figure 3.25) although the lower resolution of the Photron cameras results in a reduced measurement resolution.

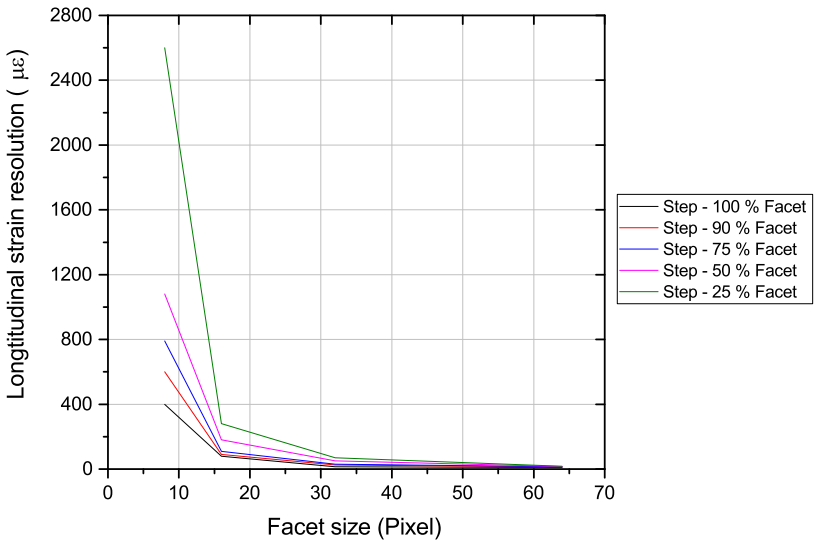

Figure 3.24: Strain measurement resolution for multiple facet and step sizes for GOM 12M camera systems.

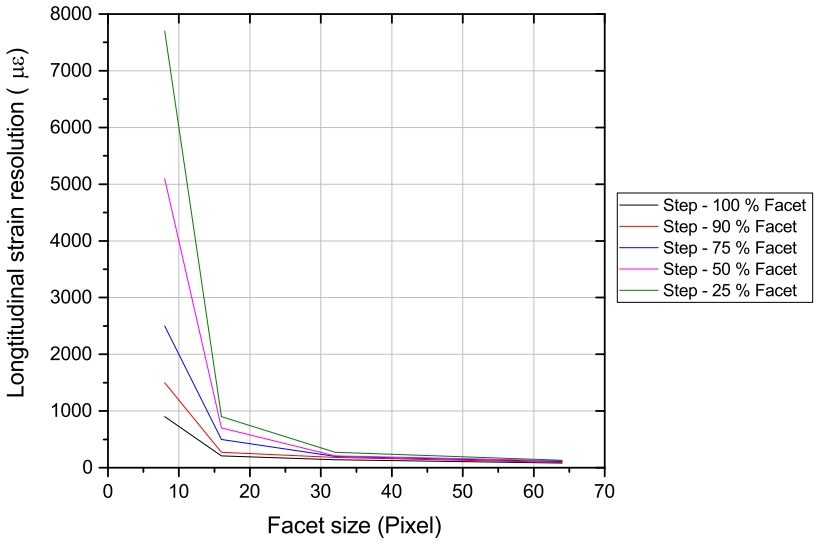

Figure 3.25: Strain measurement resolution for multiple facet and step sizes for Photron SA-X2 camera systems.

Based on Figures 3.24 and 3.25 it is clear that the measurement resolution converges once the facet size is increased above 16 pixels^2 for both cameras sets. Since this is approximately equal to the 19 pixel GOM recommended facet size, with a 80 % step size, the GOM recommended settings will be employed when possible. In order to achieve a temporal resolution of at least twenty images during a tensile test (providing three point moving average over 0.2 % modulus range) the spatial resolution will be reduced from the GOM recommended values as the frame rate is increased to improve the temporal resolution, requiring cropping of the sensor. Reducing the spatial resolution was previously discussed with respect to the undesirable strain smoothing observed by Naresh et al. (Figure 3.17). Figure 3.26 shows the effect of increasing the distance between unique facet centres relative to the GOM recommended resolution (0.95 mm). It is clear that the modulus and ultimate strain are reduced as a result of the large facet size. The local peak deformations over the facet are averaged, thus the specimen behaves with constant linearity to fracture at a reduced ultimate strain.

The DIC equipment and computation parameters are presented when used throughout this thesis, an example is provided in Table 3.5.

Table 3.5: Typical measurement parameters for GOM 12M 3D DIC.

Property		Unit
Camera	GOM 12M	
Lens	Titanar 100	
Frame rate	2	Hz
Shutter speed	85	ms
Aperture	16	f.
Imaging window	4000 x 3000	$pixel^2$
Calibration plate	CP20 90 x 72	
Measurement volume	200 x 150 x 100	mm^3
Facet size	19	pixel
Step size	16	pixel
Spatial resolution	0.8	mm
Strain resolution	26.1	με
Displacement resolution	0.09	μm

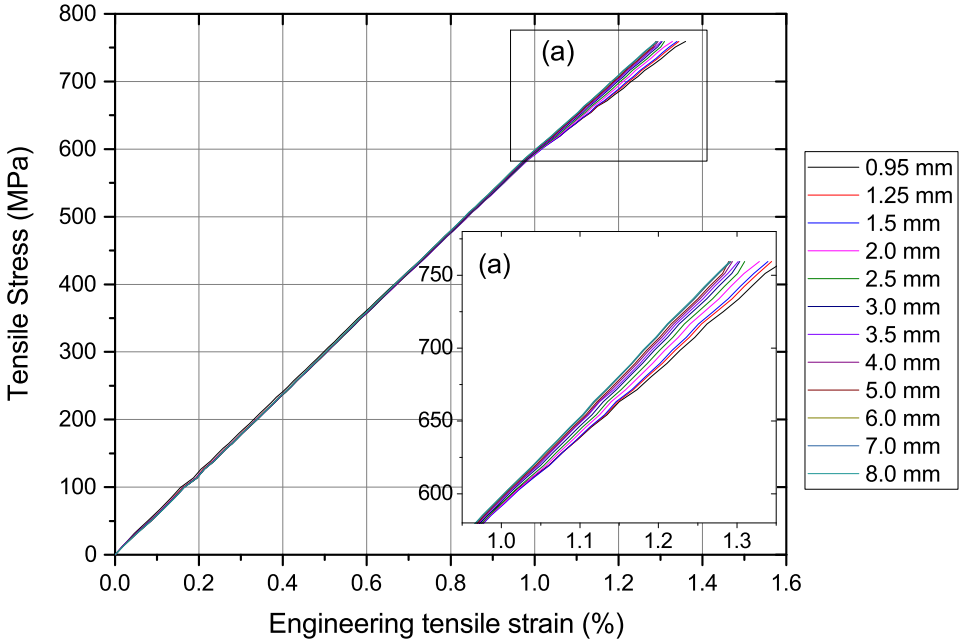

Figure 3.26: Effect of reducing spatial resolution on the quasi-static tensile response of 12K 2 x 2 twill CFRP. The induced smoothing as a result of increasing facet size is shown in subset (a) to reduce the specimens ductility at failure.

3.6 Summary

This chapter has outlined the experimental methods used throughout this thesis. This included an introduction to the materials and manufacturing methods required for this thesis due to the requirements of the automotive industry to use large tow sizes within heavy fabrics impregnated with fast curing epoxy resins to maintain acceptable costs. The Instron static and dynamic test frames have been introduced. A preliminary study demonstrated that the state of the art fast jaw system was shown to be unsuitable for the characterisation of continuously reinforced composite laminates due to poor experimental repeatability. The requirement to use straight sided specimens resulted in an inability to induce the desired strain rates since the specimen tail behaves identically to the gauge length, effectively increasing the free length. Untabbed and GFRP tabbed specimens were also shown to be unsuitable since the dynamic friction between the specimen and the fast-jaw mechanism was insufficient to load the specimen to fracture. As a result a new fixturing system must be developed. Finally, an introduction to DIC optical measurement has been provided. Optical measurements are ideally suited to characterise composites as the heterogeneous strain field can be captured on a large length scale. However, the creation of precise and accurate data requires in-depth understanding of the potential error sources. The methods presented in this chapter will be built upon over the coming chapters.

Chapter 4

Development of experimental dynamic tensile testing techniques

This Chapter commences with the characterisation of the composite material system at quasi-static strain rates according to the standardised testing techniques introduced in the previous Chapter. The aim of these preliminary experiments is to define the requirements of the dynamic test system that must be developed as concluded in the previous chapter. The Instron fast jaw LMD provided with the VHS was judged to be unsuitable for the characterisation of composites, therefore a novel loading system is required to be developed. A prototype high capacity slack rod for the characterisation of high strength metallic specimens was provided by Instron and tested. Details are provided on the development providing a novel solution for the characterisation of high performance continuous composites. The Chapter concludes with the proposal of novel coupon geometries for tension and in-plane shear based on the surface strain results of the standardised experiments. Since the specimen reduction relies on the assumption of the plane strain condition, the new geometries are experimentally validated prior to being evaluated at intermediate strain rates in Chapter 5.

4.1 Preliminary quasi-static material characterisation

In order to develop the dynamic test method and define the mechanical response of the material system, the composite laminate was characterised using standardised quasi-static experimental techniques to evaluate the two stress states considered throughout this project, tension and in-plane shear. This section outlines the experimental methods and results of these preliminary experiments.

Testing was conducted according to the methods introduced in Chapter 3. Tensile coupons were derived from the ASTM D3039-14 tensile specification, their width was increased by 7 mm to 32 mm in order to account for two unit cells to be

positioned across the width of the specimen. In-plane shear specimens were produced to the same dimensions with an off-axis stacking sequence of $[45]_8$ according to ASTM D3518-13. In order to alleviate the risk of shear damage during testing, both specimens used GFRP tabs bonded onto the specimen using Solvay VTA 260 adhesive film. Both sets of specimens were investigated using an Instron 5980 static frame with a cross-head speed of 2 mm/min, the integrated load cell was temporally synchronised with the surface strains of the specimen which were recorded using the GOM 12M DIC system. The DIC properties are shown in Table 4.1.

Table 4.1: GOM 12M 3D DIC properties for preliminary characterisation of the tensile response of the 12K 2 x 2 twill CFRP specimens at quasi-static speeds.

Property		Unit
Camera	GOM 12M	
Lens	Titanar 100	
Frame rate	2	Hz
Shutter speed	85	ms
Imaging window	4000 x 3000	$pixel^2$
Calibration plate	CP20 90 x 72	
Measurement volume	200 x 150 x 100	mm^3
Facet size	19	pixels
Step size	16	pixels
Spatial resolution	0.95	mm
Strain resolution	35	µε
Displacement resolution	0.09	µm

4.1.1 Results and discussion

The tensile stress-strain response of five specimens evaluated is shown in Figure 4.1, whilst the shear stress-strain plot is presented in Figure 4.4. The mechanical properties for both the tensile and in-plane shear were calculated according to ASTM D3039-14 and D3518-13 respectively and are summarised in Table 4.2.

The derived response to axial tensile loading is linear elastic with a Young's Modulus of 61.16 GPa (Figure 4.1). The highly repeatable nature of the elastic loading is evident due to the low 0.71 variance (SD) and resultant 1.16 % coefficient of variation (CoV) between modulus values measured using a linear curve fitting between 0.1 and 0.3 % ε_{YY}. The global longitudinal strain of the specimen is calculated based on the average strain of the specimens free length. As the specimen continues to strain

Table 4.2: Mechanical properties derived from preliminary standard tension and in-plane shear experiments of the 12K 2 x 2 twill CFRP specimens.

Property	Value	units	SD	CoV (%)
Tensile modulus	61.16	GPa	0.71	1.16
Tensile strength	867.60	MPa	34.34	3.96
Ultimate engineering tensile strain	1.43	%	0.041	2.87
Poissons ratio	0.054	N/A	0.0017	3.15
Shear modulus	3.74	GPa	0.079	2.12
Ultimate shear strength	111.63	MPa	1.84	1.64
Shear strength at yield	70.97	MPa	1.42	2.02
Engineering shear strain at yield	3.98	%	0.07	1.84
Ultimate engineering shear strain	18.76	%	0.42	2.23

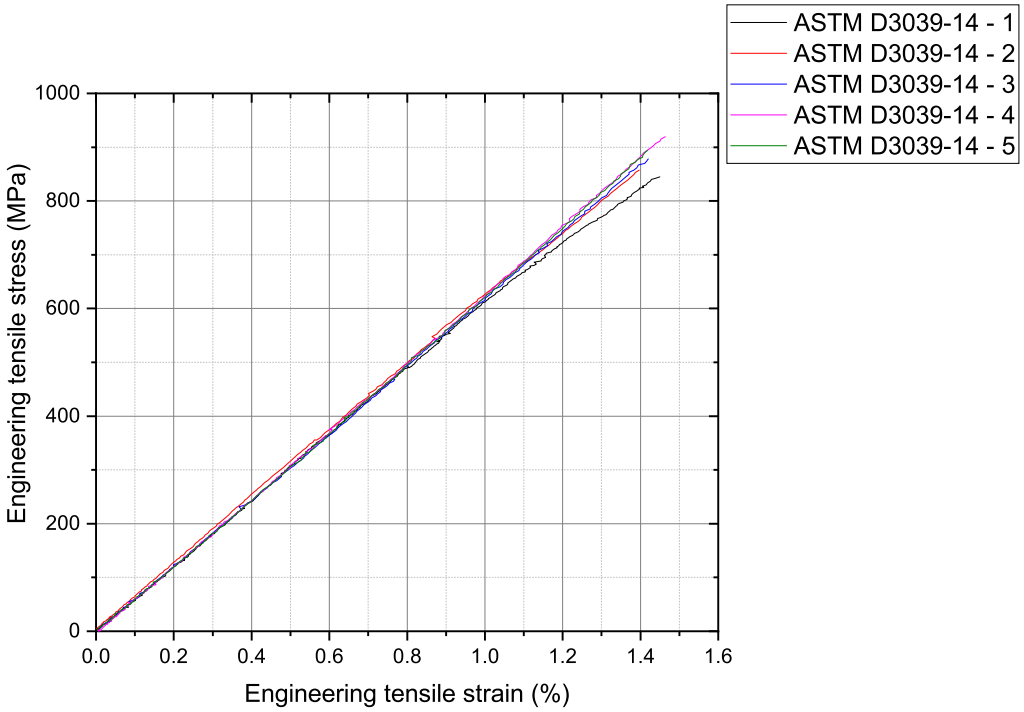

Figure 4.1: Quasi-static longitudinal engineering stress-strain response of the 12K 2 x 2 twill CFRP specimens tested according to widened ASTM composite standard D3039-14.

beyond this purely elastic region, the stiffness remains approximately constant to failure. The variation in failure strength and failure strain is a result of the different damage coalescence sequence within each specimen.

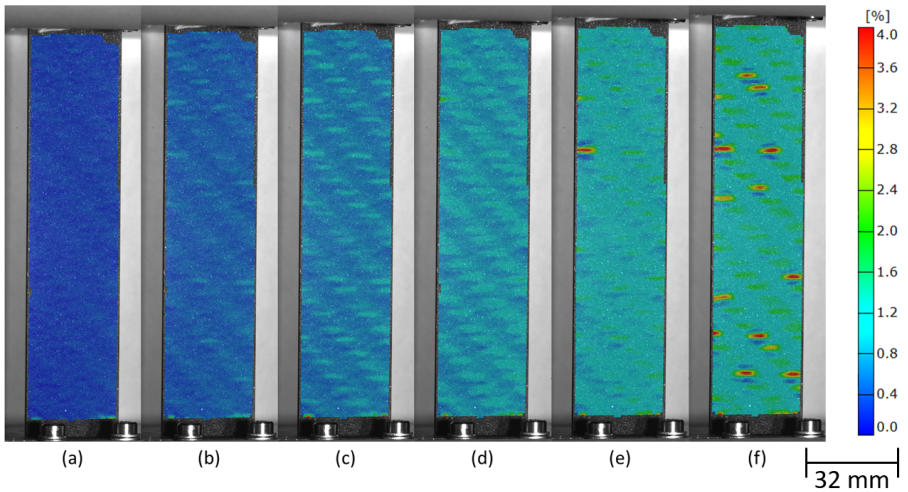

Figure 4.2: Surface strain maps overlaid on the left specimen image demonstrating the progression of longitudinal engineering strains at (a) 0.2, (b) 0.4, (c) 0.6, (d) 0.8, (e) 1.0 and (f) 1.2 % ε_{YY} of a 12K 2 x 2 twill CFRP specimen (specimen #3) undergoing a widened ASTM D3039-14 composite tensile characterisation test.

The surface strain maps (Figure 4.2) demonstrate how the specimen exhibits very little necking, with a measured Poissons contraction of 0.06 prior to the transverse fracture of the specimen. Figure 4.2 shows how the heterogeneity of the failure is consistent with the phase of the fabric weave. Longitudinal fibres undergo uniform straining and dictate the global properties of the material system prior to failure as the are the strain limited constituent, whilst in comparison the transverse fibres are strength limited, therefore they can be seen to splay with the formation of matrix cracks within the tow and at the elliptical tow boundary. The peak longitudinal strain observed in Figure 4.2 (e) is the result of splaying of the transverse tow positioned at the specimen edge and the resultant edge effects creating intra-lamina cracks at this location. The failure of the transverse tows, which is wide spread throughout the specimen by 1.2 % ε_{YY}, results in the localised overloading of the longitudinal tows, which then begin to fail. The coalescence of these failures leads to the ultimate failure in the form of transverse cracks.

Due to the random distribution of the defects within the specimen and the architecture induced stress fields ultimate failure occurs at different locations depending on the specimen under evaluation, this is shown in Figure 4.3. Many specimens experienced dual fracture, where the release of strain energy following the initial fracture creates a shock wave to occur through the material inducing a secondary

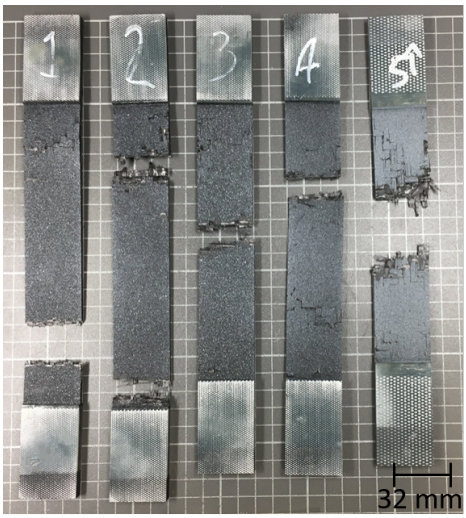

Figure 4.3: Transverse tensile failure of the 12K 2 x 2 twill CFRP specimens post widened ASTM D3039-14 tensile characterisation test.

fracture that is often observed close to the tabbed region of the specimen. A single specimen failed within a grip width of the jaws of the test frame, which could suggest that shear damage resulting from the load transfer to the specimen could have initiated the damage, however, since the extracted mechanical properties were within the 95 % confidence interval of the remaining dataset it was not discarded and it was instead assumed that at this position the statistically random weakness that initiated failure existed. Since the failure sequence discussed matches the expected response that was discussed in Chapter 2, the mechanical properties extracted from the experiment are considered as a true representative of the composite laminate.

In comparison to the longitudinal tensile response, the in-plane shear behaviour (Figure 4.4) is bi-linear with a clear yield point, Figure 4.5 shows the progression of longitudinal strains during the experiment and demonstrates the formation of the three shear regions generated during the experiment. A schematic of these shear regions is shown in Figure 4.6. The hatched area defines the rigidly gripped potion of the specimen within the jaws, region (a) represents the portion of the specimen undergoing pure shear, (b) represents intermediate shear strains, whilst (c) represents the minor shear strains constrained within the vicinity of the jaws [182]. Due to the constrained ((b) and (c) regions) undergoing limited shearing over the course of the experiment, the global shear strains are determined as a function of the pure-shear region (central 120 mm).

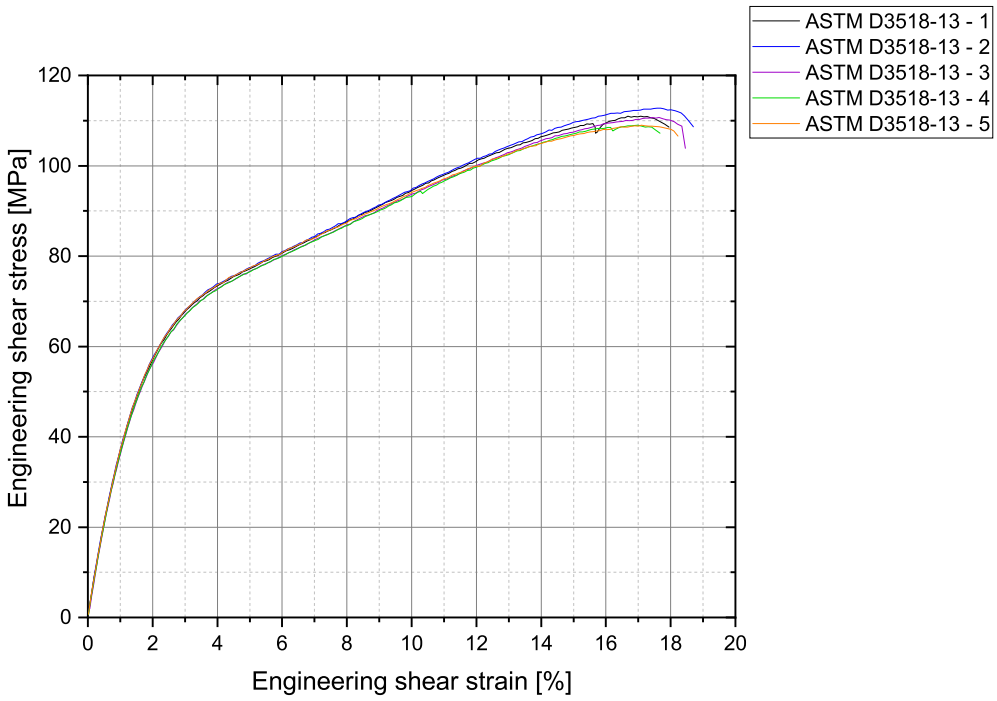

Figure 4.4: Quasi-static engineering in-plane shear stress-strain response of the 12K 2 x 2 twill CFRP specimens tested according to widened ASTM composite standard D3518-13.

The shear modulus is derived based on a linear fit between 0.2 and 0.4 % engineering shear strain, it was found to be significantly lower (3.74 GPa) in comparison to the fibre dominated longitudinal tensile properties due to its inherently weaker mechanical properties. However, due to the ductile nature of the matrix it undergoes greater strain to failure. As the specimen is loaded, the initial shear stiffness reduces due to the onset of matrix cracking, the coalescence of which induces the material yield. Post yield, the specimen necks within the pure shear region (gauge length) and exhibits strain hardening to ultimate failure due to the rising load. Based on the literature reviewed in Section 2.1.3, failure is a result of locking of the twill fabric at peak shear angle as the fibres are reorientated with the load. Figure 4.5 (f) highlights how at 8 % longitudinal strain, the shear strains generated as a result of the specimen edge effects have lead to intra-lamina cracks, (as well as inter-lamina cracks although these cannot be seen in the figure) which cause the tow ends to splay considerably inducing large longitudinal strains. The final fractured specimens are

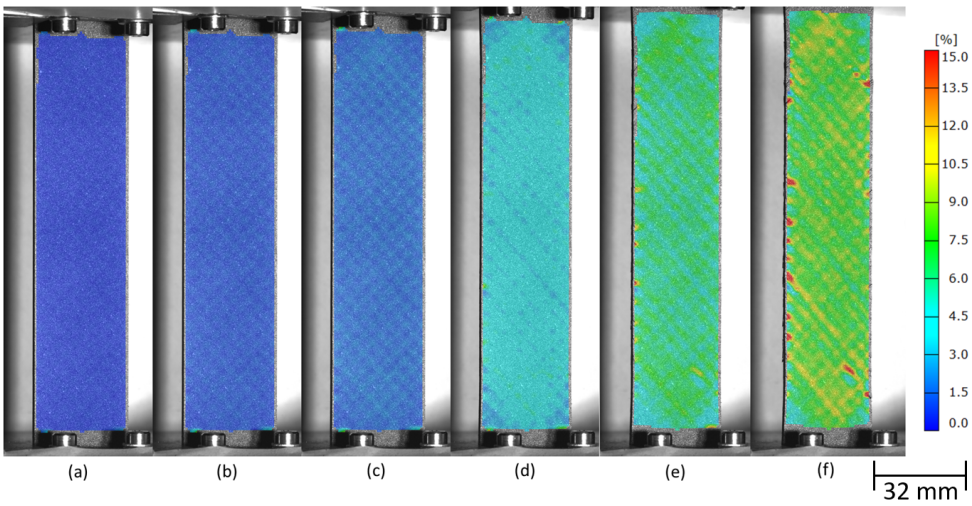

Figure 4.5: Surface strain maps overlaid on the left specimen image demonstrating the progression of longitudinal engineering strains at (a) 0.5, (b) 1.0, (c) 1.5, (d) 4.0 (e) 6.0 and (f) 8.0 % ε_{YY} of a 12K 2 x 2 twill CFRP specimen (Specimen - 3) undergoing a widened ASTM D3518-13 composite in-plane shear characterisation test.

Figure 4.6: Schematic of the shear strain regions of a composite specimen undergoing an in-plane shear experiment. [Adapted from [182]]

shown in Figure 4.7. Due to the heterogeneous nature of the damage mechanisms it can be seen that the fracture does not occur in the same location on each specimen with cracks parallel to the warp and weft fibre directions.

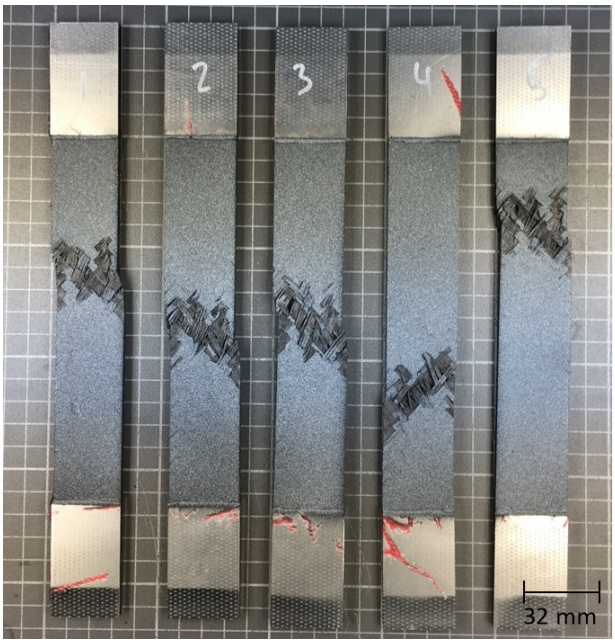

Figure 4.7: Shear failure locations of the 12K 2 x 2 twill CFRP specimens post widened ASTM D3518-13 in-plane shear characterisation test.

This section has described the quasi-static standardised characterisation of the 12K 2 x 2 twill CFRP laminate subject to longitudinal tension and in-plane shear stresses in order to determine the required performance of the dynamic test equipment. The collected data will form the statistical baseline for the development of an optimised dynamic specimen that is not affected by the size effects of the laminate architecture.

4.2 Slack adaptor

As highlighted in Section 2.2 many examples of LMD's have been developed in order to characterise composite, polymer and metallic material systems under dynamic loading conditions. The most suitable for composite characterisation as identified by Fitoussi et al. [108] is a plunger style activation instead of the fast jaws previously applied in this thesis. The slack adaptor LMD allows the user to statically apply the grips to the specimen, reducing the complexity of the system and improving the experimental repeatability. Instron kindly donated a prototype high capacity slack adaptor (henceforth referred to as the slack adaptor) which is shown in Figure 4.8, it is rated sufficiently to enable specimens with a failure load of up to 100 kN be reviewed for the first time in this research.

A section view of the Instron slack adaptor is presented in Figure 4.8. To reduce the mass a cradle design is utilised that composes of six columns rather than a solid casing as seen on previous designs. As well as reducing mass it also limits the retardation of the actuator induced by the resultant increasing air pressure of an enclosed design. When the specimen fractures during high velocity experiments, the fracture energy will lead to the vertical acceleration of the upper dynamic jaw. In order to arrest its velocity without damaging the fixturing a polymer damper is positioned at the base piston attachment. Unlike the designs by Fitoussi et al. and Southampton University, which, employed an elongated piston attached to the upper jaw to provide the inertia free acceleration period, Instron proposed to use the specimen free length to accelerate the slack adaptor cradle. As a result the dynamic upper jaw is mounted within the conical impactor. Since Instron's prototype slack adaptor was developed for the characterisation of ultra high strength steels dog boned specimens were employed, widening of the specimen within the upper jaw enabled a pinned mounting system. Two 10 mm diameter dowels are mounted through the upper grip of the specimen. At the base, a set of self aligning grips are employed, these are connected to the Kistler load cell washer.

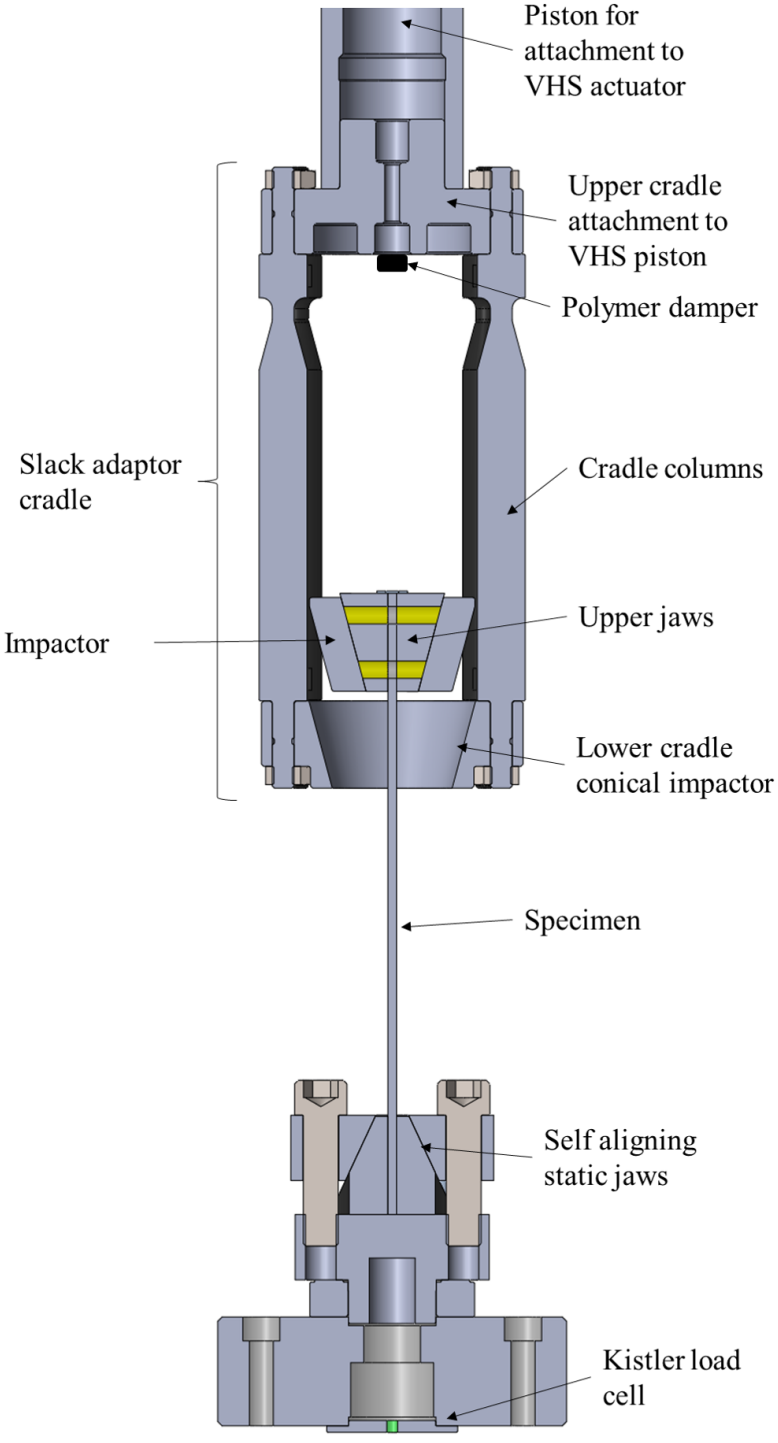

Figure 4.8: CAD model of the high capacity slack adaptor provided by Instron, the exact measurements are propriety to Instron, however the free length of the specimen is greater than 165 mm.

4.2.1 Preliminary experiments utilising the Instron pinned loading mechanism

Benchmarking of the proposed Instron pinned loading mechanism was conducted at 0.1 ms^{-1} on straight sided 600 gsm STS40 NCF MTM710-1 composite specimens with a stacking sequence of $[0]_4$. The specimens were manufactured using compression moulding as outlined in Chapter 3 and prepared into the geometry shown in Figure 4.9. Aluminium tabbing with a 1.5 mm gauge was bonded to the specimen with a 0.3 mm DP490 bondline containing glass beads.

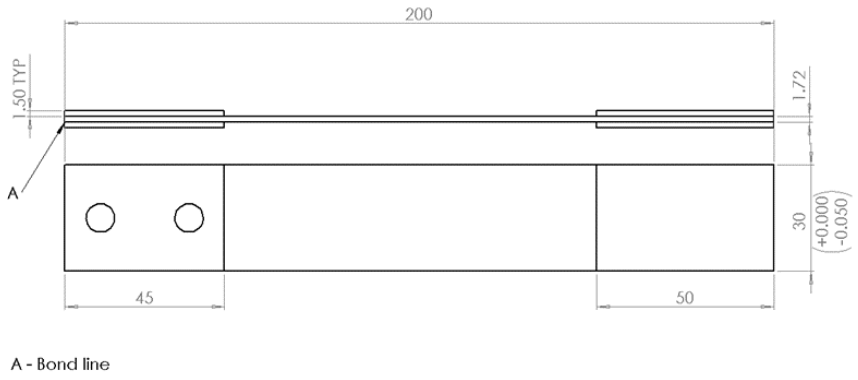

Figure 4.9: Engineering drawing of CFRP specimens tested using the Instron pinned slack adaptor mounting system, all dimensions are in mm.

Metallic coupons that are typically dog boned are able to be drilled as the specimen shoulders are significantly wider than the gauge length, as such the induced stress concentrations remain within the elastic limits of the material. In comparison the introduction of holes into the straight sided composite specimens can introduce localised defects from whence the failure initiates. Figure 4.10 shows the failure mode of the specimens tested with the pinned loading mechanism, the lower portion of the hole remains intact in the axial fibre orientation. However, extensive transverse fibre damage can be seen, this suggests that failure initiated in the transverse fibres in the vicinity of the hole. The transverse fibre cracks propagated forming extensive inter-laminar damage below the tab. Ultimately this lead to the substrate failure of the composite at the bond line. This study identified that the pinned loading mechanism is unable to load the specimen with failure initiated at the connector. Therefore the upper jaws were redeveloped (Section 4.2.2).

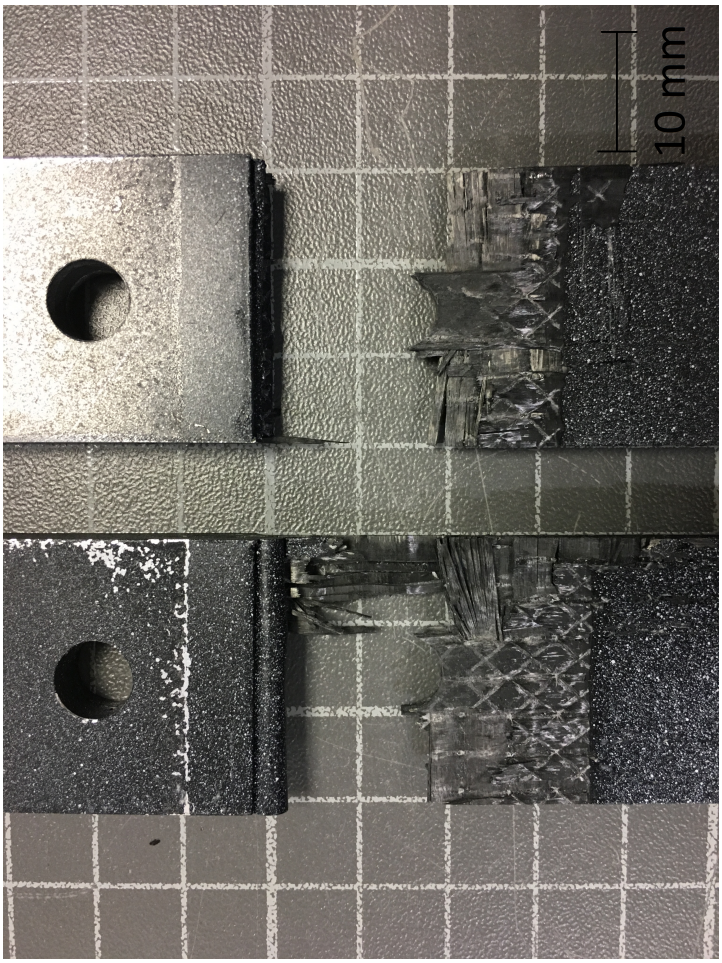

Figure 4.10: Example of fracture caused by localised stress concentrations at the pinned joint interface of Instron slack adaptor design.

4.2.2 Development of the dynamic jaw for high capacity loading of composite specimens

Following an extensive re-design the slack adaptor is shown setup within the VHS in Figure 4.11, a composite specimen is mounted within the VHS and two Photron SA-X2 cameras and ICARUS lights are setup to measure surface strains via 3D DIC. A more detailed section view of the slack adaptor is provided in Figure 4.12. The impactor was re-designed such that the upper serrated jaw faces were positioned below the impactor, this increased the acceleration distance of the cradle by 45 mm prior to engaging the load train. The lower jaws are packaged such that they sit within the inner diameter of the slack adaptor cradle, providing an additional 35

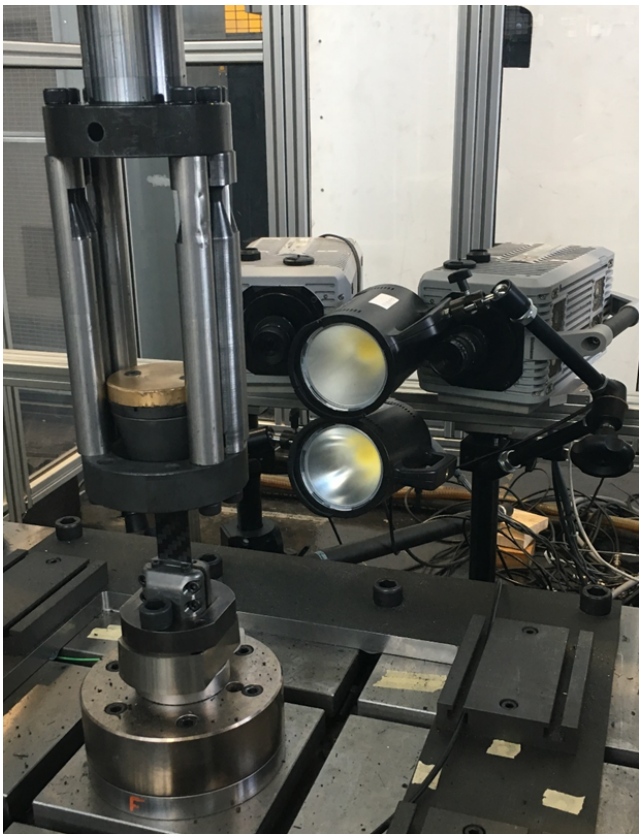

Figure 4.11: Re-designed slack adaptor in situ with a composite specimen mounted between the upper and lower jaws and two Photron SA-X2 cameras conducting 3D DIC to measure the surface strains of the specimen.

mm of acceleration distance. Thus, when a specimen with a free length of 85 mm is mounted between the jaws, the VHS is capable of achieving max velocity (20 ms^{-1}).

The impactor and upper jaws were manufactured from O1 tool steel and hardened to 56 HRC, O1 steel was used due to its high dimensional stability at elevated temperatures. Due to the impact loading of the system at the moment of contact, the impactor will experience loads in excess of that induced by the specimen and required hardening to achieve the desirable yield strength. The acceleration of the impactor during a 15 ms^{-1} experiment was extracted from LVDT readings during a preliminary test and the mass of the redesigned upper jaw (1.73 kg) enables the inertial loading of the impactor to be determined. The experimental acceleration readings were required since the desired theoretical acceleration cannot be employed as it does not consider the compliance of the load train. Linear finite element analysis of the impactor during its design enabled the author to design a factor of

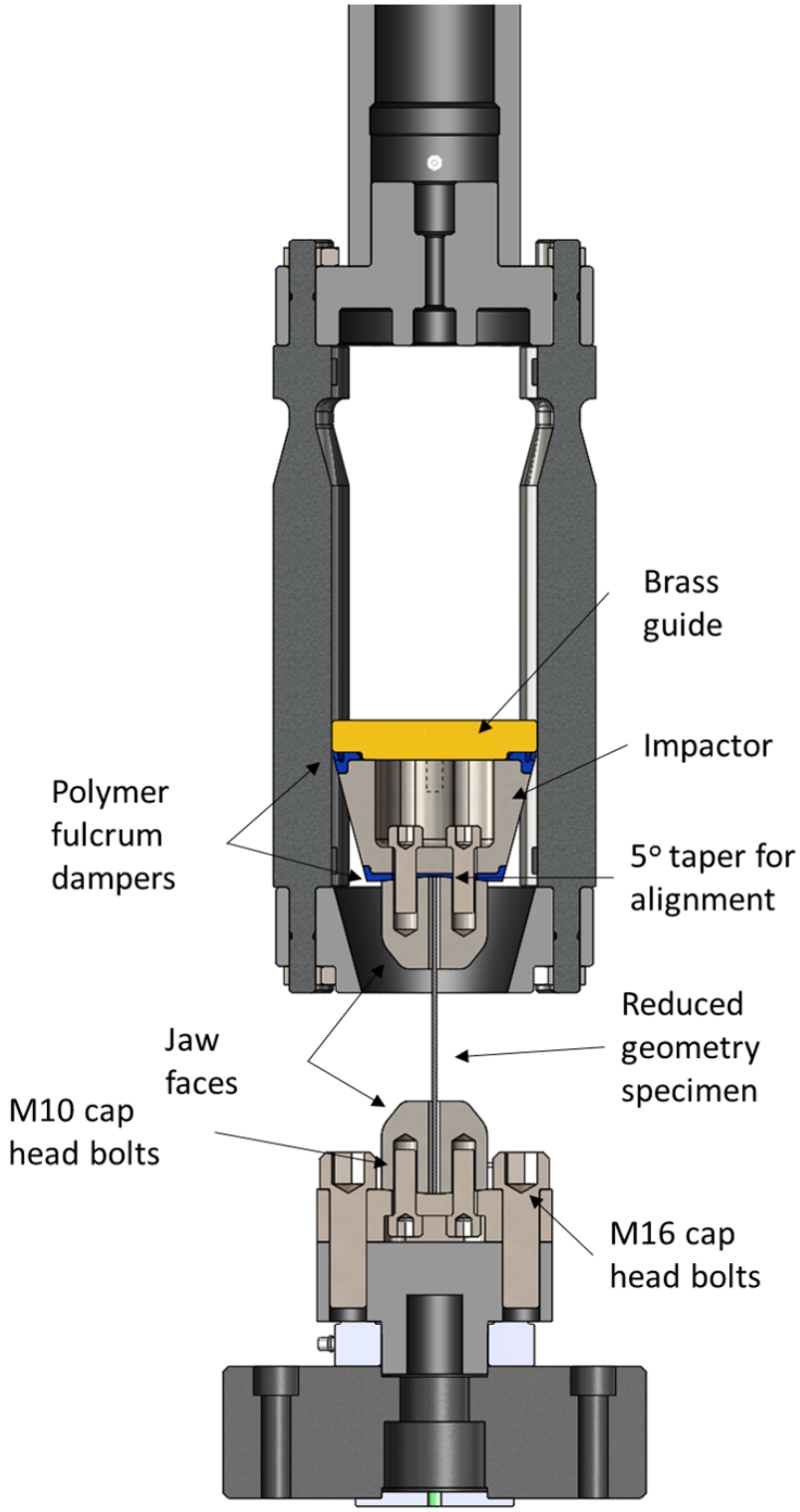

Figure 4.12: CAD model of re-designed slack adaptor that was developed over the course of this project, it contains a new impactor and upper jaw assembly as well as a re-designed lower jaw in order to increase the maximum potential strain rate of the specimen.

safety of 1.6 on yield stress to ensure that use of the impactor would not effect the results obtained despite repetitious loading. The upper jaws are mechanically attached to the impactor using two M10 12.9 cap head bolts torqued to 40 Nm. A 5° taper was positioned at the interface to self align the jaws to the central axis of the impactor, when positioned within the cradle and used in conjunction with the self aligning lower jaws this arrangement provides good vertical alignment of the load path through the central axis of the specimen and the test frame. The gripping force of the upper jaws is provided by two M6 12.9 cap head bolts either side of the specimen torqued to 12 Nm. To ensure repeatability of the specimen loading the bolts were torqued in a figure of eight starting at the lower left (relative to the front of the specimen), the torque level is staggered, increasing by 25 % with each repetitive cycle until the final torque is reached. As previously mentioned the lower jaw assembly used the same jaw faces as the upper jaw, including the 5° taper to ensure specimen alignment and allow the user to package them within the inner diameter of the slack adaptor increasing the acceleration distance.

Preliminary experiments with an early prototype upper jaw observed knocking between the impactor and the cradle prior to the specimen being loaded. This can be observed as the oscillating load measurements that occur prior to specimen engagement in Figure 4.13. This knocking introduces pre-loads to the specimen and the premature excitement of the load cell induces noise reducing the accuracy of the derived modulus. The knocking also adjusts the alignment of the initial connection of the LMD which could introduce bending strains and damage into the specimen prematurely. Upon inspection of the tested components it was evident that the upper and lower fulcrum points of the impactor were making contact. The upper fulcrum point was knocking against the cradle pillars whilst the lower fulcrum points were hitting the inside of the conical impact surface of the cradle. To alleviate this a brass guide was positioned above the impactor with a clearance to the columns of 0.05 mm (±0.002 mm), this restricted the lateral motion and rotation of the impactor as the cradle was accelerating. Since the impact of the guide with the cradle walls will also introduce knocking through the load cell, polymer dampers were 3D printed from Onyx with a continuous glass reinforcement at WMG and positioned at both the lower and upper fulcrum points. The upper damper is in constant contact with the supporting pillars inducing a small frictional loss; however, based on the experimental readings of the LVDT this do not affect the ability of the cradle to be accelerated to the desired test speeds. The side wall of the upper damper in contact with the cradle is 1 mm thick, this allows the part to flex and dampen the premature excitement of the load cell induced from the knocking of the brass guide as shown in Figure 4.13. Engineering drawings of the proposed design is shown in Appendix A.

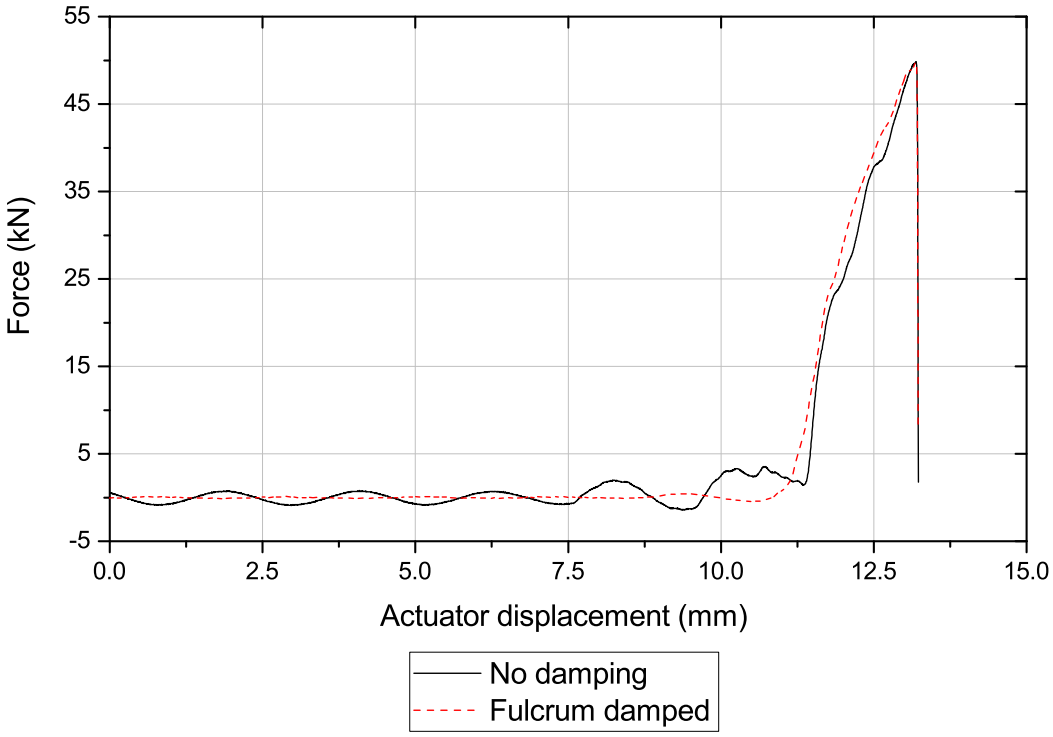

Figure 4.13: Load trace of a carbon fibre NCF epoxy composite specimen loaded at 5 ms^{-1} exhibiting knocking of the fixturing prior to the engagement of the slack adaptor

4.3 Tensile and tensile shear specimen development

The state-of-the-art review in Chapter 2 discussed how there is no standardised specimen geometry for the dynamic characterisation of composite materials. As a result many coupon geometries have been experimentally reviewed in literature. The advantage of the servo-hydraulic VHS employed in this thesis is the ability to test specimens on a larger length scale than SHTB's. The effect of the reduced specimen geometries with woven fabrics, which produce highly heterogeneous strain fields (as shown in Figure 4.2 and Figure 4.5) was highlighted by Foroutan [131]. Foroutan observed that the quasi-static behaviour of a 2 x 2 3K CFRP composite machined into small dog bone specimens contradicted the response that was observed by other authors.

In order to characterise the large weave of the 12K 2 x 2 twill CFRP investigated at the start of this chapter, the specimen width was increased to 32 mm in order to comply with the composite textile standard ASTM D6856-03 [150], which specifies a unit cell-to-width ratio of 2:1. Koohbar et al. [103] developed a process of determining the true RSE of the laminate utilising DIC measurements. Increasing the dimensions of the RoI from 80 x 80 μm^2 to 8000 x 8000 μm^2 allowed average localised strains ($\bar{\varepsilon}_{LOCAL}$) to be determined, the comparison of localised strains with the average global strains ($\bar{\varepsilon}_{GLOBAL}$) using Equation 4.1 provided the strain error (ε_{error}) for that specific window size.

$$\varepsilon_{error} = \left(\frac{\bar{\varepsilon}_{GLOBAL} - \bar{\varepsilon}_{LOCAL}}{\bar{\varepsilon}_{GLOBAL}} \right) \times 100 \tag{4.1}$$

Koohbar et al. utilised this method to demonstrate that the strain error introduced due to the localised effects of the plain weave fabric (unit cell dimensions 1.6 x 1.6 mm^2) did not converge to below 2 % error until the RoI was approximately 3000 x 3000 μm^2. The number of unit cells (N_{UC}) within this RoI is found to be 3.5 based on Equation 4.2, when δ is the unit cell width and R is the RoI width. When the RoI is averaged above this surface area, the specimen is behaving in a uniform global strain. This analysis process can be utilised to determine the true minimum width of a specimen, assuming that the deformation occurs according to the plane strain condition. Koohbar et al. determined that for the 3K plain weave CFRP laminate that the minimum RSE was 1.87 unit cells.

$$N_{UC} = \left(\frac{R}{\delta} \right)^2 \tag{4.2}$$

In order to apply St Venant's principle to a tensile sample, it is suggested to have a specimen free length to width ratio of $\lambda \geq 5$ as outlined in IS0-527-1 [146]. However; since the strain rate achieved through the experiment is inversely proportional to specimen length it must be reduced to a minimum. Wang et al. [122], Battams [107] and Longana [110, 123, 157] all reduced the free length to 100 mm for the tensile characterisation of UD CFRP utilising a servo hydraulic machine, however, the authors did not offer reasoning nor quasi-static validation of their selected specimen geometry. Berthe et al. [117] controlled the reduction of UD CFRP specimens for the characterisation of elastic properties in transverse tension (gauge region; 30 x 20 x 1.08 mm^3) and in-plane shear specimens (gauge region; 30 x 15 x 1.08 mm^3) at longitudinal strain rates of 1.1 x 10^{-3} s^{-1}, 7.1 x 10^{-3} s^{-1}, 1 x 10^{-1} s^{-1}, 1.6 x 10^{1} s^{-1}, 2.5 x 10^{1} s^{-1} and 5.0 x 10^{1} s^{-1}. The dynamic specimens were tested at quasi-static strain rates in an attempt to validate their geometry, the discrepancy in in-plane shear and transverse modulus was found to be 5.1 % and 2.7 % respectively for the high speed specimens in comparison to the standardised geometry results. Utilising DIC surface measurements Berthe et al. recognised that the significant reduction in free length resulted in geometry induced damage mechanisms. Coussa et al. [174] reduced the length to width ratio to $\lambda = 2.4$ and $\lambda = 3$ for $[\pm 45]_{2S}$ and $[0]_4$ specimens respectively. The author validated their selection of specimen geometries via correlation with macro-mechanical properties, as well as the damage mechanisms identified by the stiffness degradation and surface strain maps generated by 3D DIC. The author identified that when $\lambda \leq 2$ the non-linear performance of the $[\pm 45]_{2S}$ specimens is compromised due to the tensile stress state induced within the fibres.

The reduced geometry specimens developed for dynamic characterisation within this thesis using the following methodology to ensure that the results generated were representative of the global material system;

1. Analysis of the heterogeneity of the strain fields to determine the minimum RSE capable of defining the elastic and plastic straining of the specimen.
2. Determination of the minimum free length of the specimen capable of relieving grip induced shear strains prior to the RSE.
3. Analysis of the macro-mechanical properties of the developed coupon geometries when reviewed at quasi-static speeds must be statistically consistent with the properties generated using the ASTM standardised coupons.

4.3.1 Optimisation of ASTM D3518-13 for dynamic in-plane shear

The minimum width of the tensile shear specimen was determined based on the RSE calculated from the surface strains of the quasi-static standardised in-plane shear test conducted at the start of this chapter. Systematic windowing of the full field measurement region (32 x 142 mm^2) was conducted using eight preset quadrangular measurement areas between 1 x 1 mm^2 to 32 x 32 mm^2. The average shear strain measured over these windowed regions is defined as the localised shear strain ($\bar{\gamma}_{LOCAL}$) . Comparison of these measurements with the average global shear strains($\bar{\gamma}_{GLOBAL}$), which was calculated based on the pure shear region of the specimen (central 50 mm of gauge length), enables the error (γ_{error}) of each measurement window in comparison to the global shear strain. The error was calculated using Equation 4.3 and repeated across all five of the standard geometry specimens.

$$\gamma_{error} = \left(\frac{\bar{\gamma}_{GLOBAL} - \bar{\gamma}_{LOCAL}}{\bar{\gamma}_{GLOBAL}} \right) \times 100 \tag{4.3}$$

Reviewing the measurement error at different shear strain levels allowed the author to identify the appropriate RSE under both elastic and plastic deformation. Thus, the local and global shear strains were recorded at 0.5 % increments throughout the elastic region of the test, due to the ductility of the material beyond yield the frequency of the measurements was reduced to intervals of 2 % shear strain.

Figure 4.14 shows the polynomial fit of the error convergence of the shear strain with increasing RoI at different shear strain intervals. The fitted error converged below $\gamma_{error} < 0.5\%$ of the full field measurement at all levels of shear strain when the RoI is set to 24.2 x 24 .2 mm^2($\pm$ 1.8 x 1.8 mm^2 (95 % confidence)). When the RoI was large and the specimen had undergone shear strain to 13 % and 15 %, the error was observed to diverge, this was a result of the free edge effects created by the splaying of unsupported fibre tows at the edge of the specimen (shown in Figure 4.5), they are distorting the measurement due to their increased size relative to the smaller RoI in comparison to when the central 120 mm was used to record the global strain measurement. As a result, the RSE that will be used to record to the surface strains is 27.0 x 27.0 mm^2; thus ensuring that the RSE accommodates for the upper limit of the 95 % confidence range. However, to ensure that edge effects do not disrupt the measurement; the width is increased to 29 mm.

The research conducted by Coussa et al. [174] previously discussed highlighted the minimum length to width ratio suitable for in-plane shear characterisation is $\lambda = 2.4$. As a result, the minimum specimen free length proposed is 70 mm, based upon the

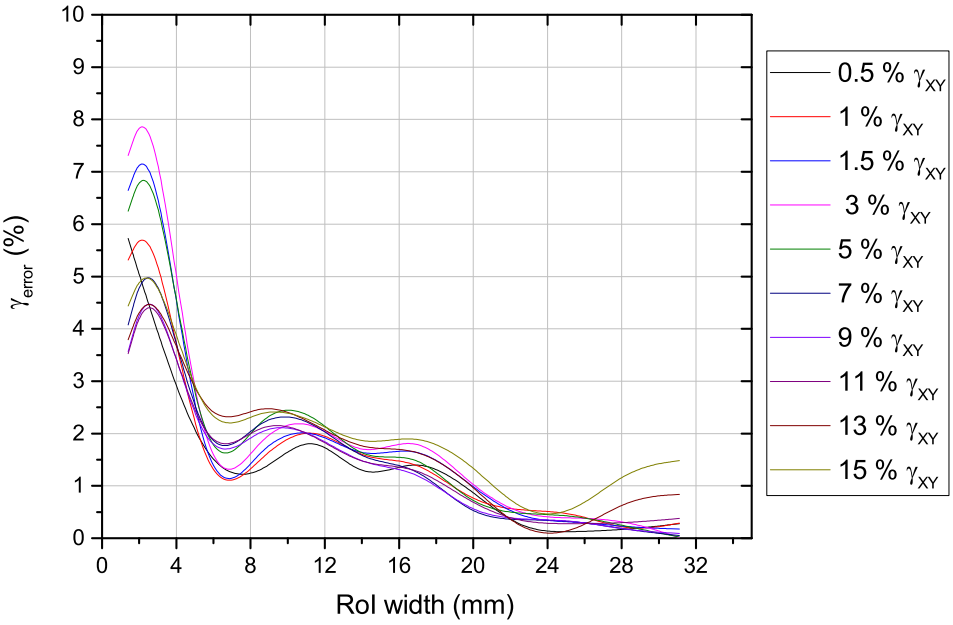

Figure 4.14: Example of polynomially fitted γ_{error} used to determine the RSE for a 12 K 2 x 2 twill CFRP in-plane shear specimen.

29 mm width previously determined. A schematic of the reduced intermediate speed shear specimen (ISSS) based on the above specimen reduction techniques is shown in Figure 4.15. The aluminium tabs were retained from the ASTM D3518-13 specimen previously evaluated, they shall assist with the alleviation of grip induced shear stresses as well as provide a suitable interface for the grips of the slack adaptor to provide sufficient mechanical grip to load the specimen to fracture. The tabs were bonded to the specimen using the 0.3 mm bondline 3M DP490 adhesive introduced in Chapter 3. Since the reduction of the specimen, particularly the determination of the width is dependent of the material behaving in a plane strain condition, the proposed ISSS specimen geometry must be experimentally validated (Section 4.3.4) prior to its use within dynamic experiments.

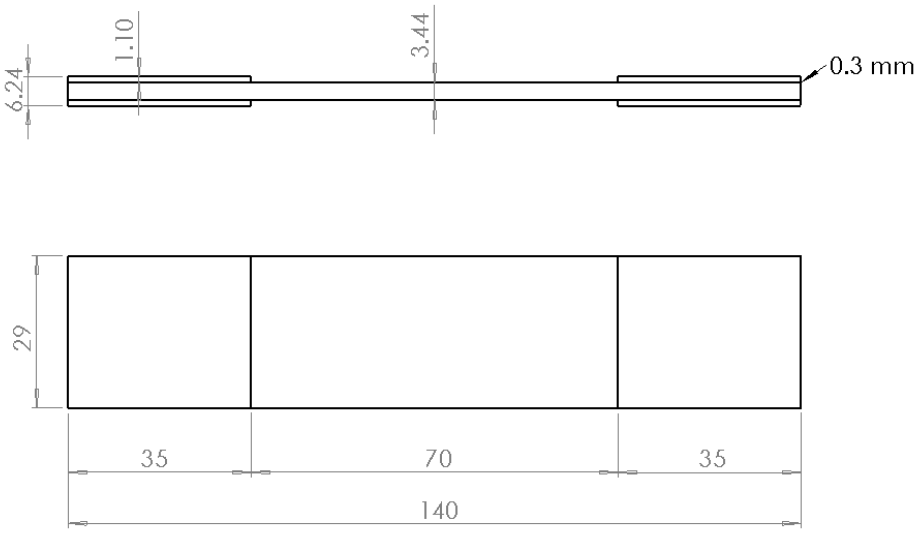

Figure 4.15: Schematic of the intermediate speed shear specimen (ISSS) proposed for the dynamic characterisation of the composite under off-axis in-plane shear loading (Dimensions in mm).

4.3.2 Optimisation of ASTM D3039-14 for dynamic tension

The tensile RSE was determined based on the standardised tensile tests conducted at the start of this chapter. The full field measurement volume occupied a region of 32 x 150 x 4 mm^3. Quadrangular windowing of this region created preset measurement volumes ranging between 4 x 4 mm^2 to 32 x 32 mm^2. The average longitudinal strain measured over these regions are defined as the localised strains ($\bar{\varepsilon}_{LOCAL}$), comparison of these measurements with the average global $\varepsilon_{\mathrm{YY}}(\bar{\varepsilon}_{GLOBAL})$ full field strain measurement using Equation 4.4 provides the measurement error for that specific window size.

$$\varepsilon_{error} = \left(\frac{\bar{\varepsilon}_{GLOBAL} - \bar{\varepsilon}_{LOCAL}}{\bar{\varepsilon}_{GLOBAL}} \right) \times 100 \tag{4.4}$$

The local and global strains were recorded at intervals of 0.2 % prior to full specimen fracture at 1.2 % $\varepsilon_{\mathrm{YY}}$. Figure 4.16 plots the evolution of the fitted $\varepsilon_{\mathrm{error}}$ for different measurement windows at global strain intervals of 0.2 %, it shows how the error converges to an error of $\varepsilon_{error} < 1\%$ within the elastic loading of the specimen

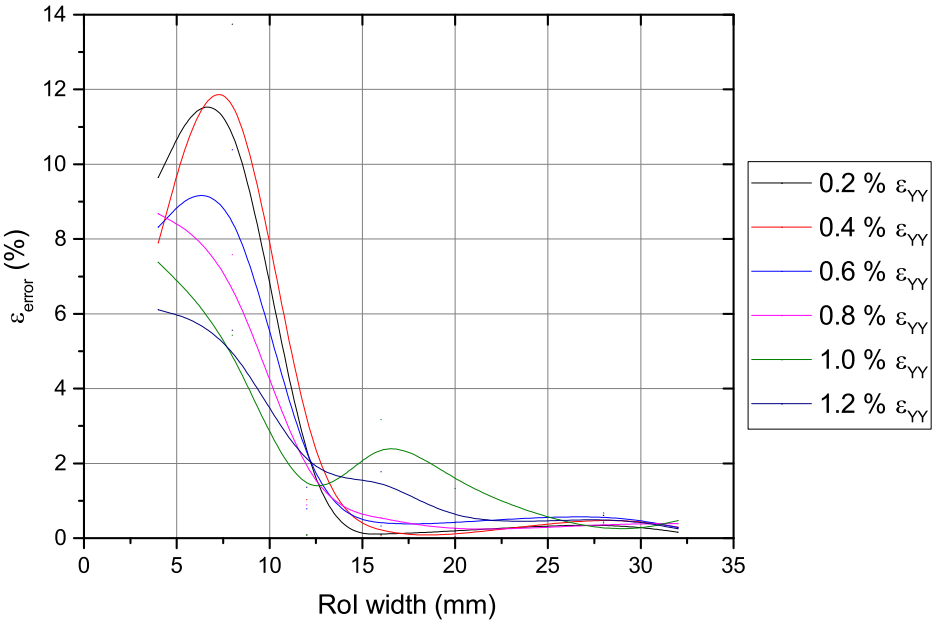

Figure 4.16: Example of polynomially fitted ε_{error} used to determine the RSE for a 12 K 2 x 2 twill CFRP tensile specimen.

(<0.8 % ε_{YY}) when the measurement window is 16 x 16 mm^2, or 1 unit cell^2 of the woven fabric. However, as the longitudinal strain was increased, convergence to within 1 % error occurred once the measurement window was increased to 26.8 x 26.8 mm^2(± 1.3 x 1.3 mm^2(95 % confidence interval)), this is 2.81 unit cells^2 of the original fabric. Koohbar et al. observed that a plain weave 3K fabric converged to below 2 % at 3.5 unit cells^2, the reduction is considered to be a result of the increased size of the unit cell and the random phase of the unit cells throughout the rest of the laminate. The delayed convergence at high levels of strain (relative to the materials ultimate limit) is due to the heterogeneous nature of the damage development across the specimen. In order to account for the variation induced in each specimen, the width is set to the upper limit of the 95 % confidence interval, therefore the minimum specimen width was determined to be 28.1 mm.

The RSE has been used to define the width of both the in-plane shear and tensile specimens, however, it also dictates the smallest free length suitable for characterising this composite material. Unlike the in-plane shear specimen where the free length is limited by the tensile loads experienced by fibres when the length to width ratio is reduced below a critical level the tensile free length can be reduced further.

The key criterion is that the tensile specimen RSE must not be affected by shear stresses induced by the mechanical grips at the specimen boundary. In order to ensure that the boundary conditions were not affecting the mechanical properties of the specimen the surface strain measurements were analysed. Increases in longitudinal strain at the specimen edges relative to the centre are an indication of the Poissons contraction of the specimen being affected by the gripping of the specimen.

To review the shear strains at the base of the specimen the longitudinal strain was measured across the specimen width for the 16 mm (1 unit cell) of specimen directly above the lower jaw at 2 mm discrete intervals for three specimens and the longitudinal strain plotted. The longitudinal strain progression of each section at 0.1 % and 1.0 % longitudinal strain for a single specimen is shown in Figure 4.17. The longitudinal strain can be observed to fluctuate across the width of the specimen, however, since the phase of the data appears to match that of the fabric weave it is not apparent whether the specimen has shear stresses induced at the lower jaw. As the specimen width contains two full unit cell, the longitudinal strain can be normalised in relation to the unit cell phase by reviewing the standard deviation of each section.

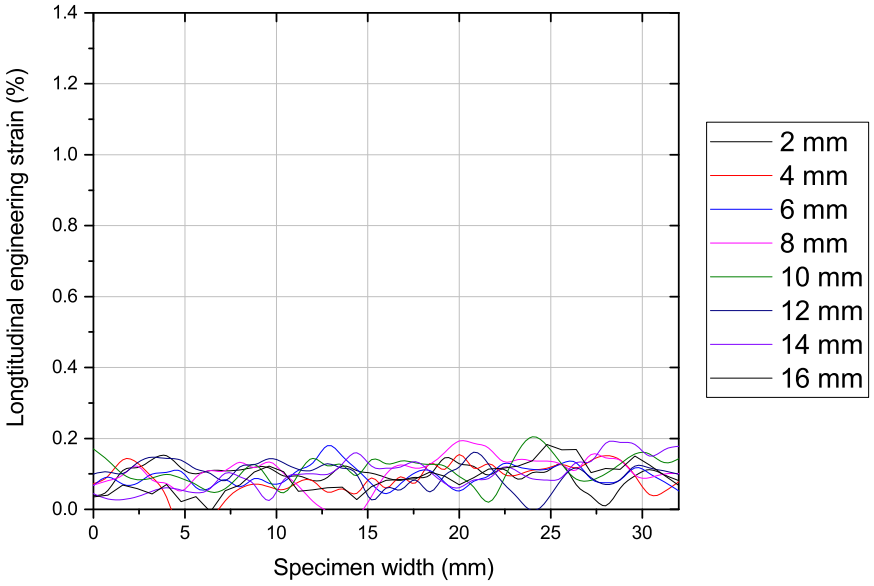

(a)

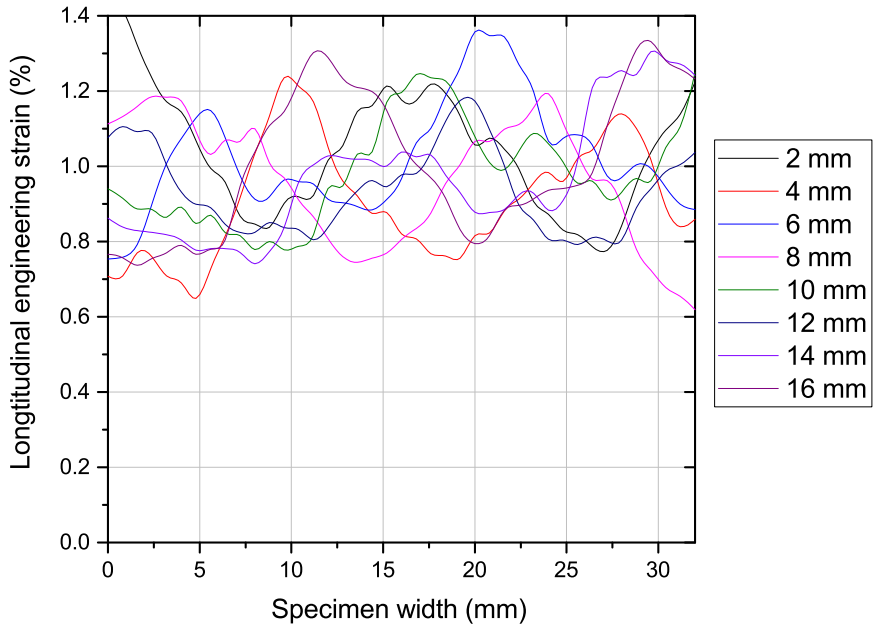

(b)

Figure 4.17: Longitudinal engineering strain progression for sections taken with increasing distance from the base of the measurement region at 0.1 % (a) and 1.0 % (b) global longitudinal strain for standardised quasi-static ASTM D3019-14 experiments.

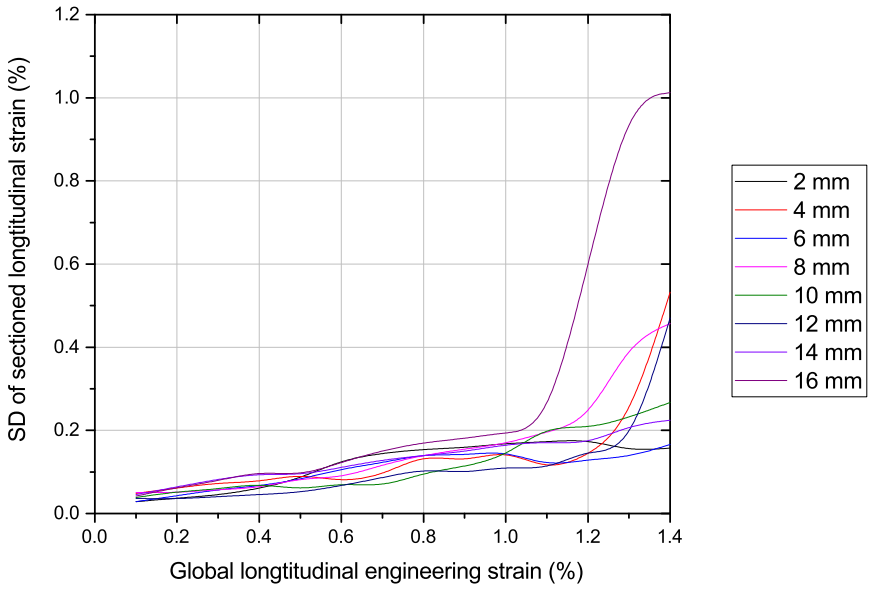

Figure 4.18: Standard deviation (SD) of longitudinal engineering strain for sections taken at 2 mm discrete intervals from the bottom of the specimen in order to normalise the deformation within a unit cell and review the grip induced shear strains.

The standard deviation of each section at strain intervals of 0.1 % until failure of the specimen at 1.4 % longitudinal strain is shown in figure 4.18. It is clear that between 0.1 % and 1.0 % the standard deviation increases for all sections in relation to the applied strain, therefore suggesting that the specimen is not subject to large shear stresses at the base of the specimen. Above 1.0 % outliers are created such as the section 16 mm from the base of the measurement region, this is due to the propagation of a transverse crack which increases the variance across the section. Other transverse cracks appear to propagate at sections 4, 8 and 12 mm. The absence of apparent shear strains may be due to the tabbing material applied, this could allow the specimen to undergo its minimal Poissons contraction without being constrained by the rigid boundary conditions of the mechanical grips. Despite the absence of shear strains at the base of the specimen, the free length was increased above the minimum RSE of 28.1 mm to 50 mm in order to limit the potential affect of misalignment that becomes greater with reducing specimen length. Based on the nominal strain rate equation and the acceleration distance provided by the modified

slack adaptor (Figure 4.12) along with the 50 mm specimen free length a peak strain rate of 320 s^{-1} could be achieved, since this is far in excess of the 100 s^{-1} required for this thesis the specimen is considered suitable.

As previously mentioned in Chapters 2 and 3, the inertial load of the specimen should be reduced as much as possible during dynamic characterisation tests in order to limit the non-linear strain rate observed. Therefore, the decision was taken to reduce the thickness of the tested laminate. The laminate thickness was reduced from $[0]_6$to $[0]_4$. This final thickness was adjudged by Lisle et al. [81] to be the minimum appropriate for tensile characterisation. The author observed that specimens with a stacking sequence of just $[0]_2$ were subject to greater inter-laminar shear stresses causing reduced stiffness in comparison to specimens with stacking sequences between $[0]_4$ to $[0]_6$.

The intermediate speed tensile specimen (ISTS) developed for dynamic testing is shown in Figure 4.19. The aluminium tabs were retained from the standard ASTM D3039-14 specimen evaluated at the start of the Chapter. A 3M DP490 0.3 mm bondline is used to adhere the tab to the specimen. As discussed with the ISSS specimen, due to the assumption of plane strain utilised in its design the specimen must be experimentally validated prior to use in dynamic characterisation experiments.

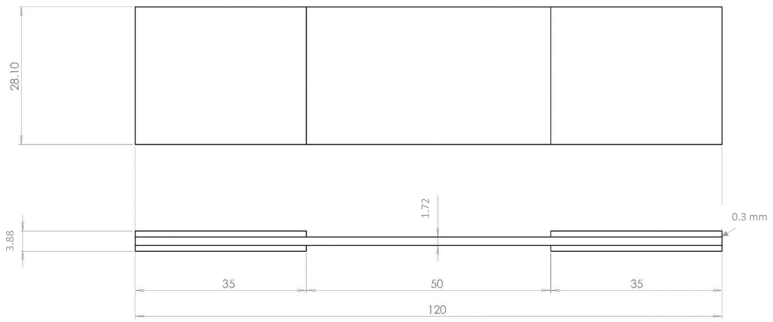

Figure 4.19: Schematic of intermediate speed tensile specimen developed for dynamic characterisation of the composite under longitudinal tension (dimensions in mm).

4.3.3 Specimens with variable cross sections

Longana introduced the concept of using variable cross section specimens for low speed servo-hydraulic testing of GFRP and CFRP UD specimens [110]. Theoretically, the introduction of variable cross-section specimens induces a deformation region that can alleviate some of the compliance observed in the load path, increasing the experimental strain rate. The use of variable cross section specimens at quasi-static speeds is well documented whereby the ply drop off's are incorporated as an alternative to using tabs when characterising laminated structures (Figure 4.20) [148, 183]. The tapered surface between gripped region and the free length has been observed to alleviate shear strains occurring at the base of the specimen free length. The concept was adopted by Longana since the author was unable to stop tab delamination during low speed tensile tests. As a result ply drop off's were incorporated into the specimen, the extracted experimental strain rates were observed to be close to the theoretical estimates over the course of the research.

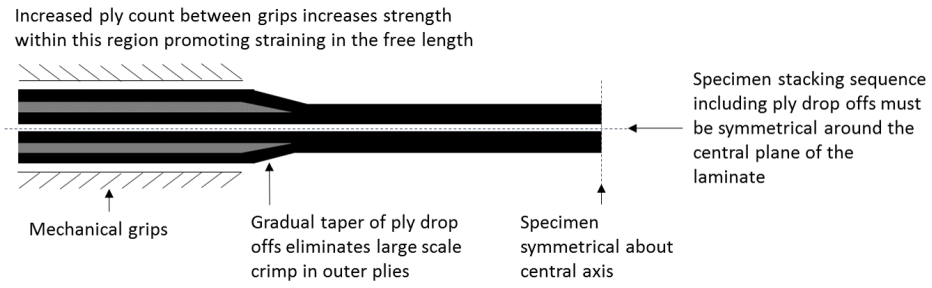

Figure 4.20: Conceptual arrangement of ply drop off's to create intermediate strain rate specimens.

4.3.3.1 Experimental assessment on the suitability of a variable cross section design for tensile specimens for loading at intermediate strain rate

To assess the performance of specimens that have a variable cross section, quasi-static assessment was conducted on bespoke specimen designs based on the ISTS specimen geometries proposed in Section 4.3.2. The engineering drawing for the Intermediate speed tensile specimen with ply drop off (ISTS-PD) is shown in Figure 4.21. Aluminium tabs were bonded to the specimen using 3M DP490 with a 0.3 mm bondline. The aluminium tabs were maintained in order provide a ductile

surface for the serrated jaws to grip rather than the highly brittle composite. The cross-head displacement speed of the Instron-5980 quasi-static frame was reduced to 0.6 mm/min in order to maintain a comparable strain rate to the standardised experiments. Two specimen variants with the same laminate stacking sequence were tested. An internal ply drop off (IPD) specimen as proposed by Longana whereby the truncated ply is sandwiched between two continuous plies was investigated alongside an external ply drop off (EXPD) specimen, where the truncated ply was positioned externally to the specimen. Three specimens of each configuration were experimentally evaluated using the Instron-5980 quasi-static frame, surface strains were recorded using 3D DIC according to Table 4.3.

Table 4.3: GOM 12M 3D DIC properties for the experimental tensile characterisation of the 12K 2 x 2 twill CFRP composite ISTS-IPD and ISTS-EXPD specimens at quasi-static speeds.

Property		Unit
Camera	GOM 12M	
Lens	Titanar 100	
Frame rate	2	Hz
Shutter speed	85	ms
Aperture	16	
Imaging window	4000 x 3000	$pixel^2$
Calibration plate	CP20 55 x 44	
Measurement volume	125 x 90 x 75	mm^3
Facet size	19	pixels
Step size	16	pixels
Spatial resolution	0.57	mm
Strain resolution	54.2	με
Displacement resolution	0.07	μm

Since the introduction of ply drop off's within the specimen requires the use of multi-plane moulding tooling, the WMG press introduced in Chapter 3 could not be used to compression mould the specimens due to the prohibitively high cost of getting tooling manufactured. Therefore, alternative tooling was produced for curing the pre-preg within an autoclave, due to the high pressure of the autoclave the manufactured components are expected to be of a similar volume fraction to those press moulded [184]. The autoclaving was conducted at Morgan Advanced Materials according the moulding specification provided by Solvay (Table 4.4) [185].

The stress-strain response of the ISTS-EXPD and ISTS-IPD specimens are shown

Table 4.4: Autoclave moulding parameters for materials with Solvalite 710-1 epoxy matrix provided by Solvay.

	Value	Units
Temperature ramp rate	2	$^oC/min$
Dwell temperature	150	^oC
Dwell period	30	min
Pressure	90	PSI
Cooling ramp rate	2	$^oC/min$

in Figure 4.22. It is clear that in comparison to the standardised results presented at the start of Chapter 4 in Figure 4.1 the specimens undergo premature failure with the average ultimate strength reduced from 867.6 MPa to 483.9 MPa (ISTS-EXPD) and 751.1 MPa (ISTS-IPD). The initial response is linear elastic of the ISTS-IPD (57.4 GPa) and ISTS-EXPD (53.6 GPa), however, it is also lower than that observed in the standardised ASTM D3039-14 experiments (61.16 GPa). As the specimens strain, damage initiation and propagation prior to the sudden transverse fracture. Figure 4.23 shows how the failure occurs local to the ply-drop off in both the ISTS-EXPD (a) and ISTS-IPD (b) specimen. This superior mechanical performance of the internal ply drop off compared to the external ply drop off was predicted by He et al. [186].

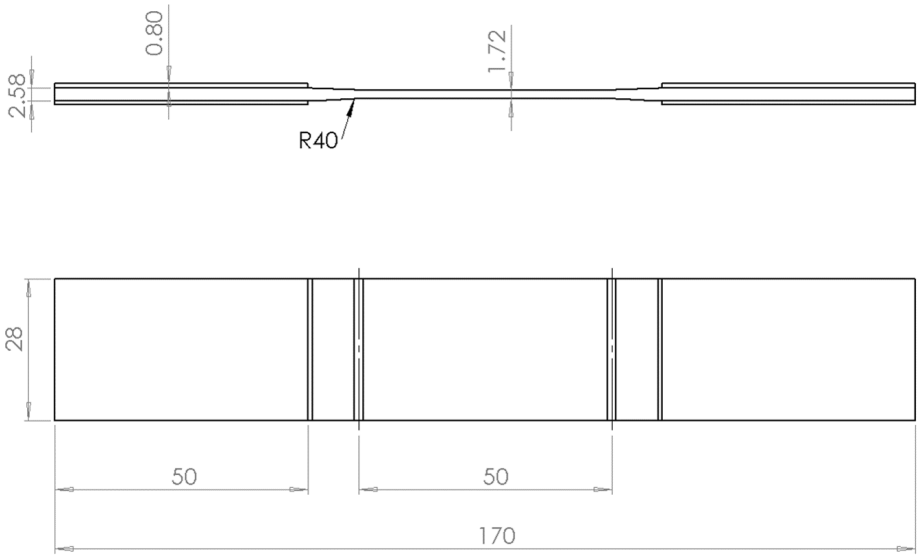

Figure 4.21: Schematic of the proposed Intermediate speed tensile specimen with ply drop off to produce a tensile specimen with a variable cross section for intermediate strain rate characterisation (dimensions in mm).

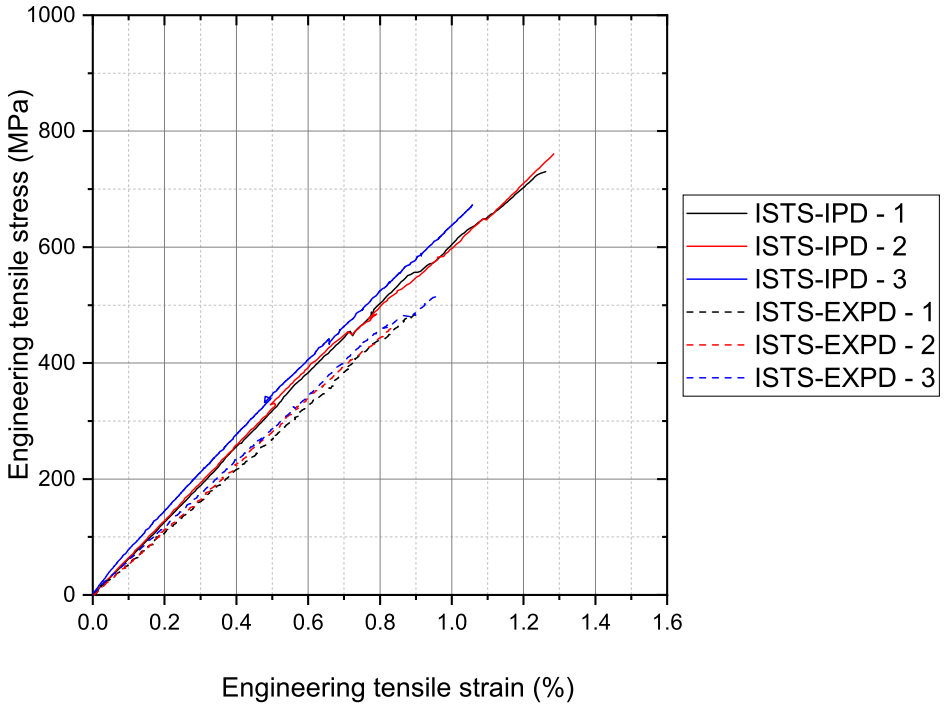

Figure 4.22: Quasi-static longitudinal engineering stress-strain response of the 12K 2 x 2 twill CFRP specimens tested using ISTS-IPD and ISTS-EXPD specimens.

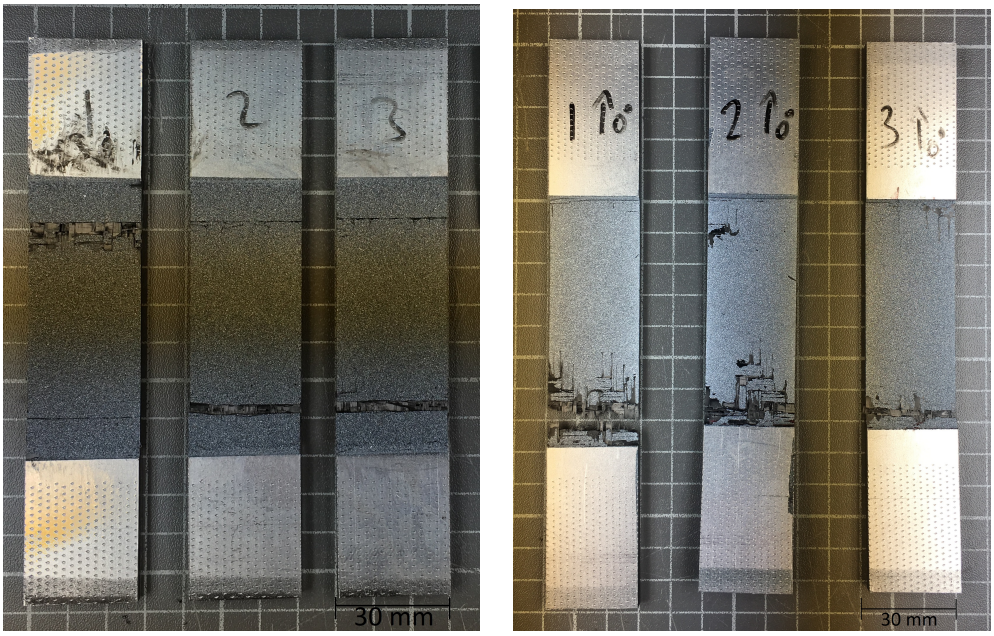

(a) (b)

Figure 4.23: Typical transverse failure within the ply-drop off region of; (a) external ply drop off (ISTS-EXPD) specimens and (b) internal ply drop off (ISTS-IPD) specimens.

Figure 4.24 shows the progression of longitudinal surface strains during the tensile loading of a ISTS-EXPD specimen, it is clear that despite the premature failure of the specimen at the ply-drop off region, damage was developing within the central gauge region with splaying of the transverse tows particularly prevalent. Strain progression can clearly be seen local to the ply drop off, the termination of plies within tapered laminate structures generates a geometric discontinuity with the formation of matrix rich pockets local to the end of the ply. It is within these pockets that the damage is initiated in the form of interlaminar shear cracks. This is evident in Figure 4.24 (a) and (b) as the tensile strains are greater at the end of the ply drop off and particularly at the free edges of the specimen. These interlaminar shear cracks propagate and lead to the premature fracture of the specimen.

The internal position of the ply drop off is thought to introduce interlaminar shear stresses created by the desire of the external ply to re-align to the loading direction. The drop off ply assists in transmitting the load along its fibre axis, applying the tensile stress of the lamina to the matrix rich region created by the crimp of the fibres as they flow. As the specimen strains and damage begins to coalesce, these

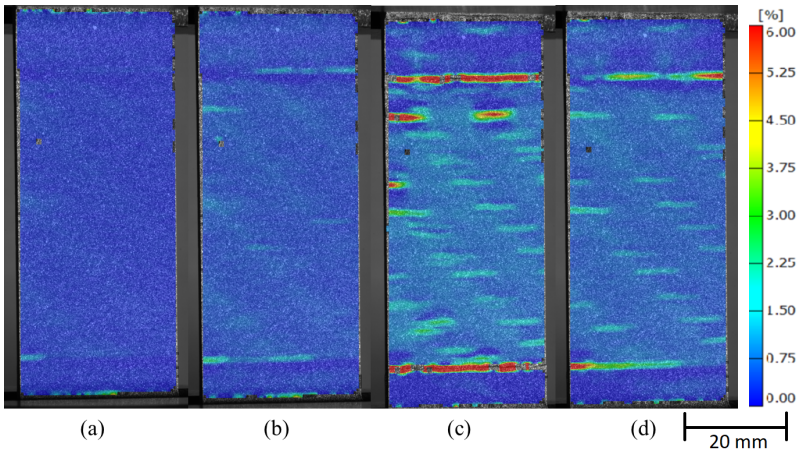

Figure 4.24: Longitudinal strain map of an internal ply drop off (ISTS-EXPD) specimen (#1) at (a) 0.2 %, (b) 0.4 %, (c) 0.6 %, and (d) 0.8 % ε_{YY} highlighting crack growth at the location of the ply drop off.

interlaminar stresses act as stress raisers inducing additional matrix cracking and fibre fracture that results in the sudden catastrophic and premature failure of the laminate.

This section has demonstrated that the application of variable cross section specimens is unsuitable for the material system evaluated in this thesis as a result of both internal and external ply drop off's inducing interlaminar damage that propagated resulting in the premature failure of the specimen, local to the end of the ply drop off. Therefore, this thesis shall employ straight sided flat specimens according to the ISTS and ISSS specimens geometries previously presented in Figure 4.19 and Figure 4.15 respectively.

4.3.4 Quasi-static validation of the ISTS and ISSS geometries

In order to validate the proposed ISTS and ISSS specimen geometries, five specimens were experimentally investigated in the quasi-static test frame at 0.6 mm/min and 0.8 mm/min respectively. The cross head displacement rate was reduced from the ASTM D3039-14 and D3518-13 rate of 2 mm/min in order to maintain the constant quasi-static strain rate that the standardised specimens had experienced. 3D DIC was employed to measure surface strains, the properties of which are shown in Table 4.5.

Table 4.5: Summary of measurement methodology for GOM 12M 3D DIC for the validation of the developed intermediate speed tensile (ISTS) and shear (ISSS) specimens.

Property		Unit
Camera	GOM 12M	
Lens	Titanar 100	
Frame rate	2	Hz
Shutter speed	95	ms
Aperture	16	
Imaging window	4000 x 3000	$pixel^2$
Calibration plate	CP20 55 x 44	
Measurement volume	125 x 90 x 70	mm^3
Facet size	19	pixels
Step size	15	pixels
Spatial resolution	0.59	mm
Strain resolution	81.6	με
Displacement resolution	0.07	μm

Figure 4.25 shows the experimental tensile stress-strain response of the ISTS specimen, the extracted mechanical properties of the ISTS specimen are presented in Table 4.6 alongside those of the ASTM D3039-14 experiment (Figure 4.1).

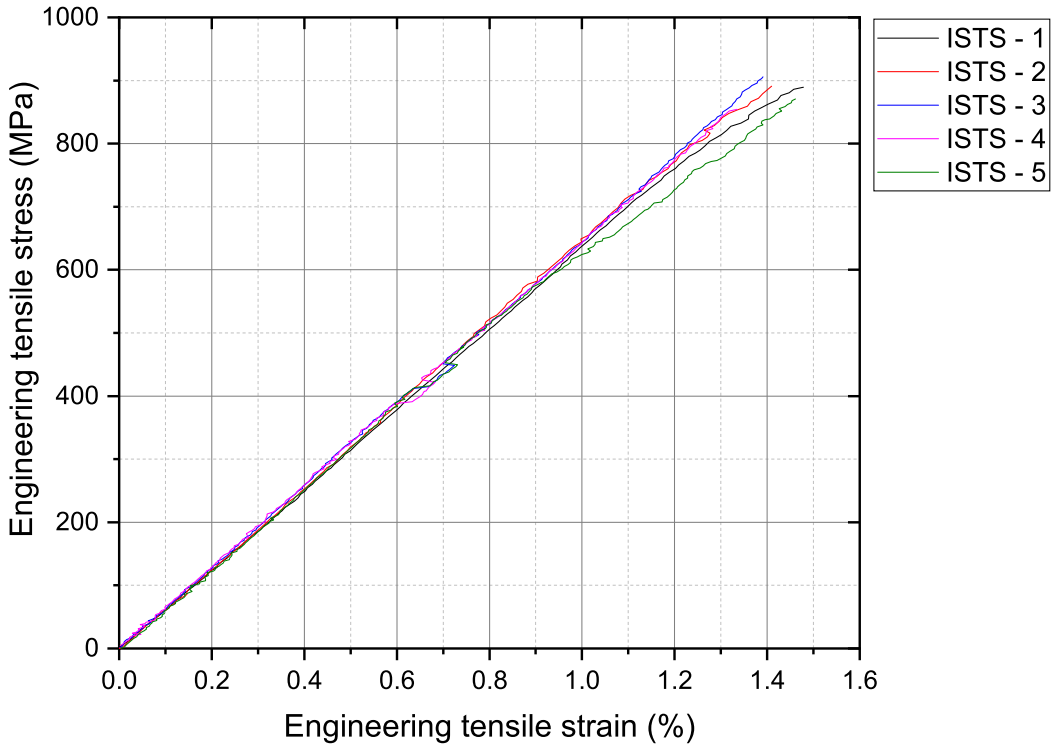

Figure 4.25: Quasi-static longitudinal engineering stress-strain response of the 12K 2 x 2 twill CFRP specimens tested using ISTS specimens.

The response of the ISTS specimen undergoes initial linear elastic loading consistent with the ASTM D3039-14 specimen (61.27 GPa vs 61.16 GPa). Figure 4.26 shows that damage accumulates in the same heterogeneous manner as the ASTM D3039-14 specimens, with peak longitudinal strains observed in the transverse tows demonstrating matrix failure within the weft tows, these cracks are visibly arrested by the weave of the fabric. As the specimen approaches ultimate strain damage accumulates, this reduces the stiffness. This response is directly comparable to the material response observed in the standard coupon experiments presented at the start of this chapter. The failure of the both ISTS and ASTM specimens occurred at similar ultimate strain (ε_{YY} = 1.41 % and 1.43 %) and strength (882.2 MPa and 867.6 MPa) respectively. Since both specimens show comparable stiffness and failure characteristics, the variance of the performance of the geometries was analysed using two way *T-tests*, the resultant *P-values* for each property are shown in Table 4.6. Since the P-value is greater than 0.05 in all of the extracted mechanical

properties it can be deduced that the two specimen geometries are considered not to be statistically different with a confidence interval of 95 %.

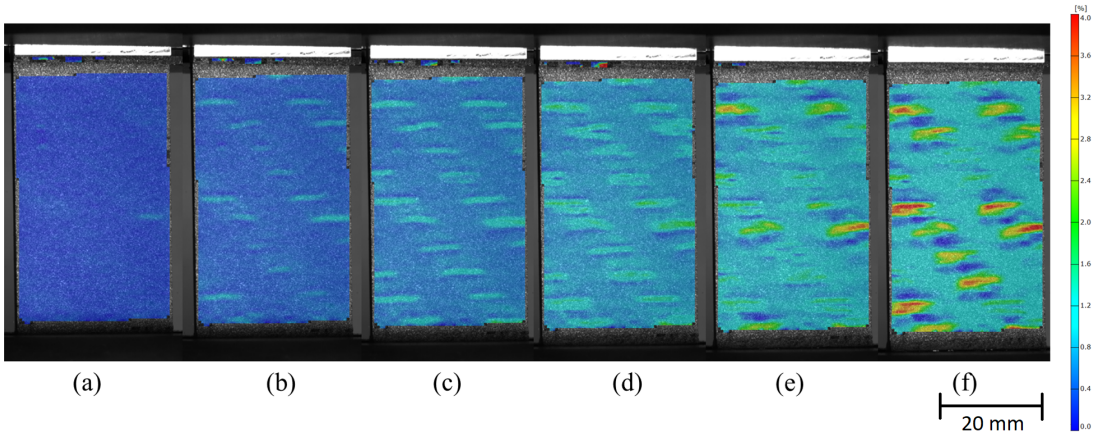

Figure 4.26: Longitudinal strain progression overlaid on the left ISTS specimen image at (a) 0.2, (b) 0.4, (c) 0.6, (d) 0.8, (e) 1.0 and (f) 1.2 % ε_{YY} of 12K 2 x 2 twill CFRP ISTS specimen undergoing an ISTS tensile test.

Table 4.6: Comparison of the mechanical properties produced using the ISTS and ASTM D3039-14 tensile specimens

Property	Unit	ASTM D3039-14 (SD)	ISTS (SD)	P-value
Modulus	GPa	61.16 (0.71)	61.27 (0.89)	0.82
Tensile strength	MPa	867.6 (34.34)	882.2 (19.49)	0.32
Ultimate engineering tensile strain	%	1.43 (0.041)	1.41 (0.057)	0.46
Poissons ratio		0.054 (0.0017)	0.054 (0.0021)	0.84

The shear stress-strain response of the ISSS specimen is shown in Figure 4.27 and the mechanical properties are presented in Table 4.7 alongside those of the ASTM D3518-13 experiment conducted at the start of the chapter. The ISSS specimen shows similar results to those of the ASTM D3518-13 specimen at different strain levels (Figure 4.4).

The ISSS specimen follows the same bi-linear engineering shear stress - engineering shear strain response of ASTM D3518-13 specimen. The average initial stiffness was

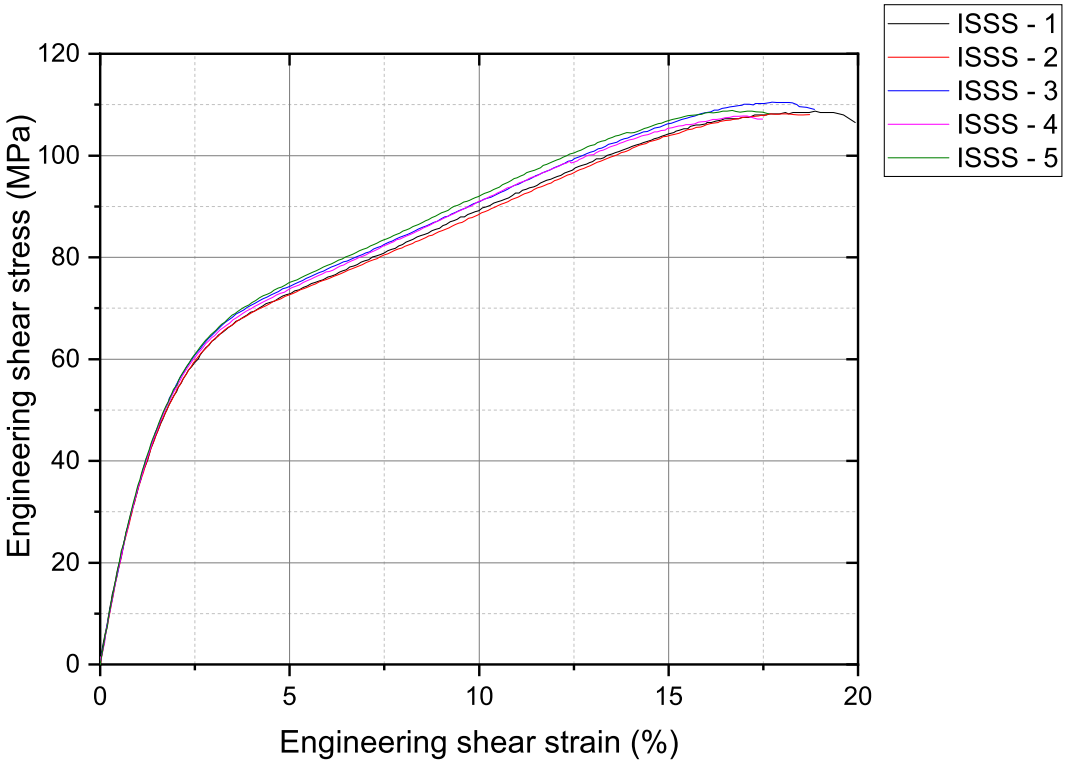

Figure 4.27: Shear stress-strain response of the ISSS specimen.

observed to be the same for both specimens (3.74 GPa) resulting in a P-value of 0.89. As the specimen continues to strain, matrix cracks are initiated and coalescence, resulting in the yielding of the laminate, the post yield strength at $\gamma = 5$ % (75.18 MPa vs 74.75 MPa) demonstrates that comparable amalgamation of the initial damage mechanisms. The strain hardening of the specimen post yield results in shear fracture of the laminate as the specimen achieves ultimate shear strength (110.94 MPa vs 111.63 MPa) and shear strain (18.58 % vs 18.76 %) comparable to the standardised specimen. The variance of the specimens at each of the damage states was reviewed using two way T-tests, the resultant P-values are shown in Table 4.7. As observed with the ISTS specimen, the P-values of the extracted mechanical properties are greater than 0.05 therefore it can be deduced that the two specimen geometries are considered not to be statistically different with a confidence of 95 %.

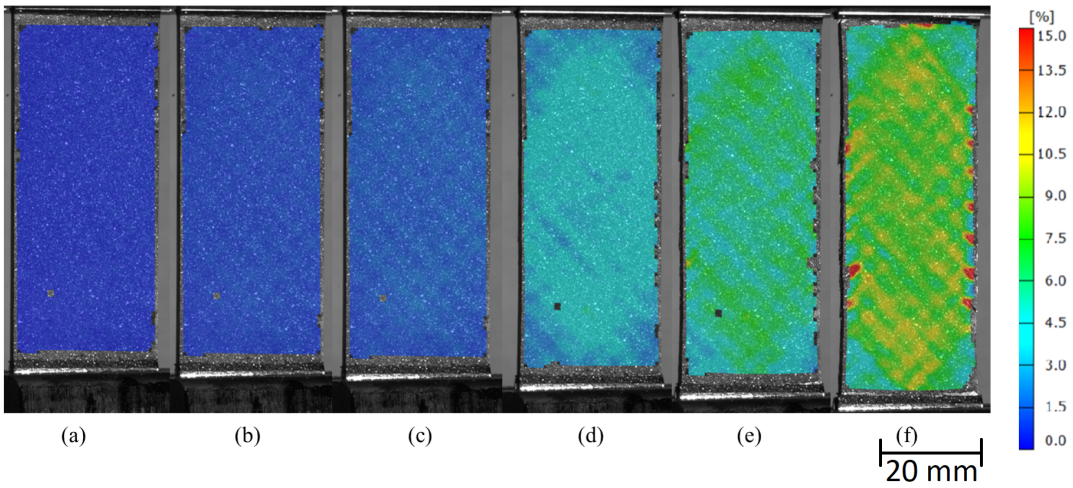

Figure 4.28: Longitudinal strain progression overlaid on the left ISSS specimen image at (a) 0.2, (b) 0.4, (c) 0.6, (d) 0.8, (e) 1.0 and (f) 1.2 % ε_{YY} of a 400 gsm 12K 2 x 2 twill MTM710-1 CFRP composite undergoing a ISSS in-plane shear characterisation test.

Table 4.7: Comparison of the mechanical properties of the ISSS and ASTM D3518-13 tensile shear specimens

Property	Unit	ASTM D3518-13 (SD)	ISSS (SD)	P-value
Shear modulus	GPa	3.74 (0.079)	3.74 (0.069)	0.89
Shear strength at yield	MPa	70.97 (0.67)	71.01 (1.63)	0.82
Engineering shear strain at yield	%	3.98 (0.11)	3.89 (0.14)	0.73
Ultimate shear strength	MPa	111.63 (1.84)	110.94 (1.35)	0.27
Ultimate engineering shear strain	%	18.76 (0.42)	18.58 (0.75)	0.63
Poissons ratio		0.78 (0.032)	0.80 (0.019)	0.30

Since both the ISTS and ISSS straight sided specimens are not statistically different than their ASTM standard counterparts, they are both considered to be suitable for use within dynamic experiments to establish the strain rate performance of the 12K 2 x 2 twill CFRP laminate. The results of these experiments are presented in Chapter 5.

4.4 Summary

This chapter has presented the results of the standardised characterisation procedure for the tensile and tensile shear response of the automotive specific 12K 2 x 2 twill Solvalite 710-1 CFRP laminate at quasi-static speeds according to ASTM standards. The mechanical response of the composite laminate was shown to be comparable with the understanding presented in literature. The DIC surface strain maps demonstrated the highly heterogeneous nature of the fabric, as a result a large specimen size must be characterised in order to achieve a macroscopic response of the laminate that can be incorporated within CAE models.

The previous chapter demonstrated that the Instron Fast Jaw system was unsuitable for use with continuously reinforced polymer composites therefore a high capacity slack adaptor was developed. As a result of the large specimen size required to be evaluated, a novel slack adaptor was produced that was capable of being loaded to 100 kN. The length of the load path was minimised using the specimen length as the acceleration distance of the LMD, thus increasing its stiffness relative to a plunger style activation and reducing out-of plane movements of the specimen, reducing risk of premature failure as a result of induced bending strains. Premature knocking of the slack adaptor against the cradle was mitigated through the application of polymer fulcrum dampers.

The Chapter concluded with the proposal of a novel coupon geometry for tensile and in-plane shear characterisation of the woven composite laminate. Specimens with variable cross sections were considered, however, the introduction of ply-drop off's introduced discontinuities that promoted premature interlaminar failure. The novel specimen reduction technique based on quadrangular windowing of the standardised specimen was employed in order to minimise the inertial load of the specimen, and minimise the free length which enables a higher strain rate to be achieved with a lower applied velocity which reduces the excitation of the load path and load cell. Experimental validation of the ISTS and ISSS specimens were required due to the plane strain assumption invoked during the reduction technique. Statistical comparison of the of the modulus, ultimate strengths and strains of both specimens with the ASTM standardised results using a T-test demonstrated their suitability for use within the dynamic characterisation experiments which will be detailed in the following chapter.

Chapter 5

Tensile and in-plane shear characterisation of a 12K 2x2 twill CFRP laminate at intermediate strain rates

This Chapter employs the dynamic characterisation technique developed over the course of Chapters 3 and 4 to characterise the 12K 2 x 2 twill CFRP automotive specific material system at discrete strain rate intervals between nominal longitudinal strain rates of 6.7×10^{-2} s^{-1} to 1.0×10^{2} s^{-1}. The longitudinal tensile response is initially presented prior to the consideration of the in-plane shear response of the material. The chapter concludes with a discussion of the results as well as the experimental technique.

5.1 Longitudinal Tension

The tensile mechanical behaviour of a composite within simulation tools is characterised according to its longitudinal modulus, ultimate strength, ultimate strain and Poissons ratio [187]. As a result, these are the mechanical properties reviewed throughout this study. Strain rates were increased from 6.7×10^{-2} s^{-1} to 1.0×10^{2} s^{-1} at approximately orders of magnitude.

5.1.1 Nominal longitudinal strain rate 6.7 x 10^{-2} s^{-1}

Assessment of the tensile response of the composite at a nominal strain rate of 6.7 x 10^{-2} s^{-1} was conducted using five repeats of a modified ASTM D3039-14 standardised specimen shown in Figure 5.1, the width was set to 28.1 mm to match that of the ISTS specimen proposed in Chapter 4. The modified ASTM D3039-14 coupon is required as the minimum frame velocity of the VHS (1 x 10^{-2} ms^{-1}) is not sufficient to generate the desired strain rate in an ISTS specimen. Therefore the free length had to be increased to lower the nominal strain rate of the experiment to 6.7 x 10^{-2} s^{-1}. Due to the low target velocity, the VHS is run in *low rate* closed loop control, thus a feedback loop is enabled to vary the servo-valve aperture which dictates the oil flow rate and thus the velocity of actuator during the test.

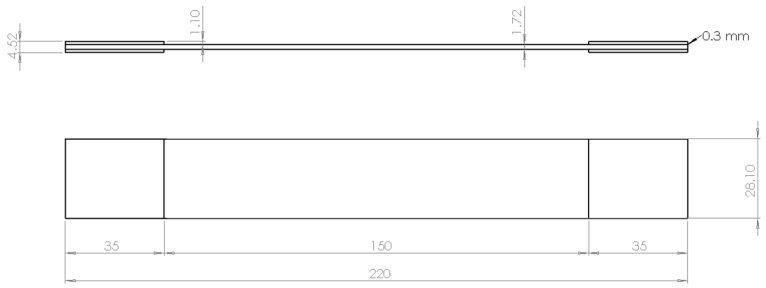

Figure 5.1: Engineering drawing showing the adapted ASTM D3039-14 specimen employed to characterise the longitudinal tensile performance of 12K 2 x 2 twill CFRP at a nominal longitudinal strain of 6.7 x 10^{-2} s^{-1} (Dimension in mm).

Strain was instrumented using 3D DIC according to the parameters outlined in Table 5.1. Due to the large specimen length relative to the pixel density of the sensor in the 1 megapixel Photron SA-X2 high speed cameras, imaging over the complete specimen length results in a low spatial resolution being achieved. As previously discussed this low spatial resolution may result in the over smoothing of the recorded surface strains. Therefore to compensate for the loss in spatial resolution, the facet size is reduced below the GOM recommended settings to 15 pixels. This small facet pixel density reduced the strain and displacement resolutions relative to that observed in the quasi-static experiments utilising the GOM 12M system.

Table 5.1: Summary of the measurement methodology for GOM 12M 3D DIC to characterise the longitudinal tensile performance of 12K 2 x 2 twill CFRP at a nominal longitudinal strain rate of 6.7 x 10^{-2} s^{-1} using modified ASTM D3039 specimens.

Property		Unit
Camera	Photron SA-X2	
Lens	Titanar 75b	
Frame rate	500	Hz
Shutter speed	500	µs
Aperture	22	f/
Imaging window	1024 x 1024	$pixel^2$
Calibration plate	CP30 MV 150 x 150	
Measurement volume	165 x 165 x 155	mm^3
Facet size	15	pixels
Step size	12	pixels
Spatial resolution	2.41	mm
Strain resolution	124.7	µε
Displacement resolution	0.13	µm

The experimental stress-strain response of the modified ASTM D3039-14 specimen loaded at a nominal longitudinal strain rate of 6.7 x 10^{-2} s^{-1} is shown in Figure 5.2. A summary of the derived mechanical properties is presented in Table 5.2, the strength and modulus have been normalised to a constant 52 % V_f to remove inherent plaque variability introduced during manufacture. The modulus was determined using a linear fit between 0.2 % and 1.0 % ε_{YY}. The CoV of the strength, modulus and ultimate strain is within the expected variation for a composite laminate (< 5 %), in comparison the high Poissons ratio variability is a result of the small engineering transverse strain (941 µε) observed during brittle failure and its proximity to the resolution and of the DIC measurement methodology (124.7 µε).

As with experiments conducted at quasi-static strain rates the loading response was linear with a catastrophic transverse fracture leading to the failure of the specimen (Figure 5.3). The location of the fracture varied between specimens, no specimens exhibited grip induced fractures close to the tabs with fracture occurring within approximately the central 100 mm of the specimens free length. Multiple specimens exhibited dual failure locations; when each of the captured image frames sequentially it was apparent that these specimens initially failed away away from the grips. The secondary fracture close to the grips is thought to be the result of a shock wave released in the specimen at the moment of macroscopic transverse crack propagates.

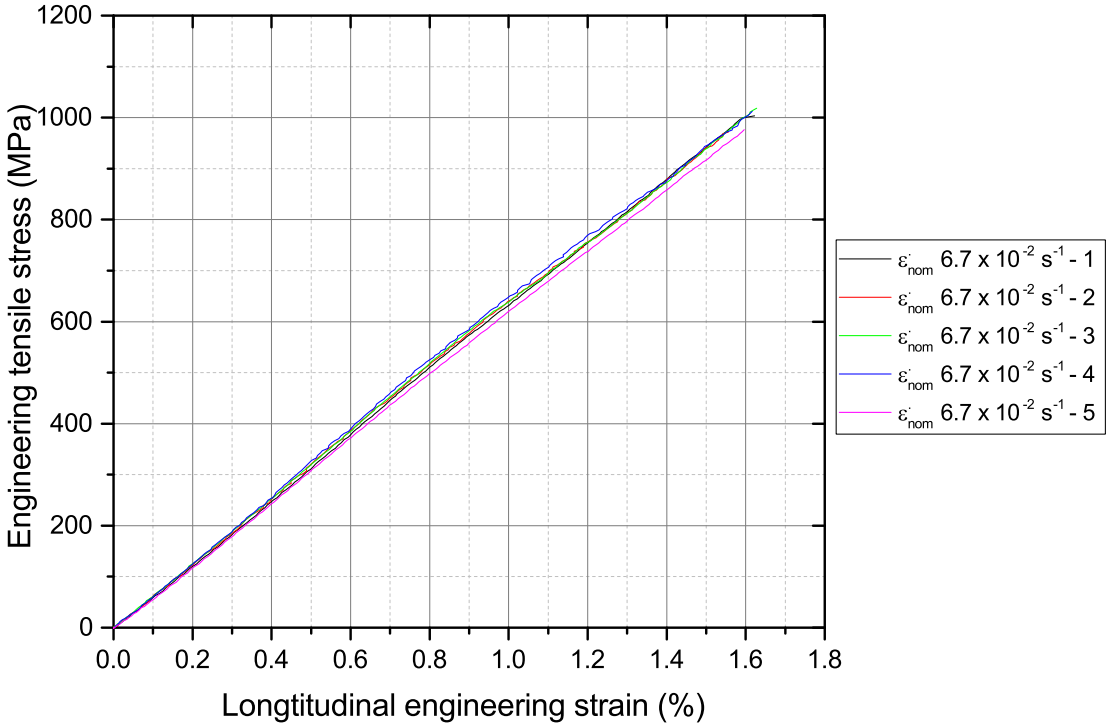

Figure 5.2: Longitudinal engineering stress-strain response of a modified ASTM D3039-14 composite specimen experimentally loaded at a nominal longitudinal strain rate of 6.7 x 10^{-2} s^{-1}.

Due to the inability to interrupt an experiment on the VHS it cannot be determined whether the observed fracture and damage mechanisms of the failed specimen were generated prior to or post ultimate failure. Therefore the fracture surfaces will not be investigated in more detail.

Table 5.2: Tensile mechanical properties of modified ASTM D3039 specimen evaluated at a nominal longitudinal strain rate of 6.7 x 10^{-2} s^{-1}.

Property	Value	units	SD	CoV (%)
Tensile modulus	62.64	GPa	1.05	1.67
Ultimate engineering tensile strength	991.76	MPa	21.47	2.16
Ultimate engineering tensile strain	1.60	%	0.029	1.81
Poissons ratio	0.049		0.0039	7.96

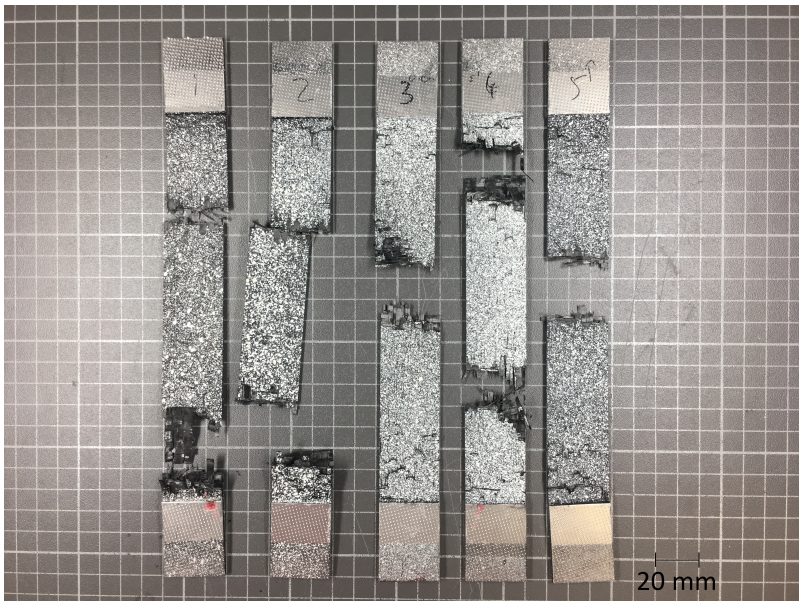

Figure 5.3: Failure locations of modified ASTM D3039-14 specimens subjected to a longitudinal tensile test at nominal longitudinal strain rate of 6.7 x 10^{-2} s^{-1}.

The frame rate of 500 Hz provided good temporal sampling of the test with a total of approximately 200 data points generated over the duration of loading. However, the use of 1 megapixel Photron SA-X2 cameras to image the full specimen length has reduced the spatial resolution by a factor of 2.5 in comparison to that achieved by the GOM 12M system. This results in greater smoothing of the collected strain measurements, as a result the longitudinal surface strains shown in Figure 5.4 are unable to display localised damage; such as the increased splaying of the transverse tows as the specimen strains, that were observed during the quasi-static analysis shown in Figure 4.2. As presented in Chapter 3 this smoothing is likely to truncate the measured ultimate strain and slightly under predict the stiffness during elastic

loading, in contrast the stiffness at failure is over predicted as the slight ductility observed as damage coalesces is not represented. Despite the reduction in spatial resolution, the greater straining of transverse tows normal to the loading direction can be observed by the phase of the magnitude of longitudinal strain propagation in Figure 5.4, despite the lower magnitude of the peak strains. This demonstrates that the matrix cracking of weft tows is still occurring at this strain rate.

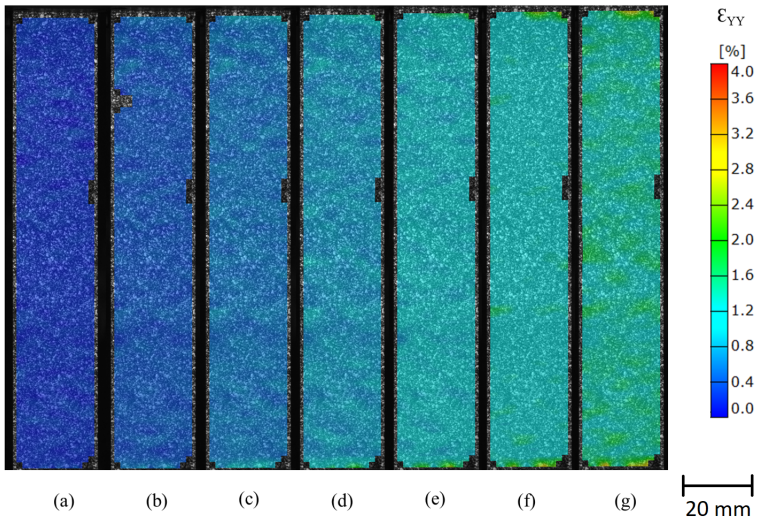

Figure 5.4: Surface strain maps overlaid on the left image of specimen #3 demonstrating the progression of longitudinal engineering strains at (a) 0.2, (b) 0.4, (c) 0.6, (d) 0.8 (e) 1.0. (f) 1.2 and (g) 1.4 % ε_{YY} of 12K 2 x 2 twill CFRP undergoing a tensile characterisation test at nominal longitudinal strain rate of 6.7×10^{-2} s^{-1}.

5.1.2 Nominal longitudinal strain rate 1.2 x 10^0 s^{-1}

The ISTS specimen introduced in Chapter 4 in order to provide a representative volume of the 12K 2 x 2 twill CFRP laminate was tested with an actuator velocity of 0.06 ms^{-1} to induce a nominal strain rate of 1.2 x 10^0 s^{-1}, five repeats of the experiment were conducted. The 3D DIC characteristics used for the experiments are shown in Table 5.3, a frame rate of 8 kHz provided approximately 70 data points over the test period. Due to the improved pixel density across the image, relative to the 6.7 x 10^{-2} s^{-1} experiment, the facet size was set to the GOM recommended size of 19 $pixel^2$ providing a strain measurement resolution of 57.2 με and a spatial resolution of 1.21 mm.

Table 5.3: Summary of the measurement methodology for Photron SA-X2 3D DIC to characterise the longitudinal tensile performance of 12K 2 x 2 twill CFRP at a nominal longitudinal strain rate of 1 x 10^0 s^{-1} using ISTS specimens.

Property		Unit
Camera	Photron SA-X2	
Lens	Titanar 75b (20 mm extender tube)	
Frame rate	8	kHz
Shutter speed	73.75	μs
Aperture	11	f/
Imaging window	1024 x 1024	$pixel^2$
Calibration plate	CP20 MV 55 x 44	
Measurement volume	65 x 65 x 45	mm^3
Facet size	19	pixels
Step size	15	pixels
Spatial resolution	1.21	mm
Strain resolution	57.2	με
Displacement resolution	0.19	μm

The longitudinal tensile stress-strain response is presented in Figure 5.5, whilst the extracted mechanical properties (normalised to 52 % V_f) are presented in Table 5.4. It is evident that the laminate maintains its linear response to brittle failure that has previously been reported. The elastic modulus was determined using a linear fit between 0.2 % and 1.0 % ε_{YY}. All CoV are within the typical 5 % tolerance set for composite materials, and the Poissons ratio variance is reduced from the 6.7 x 10^{-2} s^{-1} experiment as a result of the improved measurement resolution.

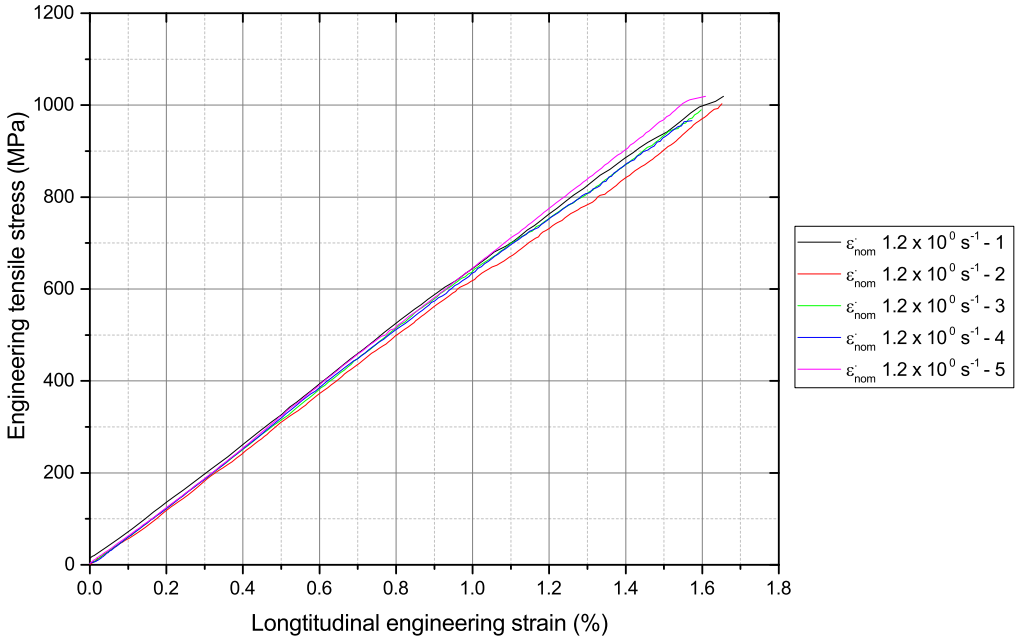

Figure 5.5: Longitudinal engineering stress-strain response of ISTS composite specimens experimentally loaded at a nominal longitudinal strain rate of 1.2×10^0 s^{-1}.

Table 5.4: Tensile mechanical properties of ISTS specimens evaluated at a nominal longitudinal strain rate of 1.2×10^0 s^{-1}.

Property	Value	units	SD	CoV (%)
Tensile modulus	63.46	GPa	1.01	1.65
Ultimate Tensile strength	999.66	MPa	24.89	2.49
Ultimate engineering tensile strain	1.62	%	0.036	2.22
Poissons ratio	0.055		0.0030	5.45

Analysis of the failure locations shown in Figure 5.6 demonstrates that tensile failure occurred within the free length of the specimen away from either jaws and as a result of a single transverse fracture. Damage is evident on the front and rear of the specimen at the tow boundaries as well as in the form of extensive inter-laminar cracking. This damage that is evident on the fractured surfaces of the specimen is supported by the progression of surface strains over the experimental period (Figure 5.7). The improved spatial resolution of the optical measurement system relative to the 6.7×10^{-2} s^{-1} experiment allows the transverse matrix cracking

to be at a similar magnitude to that observed within the quasi-static experiments (Figure 4.2).

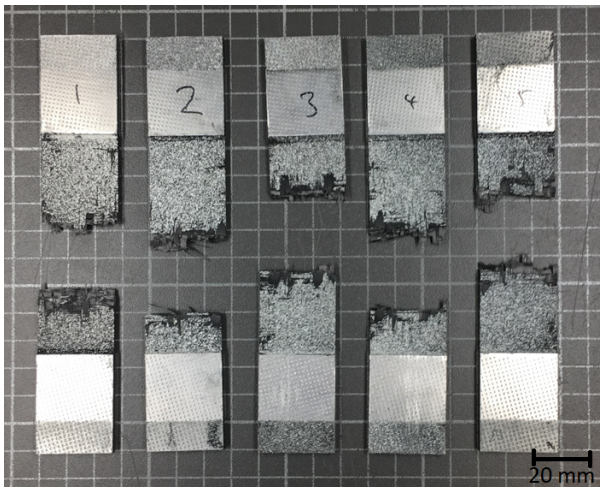

Figure 5.6: Failure locations of ISTS specimens subjected to a longitudinal tensile test at nominal longitudinal strain rate of 1.2 x 10^0 s^{-1}.

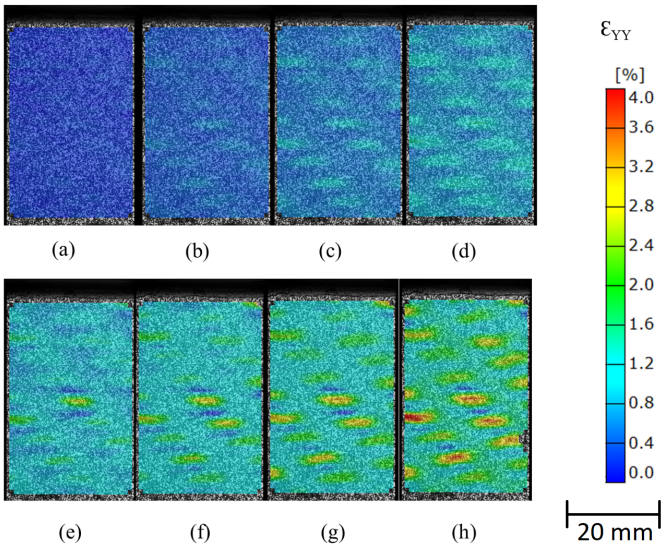

Figure 5.7: Surface strain maps overlaid on the left image of specimen #1 demonstrating the progression of longitudinal engineering strains at (a) 0.2, (b) 0.4, (c) 0.6, (d) 0.8 (e) 1.0. (f) 1.2, (g) 1.4 and (h) 1.63 % ε_{YY} of 12K 2 x 2 twill CFRP undergoing a tensile characterisation test at nominal longitudinal strain rate of 1.2 x 10^0 s^{-1}.

5.1.3 Nominal longitudinal strain rate 2.0 x 10^1 s^{-1}

Experiments with a nominal longitudinal strain rate of 2.0 x 10^1 s^{-1} were conducted on five ISTS specimens using a prescribed actuator velocity of 1 ms^{-1}. The use of an actuator velocity of 1 ms^{-1} requires the *high rate* open loop configuration of the VHS to be employed, thereby eliminating the feedback loop as discussed in Chapter 3. The 3D DIC characteristics utilised in the experiments are provided in Table 5.5. The sampling frame rate of 30 kHz enabled the collection of approximately 55 data points over the experimental period. However, to achieve this frame rate it required the sensor to be cropped to 486 x 896 $pixel^2$. Despite this, the achieved strain resolution (59.62 με) and spatial resolution (1.21 mm) was approximately equal to that of the experiment conducted at a nominal longitudinal strain rate of 1.2 x 10^0 s^{-1}.

Table 5.5: Summary of the measurement methodology for Photron SA-X2 3D DIC to characterise the longitudinal tensile performance of 12K 2 x 2 twill CFRP at a nominal longitudinal strain rate of 2 x 10^1 s^{-1} using ISTS specimens.

Property		Unit
Camera	Photron SA-X2	
Lens	Titanar 75b (20 mm extender tube)	
Frame rate	30	kHz
Shutter speed	31.75	μs
Aperture	11	f/
Imaging window	496 x 896	$pixel^2$
Calibration plate	CP20 MV 55 x 44	
Measurement volume	31.48 x 56.86 x 45	mm^3
Facet size	19	pixels
Step size	15	pixels
Spatial resolution	1.21	mm
Strain resolution	59.62	με
Displacement resolution	0.10	μm

Figure 5.8 shows the engineering stress - strain plots generated for the ISTS specimen loaded at a nominal longitudinal strain rate of 2.0 x 10^1 s^{-1}, the extracted mechanical data normalised to 52 % V_f is shown in Table 5.6. Each of the five specimens can be seen to maintain the linear behaviour of the previous strain rates, however, it is apparent that the additional energy input in the experiment by increasing the velocity is exciting the load cell, thus creating a ringing response in the load and

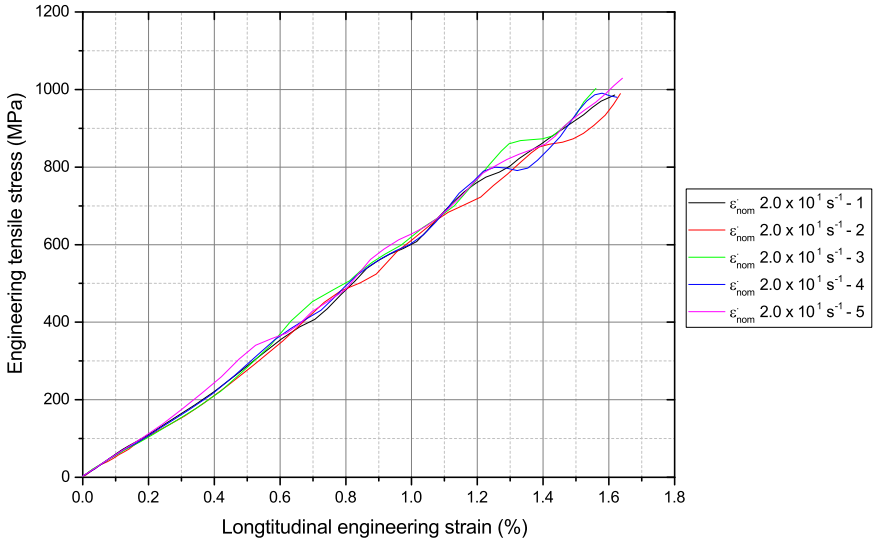

Figure 5.8: Longitudinal engineering stress-strain response of ISTS composite specimens experimentally loaded at a nominal longitudinal strain rate of 2.0 x 10^1 s^{-1}.

therefore also the derived stress. The modulus is determined by linear fit between 0.2 % and 1.0 % ε_{YY} in order to minimise the inaccuracy introduced by the ringing.

The surface strain maps shown in Figure 5.9 demonstrate the progression of longitudinal strains over the test period. It is evident that the damage mechanism behaves similarly to the material at quasi-static strain rates. The longitudinal fibres can be seen to limit the axial deformation of the specimen whilst damage can be seen to progress in the transverse tows, particularly those positioned at the free edges of the specimen. The heterogeneity of the strain map indicates that damage is coalescing across the specimen. The propagation of this random damage can be seen in Figure 5.10 that demonstrates the failure locations of the specimens. A single specimen failed in the vicinity of the lower jaw, however, since the mechanical properties were

Table 5.6: Tensile mechanical properties of ISTS specimens evaluated at a nominal longitudinal strain rate of 2.0 x 10^1 s^{-1}.

Property	Value	units	SD	CoV (%)
Tensile modulus	65.04	GPa	1.49	2.29
Tensile strength	1027.56	MPa	23.49	2.28
Ultimate engineering tensile strain	1.62	%	0.042	2.59
Poissons ratio	0.052		0.0024	4.61

within the 95 % confidence interval of the remaining experiments, the specimen was included within the final data set for this strain rate. As the velocity of the test is increased so to is energy that is released at moment of fracture, resulting in greater levels of inter-lamina damage.

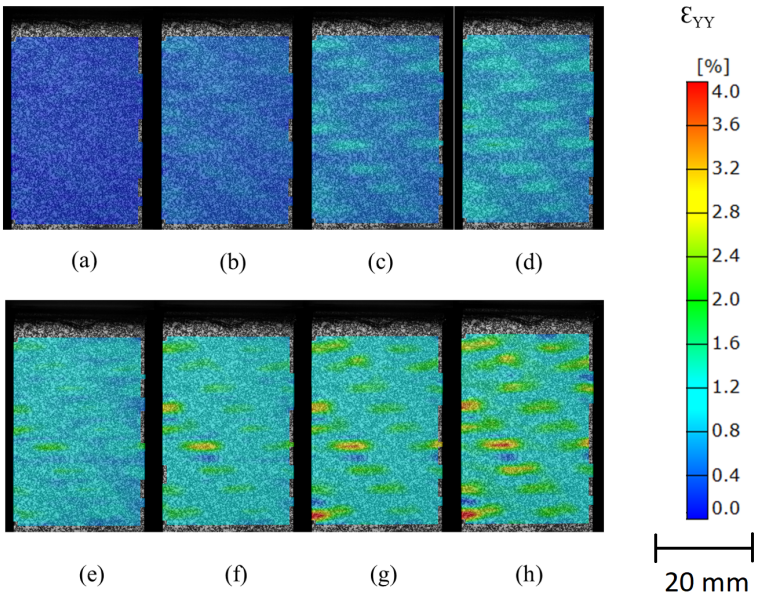

Figure 5.9: Surface strain maps overlaid on the left image of specimen #5 demonstrating the progression of longitudinal engineering strains at (a) 0.2, (b) 0.4, (c) 0.6, (d) 0.8 (e) 1.0. (f) 1.2, (g) 1.4 and (h) 1.61 % ε_{YY} of 12K 2 x 2 twill CFRP undergoing a tensile characterisation test at nominal longitudinal strain rate of 2.0 x 10^{1} s^{-1}.

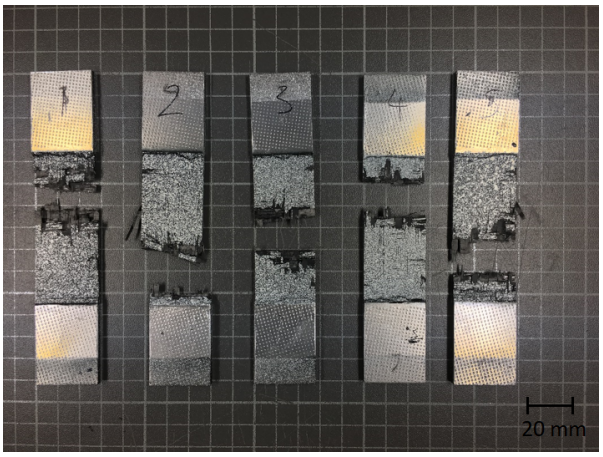

Figure 5.10: Failure locations of ISTS specimens subjected to a longitudinal tensile test at nominal longitudinal strain rate of 2.0 x 10^{1} s^{-1}.

5.1.4 Nominal longitudinal strain rate 5 x 10^1 s^{-1}

Tensile experiments at a nominal longitudinal strain rate of 5 x 10^1 s^{-1} were conducted on five ISTS specimens using the VHS in open loop to achieve an actuator velocity of 2.5 ms^{-1}. The 3D DIC characteristics used in the experiments are provided in Table 5.7. Approximately 35 data points were collected over the experimental period by increasing the frame rate of the Photron SA-X2 cameras to 67.5 kHz, this required the sensor to be cropped to 328 x 512 $pixels^2$. In order to maintain the full field measurement, the spatial resolution was reduced to 1.39 mm as a result of the facet size being reduced to 13 pixels. The spatial resolution could not be improved further since the 13 pixel facet induced an average strain resolution of 109.17 με. Facet sizes below 13 pixels with this optical measurement set up were shown to induce strain resolutions with noise greater than 1 % of the quasi-static ultimate strain which was prescribed as the minimum acceptable signal to noise ratio in Chapter 3.

Table 5.7: Summary of the measurement methodology for Photron SA-X2 3D DIC to characterise the longitudinal tensile performance of 12K 2 x 2 twill CFRP at a nominal longitudinal strain rate of 5.0 x 10^1 s^{-1} using the ISTS tensile specimen.

Property		Unit
Camera	Photron SA-X2	
Lens	Titanar 75b (10 mm extender tube)	
Frame rate	67.5	kHz
Shutter speed	13.19	μs
Aperture	5.6	f/
Imaging window	328 x 512	$pixel^2$
Calibration plate	CP20 MV 92 x 72	
Measurement volume	35.23 x 55 x 90	mm^3
Facet size	13	pixels
Step size	11	pixels
Spatial resolution	1.39	mm
Strain resolution	109.17	με
Displacement resolution	0.19	μm

The experimental engineering stress - strain plots for each of the five repeats of the ISTS specimen reviewed at a nominal longitudinal strain rate of 5.0 x 10^1 s^{-1} are shown in Figure 5.11 and the derived mechanical properties normalised to a 52 % V_f are listed in Table 5.8. The modulus was determined by a linear fit between 0.2 % and 1.0 % ε_{YY}. The resonance response observed at the previous nominal strain rate is again represented in the experiment. Since the loading period is reduced due to

increased test speed, so too are the number of oscillations as the frequency remains constant. The resonance is attributed to the low natural frequency of the slack adaptor inducing load cell inertial ringing, the natural frequency is low as a result of the mass of the fixturing. Overall the specimen behaves in a linear elastic manner, with approximately constant stiffness prior to brittle fracture. The surface strain maps shown in Figure 5.12 demonstrates that the surface damage remains consistent with the previous experiments with transverse matrix cracking of the weft tows. Due to the small facet size, the ARAMIS software has a susceptibility to drop facets out as a result of the inability to compute the unique facet location as the quantity of information within the facet is reducing.

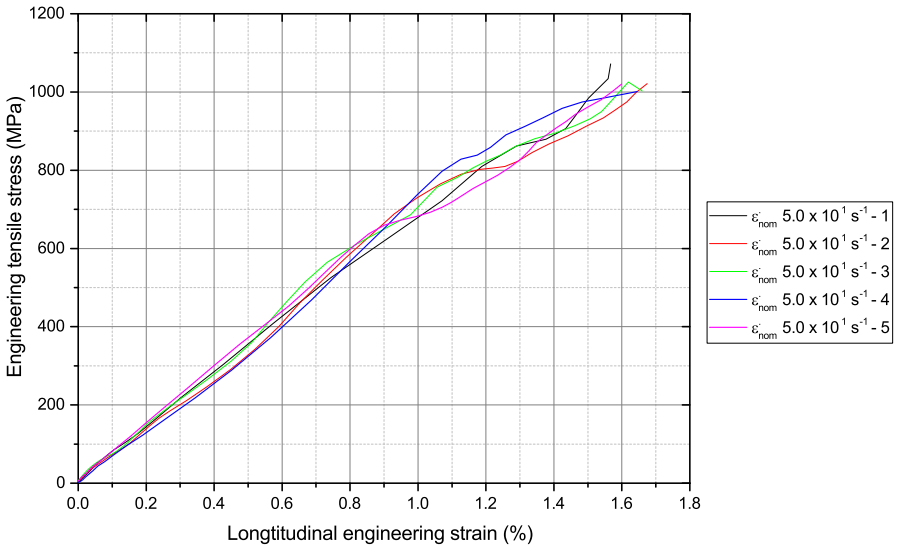

Figure 5.11: Longitudinal engineering stress-strain response of ISTS composite specimens experimentally loaded at a nominal longitudinal strain rate of 5.0×10^1 s^{-1}.

Table 5.8: Tensile mechanical properties of ISTS specimens evaluated at a nominal longitudinal strain rate of 5.0×10^1 s^{-1}.

Property	Value	units	SD	CoV
Tensile modulus	66.36	GPa	0.63	0.95
Tensile strength	1067.39	MPa	26.66	2.49
Ultimate engineering tensile strain	1.62	%	0.058	3.58
Poissons ratio	0.049		0.0037	7.55

The failed specimens are shown in Figure 5.13, each of the specimens failed as a result of a single transverse crack within the free length. The transverse crack induced within each of the specimens has an uneven fracture surface. Auxiliary

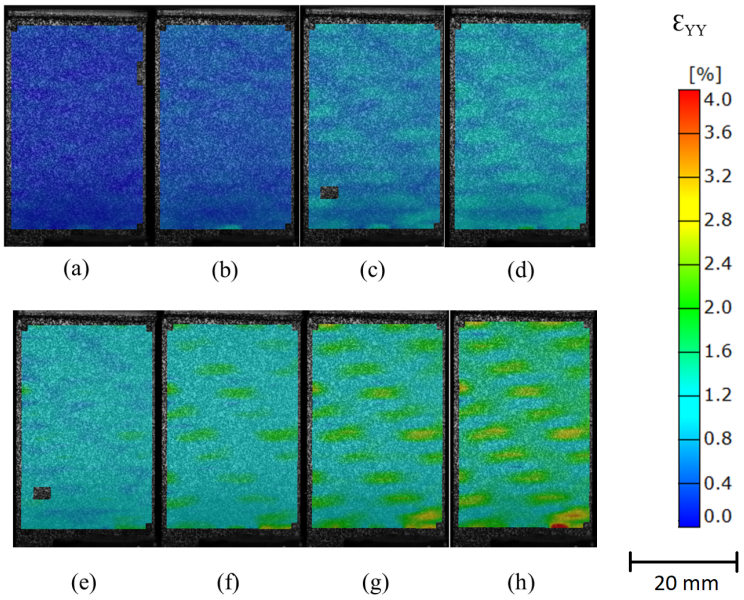

Figure 5.12: Surface strain maps overlaid on the left image of specimen #5 demonstrating the progression of longitudinal engineering strains at (a) 0.2, (b) 0.4, (c) 0.6, (d) 0.8 (e) 1.0. (f) 1.2, (g) 1.4 and (h) 1.60 % ε_{YY} of 12K 2 x 2 twill CFRP undergoing a tensile characterisation test at nominal longitudinal strain rate of 5.0 x 10^{1} s^{-1}

damage within the remaining specimen can be observed local to the tow boundaries in the form of matrix cracking and as inter-laminar cracks.

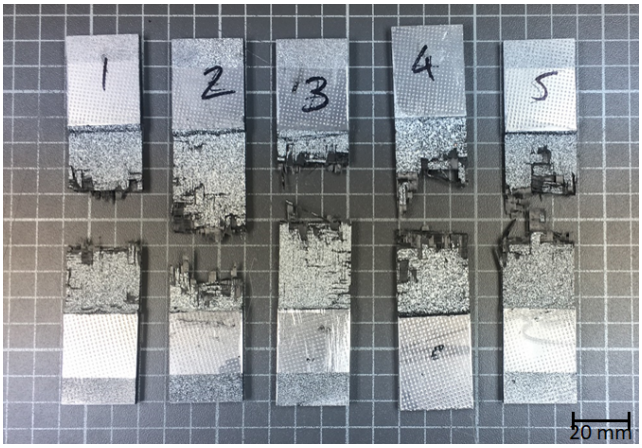

Figure 5.13: Failure locations of ISTS specimens subjected to a longitudinal tensile test at nominal longitudinal strain rate of 5.0 x 10^{1} s^{-1}.

5.1.5 Nominal longitudinal strain rate 1.0 x 10^2 s^{-1}

Tensile experiments aiming to achieve a nominal strain rate of 1.0 x 10^2 s^{-1} were conducted on five ISTS specimens using the open loop configuration of the VHS to achieve an actuator velocity of 5 ms^{-1}. The 3D DIC characteristics utilised in the experiments are provided in Table 5.9. The frame rate of 100 kHz was found to be capable of achieving ~25 data points over the experimental period, whilst maintaining full field view of the specimen. The cropped sensor size of 264 x 384 $pixel^2$ produced a spatial resolution of 1.39 mm, with a facet size of 13 pixels. This will produce a smoothing error that is comparable with the other experiments conducted, however, the small facet size will induce a larger measurement error (131.96 με). Further reduction of the facet size increased the noise beyond the 1 % of the ultimate strain threshold of the quasi-static experiments.

Table 5.9: Summary of the measurement methodology for Photron SA-X2 3D DIC to characterise the longitudinal tensile performance of 12K 2 x 2 twill CFRP at a nominal longitudinal strain rate of 1.0 x 10^2 s^{-1} using the ISTS tensile specimen.

Property	Value	Unit
Camera	Photron SA-X2	
Lens	Titanar 75b (20 mm extender tube)	
Frame rate	100	kHz
Shutter speed	8.38	μs
Aperture	5.6	f/
Imaging window	264 x 384	$pixel^2$
Calibration plate	CP20 MV 92 x 72	
Measurement volume	28.36 x 41.25x 90	mm^3
Facet size	13	pixels
Step size	10	pixels
Spatial resolution	1.39	mm
Strain resolution	131.96	με
Displacement resolution	0.22	μm

The experimental engineering stress-strain plots for the five specimens investigated at a nominal longitudinal strain rate of 1.0 x 10^2 s^{-1} are shown in Figure 5.14. It is evident that specimen #5 underwent a different response to the loading than the other four specimens evaluated which behaved in a linear manner at the onset of loading and is therefore excluded from the data set Specimen #1 also experienced a loading pattern not consistent with the expected linear results, the response is hypothesised to be a result of specimen slipping within the mechanical jaws. However,

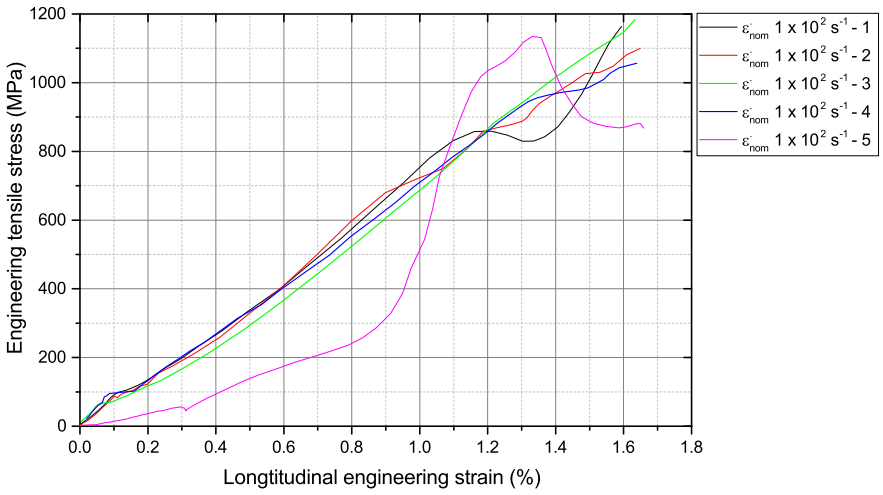

Figure 5.14: Longitudinal engineering stress-strain response of ISTS composite specimens experimentally loaded at a nominal longitudinal strain rate of 1.0×10^2 s^{-1}.

in order to capitalise on the reduced pixel density of the cropped sensor, the sensor was only focused on imaging the specimen surface, therefore is is unclear whether slipping was the cause of the deviation and it cannot be determined which jaw was responsible. The modulus determined between 0.2 % and 1.0 % longitudinal strain was within the 95 % confidence interval of the other three remaining repeats and is therefore considered within the dataset However, due to the unexplained non-linear response as the specimen approaches 1.2 % strain, the ultimate properties are not considered within the statistical analysis of the mechanical properties.The derived mechanical properties were normalised to a constant 52 % V_f and are summarised in Table 5.10. Specimens 2 - 4 exhibited increased variation in ultimate strength relative to all the previous tensile experiments in this Chapter. Since the ultimate strain and modulus variance remained consistent with the previous experiments it can be concluded that this variation in ultimate strength is either a function of the load cell ringing or the damage coalescence as the specimens approach ultimate strain.

To investigate the highly irregular and non-linear failure of specimen #5, the fracture sequence captured by the left hand Photron SA-X2 camera is shown in Figure 5.15. Since Figure 5.15 (a) is intact with no signs of failure at 1.12 % ε_{YY} the initial ductility of the specimen is considered to be the result of internal damage. External ply failure commences in Figure 5.15 (b) with the formation of a transverse crack, the lack of focus on the left and right hand side of the frame suggests that it is deforming in shear around a central plane. A longitudinal crack forms at the centre of the

.

Table 5.10: Tensile mechanical properties of ISTS specimens evaluated at a nominal longitudinal strain rate of 1.0 x 10^2 s^{-1}.

Property	Value	units	SD	CoV
Tensile modulus	69.68	GPa	1.33	1.91
Tensile strength	1109.61	MPa	42.23	3.81
Ultimate engineering tensile strain	1.63	%	0.031	1.90
Poissons ratio	0.055		0.0036	6.54

specimen by frame (c), whilst the ultimate failure as a result of both longitudinal and transverse cracking is shown in frames (d) and (e). It is clear that the failure occurred as a combination of a transverse crack and a longitudinal crack propagating through the specimen which correlates with the observed failed specimen in Figure 5.16. Since this alternative damage sequence has not been observed throughout the other experiments conducted at this strain rate, as well as in the other tensile experiments of this thesis; the result is removed from statistical analysis and is considered to be a result of a fabric or lamination defect within the specimen. The failure locations of each of the five specimens is shown in Figure 5.16, the four remaining specimens all failed as a result of a global transverse crack with no evidence of the longitudinal crack that occurred in specimen #5.

The surface strain maps taken of specimen #2 (Figure 5.17) over the experimental period indicate the expected damage sequence of the specimen when it is loaded at a nominal strain rate of 1.0 x 10^2 s^{-1}. Peak longitudinal strains appear within the transverse tows, highlighting that transverse matrix cracking remains a key damage mechanism as the specimen approaches failure. Peaks strains appear to propagate from the edges of the specimen, particularly within the transverse tows and this

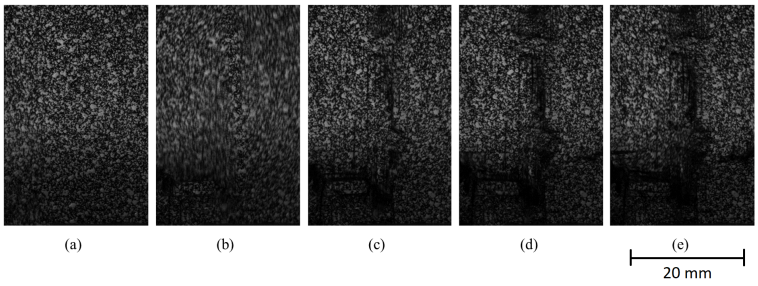

Figure 5.15: Brittle fracture sequence of specimen #5 showing failure as a result of a hypothesised fabric defect since macroscopic failure occurs as a function of both longitudinal and transverse cracking, (a) t_0 = (ε_{YY} = 1.12 %), (b) t = t_0 + 10 μs, (c) t = t_0 + 20 μs, (d) t = t_0 + 30 μs and (e) t = t_0 + 40 μs.

ultimately leads to the fracture of the specimen.

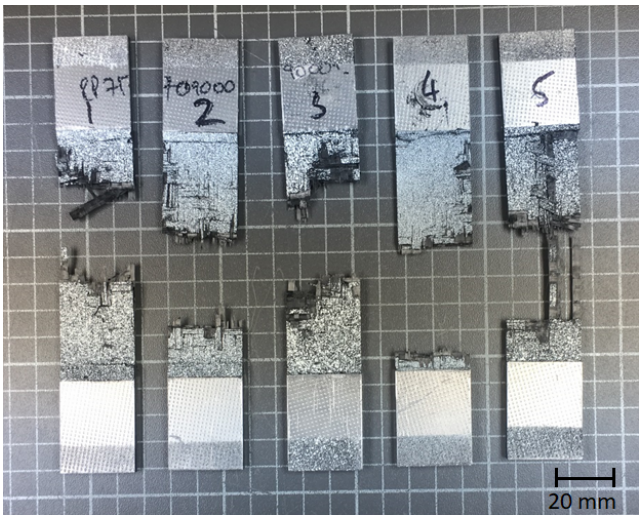

Figure 5.16: Failure locations of ISTS specimens subjected to a longitudinal tensile test at nominal longitudinal strain rate of 1.0 x 10^2 s^{-1}.

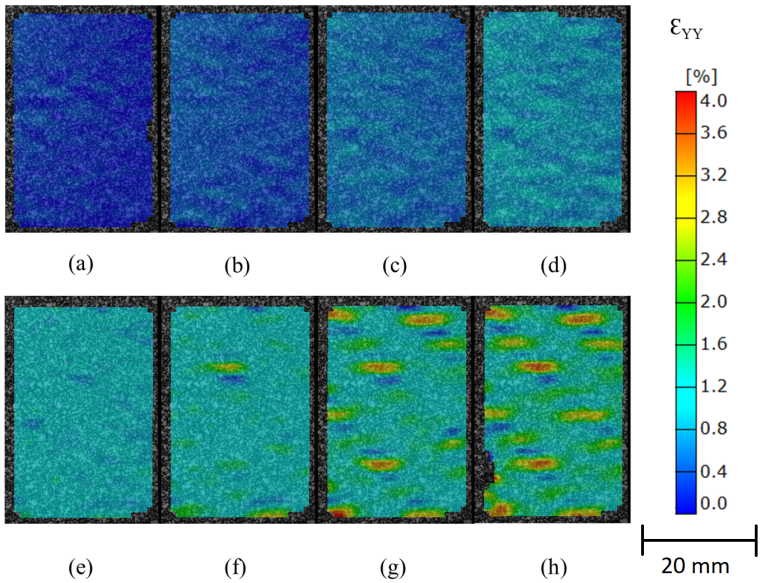

Figure 5.17: Surface strain maps overlaid on the left image of specimen #2 demonstrating the progression of longitudinal engineering strains at (a) 0.2, (b) 0.4, (c) 0.6, (d) 0.8 (e) 1.0. (f) 1.2, (g) 1.4 and (h) 1.57 % ε_{YY} of 12K 2 x 2 twill CFRP undergoing a tensile characterisation test at nominal longitudinal strain rate of 1.0 x 10^2 s^{-1}

5.1.6 Experimental strain rates

All of the experiments detailed in Sections 5.1.1 - 5.1.5 have been reported based on the nominal strain rate determined based on the actuator velocity and specimen length. However, the validity of the mechanical properties and failure mechanisms derived at each of the nominal strain rates is dependent upon the specimens being loaded at the desired strain rate magnitude over the test period. Due to the inertial effect of the specimen due to its high capcity (~ 50 kN) the experimental strain rate is not likely to be linear and therefore requires further assessment for each experiment individually. The experimental strain rate was determined as the temporal differential of the global longitudinal surface strains. The longitudinal engineering strain rate as a function of the longitudinal engineering strain for the 12K 2 x 2 twill CFRP specimens at nominal strain rates between 2.2 x 10^{-4} s^{-1} to 1.0 x 10^{-2} s^{-1} is provided in Figure 5.18.

The non-linearity of the strain rate is observed to be directly related to the nominal strain rate that the specimen has been exposed to. Increasing the actuator velocity increases the nominal and peak experimental strain rate, however, it also increases the strain rate rising period. Large increases in strain rate are also observed in multiple tests as the specimen approaches failure, this is a result of localised crack propagation inducing high strain rates and therefore distorting the derived strain rate.

The process for defining the experimental strain rate for metallic specimens is provided in the high strain rate servo-hydraulic metallic standard ISO 26203-2:2011, this determines the average experimental strain rate over the plastic straining period between yield and peak force as shown in Equation 2.1 (repeated below).

$$\dot{\varepsilon}_{exp} = F\left\{\dot{\varepsilon}\left(t_{yield}\right)...\dot{\varepsilon}\left(t_{F_{max}}\right)\right\}$$

For metallic specimens defining the experimental strain rate over this period enables the user to remove highly non-linear strain rates generated within the inertial strain rate rising period which typically occur pre-yield, as well as the high localised strain rates as a result of necking post peak force from distorting the recorded experimental strain rate. However, since the longitudinal tensile response of the laminate lacks a yield point and a period of plastic straining the experimental strain rate must be determined within the elastic region. Given the lack of relevant standards, the experimental longitudinal strain rate for tensile specimens ($\dot{\varepsilon}_{exp}\left(TENSION\right)$) in this thesis was defined by the author according to Equation 5.1, this determines the

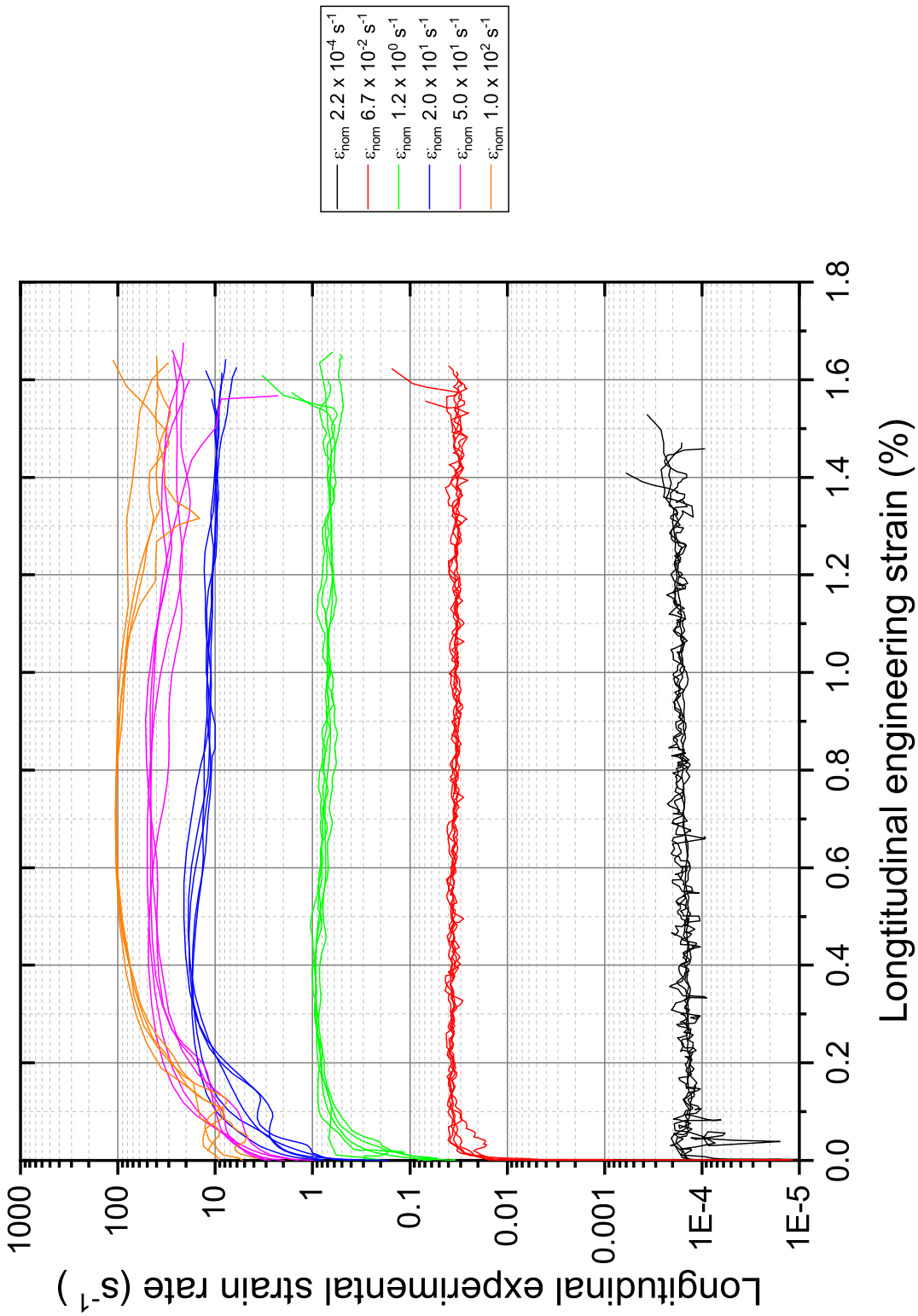

Figure 5.18: Summary of the longitudinal experimental strain rates as a function of the longitudinal engineering strain at nominal strain rate increases between 2.2 x 10^{-4} s^{-1} to 1.0 x 10^{2} s^{-1}.

average strain rate between the strain at 90 % of peak strain rate ($\varepsilon_{0.9\dot{\varepsilon}_{max}}$) and 1.4 % ε_{YY} ($\varepsilon_{0.014}$). Prescribing the minimum strain rate averaging point as 90 % of peak strain rate enables the author to remove the inertial strain rate rising period from each of the data sets, whilst the upper strain limit of 1.4 % ε_{YY} provides a discrete termination point that is within each of the experiments and prior to any localised crack growth distortion.

$$\dot{\varepsilon}_{exp}\left(TENSION\right) = \digamma\left\{\dot{\varepsilon}\left(\varepsilon_{0.9\dot{\varepsilon}_{max}}\right)...\dot{\varepsilon}\left(\varepsilon_{0.014}\right)\right\} \tag{5.1}$$

A comparison of the nominal and average experimental strain rates using Equation 5.1 is provided in Table 5.11 along with the minimum and maximum experimental strain rates observed over this measurement period.

Table 5.11: Comparison of the mean average experimental strain rates ($\dot{\varepsilon}_{exp}$) observed when characterising the tensile response of the 12K 2 x 2 twill CFRP between nominal longitudinal strain rates of 2.2 x 10^{-4} s^{-1} to 1.0 x 10^{2} s^{-1} alongside the mean maximum ($\dot{\varepsilon}_{max}$) and minimum ($\dot{\varepsilon}_{min}$) experimental strain rates.

Nominal longitudinal strain rate (s^{-1})	$\dot{\varepsilon}_{exp}$ (s^{-1})	$\dot{\varepsilon}_{max}$ (s^{-1})	$\dot{\varepsilon}_{min}$ (s^{-1})
2.2 x 10^{-4}	1.7 x 10^{-4}	2.9 x 10^{-4}	8.3 x 10^{-5}
6.7 x 10^{-2}	3.5 x 10^{-2}	4.1 x 10^{-2}	2.7 x 10^{-2}
1.2 x 10^{0}	7.2 x 10^{-1}	9.4 x 10^{-1}	5.8 x 10^{-1}
2.0 x 10^{1}	1.2 x 10^{1}	1.9 x 10^{1}	8.4 x 10^{0}
5.0 x 10^{1}	3.7 x 10^{1}	4.9 x 10^{1}	2.4 x 10^{1}
1.0 x 10^{2}	7.6 x 10^{1}	1.05 x 10^{2}	3.3 x 10^{1}

The metallic standard ISO 26203-2:2011 dictates that for the strain rate to be considered stable, the minimum and maximum observed experimental strain rates must be within ±30 % of the average. The quasi-static experiment conducted at a nominal strain rate of 2.2 x 10^{-4} s^{-1} has the largest variance of all of the experiments reported in Table 5.11 as the maximum and minimum strain rates were found to be + 71.2 % / - 50.1 % of the average experimental strain rate. It has been shown by Beaumont that this is due to the displacement control of the electro-mechanical frame [188]. In comparison using the VHS when operating in closed loop to conduct experiments at nominal strain rates of 6.7 x 10^{-2} s^{-1} and 1.2 x 10^{0} s^{-1} induced variance of + 7.1 % / - 22.9 % and + 30.6 % / - 19.4 % respectively, both of which fall within the tolerance of the metallic standard. In comparison, operating the VHS in open loop to produce nominal strain rates of 2.0 x 10^{1}, 5.0 x 10^{1} and

1.0×10^2 resulted in variances of + 54.8 % / - 30.2 %, + 33.2 % / - 34.4 % and + 38.5 % / - 56.9 % respectively. Following the strain rate rising period, each of the experiments achieved peak experimental strain rates within 5 % of the prescribed nominal strain rate, however, as the specimen continued to strain the experimental strain rate decayed, inducing this large variance. This strain rate decay was reported in literature in Section 2.2.3 and is attributed to the inertial load of the specimen retarding the actuator. As a result it is the required removal of the feedback loop in this operating mode that is attributed to the inability to produce a *stable* strain rate according to the ISO standard. Since the devised ISTS geometry is the minimum capable of achieving the desired global stress state it be considered that either the metallic standards experimental strain rate range for a composite laminate is unsuitable, or the experimental method needs further development to introduce variable servo-valve control when operating in open loop.

Figure 5.18 shows how as the actuator velocity increased, the strain at which the strain rate decay occurred was delayed. As a result the inertial effect of the specimen is reduced with increasing strain rate. It is considered that as the magnitude of the velocity increases further, the kinetic energy of the slack adaptor cradle will increase and at a critical point it may effectively overcome the inertial load of the specimen. Thus inducing an experimental strain rate with greater stability. However, when further increasing the strain rate it is also important to consider the effect of the non-linear strain rate rising period. The average $\varepsilon_{0.9\dot{\varepsilon}_{max}}$ for the 1.0×10^2 nominal strain rate experiment was found to be 0.38 % ε_{YY}, as a result the defined experimental strain rate was determined considering 62 % of the strain range of the specimen. Further increases to the nominal strain rate will be expected to delay this point reducing the volume of data used to determine the average experimental strain rate. Therefore this method for determining the average experimental strain rate in future may induce inaccuracies as only a small portion of the test would be considered.

It is concluded that the non-linear experimental strain rate range is inevitable due to the high capacity of the representative 12K 2 x 2 twill CFRP laminate retarding the actuator when controlling the VHS in open loop. The proposed method for determining the average experimental strain rate removes the diminishing effect of the strain rate rising period. In comparison the retardation of the actuator that is a result of the load induced by the representative length scale specimen cannot be removed, thus a decaying strain rate as the specimen approaches failure is introduced. This was observed at each of the discrete nominal strain rates investigated in this study, however, it is likely to be reduced as the strain rate is further increased. The strain rate decay introduces a difference between the average experimental strain rate and the prescribed nominal strain rates (Table 5.11) of up to 25.7 % (nom-

inal strain rate of 5.0 x 10^1), therefore from henceforth all analysis of the tensile intermediate strain rate experiments will be reported according to their average experimental strain rates.

5.2 Summary of the strain rate sensitivity of the longitudinal tensile response to intermediate strain rates

Table 5.12 provides a summary of the effect of intermediate strain rates on the mechanical properties for the 12K 2 x 2 twill CFRP laminate derived from tensile experiments presented in Section 5.1. The tensile modulus, strength and strain appear to increase with strain rate, whilst the Poissons ratio remains approximately constant. Between experimental strain rates of 1.7 x 10^{-4} s^{-1} and 3.5 x 10^{-2} s^{-1} in particular there appears to be a significantly large increase in ultimate tensile strength and ultimate strain. The following sections will detail the effect of strain rate on the modulus, ultimate strength and ultimate strain in more detail.

5.2.1 Effect of strain rate on the longitudinal tensile modulus

The average tensile modulus is plotted against experimental strain rate in Figure 5.19. The y error bars demonstrate the 95 % confidence interval range for the measured modulus, whilst the x error bars highlight the 95 % confidence interval for the experimental strain rate. In Figure 5.19 the strain rate can be seen to have an increasing effect on the longitudinal tensile modulus. In order to determine the statistical variance of the modulus data collected at different strain rates an *f-test* was run using one-way ANOVA analysis with a confidence interval of 95 %. The resultant *P-value* of 0.04 dictates that at least two of the means are statistically different. In order to determine which of these are different a post-hoc test is required, in this instance a Tukey's honest squared difference (HSD) test was run, the results of which are shown in Table 5.13. A different letter denotes that the result was found to be statistically different. Tukey's HSD test compares the means of every treatment to the means of every other treatment to reduce Type I error which induces false significant results. At the desired 95 % confidence interval, a trend is evident whereby the stiffness derived at each of the strain rates cannot be demonstrated to be statistically different from an order of magnitude greater and smaller than itself. However, the overall trend is increasing.

Table 5.12: Summary of the tensile mechanical properties of the 12K 2 × 2 twill CFRP experimentally investigated at discrete nominal strain rates between 2.2×10^{-4} s^{-1} and $1.0 \times 10^{2} s^{-1}$.

Nominal strain rate	s^{-1}	2.2×10^{-4}	6.7×10^{-2}	1.2×10^{0}	2.0×10^{1}	5.0×10^{1}	1.0×10^{2}	F-test P-Value
Experimental strain rate	s^{-1}	1.7×10^{-4}	3.5×10^{-2}	7.2×10^{-1}	1.2×10^{1}	3.7×10^{1}	7.6×10^{1}	
Tensile modulus (SD)	GPa	61.27 (0.88)	62.64 (1.05)	63.46 (1.01)	65.04 (1.49)	66.36 (0.63)	69.68 (1.33)	< 0.001
Ultimate engineering tensile strength (SD)	MPa	882.22 (19.79)	991.76 (21.47)	999.66 (24.89)	1027.56 (23.49)	1067.39 (26.66)	1109.61 (42.23)	< 0.001
Ultimate engineering tensile Strain (SD)	%	1.41 (0.057)	1.60 (0.029)	1.62 (0.036)	1.62 (0.042)	1.62 (0.058)	1.63 (0.031)	< 0.001
Poissons ratio (SD)		0.054 (0.0021)	0.049 (0.0039)	0.055 (0.0030)	0.052 (0.0024)	0.049 (0.0037)	0.055 (0.0036)	0.48

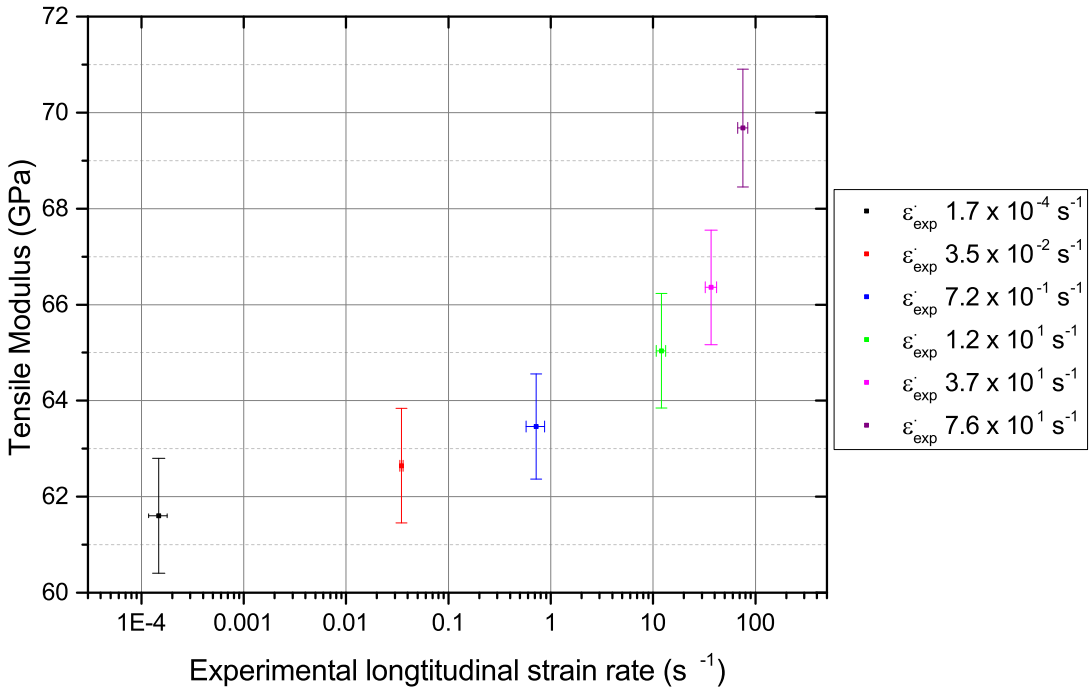

Figure 5.19: Tensile modulus recorded between 0.2 % and 1.0 % longitudinal strain at magnitude intervals of increasing experimental strain rates. Error bars depict the 95 % confidence interval for tensile modulus (y) and longitudinal experimental strain rate (x).

Table 5.13: Results of Tukey HSD statistical difference analysis on the tensile modulus recorded at different intermediate strain rates, a different letter indicates a statistically significant difference.

Experimental strain rate (s^{-1})	Statistical difference			
1.7×10^{-4}	A			
3.5×10^{-2}	A			
7.2×10^{-1}	A	B		
1.2×10^{1}		B	C	
3.7×10^{1}			C	
7.6×10^{1}				D

5.2.2 Effect of strain rate on the longitudinal tensile strength

Figure 5.20 demonstrates the increasing mean ultimate strength with increasing strain rate. The *f-test P-value* demonstrates that at least two means are different. It is clear that the quasi-static strength is less than that observed in the intermediate strain rate experiments as shown in Figure 5.20. The results of Tukey HSD test demonstrates that the tensile strength at strain rates between 3.5×10^{-2} s^{-1} and 1.2×10^{1} s^{-1}cannot be identified as independent relative to each other, nor can those measured at 1.2×10^{1} s^{-1} and 3.7×10^{1} s^{-1}; as well as 3.7×10^{1} s^{-1} and 7.6×10^{1} s^{-1}. However, each of those groups is statistically different. As a result, the statistical analysis demonstrates again that the measured ultimate tensile strength is positively sensitive to the applied strain rate. The largest increase in strength occurs between 1.7×10^{-4} s^{-1} and 3.5×10^{-2} s^{-1} strain rates.

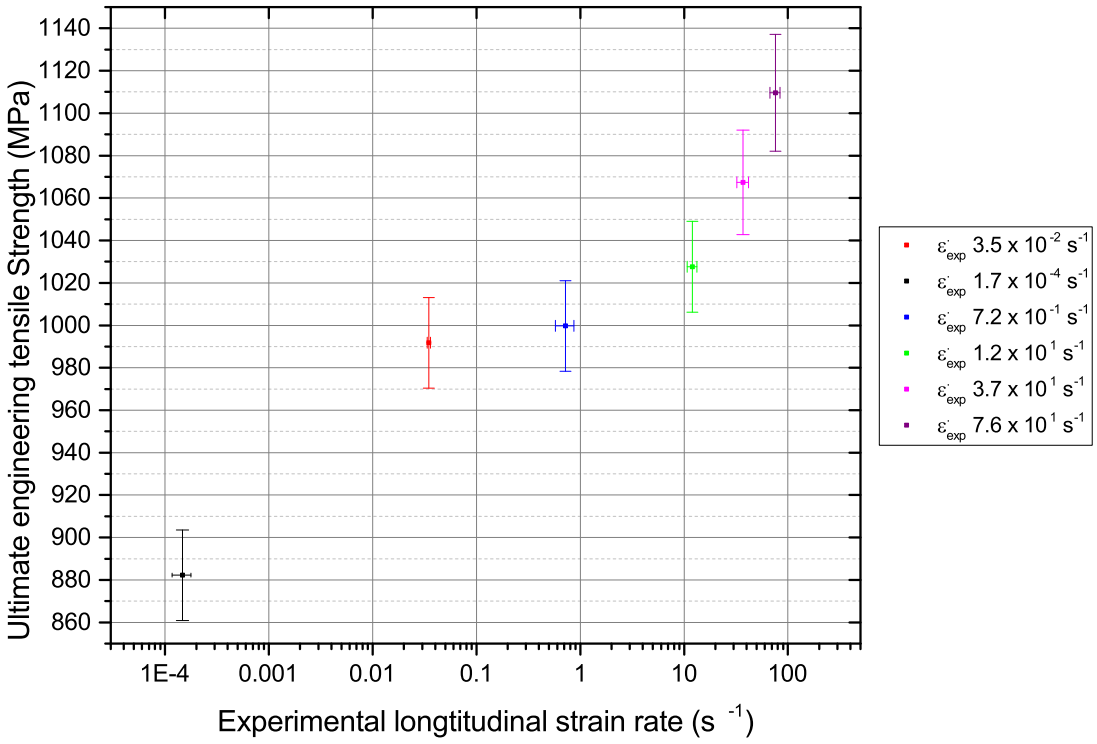

Figure 5.20: Ultimate tensile strength determined at magnitude intervals of increasing experimental strain rates. Error bars demonstrate the 95 % confidence interval for ultimate tensile strength (y) and longitudinal experimental strain rate (x).

Table 5.14: Results of Tukey HSD statistical difference analysis on the ultimate tensile strength recorded at different intermediate strain rates, a different letter indicates a statistically significant difference.

Experimental strain rate (s^{-1})	Statistical difference			
1.7×10^{-4}	A			
3.5×10^{-2}		B		
7.2×10^{-1}		B		
1.2×10^{1}		B	C	
3.7×10^{1}			C	D
7.6×10^{1}				D

5.2.3 Effect of strain rate on the ultimate longitudinal tensile strain

Figure 5.21 shows the effect of increasing experimental strain rate on the ultimate engineering tensile strain and Table 5.15 provides the results of the Tukey HSD test.

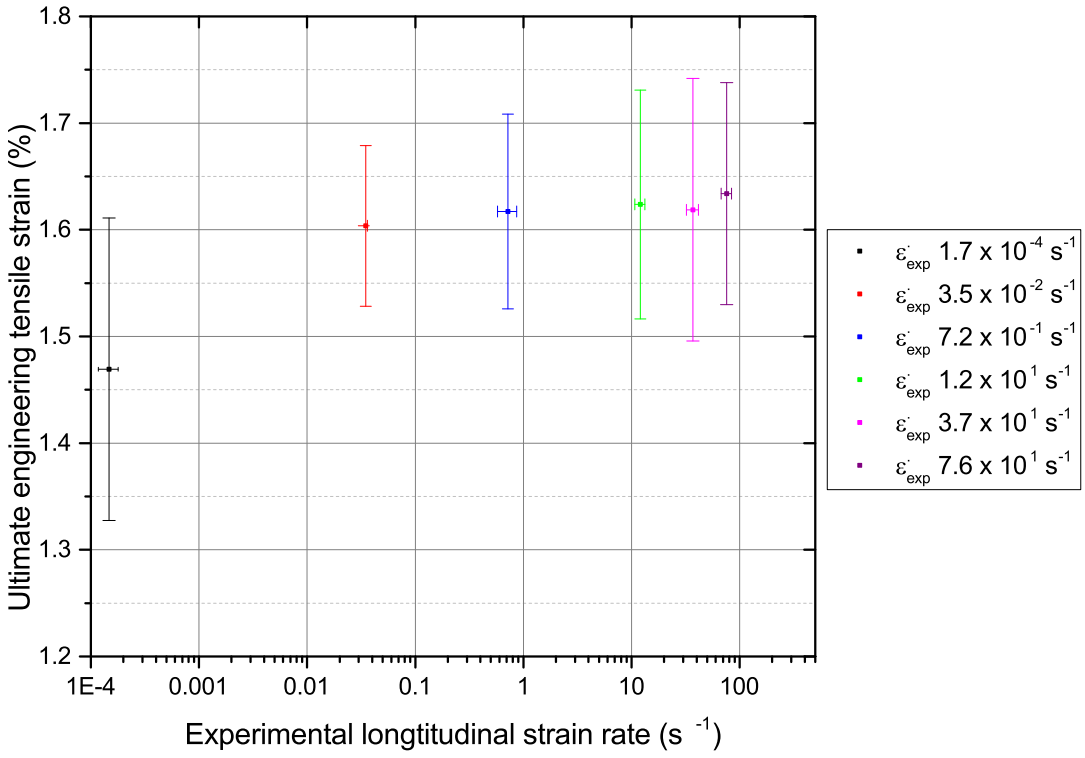

Figure 5.21: Ultimate tensile strain determined at magnitude intervals of increasing experimental strain rates. Error bars dictate the 95 % confidence interval for ultimate tensile strain (y) and longitudinal experimental strain rate (x).

It can be observed that as strain rate increases initially, so too does ultimate strain, but then it appears to plateau as the rate increases further. The intermediate strain rate experiments appeared to strain 8.8 % greater on average than at 1.7 x 10^{-4} s^{-1}.

The small variance observed within experiments conducted at 3.5 x 10^{-2} s^{-1} could potentially be related to the low spatial resolution relative to the other experiments. The greater the surface area contained within a single facet the greater the smoothing that is introduced in the specimens, thus reducing the experimental variance observed. The high speed 3D DIC system utilising the two 1 MP Photron SA-X2 cameras was required to achieve the desired temporal resolution for this experiment, however, the large specimen size required to produce the low strain rate reduced the pixel density across the surface of the specimen. The RoI could have been reduced, however, this would have risked the author not capturing the random location of the failure within the RoI which has been shown to occur at various locations along the free length.

Table 5.15: Results of Tukey HSD statistical difference analysis on the ultimate tensile strain recorded at different intermediate strain rates, a different letter indicates a statistically significant difference.

Experimental strain rate (s^{-1})	Statistical difference	
1.7 x 10^{-4}	A	
3.5 x 10^{-2}		B
7.2 x 10^{-1}		B
1.2 x 10^{1}		B
3.7 x 10^{1}		B
7.6 x 10^{1}		B

5.2.4 Effect of strain rate on Poissons ratio

The average Poissons ratio derived from the quasi-static and intermediate strain rate experiments is presented in Figure 5.22. The 95 % confidence interval for the measured Poissons ratio is indicated by the y error bars, as with the previous sections, the x error bars demonstrate the 95 % confidence interval for the average experimental strain rate. The results of the Tukey HSD analysis indicates that the means are cannot be described as different. The large variance at experimental strain rates 3.5 x 10^{-2} s^{-1}, 3.7 x 10^{1} $s^{-1}$and 7.6 x 10^{1} s^{-1} is attributed to the signal to noise ratio achieved as a result of the imaging characteristics of each experiment.

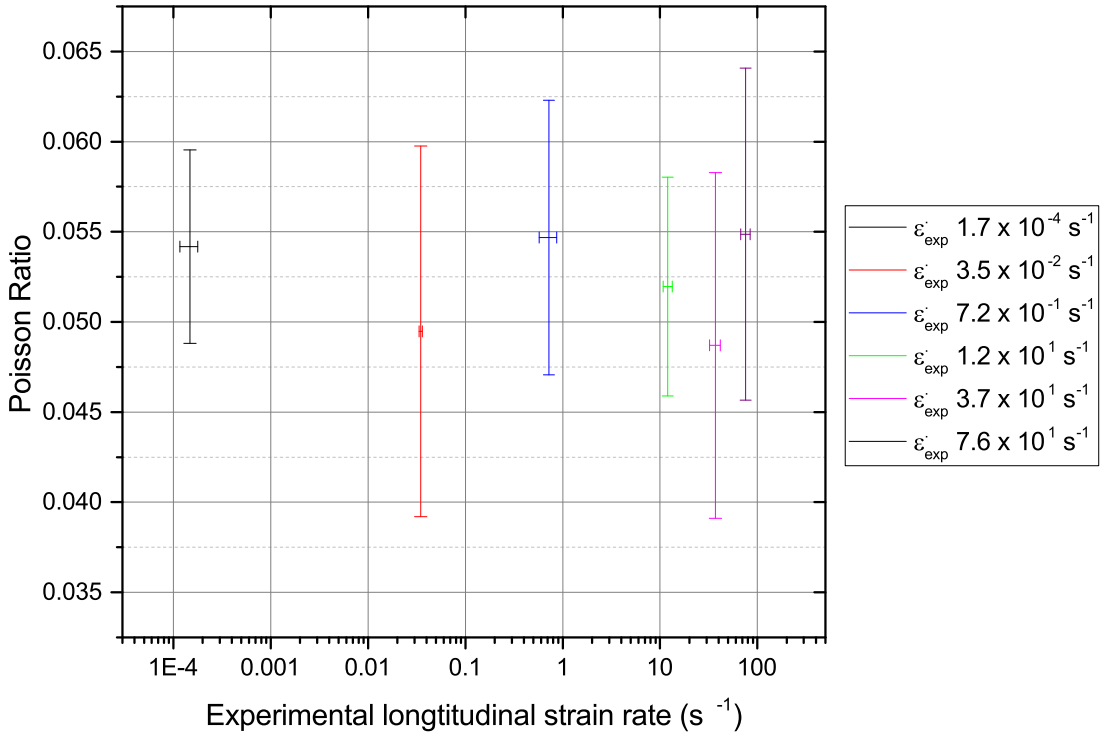

Figure 5.22: Poissons ratio derived based on tensile experiments conducted at magnitude intervals of increasing experimental strain rates. Error bars dictate the 95 % confidence interval for Poissons ratio (y) and longitudinal experimental strain rate (x).

Table 5.16: Results of Tukey HSD statistical difference analysis on the tensile Poissons ratio recorded at different intermediate strain rates, a different letter indicates a statistically significant difference.

Experimental strain rate (s^{-1})	Statistical difference
1.7×10^{-4}	A
3.5×10^{-2}	A
7.2×10^{-1}	A
1.2×10^{1}	A
3.7×10^{1}	A
7.6×10^{1}	A

5.3 In-plane shear

This section outlines the results of the in-plane shear characterisation of the 12K 2 x 2 twill CFRP laminate between nominal longitudinal strain rates of 6.7 x 10^{-2} $s^{-1}$and 1.0 x 10^{2} s^{-1}. The discrete strain rate intervals are increased at approximate orders of magnitude. A composite laminates in-plane shear response is characterised for CAE according to its shear modulus, ultimate shear strength, ultimate shear strain and yield shear strength and yield shear strain [187], therefore these are the mechanical properties obtained in the following experiments.

5.3.1 Nominal longitudinal strain rate of 6.7 x 10^{-2} s^{-1}

The minimum velocity of the VHS frame operating in closed loop 0.01 ms^{-1}, therefore the free length of the developed ISSS specimen was insufficient to induce the desired nominal longitudinal strain rate of 6.7 x 10^{-2} s^{-1}. Therefore the specimen free length was increased to that of the ASTM D3518-13 standardised geometry as was required in the tensile experiment of the same strain rate (Section 5.1.1). A schematic of the modified ASTM D3518-13 specimen with a stacking sequence of $[45]_8$ is provided in Figure 5.23, the 29 mm width is equal to that of the ISSS specimen. Five repetitions of the experiment were conducted. The high speed 3D DIC imaging system was used with a frame rate of 300 Hz according to the parameters provided in Table 5.17. The frame rate was selected in order to provide a minimum of 10 data points over the elastic portion of the experiment, with approximately 350 data points registered over

Figure 5.23: Modified ASTM D3518-13 specimen geometry for the assessment of in-plane shear response of the composite laminate at a nominal strain rate of 6.7 x 10^{-2} s^{-1} (Dimension in mm).

Table 5.17: Summary of the measurement methodology for Photron SA-X2 3D DIC to characterise the longitudinal in-plane shear performance of 12K 2 x 2 twill CFRP at a nominal longitudinal strain rate of 6.7 x 10^{-2} s^{-1} using a modified ASTM D3518-13 specimen.

Property		Unit
Camera	Photron SA-X2	
Lens	Titanar 75b	
Frame rate	300	Hz
Shutter speed	500	µs
Aperture	22	f/
Imaging window	1024 x 1024	$pixel^2$
Calibration plate	CP30 MV 150 x 150	
Measurement volume	165 x 165 x 155	mm^3
Facet size	15	pixels
Step size	12	pixels
Spatial resolution	2.41	mm
Strain resolution	131.59	µε
Displacement resolution	0.21	µm

the complete experimental period. The large ROI and 15 pixel facet size resulted in a spatial resolution of 2.41 mm being achieved. The spatial resolution could not be improved as the small facet size induced a measurement error of 131.59 µε which was at the limit of the tolerance set in this research. The spatial and strain resolution is consistent with that achieved for the tensile experiment conducted at the same nominal strain rate (Section 5.1.1), as observed in that experiment the spatial resolution is expected to induce a level of strain smoothing relative to the quasi-static experiments.

The experimental engineering shear stress-strain response of the modified ASTM D3518-13 specimens subjected to a nominal longitudinal strain rate of 6.7 x 10^{-2} s^{-1} is shown in Figure 5.24, the derived mechanical properties are listed in Table 5.18. As observed in the experiments conducted at a quasi-static strain rate (Figure 4.4) the loading response is bi-linear. The shear modulus is dictated by the initial shear straining of the matrix between and within fabric tows, it was calculted through use of a linear fit between 0.2 % and 0.6 % γ_{XY}. As the specimen strains, the shear strength of the matrix is yielded and cracks initiate and propagate, the coalescence of matrix cracking induces a yield point. The yield shear strength and shear strain were determined as the convergence of the specimens stiffness to within 5 % of the plastic strain hardening stiffness calculated between 8 % and 11 % γ_{XY}. The CoV

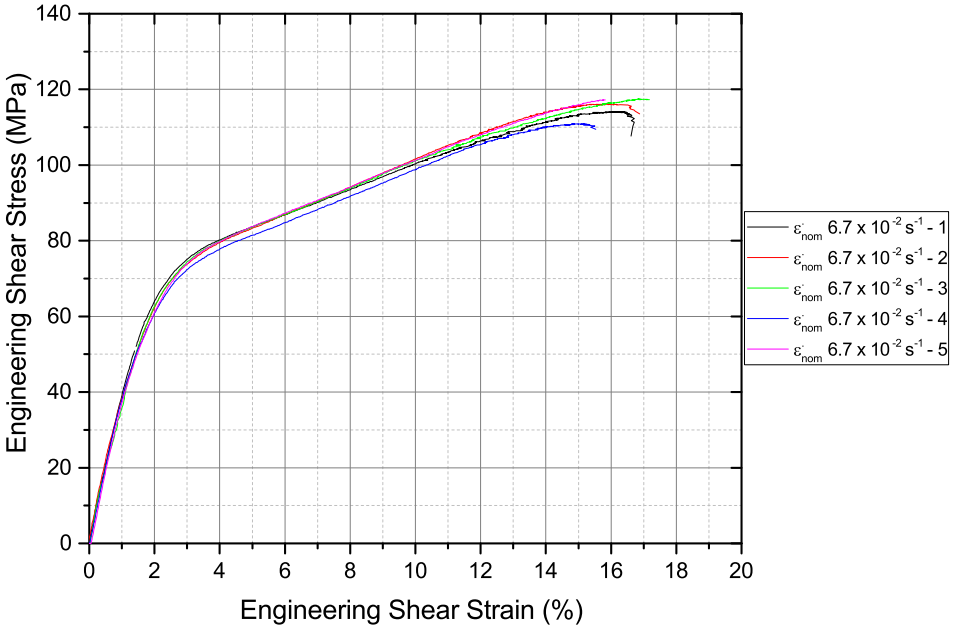

Figure 5.24: Engineering shear stress-strain response of modified ASTM D3518-13 composite specimens experimentally loaded at a nominal longitudinal strain rate of 6.7 x 10^{-2} s^{-1}.

for all of the derived mechanical properties shown in Table 5.18 is below 5 % and the order of magnitude is consistent with the variance observed at quasi-static strain rates.

Table 5.18: In-plane shear mechanical properties of modified ASTM D3518-13 composite specimens evaluated at a nominal longitudinal strain rate of 6.7 x 10^{-2} s^{-1}.

Property	Value	units	SD	CoV (%)
Shear modulus	4.04	GPa	0.091	2.26
Ultimate shear strength	115.75	MPa	2.59	2.24
Shear strength at yield	78.81	MPa	1.45	1.84
Engineering shear strain at yield	3.79	%	0.12	3.16
Ultimate shear strain	16.49	%	0.53	3.21

The longitudinal surface strains over the loading period are shown in Figure 5.25.

The reduced spatial resolution due to the large ROI with a 1 MP high speed camera has resulted in a smoothed strain field. In particular the matrix straining that was observed in Figure 4.5 (a) - (c) is no longer evident in Figure 5.25 (a) - (c). As a result of the smoothed DIC data, the capture of intra-lamaina cracks forming as a result of the shear failure of the matrix is no longer evident until they form on a macro scale as the specimen approaches failure (Figure 5.25 (g)). As the specimen strains beyond yield and deforms plastically, intra-lamina damage and tow splitting can be seen to have a large effect at the specimen free edges. These cracks propagate within the specimen leading to the shear failure of the specimen parallel to the warp and weft fibres as shown in Figure 5.26.

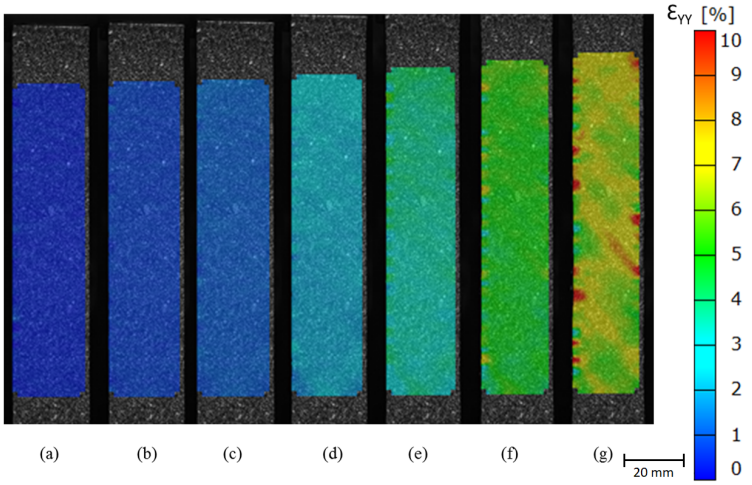

Figure 5.25: Surface strain maps overlaid on the left image of specimen #3 demonstrating the progression of longitudinal engineering strains at (a) 0.5 %, (b) 1.0 %, (c) 1.5 %, (d) 3.0 %, (e) 5.0 %, (f) 7.0 % and (g) 9.1 % ε_{YY} of a modified ASTM D3518-13 12K 2 x 2 twill CFRP specimen undergoing an in-plane shear characterisation test at nominal longitudinal strain rate of 6.7 x 10^{-2} s^{-1}.

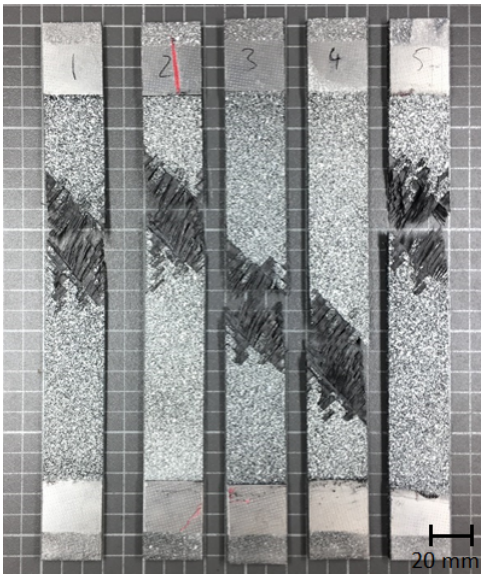

Figure 5.26: Failure locations of modified ASTM D3518-13 specimens subjected to a shear characterisation test at nominal longitudinal strain rate of 6.7 x 10^{-2} s^{-1}.

5.3.2 Nominal longitudinal strain rate of 1.0 x 10^{0} s^{-1}

In-plane shear characterisation at a nominal longitudinal strain rate of 1.0 x 10^{0} s^{-1} was conducted using the ISSS specimen developed in Chapter 4 and the VHS in closed loop to prescribe an actuator velocity of 0.07 ms^{-1}. The experiment was repeated five times. Strain was instrumented using 3D DIC with a sampling rate of 3 kHz to provide approximately 350 data points per experiment with a minimum of 10 data points over the elastic region. The DIC measurement parameters are provided in Table 5.19. Due to the low frame rate, the sensor was capable of operating at full frame, as a result a spatial resolution of 1.32 mm was achieved with a facet size of 15 pixels. Further reduction of the facet size was not possible as at large strains the deformed facets were unable to be computed, resulting in the dropping out.

Table 5.19: Summary of the measurement methodology for Photron SA-X2 3D DIC to characterise the shear performance of 12K 2 x 2 twill CFRP at a nominal longitudinal strain rate of 1.0 x 10^0 s^{-1} using ISSS specimens.

Property		Unit
Camera	Photron SA-X2	
Lens	Titanar 75b (20 mm extension tube)	
Frame rate	3	kHz
Shutter speed	331	µs
Aperture	32	f/
Imaging window	1024 x 1024	$pixel^2$
Calibration plate	CP20 55 x 44	
Measurement volume	90 x 90 x 70	mm^3
Facet size	15	pixels
Step size	13	pixels
Spatial resolution	1.32	mm
Strain resolution	86.89	µε
Displacement resolution	0.31	µm

The experimental engineering shear stress-strain response at a nominal longitudinal strain rate of 1.0 x 10^0 s^{-1} is shown in Figure 5.27, the derived mechanical properties are summarised in Table 5.20. The shear modulus was derived based on a linear fit between 0.2 % and 0.6 % γ_{XY} and found to having consistent variance with the quasi-static experiments. Post elastic shearing of the laminate the specimens follows the bi-linear response previously observed with the magnitude of the observed variance consistent with the quasi-static experiments.

Table 5.20: In-plane shear mechanical properties of ISSS specimens evaluated at a nominal longitudinal strain rate of 1.0 x 10^0 s^{-1}.

Property	Value	units	SD	CoV
Shear modulus	4.21	GPa	0.08	1.98
Shear strength at yield	92.11	MPa	1.79	2.26
Engineering shear strain at yield	4.45	%	0.01	2.81
Ultimate shear strength	124.61	MPa	2.65	2.84
Ultimate shear strain	16.49	%	0.53	3.20

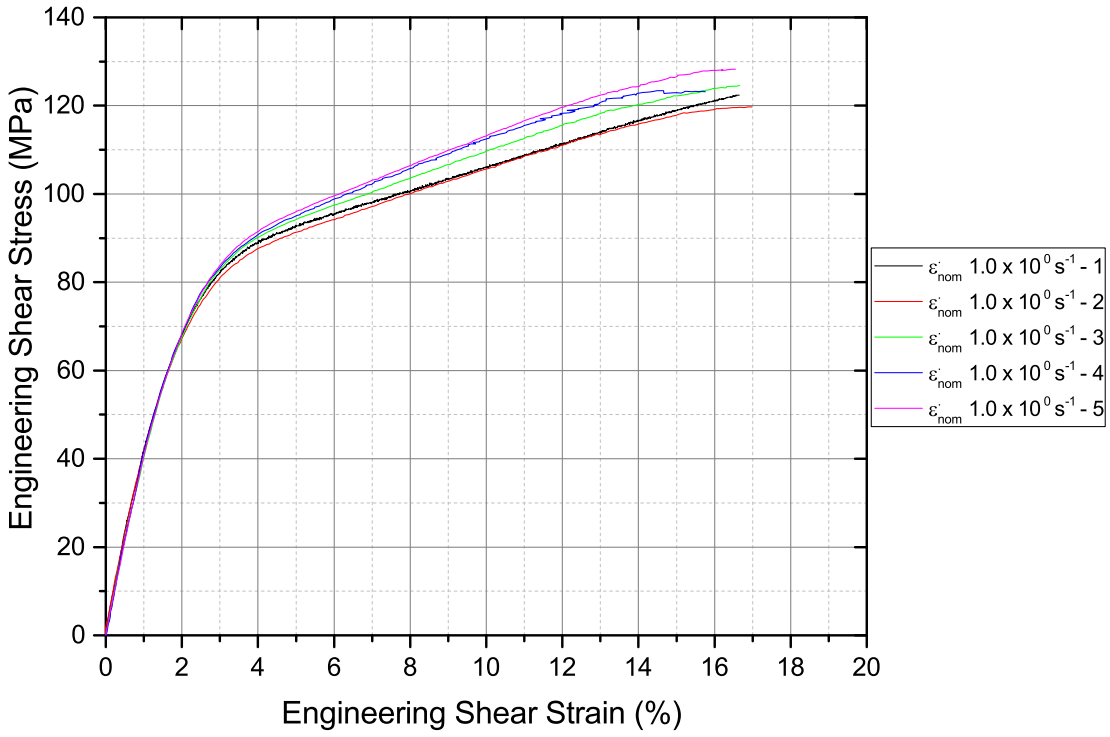

Figure 5.27: Engineering shear stress-strain response of ISSS specimens experimentally loaded at a nominal longitudinal strain rate of 1.0 x 10^0 s^{-1}.

The improved spatial resolution relative to the experiment conducted at 6.7 x 10^{-2} s^{-1} enables the author to observe matrix straining and crack initiation between the warp and weft tows cracks in Figure 5.28 (a) - (c). As the specimen yields and strain hardening occurs as a result of the rotation of the fibre, large intra-lamina cracks propagate from the free-edges of the specimen. These cracks appear to propagate through the laminate leading to ultimate fracture of the laminate parallel to the warp and weft fibres (Figure 5.29). Each of the specimens failed within the free length of the specimen with no damage observed beneath the tabs. Specimen number five failed within the vicinity of the grips, however, since the derived mechanical properties were within the 95 % confidence range of the remaining four specimens the data was included in the final dataset

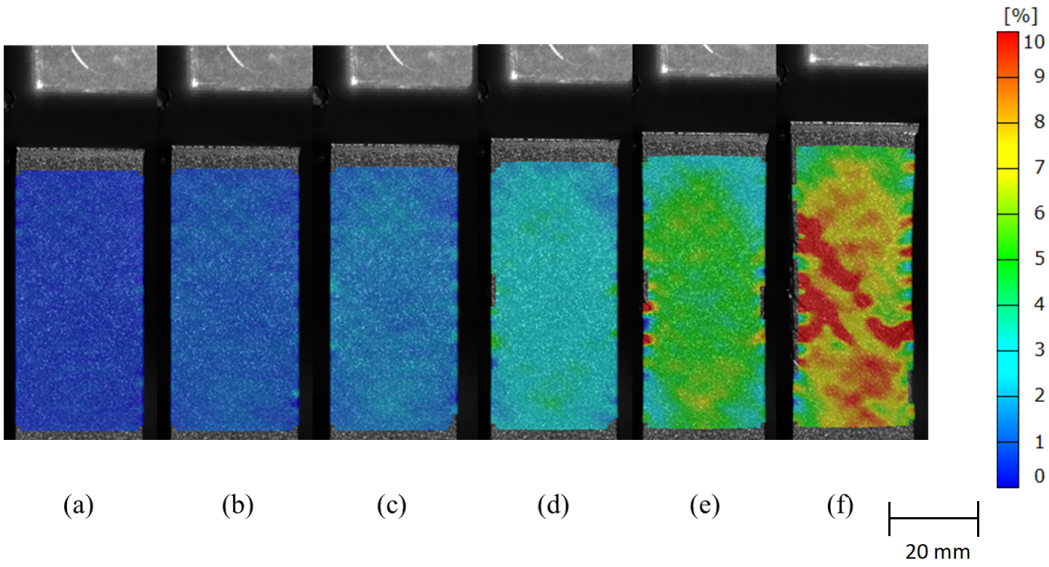

Figure 5.28: Surface strain maps overlaid on the left image of specimen #3 demonstrating the progression of longitudinal engineering strains at (a) 0.5 %, (b) 1.0 %, (c) 1.5 %, (d) 3 %, (e) 5 %, (f) 7 % and (g) 8.1 % ε_{YY} of ISSS specimen undergoing an in-plane shear characterisation test at nominal longitudinal strain rate of 1×10^{0} s^{-1}.

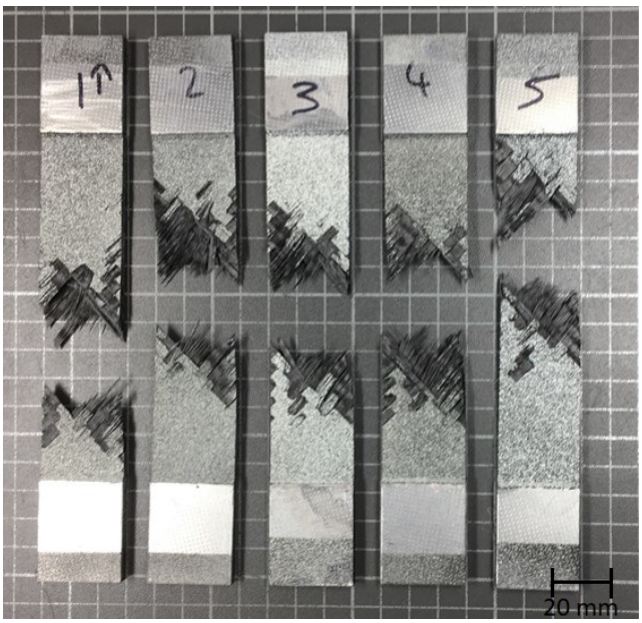

Figure 5.29: Failure locations of ISSS specimens subjected to a shear characterisation test at nominal longitudinal strain rate of 1.0×10^{0} s^{-1}.

5.3.3 Nominal longitudinal strain rate of 1.0 x 10 ^{1} s^{-1}

In-plane shear characterisation at a longitudinal nominal strain rate of 1.0 x 10^{1} s^{-1} was conducted using the ISSS specimen and the VHS in open loop to achieve a prescribed actuator velocity of 0.7 ms^{-1}. In order to provide approximately 350 data points over the full test period and a minimum of 10 data points over the elastic region 3D DIC was conducted at 30 kHz using the Photron SA-X2 cameras according to the parameters shown in Table 5.19. To achieve 30 kHz, the sensor was cropped to 896 x 496 $pixel^2$, yet the achieved spatial resolution (1.24 mm) and strain resolution (73.26 με) was consistent with that observed over the previous in-plane shear tests at 1 x 10^{0} s^{-1}.

Table 5.21: Summary of the measurement methodology for Photron SA-X2 3D DIC to characterise the shear performance of ISSS specimen at a nominal longitudinal strain rate of 1.0 x 10^{1} s^{-1}.

Property		Unit
Camera	Photron SA-X2	
Lens	Titanar 75b (20 mm extension tube)	mm
Frame rate	30	kHz
Shutter speed	40	μs
Aperture	11	f/
Imaging window	896 x 496	pixel
Calibration plate	CP20 MV 55 x 44	
Measurement volume	74.38 x 41.17 x 65	mm
Facet size	15	pixels
Step size	13	pixels
Spatial resolution	1.25	mm
Strain resolution	73.26	με
Displacement resolution	0.29	μm

The experimental engineering shear stress - strain curves for each of the five specimens is presented in Figure 5.30 and a summary of the mechanical properties is provided in Table 5.22. The material response remains bi-linear with strain hardening to fracture observed post yield. The shear modulus was determined between 0.2 % and 0.6 % γ_{XY} and found to having consistent variance with the quasi-static experiments.

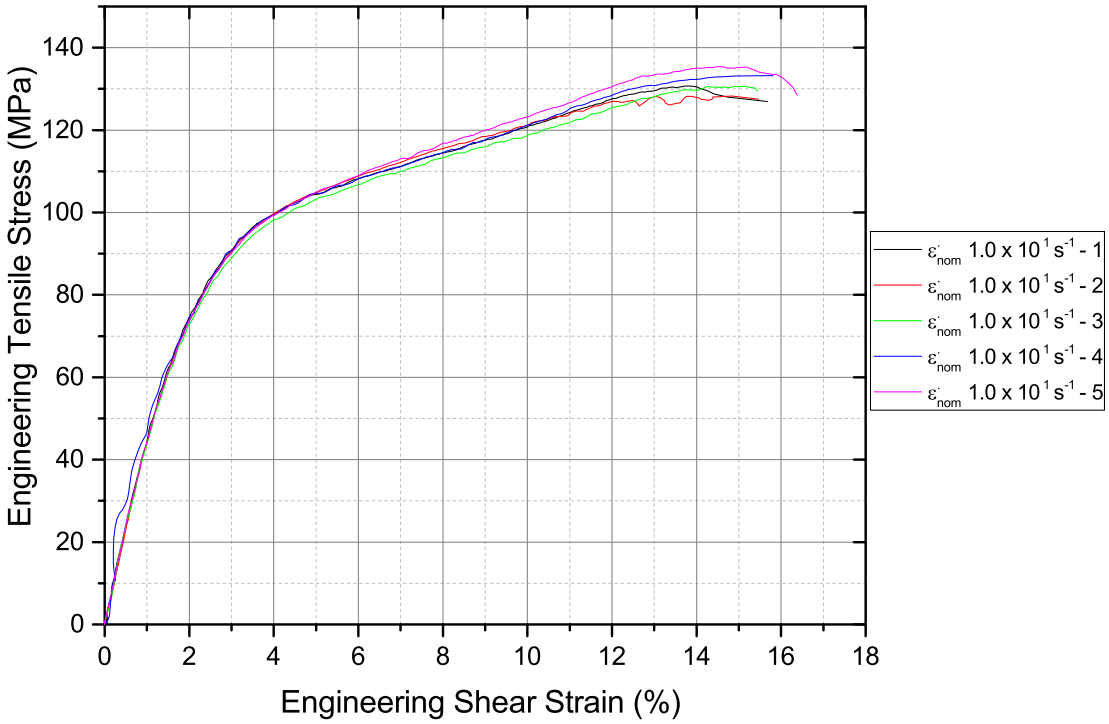

Figure 5.30: Engineering shear stress-strain response of ISSS specimens experimentally loaded at a nominal longitudinal strain rate of 1.0 x 10^{1} s^{-1}.

Table 5.22: In-plane shear mechanical properties of ISSS specimens evaluated at a nominal longitudinal strain rate of 1.0 x 10^{1} s^{-1}.

Property	Value	units	SD	CoV
Shear modulus	4.54	GPa	0.11	1.45
Shear strength at yield	92.11	MPa	1.79	0.88
Engineering shear strain at yield	4.45	%	0.01	3.05
Ultimate shear strength	133.55	MPa	2.78	2.11
Ultimate shear strain	15.62	%	0.76	4.86

Specimen #4 can be seen to experience load cell ringing at the onset of loading, this is considered to be a result of the upper fulcrum damper becoming worn during the initial experiments of this data set As shown in Section 4.2.2 the absence of damping at the fulcrum points on the impactor can induce extensive ringing in the load cell as it knocks against the slack adaptor cradle prior to engagement of the specimen. The calculated shear modulus of specimen #4 (5.49 GPa) was found to

be outside the 95 % confidence interval for the remaining experiments at this strain rate, as a result is has been excluded from the dataset and only four experiments are considered when determining the average and variance of the shear modulus at 1.0×10^{1} s^{-1}. Since the ringing is dampened prior to fracture the ultimate shear strength and shear strain is included in the statistical analysis of the respective properties.

The surface strain maps shown in Figure 5.31 demonstrates the progression of longitudinal strains over the test period. The damage sequence is consistent with that of the experiments previously shown with shear matrix cracks evident in Figure 5.31 (c) as the specimen yields. Intra-lamina cracks form as a result of the free edge stresses within the pure shear region which propagate and cause global fracture parallel to the warp and weft fibres. The fracture locations shown in Figure 5.32 demonstrates that all specimens fractured central to their respective free-lengths.

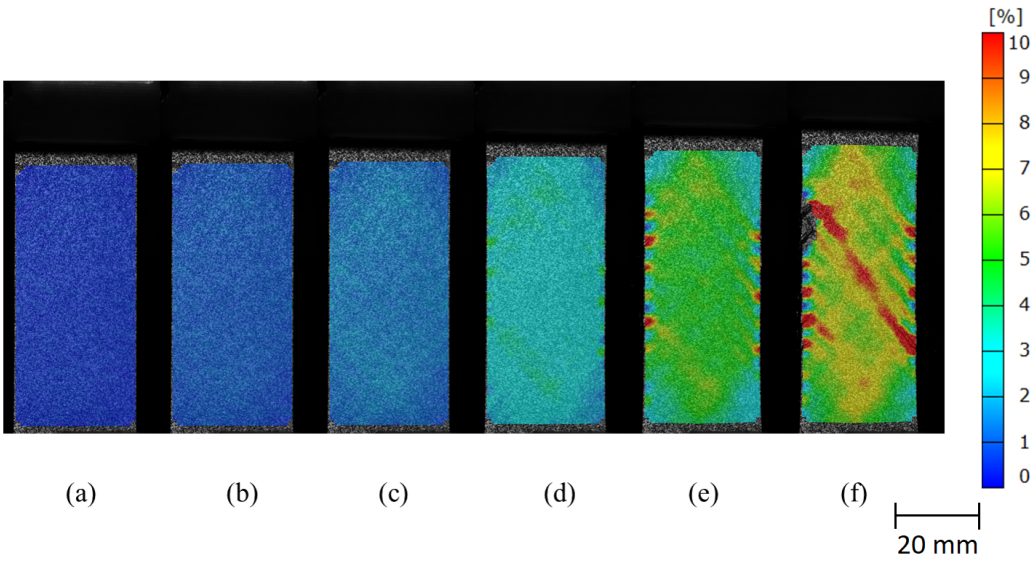

Figure 5.31: Surface strain maps overlaid on the left specimen image demonstrating the progression of longitudinal engineering strains at (a) 0.5 %, (b) 1.0 %, (c) 1.5 %, (d) 4.0 %, (e) 6.0 % and (f) 7.3 % ε_{YY} of an ISSS specimen evaluated at longitudinal nominal strain rate of 1.0×10^{1} s^{-1}.

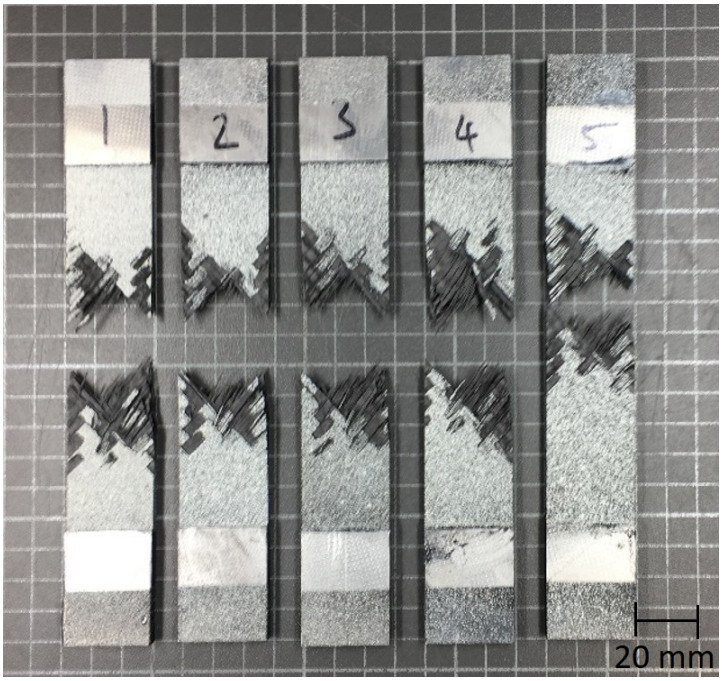

Figure 5.32: Failure locations of ISSS specimens subjected to a shear characterisation test at nominal longitudinal strain rate of 1.0×10^{1} s^{-1}.

5.3.4 Nominal longitudinal strain rate of 5.0×10^{1} s^{-1}

In-plane shear experiments at a nominal longitudinal strain rate of 5.0×10^{1} s^{-1} was conducted on five ISSS specimens using the VHS in open loop to achieve an actuator velocity of 2.5 ms^{-1}. The 3D DIC characteristics used in the experiments are provided in Table 5.19. Approximately 115 data points were collected over the experimental period with 6 defining the elastic region, this was achieved by increasing the frame rate of the Photron SA-X2 cameras to 54 kHz, this required the sensor to be cropped to 304 × 768 $pixel^2$. In order to maintain the full field measurement, the spatial resolution was reduced to 1.61 mm as a result of the facet size being reduced to 15 pixels. The spatial resolution could not be improved further since the 15 pixel facet induced an average strain resolution of 146.17 με, therefore a reduced facet size exceeded the permitted strain resolution in this study.

Table 5.23: Summary of the measurement methodology for Photron SA-X2 3D DIC to characterise the shear performance of ISSS specimen at a nominal longitudinal strain rate of 5.0 x 10^1 s^{-1}.

Property		Unit
Camera	Photron SA-X2	
Lens	Titanar 75b (10 mm extension tube)	mm
Frame rate	54	kHz
Shutter speed	52.5	µs
Aperture	5.6	f/
Imaging window	304 x 768	$pixel^2$
Calibration plate	CP20 MV 92 x 72	
Measurement volume	82.5 x 32.7x 90	mm^3
Facet size	15	pixels
Step size	12	pixels
Spatial resolution	1.61	mm
Strain resolution	146.17	µε
Displacement resolution	0.29	µm

The experimental engineering shear stress-strain response of each of the five ISSS specimens loaded at a nominal longitudinal strain rate of 5.0 x 10^1 s^{-1} are shown in Figure 5.33. The derived mechanical properties are shown in Table 5.24. At this strain rate the raw data shown in Figure 5.33 (a) becomes subject to load cell ringing, this is considered to be due to the loading rate exciting the piezoelectric load cell at close to the natural frequency of the slack adaptor and actuator piston assembly. As a result a 5^{th} order polynomial was fitted through the data (Figure 5.33 (b)), the polynomial provides a good fit to the experimental data. The raw data was used to measure the shear modulus between 0.2 % and 0.6 % γ_{XY}, along with the ultimate strain measurement. In comparison the ultimate shear strength and yield phenomenon was calculated based on the polynomial fit of the data. The determination of the yield phenomenon based on the fitted data has significantly reduce the observed CoV.

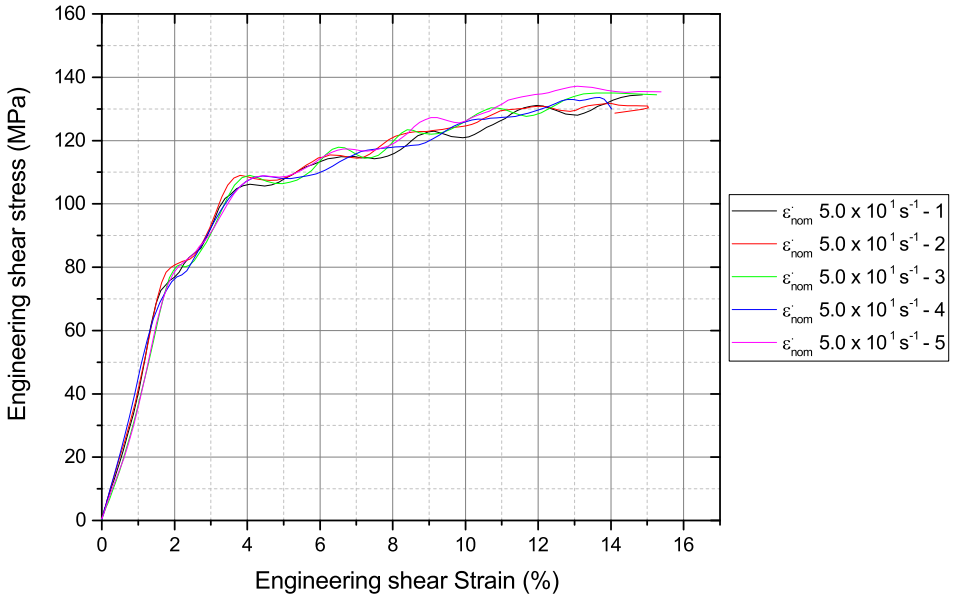

(a)

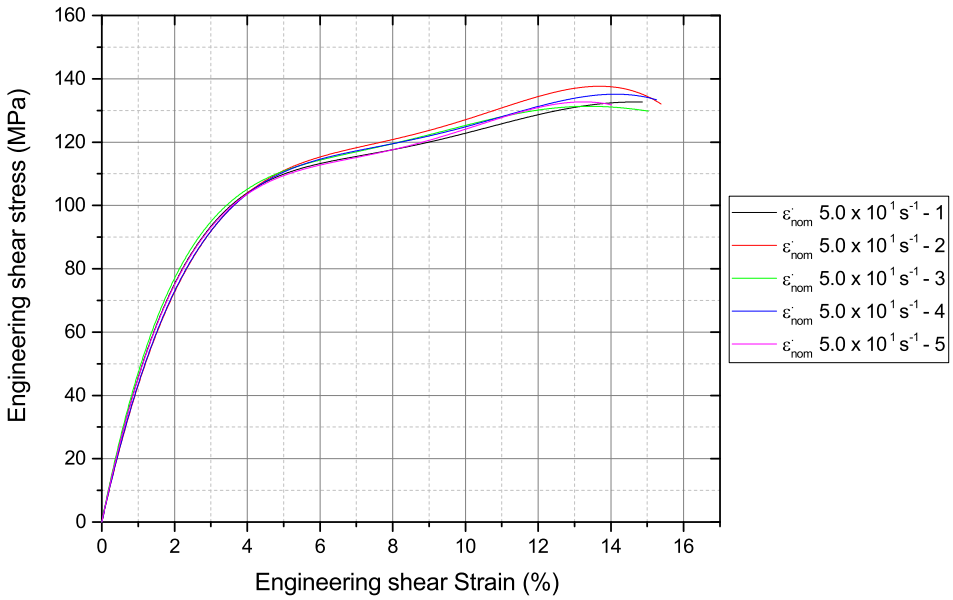

(b)

Figure 5.33: Engineering shear stress-strain response of ISSS specimens experimentally loaded at a nominal longitudinal strain rate of 5.0 x 10^{1} s^{-1}, (a) raw data, (b) 5^{th} order polynomial fitting.

Table 5.24: In-plane shear mechanical properties of ISSS specimens evaluated at a nominal longitudinal strain rate of 5.0 x 10^1 s^{-1}.

Property	Value (SD)	units	SD	CoV (%)
Shear modulus	4.69	GPa	0.12	2.93
Shear strength at yield	114.06	MPa	0.91	0.80
Engineering shear strain at yield	5.90	%	0.065	1.10
Ultimate shear strength	136.29	MPa	3.78	4.39
Ultimate shear strain	15.48	%	0.68	2.77

Figure 5.34 shows the progression of longitudinal surface strains. Cropping of the image sensor in order to achieve the desired frame rate has resulted in a reduction of the spatial resolution. This is evident due to the inability to detect the matrix cracking as the specimen approaches yield between Figure 5.34 (a) - (c). As the specimen strains plastically, damage appears to coalesce as a result of intra-lamina cracks forming at the free edges of the specimen. The ultimate fracture of the specimen was observed to occur within the centre of the free length (Figure 5.35) in 80 % of specimen investigated. Specimen #2 was observed to fail close to the upper jaw, however, since the derived mechanical properties were observed to be within the 95 % confidence interval of the remaining specimens the experiment was considered valid and the results included in the statistical analysis.

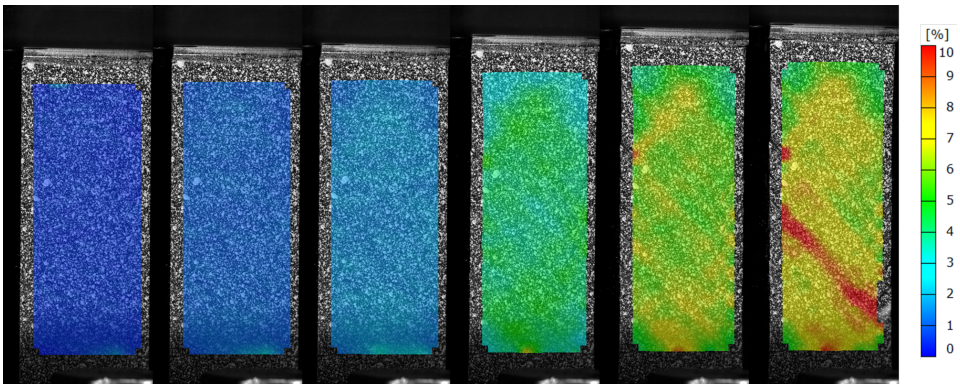

Figure 5.34: Surface strain maps overlaid on the left image of specimen #4 demonstrating the progression of longitudinal engineering strains at (a) 0.5 %, (b) 1.0 %, (c) 1.5 %, (d) 4.0 %, (e) 6.0 % and (f) 7.3 % ε_{YY} of an ISSS specimen evaluated at longitudinal nominal strain rate of 5.0 x 10^1 s^{-1}.

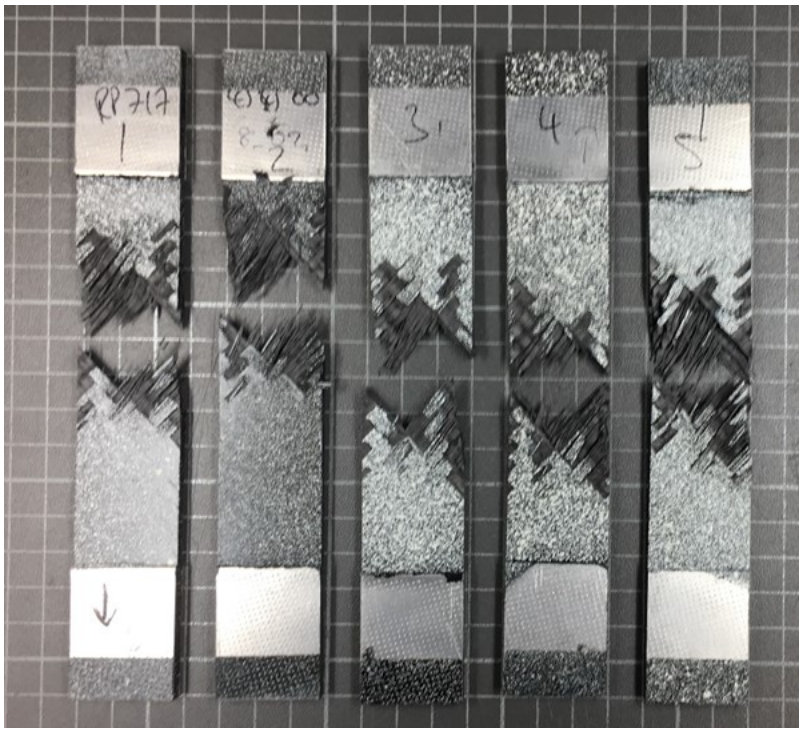

Figure 5.35: Failure locations of ISSS specimens subjected to a shear characterisation test at nominal longitudinal strain rate of 5.0× 10^1 s^{-1}.

5.3.5 Nominal longitudinal strain rate of 1.0 × 10^2 s^{-1}

In-plane shear characterisation at a nominal strain rate of 1.0 x 10^2 s^{-1} was conducted using the ISSS specimen and the VHS in open loop to achieve a prescribed actuator velocity of 7 ms^{-1}. The 3D DIC characteristics used in the experiments are provided in Table 5.25. Approximately 80 data points were collected over the experimental period with five points defining the elastic region, this was achieved by increasing the frame rate of the Photron SA-X2 cameras to 90 kHz which required the sensor to be cropped to 240 x 512 $pixel^2$. The resultant spatial resolution was consistent with the 5.0 x 10^1 s^{-1}experiment (1.59 mm), this was achieved through slightly reducing the RoI, and reducing the facet size to 13 pixels. The spatial resolution could not be improved further due to achieved strain resolution at 13 pixels.

Table 5.25: Summary of the measurement methodology for Photron SA-X2 3D DIC to characterise the shear performance of ISSS specimen at a nominal longitudinal strain rate of 1.0 x 10^2 s^{-1}.

Property		Unit
Camera	Photron SA-X2	
Lens	Titanar 75b (10 mm extension tube)	
Frame rate	90	kHz
Shutter speed	9.8	µs
Aperture	8	f/
Imaging window	240 x 512	$pixel^2$
Calibration plate	CP20 MV 92 x 72	
Measurement volume	29.29 x 62.5 x 70	mm^3
Facet size	13	pixels
Step size	9	pixels
Spatial resolution	1.59	mm
Strain resolution	158.75	µε
Displacement resolution	0.31	µm

The experimental engineering shear stress - shear strain response is shown in Figure 5.36. The raw data (Figure 5.36 (a)) shows clear signs of load cell inertial ringing as described in the experiment conducted at a nominal strain rate of 5.0 x 10^1 s^{-1}, as a result a 5^{th} order polynomial fitting is provided to the data. The shear modulus was determined between 0.2 % and 0.6 % γ_{XY} of the raw data, along with the ultimate strain measurement. In comparison the ultimate shear strength and yield phenomenon was calculated based on the polynomial fit of the data. It is evident that during the elastic loading of specimen #5 that damage occurs prematurely as the stiffness is significantly reduced as it strains beyond 1.46 %. This premature stiffness loss as well as the grip failure location of both specimen 4 and 5 (Figure 5.38) results in their omission from the statistical analysis.

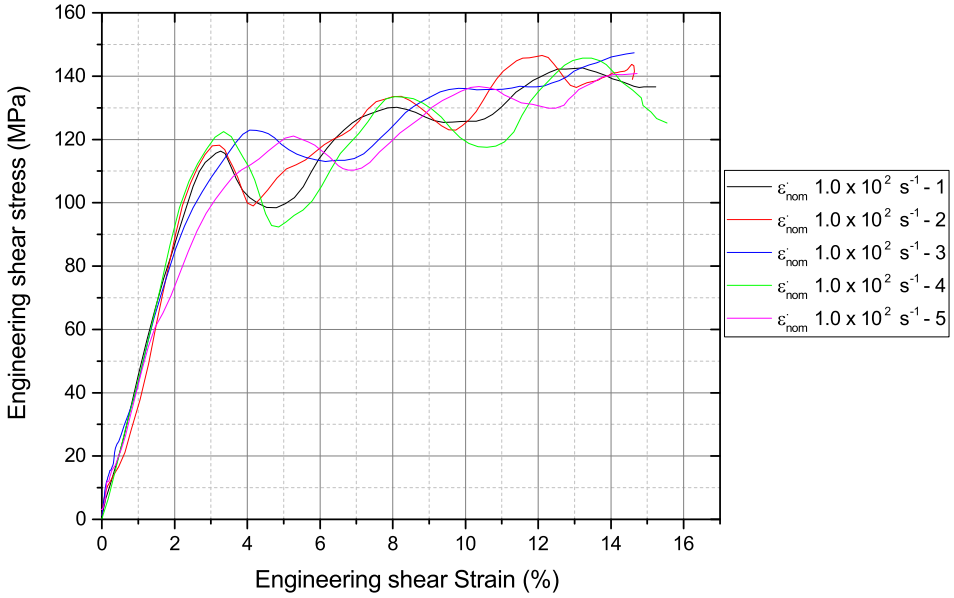

(a)

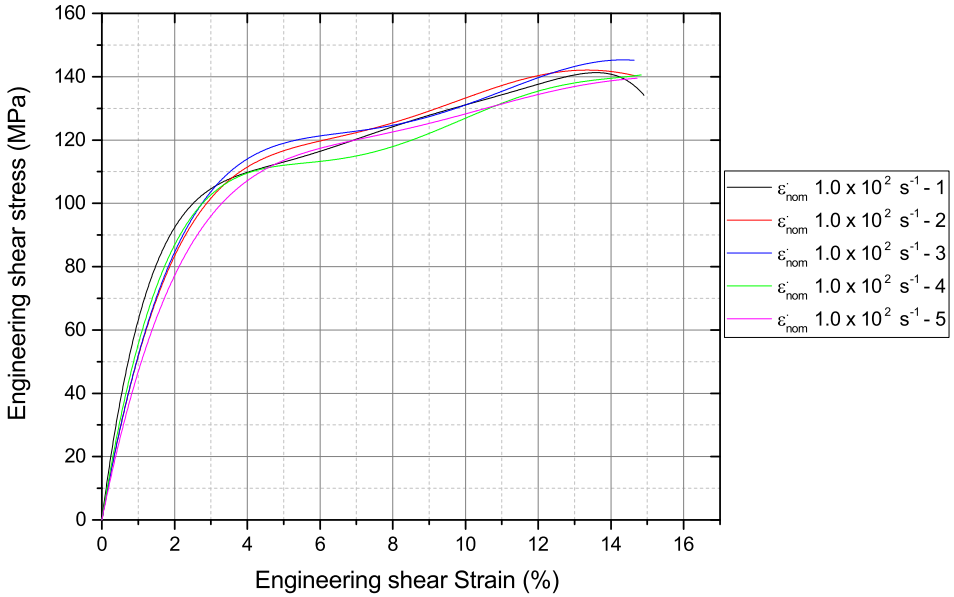

(b)

Figure 5.36: Engineering shear stress-strain response of ISSS specimens experimentally loaded at a nominal longitudinal strain rate of 1.0 x 10^2 s^{-1}, (a) raw data, (b) 5^{th} order polynomial fitting.

Table 5.26: In-plane shear mechanical properties of ISSS specimens evaluated at a nominal longitudinal strain rate of 1.0 x 10^2 s^{-1}.

Property	Value	units	SD	CoV
Shear modulus	5.15	GPa	0.12	2.39
Shear strength at yield	116.79	MPa	1.41	1.21
Engineering shear strain at yield	6.39	%	0.26	4.05
Ultimate shear strength	142.92	MPa	1.95	1.37
Ultimate shear strain	15.08	%	0.43	2.83

The development of longitudinal surface strains within the specimen over the duration of the experiment is shown in Figure 5.37. In comparison to the previous strain maps shown throughout this Chapter, Figure 5.37 has experienced a greater loss of facets as the specimen approaches failure. This is a result of the distortion of the grey scale being very large due to localised cracking and damage propagation, thus the DIC software is unable to match the facet in sequential images. The small facet size was required to record a spatial resolution that was similar to that used in all the previous experiments with the highly cropped sensor in order to achieve the desired temporal resolution. The elastic damage recorded in Figure 5.37 (a) - (c) shows uniform straining of the specimen, however, as the specimen yields and begins failing in a plastic manner the strain map becomes more heterogeneous. Shear cones develop at the end of the free lengths as cracks begin to propagate between tows as the strain increases and the fabric realigns itself. Ultimate fracture occurs in the form of a shear fracture parallel to the warp and weft tows as shown in Figure 5.38. As previously discussed three specimens failed towards the centre of the free length, whilst specimens 4 and 5 failed within the lower jaw.

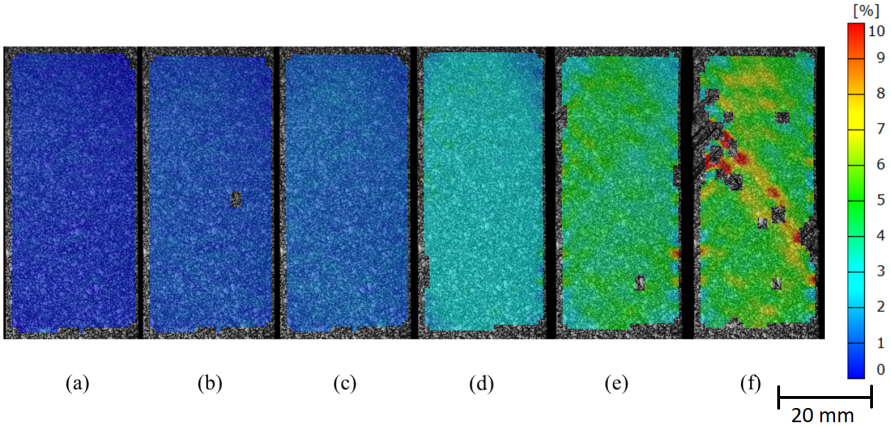

Figure 5.37: Surface strain maps overlaid on the left image of specimen #3, demonstrating the progression of longitudinal engineering strains at (a) 0.5 %, (b) 1.0 %, (c) 1.5 %, (d) 4.0 %, (e) 6.0 % and (f) 7.2 % ε_{YY} of an ISSS specimen evaluated at a nominal longitudinal strain rate of 1.0 x 10^2 s^{-1}.

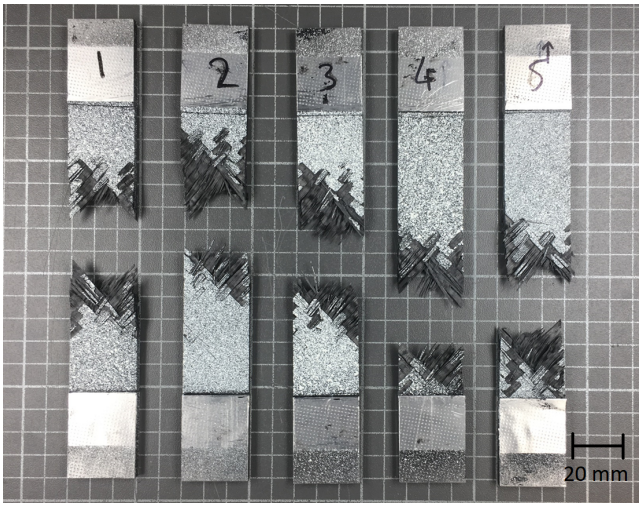

Figure 5.38: Failure locations of ISSS specimens subjected to a shear characterisation test at nominal longitudinal strain rate of 1.0 x 10^2 s^{-1}.

5.3.6 Experimental strain rates

The experiments conducted in Sections 5.3.1 to 5.3.5 have been presented based upon their nominal longitudinal strain rates calculated according to the actuator velocity and the free length of the specimens. However, as previously shown for the tensile response (Section 5.1.6), the experimentally derived strain rate is not expected to be linear over the test period as a result of the inertial behaviour of the material and the load path. In order to assess the stability of the strain rate in each experiment, the experimental longitudinal strain rate was calculated as the differential of longitudinal strain measured directly on the specimen surface. Figure 5.39 compares the longitudinal experimental strain rates for each individual in-plane shear experiment conducted in Sections 5.3.1 to 5.3.5 as a function of global shear strain.

The bi-linear response of the laminate enables a similar approach for the determination of the average experimental strain rate as the metallic high strain rate standard ISO 2603-2:2011 to be employed. The metallic standard dictates that the average experimental strain rate of each experiment is calucalted over the plastic straining period of the test between yield and peak force. As the in-plane shear specimens do not exhibit the large necking failure observed in metallic specimens, terminating the strain rate measurement at peak force was unsuitable due localised crack growth distorting the measurement as shown in Figure 5.39. As a result the average in-plane shear longitudinal experimental strain rate ($\dot{\varepsilon}_{exp}\left(SHEAR\right)$) was determined for each test according to Equation 5.2. The strain rate is determined between the strain at yield (γ_{yield}) and 11 % shear strain ($\gamma_{0.11}$). Selecting a constant strain limit as the upper range of the strain rate measurement enabled the author to ensure that no localised crack growth distorted derived average.

$$\dot{\varepsilon}_{exp}\left(SHEAR\right) = \digamma\left\{\dot{\varepsilon}\left(\gamma_{yield}\right)...\dot{\varepsilon}\left(\gamma_{0.06}\right)\right\} \tag{5.2}$$

A comparison of the nominal and average experimental strain rates calculated according to Equation 5.2 is provided in Table 5.27 along with the minimum and maximum experimental strain rates observed over this measurement period. It is clear that unlike the tensile specimens (which experienced significant variation between the nominal and experimental strain rates as a result of the decay induced by the high capacity specimens) when the experimental strain rate is determined during a period strain hardening the difference between experimental and nominal longitudinal strain rate for the in-plane shear experiments was less.

The stability of the experimental strain rate measured between γ_{yield} and $\gamma_{0.11}$ was

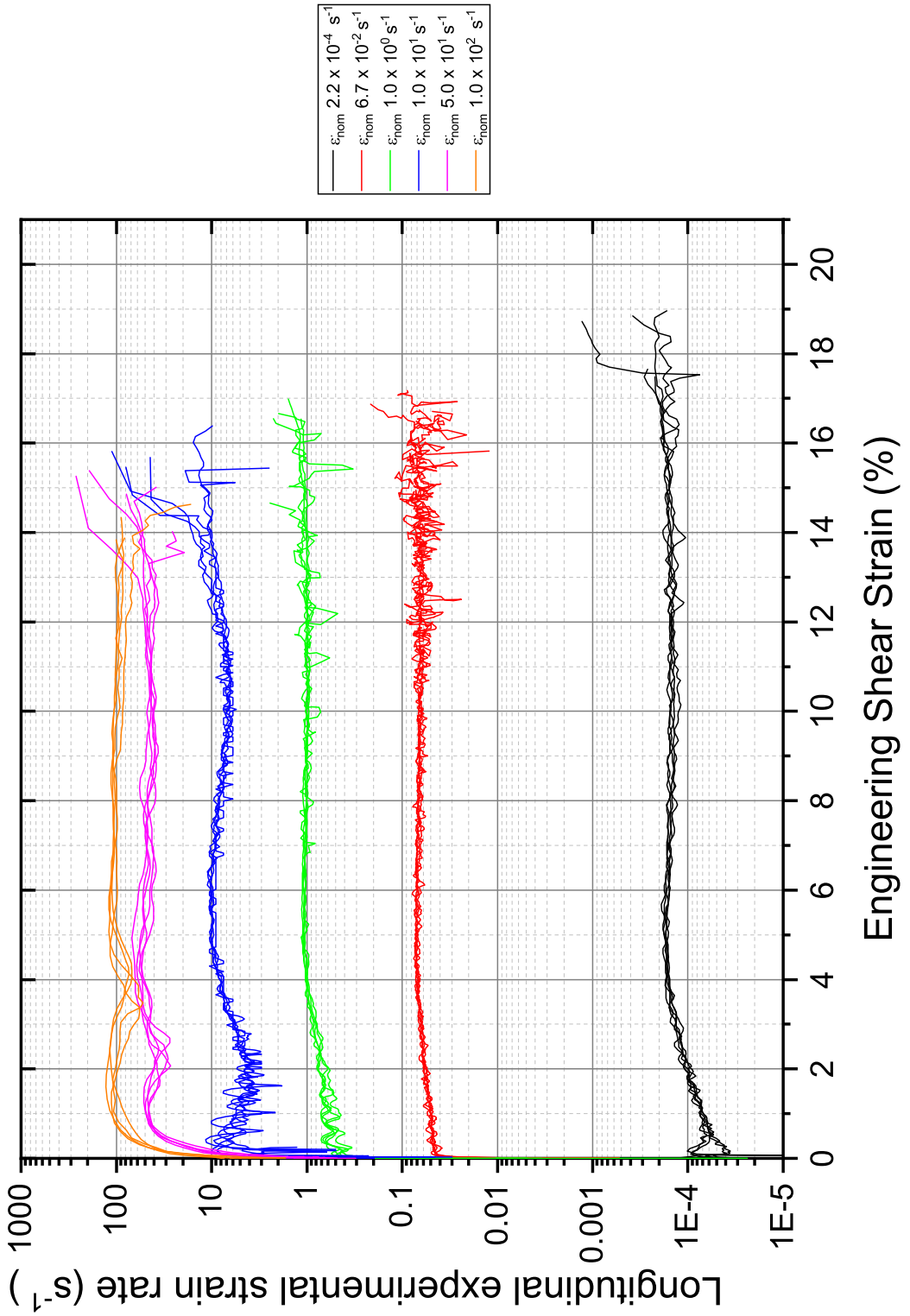

Figure 5.39: Summary of the experimental longitudinal strain rates as a function of the engineering shear strain at nominal longitudinal strain rate increases between 2.2 × 10^{-4} s^{-1} to 1.0 × 10^{2} s^{-1}.

Table 5.27: Comparison of the mean average experimental strain rates ($\dot{\varepsilon}_{exp}$) observed when characterising the in-plane shear response of the 12K 2 x 2 twill CFRP between nominal longitudinal strain rates of 2.2 x 10^{-4} s^{-1} to 1.0 x 10^{2} s^{-1} alongside the mean maximum ($\dot{\varepsilon}_{max}$) and minimum ($\dot{\varepsilon}_{min}$) experimental strain rates.

Nominal longitudinal strain rate (s^{-1})	$\dot{\varepsilon}_{exp}$ (s^{-1})	$\dot{\varepsilon}_{max}$ (s^{-1})	$\dot{\varepsilon}_{min}$ (s^{-1})
2.2 x 10^{-4}	1.5 x 10^{-4}	1.8 x 10^{-4}	1.3 x 10^{-4}
6.7 x 10^{-2}	6.7 x 10^{-2}	7.5 x 10^{-2}	5.5 x 10^{-2}
1.0 x 10^{0}	1.0 x 10^{0}	1.1 x 10^{0}	7.7 x 10^{-1}
1.0 x 10^{1}	8.2 x 10^{0}	1.1 x 10^{1}	5.9 x 10^{0}
5.0 x 10^{1}	4.8 x 10^{1}	6.1 x 10^{1}	3.8 x 10^{1}
1.0 x 10^{2}	1.0 x 10^{2}	1.2 x 10^{2}	7.8 x 10^{1}

found to be within ± 30 %[1] of the average experimental strain rate for all of the nominal strain rates except for the nominal 1.0 x 10^{1} s^{-1} experiment. This was the first experiment that required the VHS to be operated in high rate open loop control. As a result the + 31.96 %/- 27.68 % variance introduced is due to the retardation of the actuator as a result of the inertial load of the specimen. As the velocity of the experiment was increased the kinetic energy of the LMD was capable of overcoming the inertial load of the specimen the variance was reduced such that at a nominal strain rate of 1.0 x 10^{2} s^{-1} the variation of the mean was found to be + 15.31 %/- 24.44 %. The stability of the experimental strain rate prior to yield was affected by the inertial effect of the specimen in all experiments that required the use of open loop control as shown in Figure 5.39. The largest reduction was observed during the nominal 1.0 x 10^{1} s^{-1} test, the experimental strain rate reduced by 63.6 % on average, in contrast during the 1.0 x 10^{2} s^{-1} experiment this reduction was reduced to 46.5 % on average respectively. Therefore increasing the kinetic energy of the test is reducing the effect of the specimens inertial load and stabilising the strain rate further across the entire experiment and not just during plastic strain hardening regime.

In conclusion the determination of the experimental strain rate during the strain hardening region of the test yielded an average strain rate similar to that prescribed nominally. However, since the experimental strain rate was shown to be 18.3 % less than that nominally prescribed during the 1.0 x 10^{1} s^{-1} experiment, from hence-

[1]Servo-hydraulic metallic high strain rate characterisation standard ISO 26203-2:2011 dictates a stable experiment as the experimental strain rate range being within ± 30 % of the mean strain rate between yield and peak force, for further information refer to Section 5.1.6.

forth the experimental strain rates will be quoted when discussing the strain rate sensitivity of the in-plane shear properties.

5.4 Summary of the strain rate sensitivity of the in-plane shear response to intermediate strain rates.

Table 5.28 provides a summary of the effect of intermediate strain rates on the in-plane shear mechanical properties for the 12K 2 × 2 twill CFRP laminate. It is evident that the in-plane shear behaviour of the laminate is sensitive to strain rate through the intermediate strain rate regime. The effect of increasing strain rate has a positive influence on the modulus, and shear strength, both at yield and fracture. The following sections will demonstrate the effect of strain rate on the modulus, shear strength and shear strain at yield, ultimate shear strength and ultimate shear strain in more detail.

Table 5.28: Summary of the average in-plane shear mechanical properties of the 12K 2 × 2 twill CFRP experimentally investigated at discrete nominal strain rates between 2.2×10^{-4} s^{-1} and 1.0×10^{2} s^{-1}. Variance is provided in brackets.

Nominal strain rate	s^{-1}	2.2×10^{-4}	6.7×10^{-2}	1.0×10^{0}	1.0×10^{1}	5.0×10^{1}	1.0×10^{2}	F-test p-value
Experimental strain rate	s^{-1}	1.5×10^{-4}	6.7×10^{-2}	1.0×10^{0}	8.2×10^{0}	4.8×10^{1}	1.0×10^{2}	
Shear Modulus	GPa	3.74 (0.069)	4.04 (0.09)	4.21 (0.08)	4.39 (0.06)	4.69 (0.13)	5.15 (0.12)	< 0.001
Shear strength at yield	MPa	71.01 (1.63)	78.81 (1.44)	93.21 (2.11)	105.26 (0.93)	114.06 (0.91)	116.79 (1.41)	< 0.001
Shear strain at yield	%	3.95 (0.18)	3.79 (0.12)	4.73 (0.13)	5.24 (0.16)	5.90 (0.065)	6.39 (0.26)	< 0.001
Ultimate Shear Strength	MPa	110.94 (1.07)	115.75 (3.79)	124.02 (3.52)	131.72 (2.78)	136.29 (3.78)	142.92 (1.95)	< 0.001
Ultimate Engineering Shear Strain	%	18.58 (0.75)	16.11 (0.39)	16.49 (0.53)	15.62 (0.76)	15.48 (0.68)	15.08 (0.43)	< 0.001

5.4.1 Effect of longitudinal strain rate on the in-plane shear modulus

The effect of increasing strain rate on the shear modulus is shown in Figure 5.40. The y error bars demonstrate the 95 % confidence interval range for the measured shear modulus, whilst the x error bars highlight the 95 % confidence interval for the experimental strain rate. Statistical analysis of the average and variance of each of the results recorded at increasing strain rate was reviewed using an ANOVA *f-test*. The returned *p-value* of <0.001 demonstrates that at least two of the means are different. The results of the Tukey's HSD test on the shear modulus is shown in Table 5.29 and demonstrates that modulus recorded shows an increasing trend with strain rate although the experiments conducted between 6.7×10^{-2} s^{-1} and 1.0×10^{0} s^{-1}; nor, 1.0×10^{0} s^{-1} and 8.2×10^{0} s^{-1} could not be identified as statistically different despite the discrete increases in strain rate.

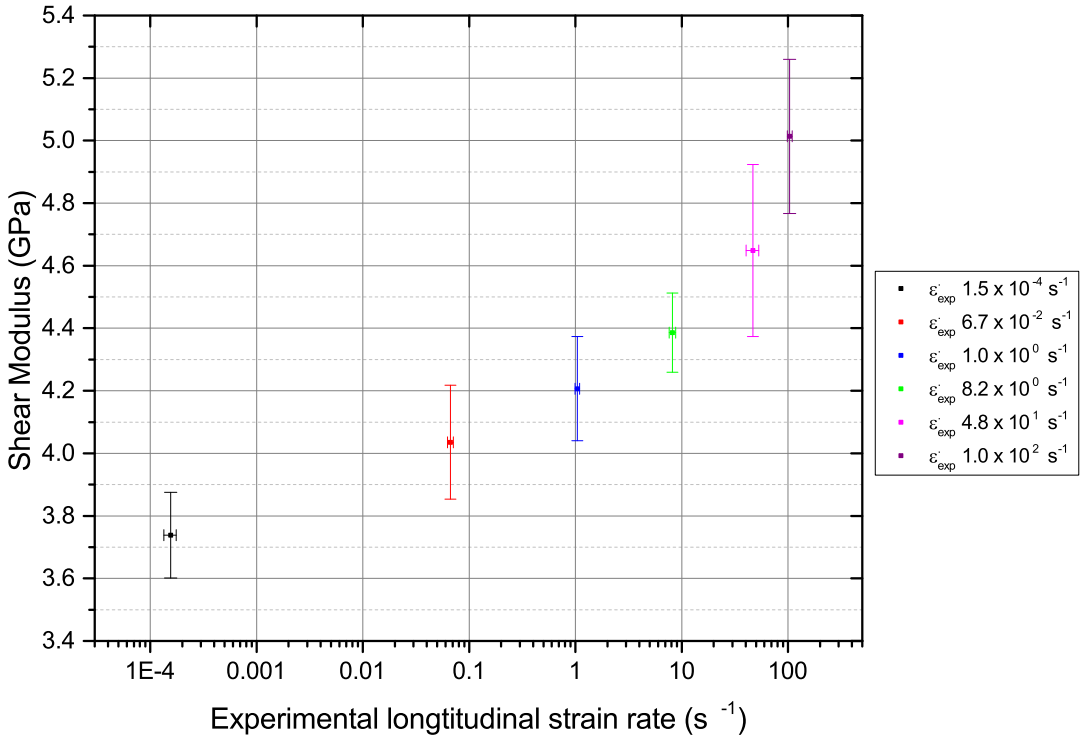

Figure 5.40: Experimental engineering shear modulus determined between 0.2 % and 0.6 % shear strain against experimental longitudinal strain rate. Error bars depict the 95 % confidence interval for shear modulus (y) and longitudinal strain rate (x).

Table 5.29: Results of Tukey's HSD statistical difference analysis on the shear modulus recorded at different intermediate strain rates, a different letter indicates a statistically significant difference.

Strain rate (s^{-1})	Statistical difference				
1.5×10^{-4}	A				
6.7×10^{-2}		B			
1.0×10^{0}		B	C		
8.2×10^{0}			C		
4.8×10^{1}				D	
1.0×10^{2}					E

5.4.2 Effect of longitudinal strain rate on yield shear strength and shear strain

In Table 5.28 the yield behaviour of the laminate was observed to change with increasing strain rate. The onset of strain hardening plastic damage was shown to be delayed to higher levels of shear strain and shear strength with increasing strain rate as shown in Figure 5.41 and Figure 5.42 respectively. The y error bars demonstrate the 95 % confidence interval range for the measured shear strength and shear strain respectively, whilst the x error bars highlight the 95 % confidence interval for the experimental strain rate. Statistical analysis of the average and variance of each of the results recorded at increasing strain rate was reviewed using an ANOVA *f-test*, and a Tukey's HSD test, the results are shown in Table 5.30 and Table 5.31.

The shear strain at yield was shown to increase with increasing strain rate between 6.7×10^{-2} s^{-1} and 4.8×10^{1} s^{-1}, however, the difference between 1.5×10^{-4} s^{-1} and 6.7×10^{-2} s^{-1}; as well as 4.8×10^{1} s^{-1} and 1.0×10^{2} s^{-1} was found to not be significant. In comparison the shear strength at yield was observed to increase with increasing strain rate, with each magnitude experimentally investigated returning a statistically independent value.

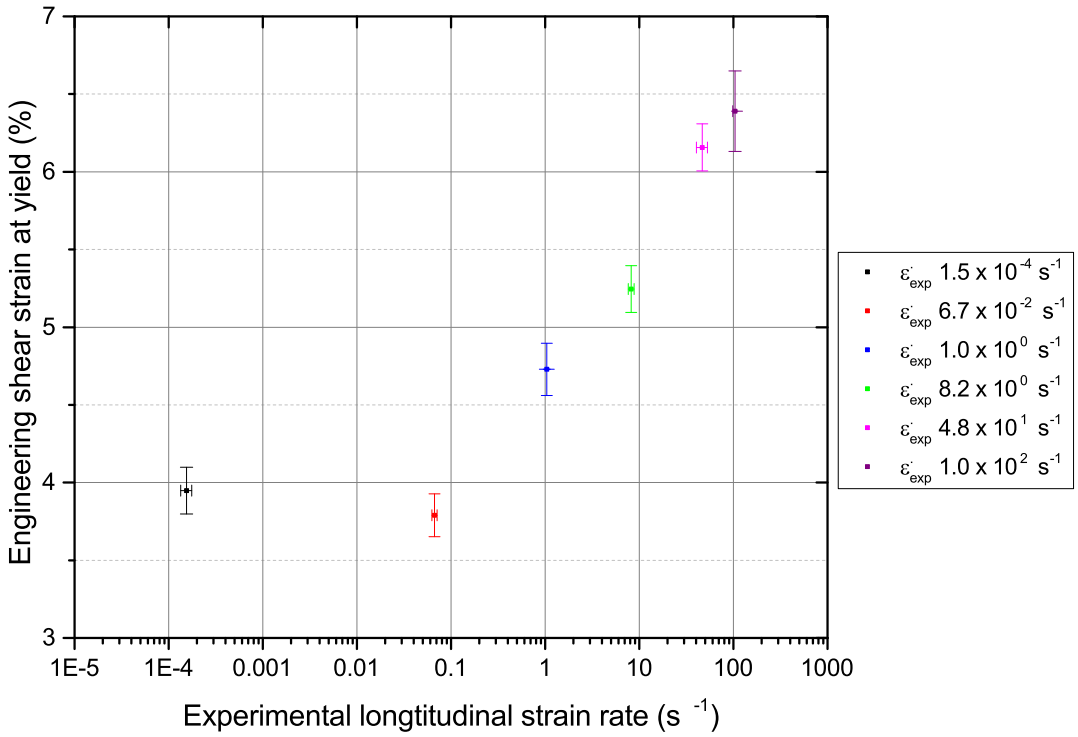

Figure 5.41: Average experimental engineering shear strain at yield plotted at magnitude increases in longitudinal engineering strain rate. Error bars depict the 95 % confidence interval for shear strain (y) and longitudinal strain rate (x).

Table 5.30: Results of Tukey's HSD statistical difference analysis on the engineering shear strain at yield recorded at different intermediate strain rates, a different letter indicates a statistically significant difference.

Strain rate (s^{-1})	Statistical difference			
1.5×10^{-4}	A			
6.7×10^{-2}	A			
1.0×10^{0}		B		
8.2×10^{0}			C	
4.8×10^{1}				D
1.0×10^{2}				D

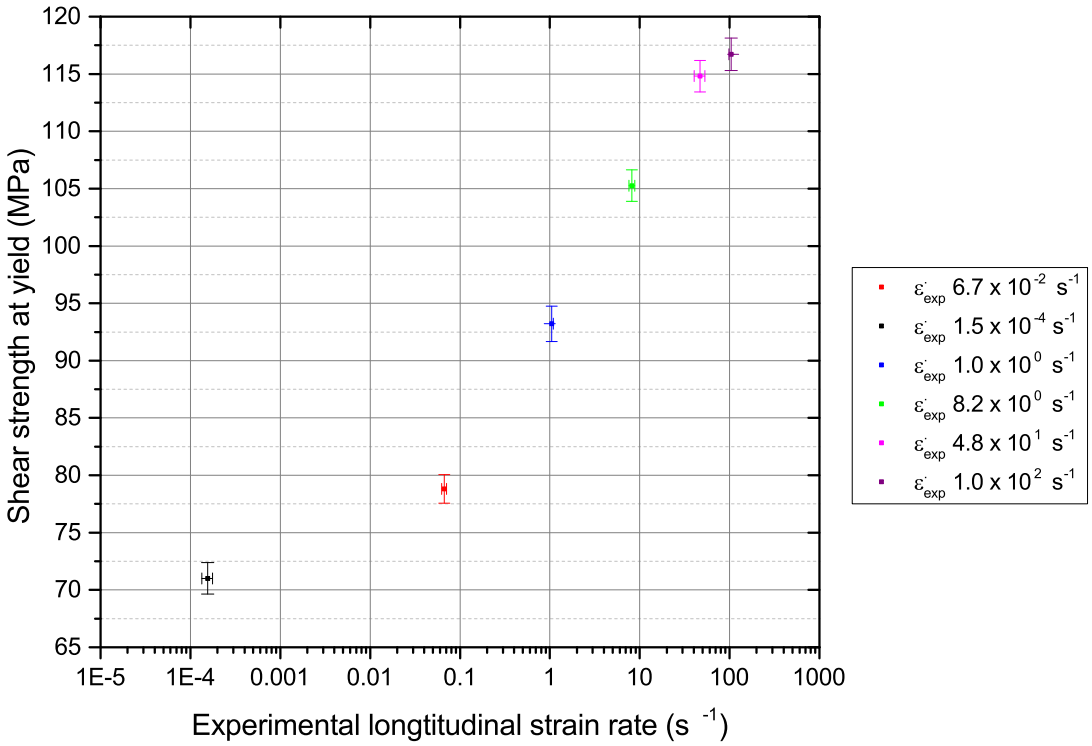

Figure 5.42: Average experimental engineering shear strength at yield plotted at magnitude increases in longitudinal engineering strain rate. Error bars depict the 95 % confidence interval for shear strength (y) and longitudinal strain rate (x).

Table 5.31: Results of Tukey's HSD statistical difference analysis on the shear strength at yield recorded at different intermediate strain rates, a different letter indicates a statistically significant difference.

Strain rate (s^{-1})	Statistical difference					
1.5×10^{-4}	A					
6.7×10^{-2}		B				
1.0×10^{0}			C			
8.2×10^{0}				D		
4.8×10^{1}					E	
1.0×10^{2}						F

5.4.3 Effect of longitudinal strain rate on the in-plane shear ultimate strength

The effect of increasing strain rate on the ultimate shear strength is shown in Figure 5.43. The y error bars demonstrate the 95 % confidence interval range for the measured shear modulus, whilst the x error bars highlight the 95 % confidence interval for the experimental strain rate. Statistical analysis of the average and variance of each of the results recorded at increasing strain rate was reviewed using an ANOVA f-test. The returned p-value of <0.001 demonstrates that at least two of the means are different. The Tukey's HSD test demonstrated that all ultimate shear strengths recorded were statistically independent.

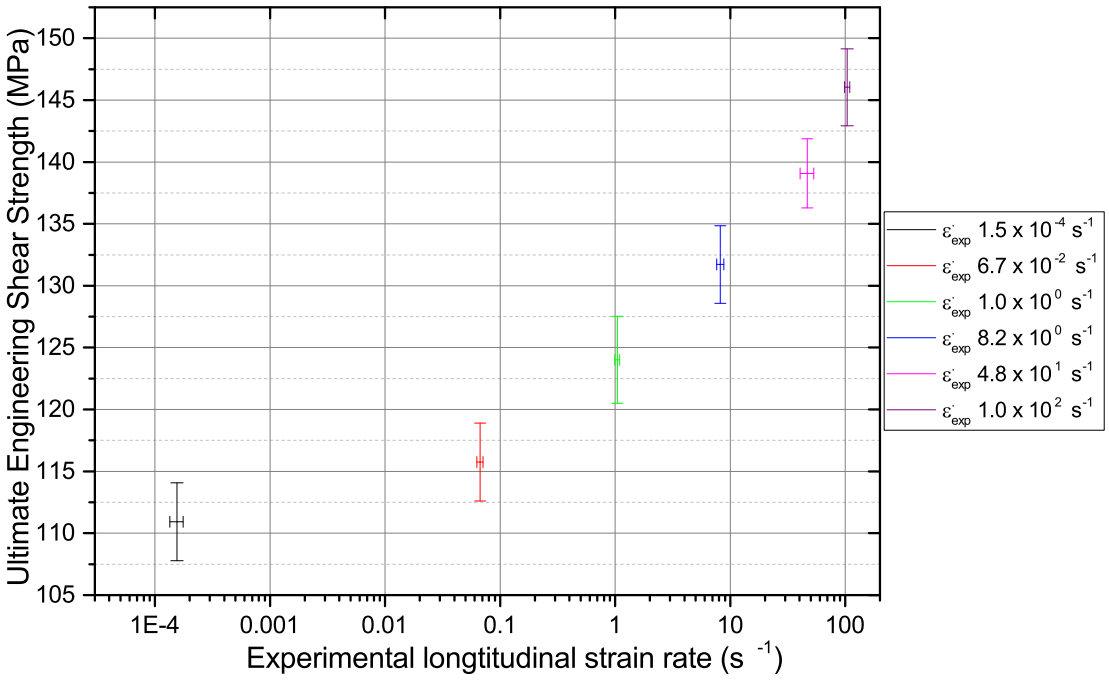

Figure 5.43: Average experimental ultimate shear strength plotted at magnitude increases in longitudinal engineering strain rate. Error bars depict the 95 % confidence interval for shear modulus (y) and longitudinal strain rate (x).

Table 5.32: Results of Tukey's HSD statistical difference analysis on the ultimate shear strength recorded at different intermediate strain rates, a different letter indicates a statistically significant difference.

Strain rate (s^{-1})	Statistical difference					
1.5×10^{-4}	A					
6.7×10^{-2}		B				
1.0×10^{0}			C			
8.2×10^{0}				D		
4.8×10^{1}					E	
1.0×10^{2}						F

5.4.4 Effect of longitudinal strain rate on the ultimate engineering shear strain

The effect of increasing strain rate on the ultimate engineering shear strain is shown in Figure 5.44. The y error bars demonstrate the 95 % confidence interval range for the measured ultimate engineering shear strain, whilst the x error bars highlight the 95 % confidence interval for the experimental strain rate. It is clear that as the experimental strain rate is increasing the ultimate shear strain is reducing. The f-test p-value of <0.001 shows that there is statistical difference between the results, the findings of the Tukey's HSD method (Table 5.33) shows that the shear strain observed from the quasi-static test is independent of the other results. Whilst the 6.7×10^{-2} s^{-1} and 1.0×10^{0} s^{-1} were not sufficiently different from one another, neither were 6.7×10^{-2} s^{-1} / 8.2×10^{0} s^{-1} / 4.8×10^{1} s^{-1} nor 8.2×10^{0} s^{-1} / 4.8×10^{1} s^{-1} / 1.0×10^{2} s^{-1}. This highlights the trend of reducing ultimate shear strain with strain rate.

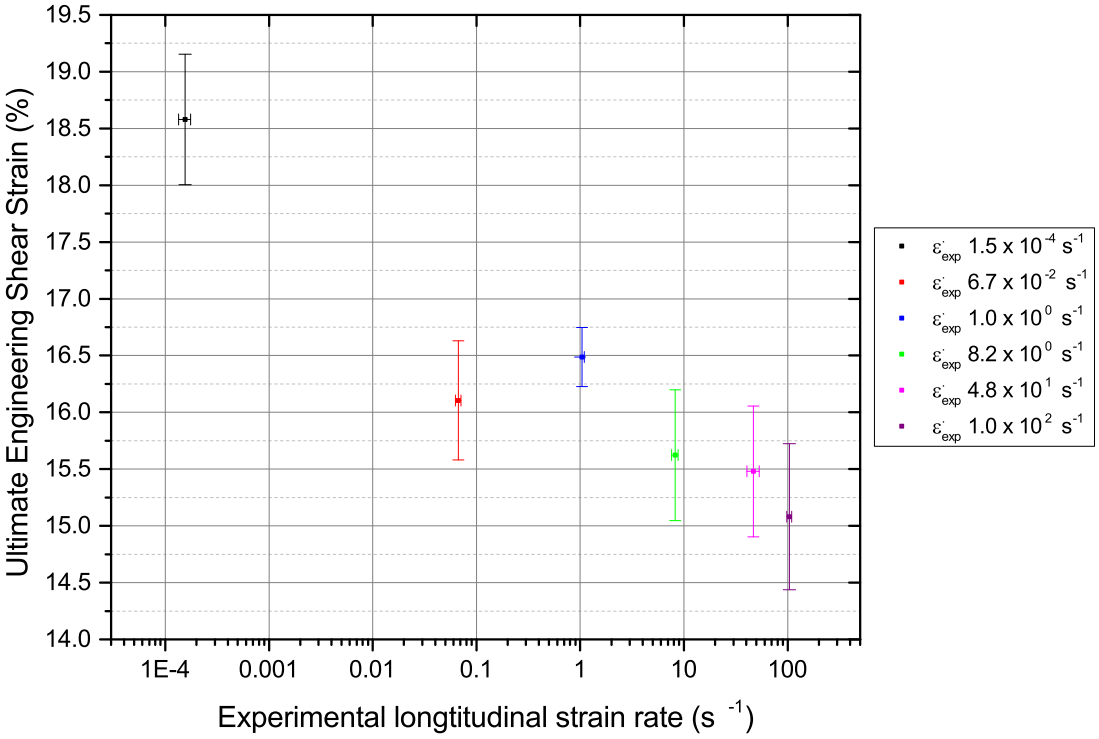

Figure 5.44: Average experimental ultimate shear strain plotted at magnitude increases in longitudinal engineering strain rate. Error bars depict the 95 % confidence interval for shear modulus (y) and longitudinal strain rate (x).

Table 5.33: Results of Tukey's HSD statistical difference analysis on the ultimate shear strain recorded at different intermediate strain rates, a different letter indicates a statistically significant difference.

Strain rate (s^{-1})	Statistical difference			
1.5×10^{-4}	A			
6.7×10^{-2}		B	C	
1.0×10^{0}		B		
8.2×10^{0}			C	D
4.8×10^{1}			C	D
1.0×10^{2}				D

5.5 Discussion

A review of the experimental results presented throughout this Chapter is conducted across three sections. Initially a review of the intermediate strain rate sensitivity of the tensile response of the 12K 2 x 2 twill CFRP is presented, this is followed by a discussion of the in-plane shear behaviour. Finally, a discussion on the experimental methodology is provided.

5.5.1 Strain rate sensitivity of the tensile behaviour

Section 5.1 presented the results of the experimental tensile characterisation study on the automotive specific 12K 2 x 2 twill CFRP laminate to review the effect of increasing the experimental longitudinal strain rate from 1.7×10^{-4} s^{-1} to 7.6×10^{1} s^{-1}.

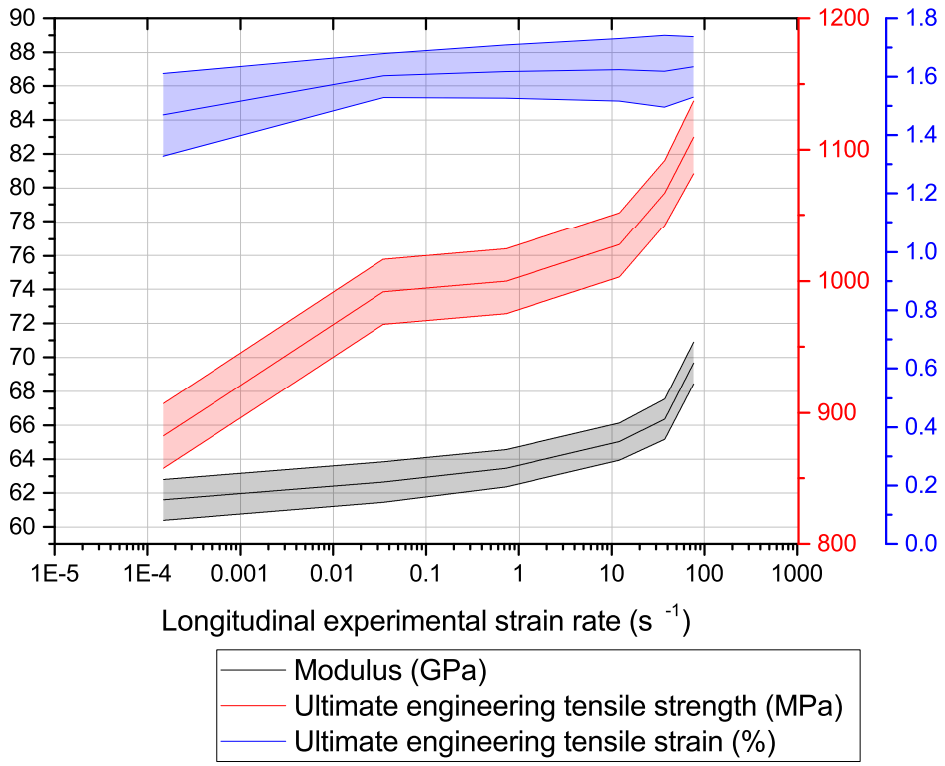

Figure 5.45: Summary of the effect of increasing experimental longitudinal strain rate between 1.7×10^{-4} s^{-1} and 7.6×10^{1} s^{-1} on the tensile modulus, ultimate strength and ultimate strain of 12K 2 x 2 twill CFRP laminate, the shaded band represents the 95 % confidence interval for each experiment.

In each of the experiments the linear response to failure was consistent with that observed at quasi-static strain rates. Figure 5.45 demonstrates the relationship of tensile modulus, ultimate engineering strength and ultimate engineering strain with strain rate. The Poissons ratio was also recorded however, it showed no sensitivity to strain rate within the experimental error achieved.

Strain rate sensitivity of modulus

The tensile modulus was measured by linear fit for all experiments over a constant 0.2 to 1.0 % ε_{YY} range. The sensitivity to strain rate is exponential with the largest increase (13.7 %) observed between 3.7 x 10^1 $s^{-1}$and 7.6 x 10^1 s^{-1}. This increase in stiffness challenges the early work by Welsh and Harding [127], whom identified insensitivity in modulus and strength within the intermediate regime for woven carbon fibre polymer composites. Welsh and Harding's research was supported by Wang et al. [122] , who found that the modulus of UD carbon-epoxy laminates investigated up to 4.2 x 10^1 s^{-1} was insensitive. However, the authors of a more recent study that employed large specimens within a servo-hydraulic machine observed that the elastic behaviour of UD carbon-epoxy laminates showed an increase of 4.5 % up to 6.3 x 10^1 s^{-1} [110, 123]. This result is relevant to this study as the carbon fibre employed was also a T700 high strength fabric. Since the fibres can be considered to be consistent the increased modulus sensitivity is attributed to the discontinuities within the woven architecture. It is hypothesised that the large resin rich pockets created by the interstitial sites of the crimped heavy 400 gsm fabric as well as the resin rich tow boundaries created by the large 12K tow size are sensitive to strain rate in a viscoelastic manner as suggested by literature. The stiffening of these small localised resin regions will improve the stress transfer between fibre tows thus improving the mechanical response of the complete laminate in a much greater manner than in a UD laminate.

Strain rate sensitivity of ultimate engineering strain

The ultimate strain of the laminate was shown to increase by 13.5 % between experimental strain rates of 1.7 x 10^{-4} s^{-1} and 3.5 x 10^{-2} s^{-1}, however, as the strain rate was increased further between 3.5 x 10^{-2} s^{-1} and 7.6 x 10^1 s^{-1} the ultimate strain was deemed to be statistically insensitive to strain rate within the error of the DIC measurements. The work by Longana [110] did not consider failure, however, the research in this thesis is in contrast to that conducted by Foroutan et al. [130]. Foroutan et al. observed a reduction of 43.1 % in ultimate strain for a 3K 2 x 2

twill carbon-epoxy laminate up to 5.0×10^{2} s^{-1}. However, unlike the representative length scale specimens employed in this research, Foroutan et al. used samples with a gauge area smaller than the size of a single unit cell. As a result it is likely that the authors results were affected by size effects. Therefore the large step change increase in ultimate strain that was reported in this thesis has not been identified before.

Since carbon fibres have been reported as lacking an inherent viscoelastic property, this strain rate sensitivity is unexpected. However, as the sensitivity is limited to an increase of two orders of magnitude at the lower end of the investigated range it is hypothesised that a change in damage coalescence occurs between experimental strain rates of 1.7×10^{-4} s^{-1} and 3.5×10^{-2} s^{-1} allowing the specimen to strain further. The large interstitial and tow elliptical boundary resin rich regions act as stress raisers and areas for matrix crack initiation. The stiffening of these regions as a result of their viscoelasticity improving the load transfer and delay the initiation of localised failures, whilst as a result of the time dependent nature of crack growth the propagation of the induced cracks will be reduced. As a result it is considered that failure is induced by the ultimate failure strain of the crimped longitudinal fibres rather than due to the cracks propagated within the matrix. Therefore it is suggested that large tow fabrics are more sensitive to strain rate than UD and woven fabrics with tow sizes between 1 and 6 K. Since this is a hypothesis further analysis is required in order to establish the function capable of defining the increase in ultimate strain between 1.7×10^{-4} s^{-1} and 3.5×10^{-2} s^{-1}. This strain rate regime is the below the capability of the VHS therefore, the use of a low rate servo-hydraulic frame with the developed high capacity slack adaptor LMD will enable the user to capture the mechanical behaviour in this region. The use of a feedback loop will enable the user to define a loading hysteresis to review the damage propagation and identify the strain rate at which the rate of damage becomes a critical factor in the performance of the laminate in tension.

Strain rate sensitivity of ultimate engineering strength

The ultimate strength was found to increase with strain rate and is related to the effect of increasing modulus with experimental strain rate. However, unlike the modulus which followed an exponential increase, the largest increase in tensile strength (12.4 %) occurred between 1.7×10^{-4} s^{-1} and 3.5×10^{-2} s^{-1}, this is attributed to the increase in ultimate strain by 8.8 % over the same strain rate increase. As previously described this step change phenomenon was not observed in the characterisation of

UD laminates and is therefore attributed to the large heterogeneity of the woven laminate.

Beyond this initial large increase, the ultimate tensile strength increased by a further 11.9 % between 3.5×10^{-2} s^{-1} and 7.6×10^{1} s^{-1}. The tensile strength sensitivity follows an exponential trend pattern. This is consistent with that observed by the increasing modulus since the ultimate strain has been shown to be insensitive to strain rate above 3.5×10^{-2} s^{-1}. Since the fracture surfaces have not been studied as part of this research it is not possible to define the cause of this non-linear increase in strength. However, it is considered to be related to the viscoelastic nature of the matrix within those large resin rich pockets previously described. The fracture surfaces have not been investigated in this thesis since the VHS is incapable of controlling the post failure behaviour of the specimen. This results in the full disintegration of the laminate, with further damage initiation and propagation.

The Poissons ratio was shown to be insensitive to strain rate through the intermediate regime within the error achieved with the DIC optical measurement. The variance was shown to increase as the strain rate increased due to a reduction in the strain resolution achieved due to requiring smaller facet sizes as the sensor was cropped. The insensitivity of the Poissons ratio in combination with the consistent global transverse failure suggests that the damage mechanisms within the specimen remain consistent with increasing strain rate. This is supported by a review of the surface strain maps which demonstrated that the strain limited constituent remained the longitudinal fibres with limited weft tow splaying observed.

5.5.2 Strain rate sensitivity of the in-plane shear response

Section 5.2 has presented the findings of the experimental investigation into the effect of intermediate strain rates on the in-plane shear response of the automotive specific 12K 2 x 2 twill CFRP laminate. Figure 5.46 provides a summary of how the (a) shear modulus, shear strength at yield and shear strain at yield; and (b) ultimate engineering shear strength and ultimate engineering shear strain vary with increasing experimental strain rate. Despite the observed strain rate sensitivity, each of the experiments followed the bi-linear load response of the quasi-static experiments with shear failure of the specimen occurring with cracks parallel to the warp and weft tows.

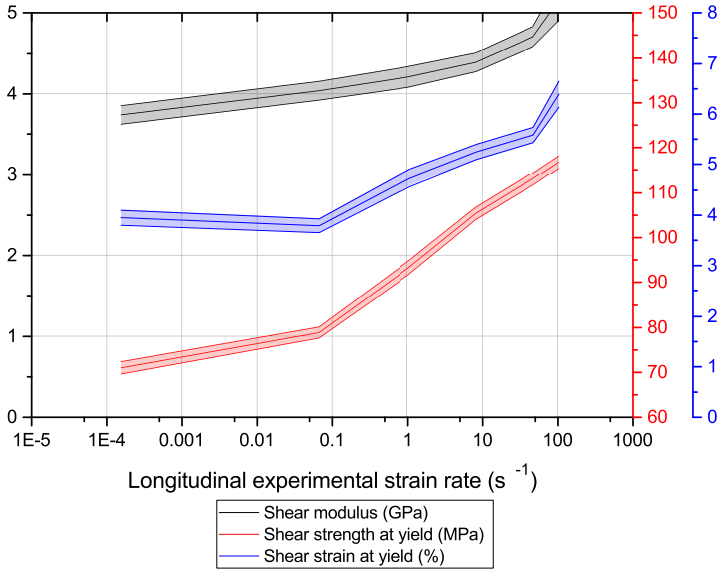

(a)

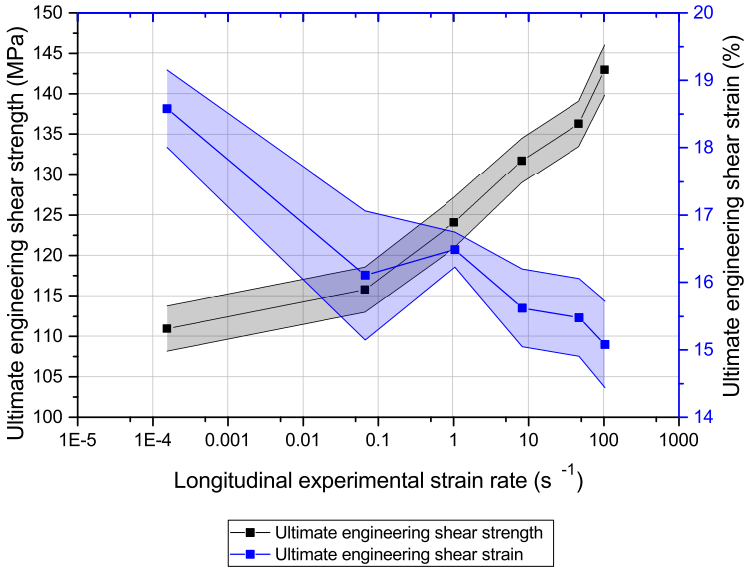

(b)

Figure 5.46: Summary of the effect of increasing experimental longitudinal strain rate between 1.5 x 10^{-4} s^{-1} and 1.0 x 10^{2} s^{-1} on the (a) shear modulus, shear strength at yield and shear strain at yield; and (b) the ultimate engineering shear strength and ultimate engineering shear strain of the automotive specific 12K 2 x 2 twill CFRP laminate, the shaded band represents the 95 % confidence interval for each experiment.

The longitudinal strain progression maps demonstrated that the ultimate fracture remained consistent within all specimens. Shear matrix cracking was observed to occur as the specimen began to yield (not evident in the 6.7×10^{-2} s^{-1} experiment due to the low spatial resolution), as the strain continued to rise the matrix cracks propagated, particularly within the vicinity of the specimen edges. Damage local to the edge of the specimen resulted in inter-lamina cracks developing. The final fracture of the specimen was consistent with the description provided by Li et al. [135], it was the result of the coalescence of matrix damage forming macroscopic intra and inter lamina cracks as the fibres rotated, tensile fracture was observed in fibres rotated into the loading direction. Due to the inability to review the fracture surfaces of the investigated specimens since the damage may be produced during fracture or the disintegration of the laminate post test, it is not possible to deduce whether the increasing mechanical behaviour is a result of matrix viscoelastic properties or the time period for damage development reducing.

Strain rate sensitivity of shear modulus

The shear modulus was observed to increase by 37.7 % between 1.5×10^{-4} s^{-1} and 1.0×10^{2} s^{-1} . Although a different fabric architecture, the scale of the performance increase is supported by Longana et al. [110] who observed a 30.9 % increase in shear modulus of UD carbon-epoxy tested using 12° off axis tensile test between 1.25×10^{-4} s^{-1} and 6.3×10^{1} s^{-1}. In contrast Bergmann et al. [134] observed a 6.7 % increase in modulus of a 3K 2 x 2 twill weave [±45] fabric between 1.0×10^{-3} s^{-1} and 2.0×10^{1} s^{-1}, in comparison the 12K 2 x 2 twill CFRP investigated in this thesis increased by 17.4 % when the strain rate was increased between 1.5×10^{-4} s^{-1} and 8.2×10^{0} s^{-1}. The initial modulus of the 3K fabric was greater than that of the 12K fabric reviewed within this study which may be a result of the reduced volume of the matrix rich regions. Since the rate sensitivity is often attributed to the viscoelastic nature of the matrix [119, 135] the reduction in sensitivity may be a direct result of the reduced matrix volume.

Strain rate sensitivity of engineering shear strength and shear strain at yield

The onset of plastic straining, defined as the yield of the laminate in these experiments, is determined as the culmination of matrix cracking prior to the strain

hardening induced by the rotation of the woven fabric. The shear strain at yield was found to increase by 61.8 % between 1.5×10^{-4} s^{-1} and 1.0×10^{2} s^{-1} whilst the shear stress at yield was observed to increase by 64.5 % over the same strain rate regime. The increased strain to yield may be explained as a result of the reduced period for matrix crack coalescence that is required to induce plastic straining. Fitoussi et al. [108] investigated the response of a woven CFRP at 6.0×10^{1} s^{-1} and identified that macroscopic damage (detectable reduction in stiffness) did not occur until the specimen had strained over three times as far in comparison to the quasi-static experiment. This lower crack density as well as the stiffening of the matrix system as a result of its viscoelastic response will increase the shear stress achieved for a given shear strain. However, in this thesis increasing the strain rate between 4.8×10^{1} $s^{-1}$and 1.0×10^{2} s^{-1} yielded an increase to the strain at yield of 8.3 %, however, the strength increased by only 2.4 % over the same rate difference. This could be related to the increased ringing that was observed at this strain rate and the subsequent requirement to rely on fitted rather than raw data that is the ability to determine the true yield point.

Strain rate sensitivity of ultimate engineering shear strength

The ultimate shear strength was also observed to increase with increasing strain rate, 28.8 % between 1.5×10^{-4} s^{-1} and 1.0×10^{2} s^{-1}. This is significantly less than Foroutan et al. [130] who investigated a 2 × 2 twill carbon-epoxy composite using very small specimens on a SHTB, who observed that peak shear stress increased by 88.5 % between quasi-static and 203 s^{-1}. In comparison Bergmann et al. [134] observed a shear strength increase of 18.3 % between quasi static and 2.0×10^{1} s^{-1}, this is a similar to the 18.8 % increase observed between 1.5×10^{-4} s^{-1} and 8.2×10^{0} s^{-1} in this research. Due to the difference in fibre and matrix materials, volume fraction, and test methodology (different LMD and strain instrumentation) it is not possible to determine whether the strain rate sensitivity of the shear strength is independent of tow size of the twill fabric. However, it represents a potential objective for further research using different material systems to conduct round robin testing to review the effects of different localised material effects with increasing strain rate.

The ultimate shear strain was shown to follow an overall decreasing trend with increasing strain rate. However, it is thought that the initial reduction was induced by the optical measurement system. Between experimental strain rates of 1.5×10^{-4} s^{-1} and 6.7×10^{-2} s^{-1} the ultimate shear strain was reduced by 13.3 %, yet when the strain rate was subsequently increased to 1.0×10^{0} s^{-1}, the ultimate shear strain increased. In order to induce a strain rate of 6.7×10^{-2} s^{-1} the free length of the

specimen had to be increased. Since imaging over the entire free length was required to establish a representative response of the laminate the spatial resolution was reduced. At quasi-static test speeds in Chapter 3 this reduction in spatial resolution was shown to induce smoothing errors, therefore it is considered that the ultimate shear strain at 6.7×10^{-2} s^{-1} is not representative of the laminates true behaviour. As a result future experiments are recommended to be instrumented with both 3D DIC to provide an understanding of the strain propagation over the test period and a high speed optical extensometer positioned at the rear of the specimen to measure the average longitudinal strains simultaneously with high temporal resolution.

5.5.3 Experimental method

The slack adaptor developed throughout this thesis was shown to have greater experimental repeatability in comparison to the Instron Fast Jaw solution reviewed in Chapter 3. Few specimens failed within the vicinity of the gripping mechanism. Those that did were shown to fail within the 95 % confidence interval of the remaining repetitions and therefore were considered to be failures due to statistical defects of the material rather than induced by fixturing.

The conical impactor (Figure 4.12) was designed with upper and lower fulcrum dampers to reduce the knocking of the specimen prior to the engagement of the specimen. The dampers were designed to be replaced after five repeats of a given strain rate. Load cell ringing as a result of the premature knocking of the fixture within the cradle prior to engagement of the LMD was shown to have a catastrophic effect on the shear modulus of a single experiment (Section 5.3.3) when the upper fulcrum damper failed prematurely.

Resonance was observable within the load traces of both the tensile and shear experiments when the prescribed velocity was increased. This is a result of the impact occurring close to, or at the natural frequency of the LMD system. It occurred at different impact speeds in the tensile and shear experiments, as a result of the different stiffness and geometry of each specimen adjusting the natural frequency. As a result the author considers it appropriate for a secondary load instrumentation to be fitted within the system. It must be positioned as close to the specimen as possible in order to raise the natural frequency and reduce the inertial mass [88].

Use of the VHS in low rate mode provided a feedback loop to control the aperture of the servo-valve. As a result the oil flow rate and therefore the velocity of the actuator could be adjusted over the test duration to achieve a more consistent velocity and

strain rate. As a result when the low rate mode was employed the variation in experimental strain rate was within the ±30 % of the average that prescribes a stable test within ISO 26203-2:2011 [92]. However, when the test velocity was increased and required the use of open loop control the strain rate variance for all tensile specimens investigated was outside of this tolerance. Increasing the velocity was shown to delay the point at which the strain rate decay occurred as a result of the high capacity specimen. However, it was also shown to increase the strain rate rising period, maintaining the non-linearity of the specimen. The inability to produce stable strain rates potentially induces accelerations within the specimen and when combined with the large mass of the LMD (which is required for withstanding the high loads of the specimens) this potentially induces transient loads varying the damage propagation within the specimen. Although the open loop nature of the VHS does not allow the use of a live feedback loop, the valve drive can be adjusted based on the outcome of a single benchmark experiment. The fixturing developed as part of this thesis is considered to be appropriate for the trial of a variable valve drive program as it has demonstrated great experimental reliability and the static positioning of the specimen within both the upper and lower jaw provides the user with great control over the impact height of the LMD. The use of such variable valve control was not trialled within this thesis, however, it is suggested that it may be a suitable methodology for removing the strain rate reduction observed at the end of the experiment, therefore it is suggested as a method for future exploration.

An alternative to the use of variable valve control is the use of a mechanical damper positioned within the load path. The damper will introduce controlled compliance of the system and will remove the peak strain rate observed in experiments conducted with low kinetic energy of the LMD. However, the use of a damper will also induce greater non-linearity with regards to the strain rate rising period, therefore care must be taken. Previous studies have employed the use of a polymer washer (e.g. nitrile/polyethylene) to alleviate ringing when running experiments at increased test velocities. However, this is not considered desirable by the author since the polymer itself will be highly sensitive to the strain rate it is impacted at, and therefore the compliance of the damper will change over the test period, as a result, a material such as brass is suggested.

5.6 Summary

This Chapter has successfully characterised the automotive specific 12K 2 x 2 twill CFRP in both longitudinal tension and in-plane shear.

The quasi-statically observed linear elastic straining prior to brittle fracture was prevalent at all strain rates investigated in this thesis. Modulus was shown to follow an exponential growth with increasing strain rate, a 13.7 % increase was observed between experimental strain rates of 2.2×10^{-4} $s^{-1}$and 6.4×10^{1} s^{-1}. The increase was observed to be significantly greater than that for UD CFRP laminates which is thought to be a result of the stiffening of the large resin-rich pockets within the material created at interstitial sites and tow boundaries. Ultimate tensile strain was shown to increase by 8.8 % between experimental strain rates of 2.2×10^{-4} $s^{-1}$and 3.5×10^{-2} s^{-1}. Further discrete strain rate rises between 3.5×10^{-2} $s^{-1}$and 6.4×10^{1} s^{-1} showed that at a 95 % confidence level, the ultimate strain was not statistically strain rate dependent. The lack of an inherent viscoelastic behaviour for carbon fibres suggests that the increase in ultimate strain with strain rate is a result of the delayed rate of damage coalescence as the loading period reduces. Ultimate tensile strength was shown to increase with strain rate. Since the specimens continued to exhibit elastic brittle failure, the increased strength with strain rate is related to effect of increasing modulus. A 12.4 % increase in ultimate strength occurred between 2.2×10^{-4} $s^{-1}$and 3.5×10^{-2} s^{-1}, considering the only slight increase in modulus over this regime, the increased strength is a result of the large change in ultimate strain that was observed over the same strain rate regime. Between 3.5×10^{-2} $s^{-1}$and 6.4×10^{1} s^{-1} the strength was found to increase in an exponential manner by a further 11.9 % as a result of the increased modulus since the ultimate strain was shown to not increase above 3.5×10^{-2} s^{-1}. Poissons ratio was shown to be insensitive to strain rate within the experimental error. The damage propagation visible on the DIC surface strain maps demonstrated extensive matrix cracking within and surrounding the weft tows and each specimen failed as a result of a transverse crack irrespective of the experimental strain rate. It is suggested that the global failure mechanism was not dependent upon strain rate.

The bi-linear in-plane shear response with strain hardening observed between yield and fracture that was observed at quasi-static strain rates was replicated at longitudinal experimental strain rates up to 1.0×10^{2} s^{-1}. In general literature highlighted that the rate sensitivity of the matrix dominated properties to be greater than those in tension. Strain rate dependency for the 12K 2 x 2 twill CFRP was observed in the shear modulus, shear stress and shear strain at yield and the shear stress and shear

strain at fracture. Shear modulus was shown to be highly sensitive to the longitudinal strain rate applied increasing exponentially by 37.7 % between longitudinal experimental strain rates of 1.5×10^{-4} $s^{-1}$and 1.0×10^{2} s^{-1}. The yield point of the shear experiment occurs at coalescence of matrix cracking prior to strain hardening induced by the rotation of the warp and weft fibres to the direction of the fibres. Yield shear stress was shown to increase 64.5 % between 1.5×10^{-4} $s^{-1}$and 1.0×10^{2} s^{-1}, the increase was statistically different at each of the discrete strain rates evaluated. Yield shear strain increased 61.8 % between 1.5×10^{-4} s^{-1} and 1.0×10^{2} s^{-1}. The yield shear strain measured at 6.7×10^{-2} s^{-1} decreased, this was in opposition of the trend and the increasing yield shear stress at 6.7×10^{-2} s^{-1}. As a result, this yield shear strain was considered to be a result of the strain smoothing induced by the optical measurement settings required to conduct the experiment at such a low strain rate on the Instron VHS. The difference between 4.8×10^{1} s^{-1} and 1.0×10^{2} s^{-1} was not statistically different and suggests a plateauing of the shear strain at yield as the strain rate may increase further. Ultimate failure of the specimen was found to occur at higher shear stress yet lower shear strain as the strain rate was increased. Ultimate shear stress was statistically independent at each characterised longitudinal strain rate. An increase of 18.8 % was observed between 1.5×10^{-4} $s^{-1}$and 8.2×10^{0} s^{-1}, this was similar to the sensitivity of a 3K 2 x 2 twill CFRP in literature that was investigated up to 2.0×10^{1} s^{-1}, potentially highlighting an insensitivity of the fabric architecture when loaded in shear when considering ultimate shear stress. Further increasing the strain rate between 8.2×10^{0} s^{-1} and 1.0×10^{2} s^{-1} yielded an additional 7.5 % increase in ultimate strength. Ultimate shear strain was shown to decrease by 20.4 % as the strain rate was increased between 1.5×10^{-4} $s^{-1}$and 1.04×10^{2} s^{-1}.

The large specimen that was required to produce a representative volume of the 12K 2 x 2 twill CFRP laminate resulted in high capacity specimens that induced the inertial effect of the high capacity specimen retarded the actuator causing a non-constant experimental strain rates. The lack of yield and necking phenomena required by the metallic high rate test standard to dictate the experimental strain rate required new limits to be defined. To remove the initial strain rate rising period and large strain rate spikes as a result of local crack growth at fracture the experimental average strain rate and strain rate range in this thesis were determined at discrete strain ranges for ISTS ($\varepsilon_{(0.9\dot{\varepsilon}_{max})}$ to 1.4 % ε_{YY}) and ISSS (γ_{yield} to 11 % γ_{XY}) specimens respectively. Each ISTS experiment was able to achieve the nominal stain rate based on the prescribed actuator velocity. However, once the actuator velocity was increased beyond 1 ms^{-1} the removal of the feedback loop resulted in an increase of the experimental strain rate range beyond ±30 % of the average experimental strain rate. As the test velocity was increased the non-linearity of the strain rate increased; with increasing strain rate rising period, whilst the

strain at strain rate decay was delayed. Thus it is hypothesised that as the velocity is further increased the strain rate decay in the test will be reduced to a negligible level due to the higher kinetic energy of the LMD, however, the large variance will still exist as result of the increased strain rising period. Therefore it is not possible to induce a constant linear strain rate over the test period due to the highly brittle response of the laminate. The ISSS specimen has a lower capacity relative to the ISTS coupon and therefore the difference between experimental and nominal strain rate is significantly reduced. The experimental response derived at a nominal strain rate of 1.0×10^{1} s^{-1} was the initial in-plane shear experiment to be run in open loop. Due to the low kinetic energy the experimental strain rate was found to be on the ± 30 % variance threshold. However,as the input velocity was increased the strain variance was reduced and the difference between nominal and experimental strain rates was reduced. It is clear that the definition of strain rate between yield and 11 % γ_{XY} removes the non-linear strain rate rising period for each of the experiments and was not affected by localised cracking as the test approached fracture.

Chapter 6

Implications of intermediate strain rate behaviour on the finite element modelling of composite structures

The preceding chapters have reviewed the quasi-static and intermediate strain rate tensile and in-plane shear response of an automotive specific 12K 2 x 2 twill CFRP laminate. The aim of this chapter is to review the ability of explicit FE composite models to predict the performance of structures utilising the strain rate data characterised in Chapter 5. This is initially achieved through single element assessments of the quasi-static tensile and shear response of the composite, followed by the building block model approach to review the capability of the modelling methodology.

6.1 Introduction

The importance of FE simulations in reducing the quantity of prototype build phases pre-production in the automotive industry was highlighted in Chapter 1. FE techniques discretise a continuum medium into a finite number of elements to form a mesh that consists of 1D, 2D or 3D elements. Of these element types, both 2D (shell) and 3D (solid) elements are suitable architectures for modelling the response of composite materials. Solid element modelling typically conducts analysis of composites at a fibre/resin/interface length scale [45]. Each of the individual constituents are modelled as solid elements with contact laws defining their interaction. Various studies have demonstrated their potential for accurately modelling the development and transfer of stress concentrations; particularly at free-edges [46]. However, due to the high computational requirements of this modelling method, it is often limited to microscopic modelling and used for the development of a material system

and is unsuitable for full vehicle or component level modelling [47]. To reduce computational expense a composite material can be modelled using 2D shell elements. Multiple through-thickness integration points represent the laminates stacking sequence; which is not possible when using solid elements [48]. A number of different shell formulations are available based on their number of integration points. Under-integrated elements with a single integration point at the centre of the element are computationally less expensive, however, they are often soft and suffer from zero energy modes known as *hourglassing*. Fully integrated elements have a greater number of integration points and are not prone to hourglassing, however, they are computationally more expensive as a result of their greater number of integration points [189].

FE analyses to resolve time dependent ordinary or partial difference equations employ two methods; implicit and explicit. Low speed events are typically modelled using implicit methods which determine the solution, dependent upon the state of the system at both the current and later times, as a result they are highly computationally intensive. Implicit methods are typically composed of few large time-steps since the model is considered unconditionally stable. The stiffness matrix for the complete system is generated, with each degree of freedom (DOF) designated its own row/column. The inverse of the stiffness matrix is then resolved to calculate the displacement relative to the applied force. If the error of the internal energy of the system in comparison to that externally applied is outside of a predefined tolerance then a smaller time-step is attempted. Convergence of the error within a time-step resolves the load case [189, 190]. In contrast an explicit analysis uses a large number of computationally in-expensive small time steps that do not require the inverse of the stiffness matrix to be determined, instead the forces are resolved based on the nodal masses and accelerations directly. As a result a single process is used to resolve the complete model with no iterations. The small time-step must be set sufficiently such that it is less than the period for a single wave to travel through the smallest element thereby conforming to Courant-Friedrichs-Lewy criterion [191].

High speed deformations employ explicit methodologies. As such the modelling of dynamic automotive crash events requires the use of an explicit solver. The main solvers used to run such simulations are Abaqus explicit, PAM-crash and LS-DYNA. LS-DYNA is widely adopted within the automotive industry as a result of its specialist capabilities for modelling vehicle components such as airbags and seatbelts [189] and is used extensively within Jaguar Land Rover, and as a result is employed in this thesis.

6.2 Material card

LS-DYNA contains a wide variety of constitutive material models including a range of composite specific orthotropic material cards. There is a range of composite specific material cards, each providing the ability to define damage and failure criteria differently depending on the material. Table 6.1 provides a comparison of the composite specific material cards, further information can be found in the material card LS-DYNA manual [187] and Tabiei [192].

The focus of this Chapter is the application of strain rate material data therefore all material cards except *MAT_054, *MAT_058, *MAT_158 and *MAT_162 will not be considered for further review as they are incapable of modelling the strain rate sensitivity of the laminate. *MAT_054 is only suitable for UD architectures and cannot model the balanced nature of a woven fabric, therefore is also excluded [187]. *MAT_158 determines the strain rate characteristics using the Maxwell viscoelastic model and the adjustment of strength and failure strain of the element is limited to 15 %, which as shown in Chapter 5 is insufficient for the material system evaluated in this thesis. *MAT_162 is suitable for further review due to its application of an logarithmic function to model the modulus and strength rate sensitivity [193]. *MAT_058 describes the composite failure through the Hashin failure criterion enabling the user to model the tensile, shear and compressive response of the woven material system [187]. *MAT_058 is the only card relevant for consideration in this study due to its ability to represent the woven, strain rate sensitive nature of the laminate reviewed in this thesis. Initial stiffness is modelled as linear with an exponential damage model that is used to replicate the damage prior to brittle fracture in tension and material yielding in shear. Strain rate functions can be input directly and the effect of strain rate is not limited with strain rate averaging applied over a user defined average time-step range.

However, due to the additional licenses cost, additional computational expense of *MAT_162 [194] and the widespread adoption of *MAT_058 in the automotive industry, the decision was made in partnership with industrial sponsors to focus on *MAT_058 [195]. The following section will discuss an appropriate definition of the material card in more detail.

Table 6.1: Comparison of LS-DYNA composite specific material cards.

Material card	Failure criterion	Linear stiffness	Damage modelling	Fabric type	Strain rate modelling		Additional licensing fees
					Stiffness	Strength	
*MAT_002	×	✓	×	UD/woven	×	×	×
*MAT_022	Chang-Chang	✓	×	UD/woven	×	×	×
*MAT_54	Chang-Chang	✓	×	UD	×	✓	×
*MAT_58	Hashin	✓	✓	UD/woven	×	✓	×
*MAT_158	Hashin	✓	✓	UD/woven	×	✓ (max 15 %)	×
*MAT_162	Hashin	×	✓	UD/woven	✓	✓	✓
*MAT_261	Pinho	✓	✓	UD/woven	×	×	×
*MAT_262	Camanho	✓	✓	UD/woven	×	×	×

6.2.1 *MAT_LAMINATED_COMPOSITE_FABRIC

Material card *MAT_058 for laminated composites is capable of modelling composite material behaviour of UD or woven material systems using shell elements under the assumption of plane stress. It requires the input of modulus, ultimate strength and ultimate strain to define the tensile and compressive failure, whilst the bi-linear shear response is dictated by the shear modulus, shear stress and shear strain at yield and at fracture. It incorporates an orthotropic elastic stress-strain relationship with a continuum damage model to replicate the stiffness reduction induced by damage for tensile, compression and shear. The four dominant failure modes (tensile fibre failure, tensile matrix failure, compressive fibre buckling or kinking and compressive matrix failure) are dictated using a modified Hashin failure criterium whilst constant post failure minimum stress limit is controlled by user defined *SLIMxx* values (Equation 6.1). If post failure the element maintains 100% of its strength then SLIM*xx* is set to 1.0, until the element is eroded using the *ERODS* function (determined according to Equation 6.2).

$$\sigma_{residual} = SLIMxx \times \sigma_{max} \tag{6.1}$$

$$ERODS = \frac{2}{\sqrt{3}} \times \left(3 \left(\frac{(\varepsilon_{11} + \varepsilon_{22})}{2} \right)^2 + \left(\frac{(\varepsilon_{11} - \varepsilon_{22})}{2} \right)^2 + (\varepsilon_{12})^2 \right)^{\frac{1}{2}} \tag{6.2}$$

To define the material card and assess its ability to predict the response of the laminate structure single element models (Figure 6.1) were created. A single element was created in PRIMER (Oasys pre-processor) with node spacing of 10 mm. The element was defined using the *PART_COMPOSITE card with TYPE 16 (Fully integrated) shells to reduce the risk of hourglassing. The fibre orientation was prescribed as *Beta (β)* relative to the element direction. Deformation is introduced into the model by providing nodes 3 and 4 with an initial velocity and prescribed motion of 100 mms^{-1}. Since rows 8 and 9 of the material card were left undefined, the material card was insensitive to strain rate. Therefore the result of the single element model is insensitive to strain rate. Further information on the control profile can be found in Appendix B.

The material card is defined using true stress (σ_{True}) and true strain (ε_{True}) therefore the data previously collated in Chapters 4 and 5 requires transformation according to Equations 6.3 and 6.4. The quasi-static material card is defined in full in Appendix B.

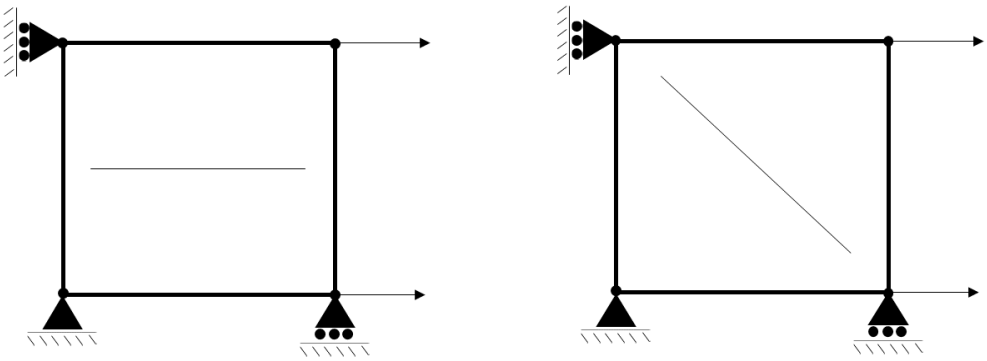

Figure 6.1: Single element models for reviewing the material card in (a) tension, (b) shear.

$$\varepsilon_{True} = ln(1 + \varepsilon_{eng}) \tag{6.3}$$

$$\sigma_{True} = \sigma_{eng} \times (1 + \varepsilon_{eng}) \tag{6.4}$$

Where; ε_{eng} - engineering strain and σ_{eng} - engineering stress.

6.2.1.1 Tension

The stress-strain response of the single element model is shown in Figure 6.2. The response can be split into three sections, initially the element behaves in a linear manner with stiffness of that prescribed in the material card. However, as the stress experienced by the element approaches the failure strength (XT) then the element softens with reducing stiffness to XT. Finally the element undergoes strain softening to fracture until it reaches the prescribed minimum stress limit (SLIMT = 0.01). A value of SLIMT = 0.0 is not recommended as it can reduce the stability of the model [187].

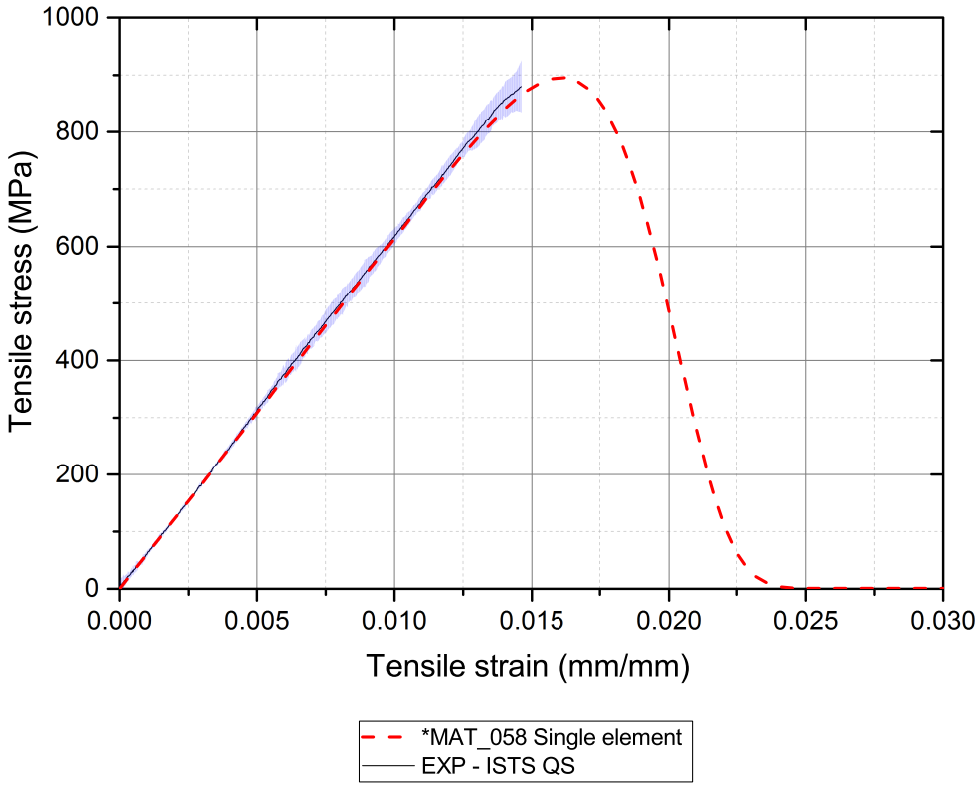

Figure 6.2: Comparison of the quasi-static tensile stress-strain response and *MAT_058 single element FE model.

In Figure 6.2 the modelled response can be seen to undergo strain softening as it approaches XT. This is a result of the exponential continuum damage law that exaggerates the stiffness loss of the laminate as it approaches failure relative to the experimental result. The damage parameter (ω_{ij}) is embedded within the compliance matrix $[H]$ (Equation 6.5) and takes the form shown in Equation 6.6. ω_{ij} is an exponential decay function that varies according to the relationship between the momentary strain of the element (ϵ_{ij}), the Hooke's law driven failure strain (ϵ_h) and a dimensionless damage constant *(m)*. The damage constant is dependent upon the failure strain prescribed in the material card (ϵ_q) and ϵ_h.

$$[H] = \begin{bmatrix} \frac{1}{(1-\omega_{11})E_{11}} & -\frac{\upsilon_{12}}{E_{11}} & 0 \\ -\frac{\upsilon_{12}}{E_{11}} & \frac{1}{(1-\omega_{22})E_{22}} & 0 \\ 0 & 0 & \frac{1}{(1-\omega_{11})G_{12}} \end{bmatrix} \tag{6.5}$$

$$\omega_{ij} = 1 - e^{-\frac{1}{me}(\frac{\epsilon_{ij}}{\epsilon_h})^m} \tag{6.6}$$

$$m = \frac{1}{\ln(\frac{\varepsilon_q}{\varepsilon_h})} \tag{6.7}$$

$$\varepsilon_h = \frac{X_{ij}}{E_{ij}} \tag{6.8}$$

Where; E_{11}- longitudinal tensile modulus, E_{22}- transverse tensile modulus, G_{12}- shear modulus, E_{ig}- modulus in loading axis, X_{ij} - strength in loading axis.

A MATLAB script was generated to review the effect of varying m on the stress-strain response of the single element. The results are shown in Figure 6.3. It is clear that as m is increased the ductility of the failure is reduced. As the difference between ϵ_q and ϵ_h is reduced, m approaches infinity further reducing the ductility of the fracture, however, a maximum limit must be induced since $\varepsilon_q \neq \varepsilon_h$ as $m = 1/0$ which would make the damage model unresolvable. The strain at peak force (0.0159 mm/mm) extracted from the single element model is far greater than that prescribed in the material card. The corresponding m value was calculated

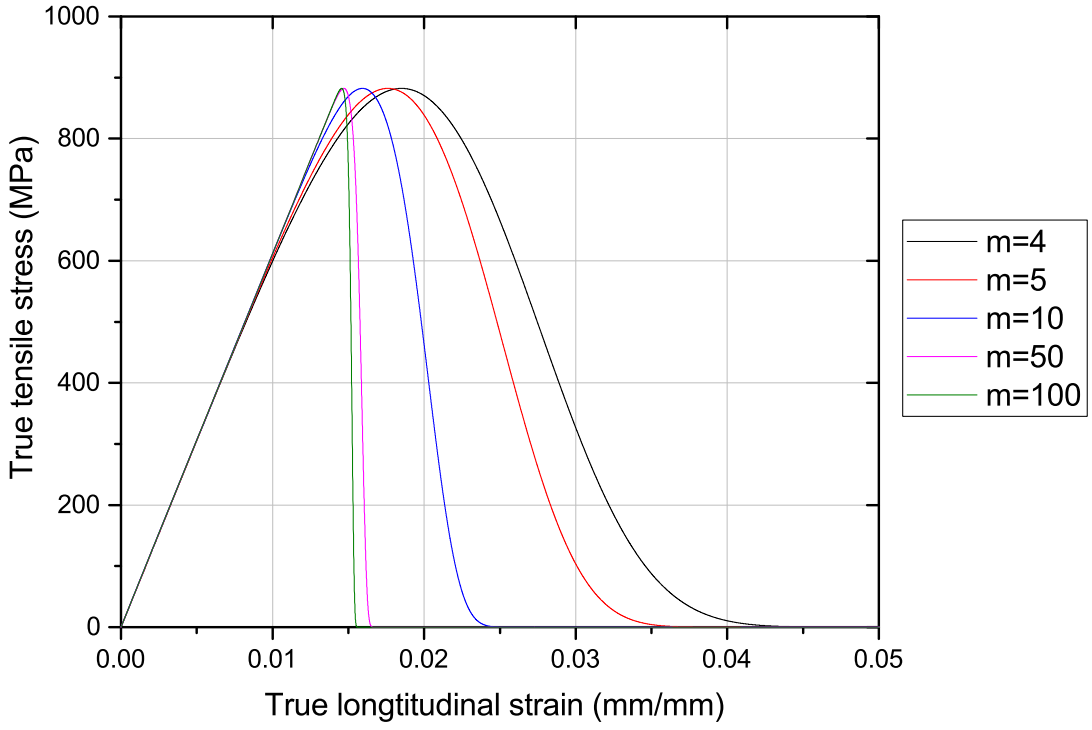

Figure 6.3: Effect of damage parameter m on the failure response of the laminate

using Equation 6.7 to determine that the maximum damage constant is approximately $m = 10$.

6.2.1.2 Shear

The shear stress-strain response of the single element model is plotted against the 95 % confidence interval of the experimental data in Figure 6.4. The bi-linear performance of the composite has clearly been replicated by the model, this is achieved by setting the shear minimum stress limit of the element to the the ultimate shear strength (SLIMS = 1.0). The non-linear stiffness up to the yield point is provided by the same exponential damage model that is used to model the increased ductility as the composite approaches tensile fracture (Equation 6.6). Shear strain at yield (GAMMA1) and shear stress at yield (TAU1) are substituted into Equation 6.7 to determine the damage constant. Based on the prescribed shear modulus, and shear strength and shear strain at yield, m was calculated as $m = 1.37$, which is below the maximum threshold identified in the previous section. As a result of the desired

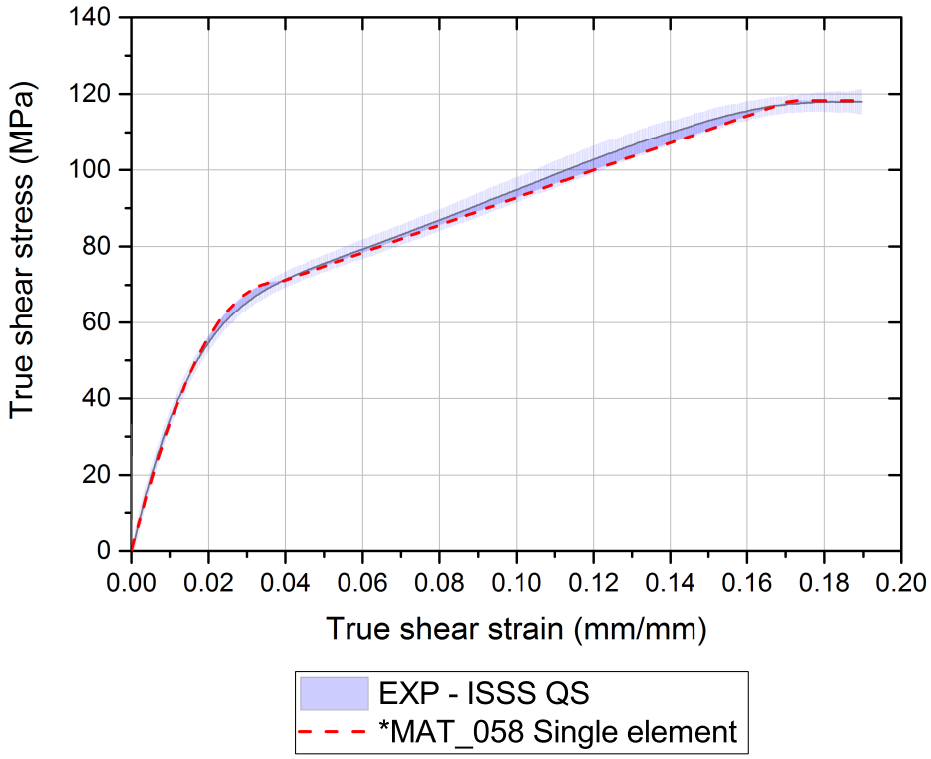

Figure 6.4: Comparison of in-plane shear stress-strain response of experimental ISSS coupons and MAT_058 single element FE models

damage constant being achieved, yield can occur at the prescribed point. Due to the exponential decay of the damage law, the gradient of the curve as it passes through yield must be approaching zero, which results in an increase in the stiffness of the element as it approaches yield in relation to the experimental response. Post yield the strain hardening of the composite is replicated with a linear relationship until the prescribed ultimate shear strength (SC) and shear strain (GMS) are achieved. The requirement of SLIMS = 1.0 to achieve the desired bi-linear response this maximum strength is maintained until the element is eroded using ERODS = 0.22 (Equation 6.2), this enables the author to replicate the strain softening that occurs as this particular material system approaches maximum shear strength.

6.2.2 Rate sensitive constitutive modelling

Strain rate mechanical data in *MAT_058 is introduced as load curves into the 8^{th} and 9^{th} row of the material card. The only parameters that can be adjusted with rate are the ultimate tensile and compressive strengths in both 11 and 22 axes, as well as the shear strain and strength at yield and fracture. Linear strain rate scaling was used to represent the strain rate effect of both glass and carbon fibre epoxy composites by Ochola et al. [196]. However,commonly more complex non-linear regression models are employed. Brown et al. [95] and Coulton et al. [197] employed the Johnson-Cook strain rate scaling, to represent the strain rate sensitivity. Coulton et al. utilised the non-linear fitted data within a dynamic punch model within *MAT_058, although they did not comment on the fit of the scaling with the experimental results, they observed reduced variance between the modelled and experimental force displacement plots on a system length scale. Johnson-Cook scaling takes the form of Equation 6.9, where M is an arbitrary mechanical property, $\dot{\varepsilon}$ is the instantaneous strain rate, $\dot{\varepsilon_0}$ is the quasi-static strain rate, α is the quasi-static value of the mechanical property and C is the strain rate scaling value.

$$M\left(\dot{\varepsilon}\right) = \alpha\left(1 + C\left(\ln\frac{\dot{\varepsilon}}{\dot{\varepsilon_0}}\right)\right) \tag{6.9}$$

Shokrieh et al. [116, 119, 121, 198] has published multiple journal articles regarding the tensile and compressive properties of UD glass-epoxy laminates. The author utilised a rearranged Cowper-Symonds expression that has previously been employed as the strain rate scaling function within LS-DYNA material card *MAT_POWER_LAW_PLASTICITY (*MAT_018) [199]. Cowper-Symonds is expressed using Equation 6.10, where ψ is a strain rate scaling constant.

$$M\left(\dot{\varepsilon}\right) = \alpha + \left(\frac{\dot{\varepsilon}}{C}\right)^{\psi} \tag{6.10}$$

Examples of typical values for α, C and ψ were provided by Shokrieh et al. [119] and are provided in Table 6.2. Two separate sets of values, and therefore curves; were required to model the shear behaviour of a laminate with a transition at 7.55 s^{-1}. In the work presented here, the Cowper-Symonds scaling was unable to converge to a solution for the response of ultimate shear strain with increasing shear strain rate, as shown in Table 6.3. Johnson-Cook scaling was also considered, however, the regression models resultant R^2 values were < 0.8 for representing the longitudinal strain and shear strain at yield. As a result, a linear phenomenological model (Figure 6.5) of the mechanical behaviour of the composite reviewed in Chapters 4 and 5 was employed with linear interpolation conducted between the determined data points.

Table 6.2: Typical values used for Shokrieh et al. in Cowper-Symonds in-plane shear regression model [119].

Mechanical Property	α	$1/C$	ψ
Ultimate shear strength (MPa)	29.027	17.462	0.076
Shear modulus (GPa)	5.173	-1.177	0.043
Ultimate shear strain (%) $\dot{\gamma} < 7.55$ s^{-1}	0.0309	3.87×10^{-4}	-0.5
Ultimate shear strain (%) $\dot{\gamma} > 7.55$ s^{-1}	0.0305	4.45×10^{-6}	1.5

Table 6.3: R2 value for different non-linear regression models

Mechanical Property	LS-DYNA notation	Units	Non-linear Regression Model	
			Cowper-Symonds	Johnson-Cook
Tensile strength	XT/YT	MPa	0.8672	0.9067
Tensile strain	E11T/E22T	mm/mm	0.6938	0.7724
Shear stress at yield	TAU1	MPa	0.9632	0.9592
Shear strain at yield	GAMMA1	mm/mm	0.9217	0.7842
Ultimate shear strength	SC	MPa	0.9587	0.9474
Ultimate shear strain	GMS	mm/mm	-5 (failed)	0.9987

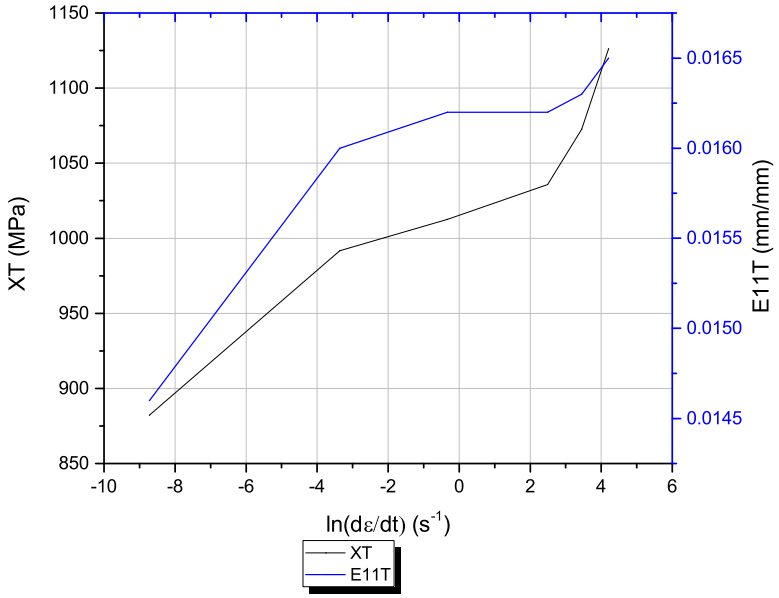

(a)

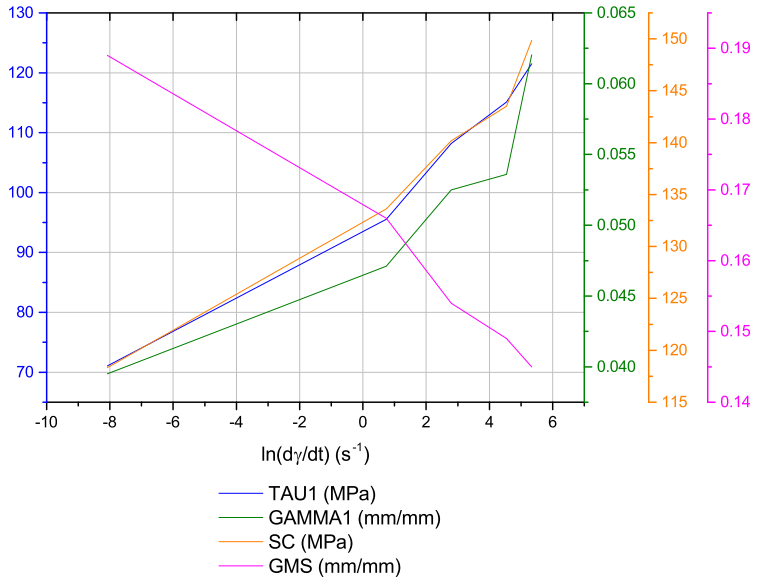

(b)

Figure 6.5: Linear phenomenological model employed within *MAT_058 to represent the (a) tensile; strength (XT) and strain (E11T), and (b) shear; strength at yield (TAU1), strain at yield (GAMMA1), ultimate strength (SC) and ultimate strain (GMS), properties of the composite material system.

6.2.2.1 Tension

The effect of strain rate was reviewed in LS-DYNA on an ISTS coupon length scale composed of 1 mm quad type 16 elements as shown in Figure 6.6. The laminate was modelled using four plies within *PART_COMPOSITE with $\beta = 0$ for each ply. Initially the model was developed to merely simulate the response of the coupons gauge length, however, applying the prescribed motion to the upper set of nodes when simulating only the gauge length response produced virtual stress concentrations that caused the structure to fail prematurely. As a result the full coupon was modelled including the tabs and this was found to alleviate the stress concentrations and induce failure at the centre of the gauge. The tabs were modelled using *MAT_ELASTIC with modulus set to 68.9 GPa to replicate the aluminium tabbing. The prescribed motion was derived from the experimental response of the coupon to establish the same average strain rate and applied to a coating of rigid shells at the free surface of tabs, with only Y DOF. The stationary gripped surface was modelled using rigid shells on the tab surface fixed in all DOF. A cross-section positioned at the centre of the coupon was used to measure the load induced in the part.

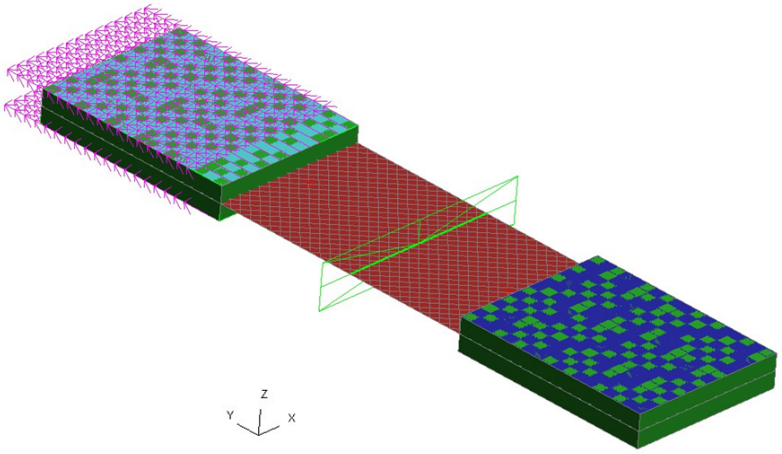

Figure 6.6: ISTS coupon (width 28.1 mm - full dimensions Figure 4.19) model to review the effect of tensile strain rate modelling within *MAT_058, tabs are modelled using *MAT_001 (68.9 GPa), a cross section through the centre of the specimen is used to measure load and the experimental derived velocity is applied as a prescribed motion.

The average experimental tensile stress-strain plots are shown in Figure 6.7 along with the modelled *MAT_058 responses. As recorded in the previous chapter the

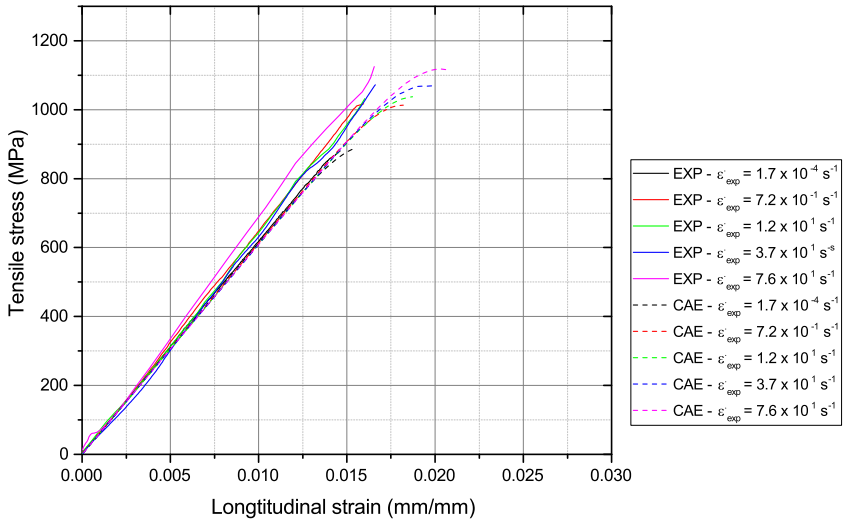

Figure 6.7: Comparison of the experimental and *MAT_058 modelled tensile stress-strain response of the ISTS specimen with increasing strain rate.

experimental response increases in stiffness with strain rate, the specimens also have greater strain to failure prior to increasing strength with strain rate. In contrast, the modelled behaviour is of constant stiffness with increasing ultimate strain and strength with strain rate due to the constraints of the material card. As with the quasi-static model, the brittle fracture cannot be predicted due to the limited m parameter. As a result the ultimate strain input in the load curve LCE11T and LCE22T is ignored by the model which strains significantly further than the experimental result.

The effect of the increasing ultimate strain and lack of stiffness adjustment was reviewed by integrating both the modelled and experimental responses to derive the strain energy. A comparison between the modelled and experimental strain energy is provided in Table 6.4. At quasi-static rates of loading the model absorbs 15.4 % more energy as a result of the inability to replicate the truly brittle fracture. As the strain rate is increased in both the model and experimental this inaccuracy is increased. When a longitudinal strain rate of 7.6 x 10^{1} s^{-1} is applied the strain energy was over predicted by 27.0 % relative to the experimental response at that strain rate.

Table 6.4: Comparison of the experimental and modelled strain energies induced through during tensile loading of the ISTS specimen.

Experimental strain rate (s^{-1})	Experimental strain energy (J)	Modelled strain energy (J)	Difference (%)
1.7×10^{-4}	15.6	18.0	15.4
7.2×10^{-1}	19.8	23.9	20.7
1.2×10^{1}	19.9	24.9	25.1
3.7×10^{1}	20.5	25.8	25.9
7.6×10^{2}	23.7	30.1	27.0

6.2.2.2 In-plane shear

Rate sensitive in-plane shear modelling used the same methodology outlined in Section 6.2.2.1, with a few modifications. The gauge area was extended and widened to replicate the ISSS coupon, and the composite laminate was also composed of eight plies with $\beta = 45$.

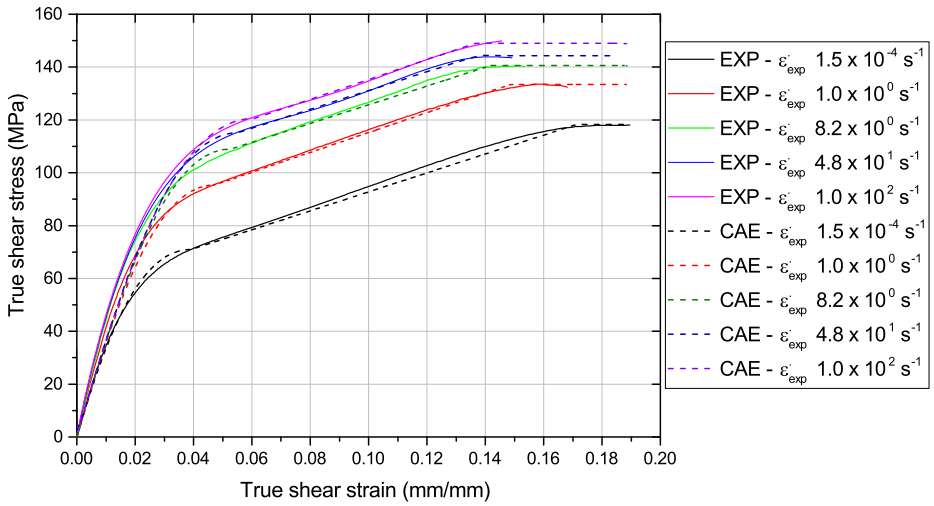

Figure 6.8: Comparison of the experimental and *MAT_058 modelled shear stress - shear strain response of the ISSS specimen with increasing strain rate.

The experimental and *MAT_058 modelled true shear stress - true shear strain response is shown in Figure 6.8. The laminate can be seen to undergo the bi-linear response of each of the separate strain rates that were investigated. As with the tensile response, shear modulus is not dictated by the applied strain rate, therefore the stiffness of the experimentally obtained results is not capable of being replicated. This does not have an effect on the ability to predict the yield point, since both *TAU1* and *GAMMA1* are increasing with strain rate and m does not increase above 10. The linear behaviour between yield and peak shear stress shows good correlation with the experimental response. Beyond peak stress the ultimate shear strain is not able to be adjusted, as a result the component fails in accordance to the prescribed *ERODS* value and over predicts failure strain.

As a result of the high post failure minimum shear strength being maintained beyond the experimental failure shear strain, the strain energy increases significantly as shown in Table 6.5. When considering the quasi-static response (1.5×10^{-4} s^{-1}), the modelled response was observed to be within 1.3 % of the experiment. This inaccuracy is induced within the strain hardening of the experiment which does not follow a truly linear prediction as modelled in *MAT_058. At a strain rate of 1.0×10^{2} s^{-1} the modelled and experimental strain energies are 159.9 J and 116.8 J respectively, this equates to an additional 36.9 % strain energy being absorbed within each element prior to erosion.

Table 6.5: Comparison of the experimental and modelled strain energies induced through during tensile loading of the ISTS specimen.

Experimental strain rate (s^{-1})	Experimental strain energy (J)	Modelled strain energy (J)	Difference (%)
1.5×10^{-4}	117.0	115.5	1.3
1.0×10^{0}	121.4	139.2	14.6
8.2×10^{0}	117.4	150.2	28.0
4.8×10^{1}	117.2	152.2	29.9
1.0×10^{2}	116.8	159.9	36.9

The undesirable increase in strain energy post experimental fracture could be overcome by modifying the setup of the material card. Rather than setting the material card to replicate the bi-linear response of the composite as previously shown, setting TAU1 = SC and GAMMA1 = GMS, the exponential decay of the damage law between the origin and yield can be used to model the shear behaviour of the laminate as a parabolic function. The shear stress - shear strain curves plotted in

Figure 6.9 were modelled using this parabolic modelling methodology. In contrast to the experimental response which underwent bi-linear yield and strain hardening, the stiffness of the simulated parabolic response is initially less than the experiment. However,as the specimen strains further this initial reduced stiffness is compensated as ultimate shear strain is approached. Dictating ultimate failure using *TAU1* and *GAMMA1* enables *SLIMS* < 1, this has enabled the author to terminate the elements according to the experimentally observed rate sensitive failure shear strain.

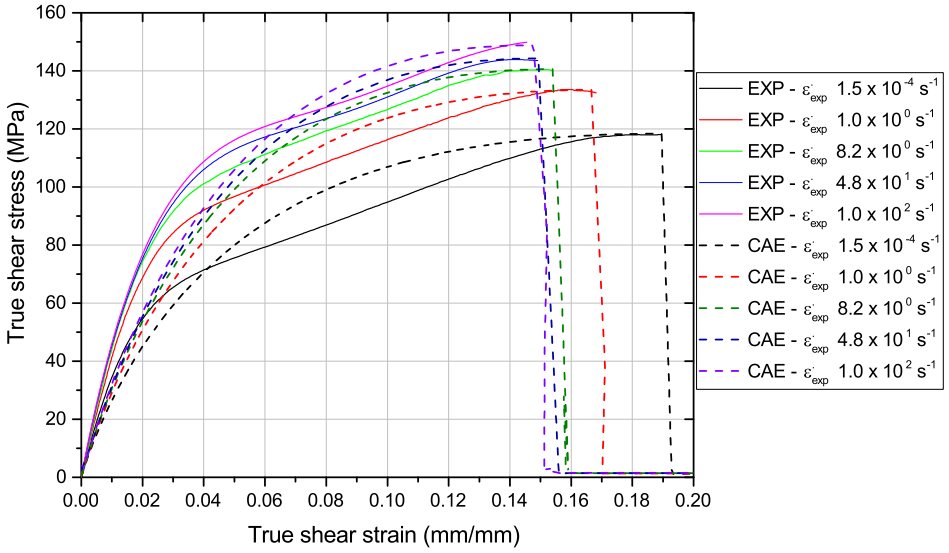

Figure 6.9: Comparison of the experimental and *MAT_058 modelled shear stress - shear strain response of the ISSS specimen with increasing strain rate. The conventional bi-linear shear response is replaced by a single exponential decay function as TAU1 = SC and GAMMA1 = GMS.

Unlike the bi-linear model which experienced increased strain energy as a result of the inability to terminate the element with truncating shear strain as the strain rate increased parabolic modelling of the failure resulted in a significantly reduced inaccuracy between 1.0 x 10^{0} s^{-1} and 1.0 x 10^{2} s^{-1} as shown in Table 6.6. However, the 8.1 % error modelled at 1.5 x 10^{-4} s^{-1} is greater than the 1.3 % observed with the bi-linear response. This is attributed to the longer plastic straining period observed at this experiment increasing the time which the modelled stress was greater than that experimentally observed due to the exponential decay. As the shear strain to failure was reduced the exponential decay reduced the time above experimental stress due to the constant stiffness initially applied. Due to the different advantages

and disadvantages of each of these two modelling approaches both the parabolic and bi-linear modelling approaches will be considered for correlation modelling with a multi-axial laminate under tensile loading in the following section.

Table 6.6: Comparison of the experimental and modelled strain energies induced through during tensile loading of the ISTS specimen.

Experimental strain rate (s^{-1})	Experimental strain energy (J)	Modelled strain energy (J)	Difference (%)
1.5×10^{-4}	117.0	126.5	8.1
1.0×10^{0}	121.4	124.8	2.8
8.2×10^{0}	117.4	120.4	2.6
4.8×10^{1}	117.2	120.3	2.7
1.0×10^{2}	116.8	122.5	4.9

6.3 Coupon level building block assessment on a quasi-isotropic ISTS tensile test at intermediate strain rates.

The previous section discussed the strain rate modelling capabilities of *MAT_058 when considering a single stress state, tension and tensile shear. The following section will review the ability of *MAT_058 to predict the failure of an ISTS coupon with a quasi-isotropic $[0/45]_S$ stacking sequence (ISTS-QI). In order to replicate the laminate, *PART_COMPOSITE was prescribed as four plies with $\beta = 0$ and $\beta = 45$ for the outer and inner plies respectively. The prescribed motion was prescribed based on the velocity recorded at the surface of the specimen using the DIC characteristics shown in Table 6.7. The prescribed velocity is determined based on the velocity measured at the specimen as this removes the compliance of the load frame which is not being modelled in this instance. Tests were conducted at three speeds, 0.6 mm/min using the Instron 5980 electromechanical frame and 0.08 ms^{-1} and 1 ms^{-1}on the VHS servo-hydraulic frame to induce nominal strain rates of 2.0×10^{-4} s^{-1}, 1.6×10^{0} s^{-1} and 2.0×10^{1} s^{-1}. At each of these respective test velocities the optical strain measurement was conducted at 2 Hz, 8 kHz and 30 kHz to provide a minimum of 50 data points per test.

Table 6.7: Summary of measurement methodology for GOM 12M 3D DIC for the validation of the intermediate speed specimen geometries.

Property	Unit			
Camera		GOM 12M	Photron SA-X2	Photron SA-X2
Lens		Titanar 100	Titanar 75b (20 mm extender tube)	Titanar 75b (20 mm extender tube)
Frame rate	Hz	2	8×10^3	30×10^3
Shutter speed	s	95×10^{-3}	73.75×10^{-6}	31.75×10^{-6}
Aperture		16	11	11
Imaging window	$pixel^2$	4000 x 3000	1024 x 1024	496 x 896
Calibration plate		CP20 55 x 44	CP20 MV 55 x 44	CP20 MV 55 x 44
Measurement volume	mm^3	125 x 90 x 70	65 x 65 x 45	31.48 x 56.86 x 45
Facet size	pixel	19	19	19
Step size	pixel	15	15	15
Spatial resolution	mm	0.59	1.21	1.21
Strain resolution	με	81.6	57.2	59.62
Displacement resolution	μm	0.07	0.19	0.10

The average experimental stress-strain response based on five repetitions at each of the prescribed test velocities is shown in Figure 6.10, the shaded area represents a single standard deviation of the mean. The behaviour at each of the strain rates was consistent with the response of the lamina with the lowest longitudinal strain - those loaded in tension. The laminate initially behaved in a linear manner, as the specimen strained it appeared to undergo a degradation in stiffness, this is thought to be due to the introduction of inter-lamina shear stresses induced by the varying fibre orientation. This was most prevalent at quasi-static strain rates with the dynamic experiments appearing to remain linear to a greater strain. Ultimate failure was the result of catastrophic transverse cracking (Figure 6.11). As observed in Chapter 5, stiffness, failure strength and failure strain all increased with strain rate. Unlike the failure of the longitudinal ISTS specimens, there was not a step change in the ultimate strain recorded between quasi-static and dynamic experiments.

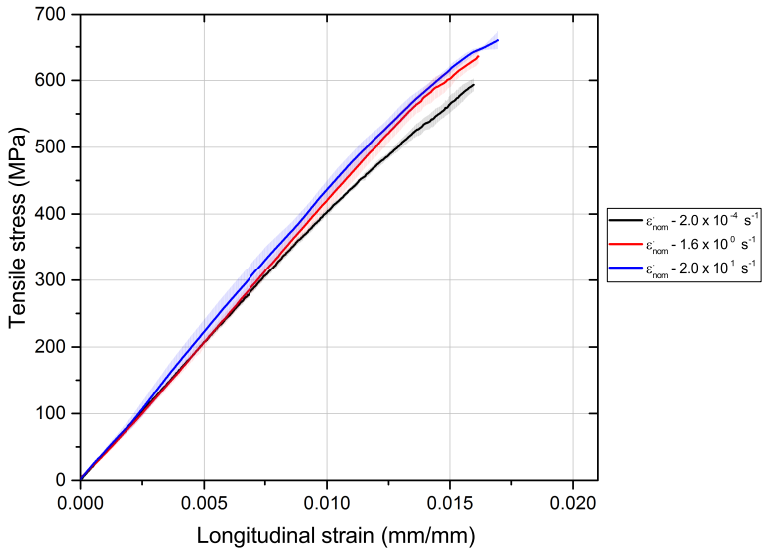

Figure 6.10: Experimental engineering stress-strain response of the ISTS-QI specimen evaluated at 0.2 mm/min, 0.08 ms^{-1} and 1 ms^{-1} to induce nominal strain rates of 2.0 x 10^{-4} s^{-1}, 1.6 x 10^{0} s^{-1} and 2.0 x 10^{1} s^{-1}. The shaded area represents 1 standard deviation of the five test mean result.

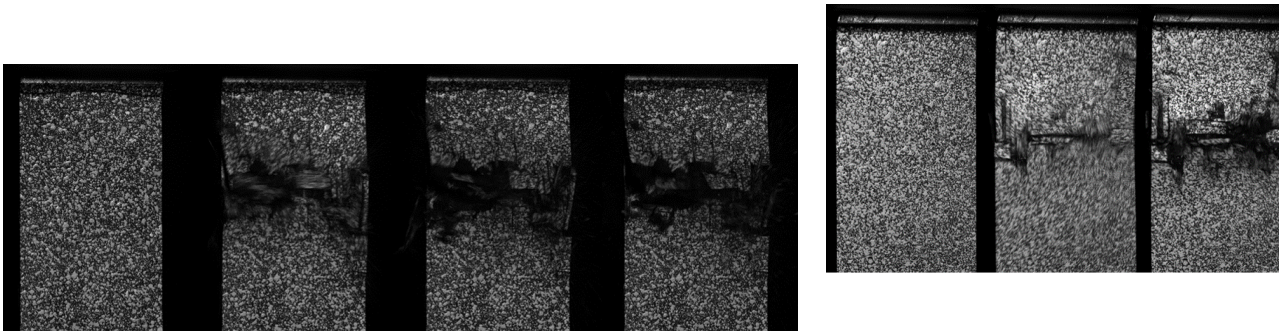

(a) (b)

Figure 6.11: Brittle fracture sequence of the ISTS quasi-isotropic specimen evaluated at an experimental strain rate of (a) 1.1 x 10^{0} s^{-1}and (b) 1.3 x 10^{1} s^{-1}.

The quasi-static model used a strain rate insensitive material card, and therefore was able to be run at a constant prescribed motion of 100 mms^{-1}in order to re-

duce computational time. In comparison, the displacement control of the nominal 1.6 x 10^0 s^{-1} and 2.0 x 10^1 s^{-1} experiments was calculated as the average velocity of the specimen over the test period. It was measured using the Photron 3D DIC equipment, and prescribed as 56 $mms^{-1}$and 647 mms^{-1} respectively. The V_f of each of the material cards was normalised to the mean 52 % derived from the thickness of the experimental components.

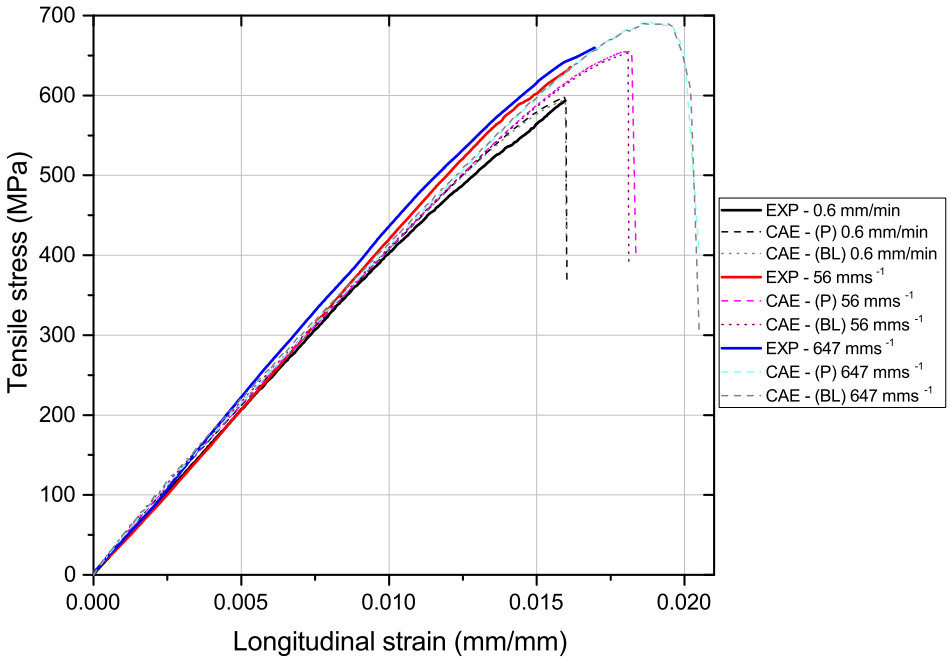

Figure 6.12: Comparison of the experimental and *MAT_058 modelled response (shear was modelled considering both the bilinear (BL) and parabolic (P) methodologies) of ISTS-QI specimens subjected to tensile experiments with a prescribed velocity of 0.6 mm/min (quasi-static), 56 mms^{-1} and 647 mms^{-1}.

Figure 6.12 compares the modelled and average experimental response at each of the test velocities. At quasi-static strain rates the both the parabolic and bi-linear models are capable of approximately predicting the desired failure stress and strain. The bi-linear quasi-static model was capable of predicting a failure stress of 594.6 MPa, 0.8 % greater than the experimental response, in contrast the parabolic shear model was 1.5 % greater than the experimental response. However, as the strain rate was increased, it can be seen in Figure 6.12 that the ultimate strain is over predicted by 12.7 % and 10.9 % in relation to that observed in both the 56 $mms^{-1}$and 647 mms^{-1}

experiments. This is thought to be a result of the tensile damage parameter m inducing greater tensile strains into the specimen due to the inability to replicate the true brittle fracture of the laminate. Despite the increase in ultimate strain, the in-accuracy in the predication of peak stress in both experiments was shown to be 2.8 % and 4.7 % respectively.

Table 6.8: Comparison of the experimental and modelled strain energies induced through during tensile loading of the ISTS specimen.

Nominal strain rate (s^{-1})	Average experimental velocity	Experimental peak stress (MPa)	Modelled peak stress (MPa) - Bi-linear shear	Modelled peak stress (MPa) - Parabolic shear
2.0×10^{-4}	0.6 mm/min	593.1	594.6	598.4
1.6×10^{0}	56 mms^{-1}	635.3	653.1	655.1
2.0×10^{1}	647 mms^{-1}	659.8	690.7	691.7

Figure 6.13 compares the modelled and average experimental responses based on the prescribed velocity. It is evident that irrespective of the strain rate applied the initial stiffness (subset (a)) is greater for the bi-linear modelling methodology that the parabolic approach. In contrast as the model approaches failure (subset (b)) the parabolic methodology has greater strength. This same phenomenon was observed in the previous Section when isolating the shear behaviour of the laminate. The advantage of using the parabolic methodology had been to induce the correct shear failure strain and thus the correct fracture energy. However,it appears that the ability to model the shear fracture behaviour has a significantly lower effect when combined with the tensile parameters, as both methodologies produce less than 1.5 % error on a quasi-static strain rate and at dynamic strain rates the error is considered to be driven by the tensile damage parameter.

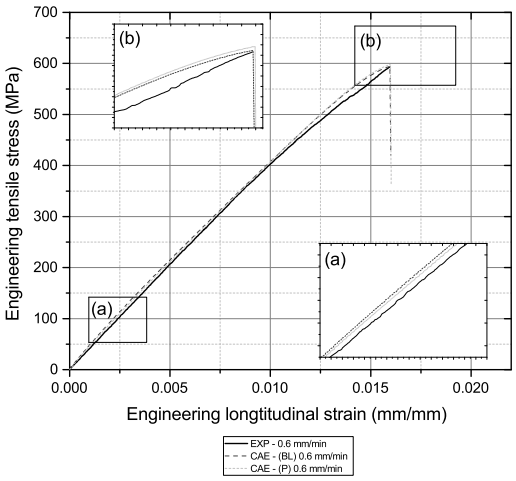

(a)

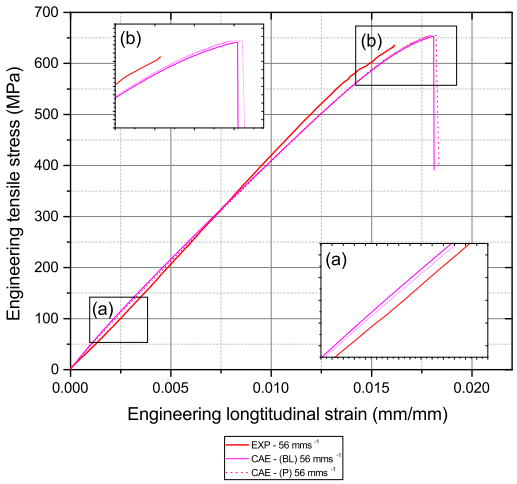

(b)

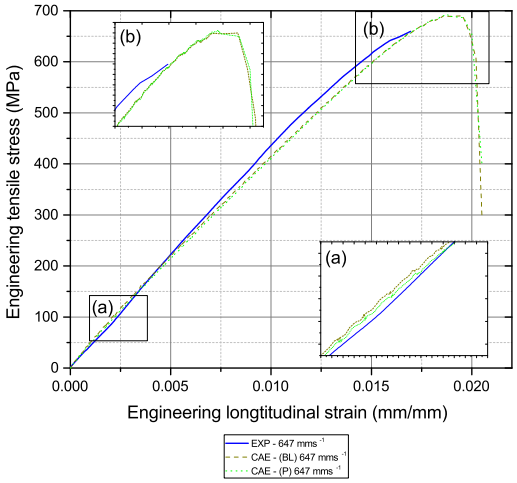

(c)

Figure 6.13: Individual comparison of the experimental and *MAT_058 modelled response of ISTS-QI specimens subjected to (a) quasi-static 0.6 mm/min, (b) 56 mms^{-1} and (c) 647 mms^{-1} tensile tests. The initial stiffness in each case is greater in the modelled response (inset (a)), particularly the bi-linear approach that closer represents the true shear stiffness of the laminate. As the model near erosion the parabolic modelling methodology induces greater strength (inset (b)) as the model nears a constant ultimate strength.

6.4 Summary

This Chapter has reviewed the ability to model the strain rate sensitivity of the automotive specific woven fabric evaluated in Chapter 5 using LS-DYNA and in particular the composite specific *MAT_058 laminated composite fabric material card.

The quasi-static characteristics of *MAT_058 were reviewed using single element models in order to induce the desired tension and shear stress states in a stable manner. The tensile single element model demonstrated that *MAT_058 is unable to induce the brittle fracture that is observed experimentally as a result of the exponential damage law that creates a more ductile fracture. The same damage law is more successfully employed to predict the shear stiffness degradation as a result of matrix cracking between the origin and yield. Post linear strain hardening, the peak shear stress must be maintained until element erosion as a result of the 100 % strength (SLIMS = 1.0) requirement to induce the bi-linear response.

Strain rate phenomena were introduced using a linear interpolation phenomenological model, popular Cowper-Symonds and Johnson-Cook scaling were trialled to model the sensitivity of the mechanical behaviour with strain rate. However, neither could produce a representative recessional fit to the experimental data. The inability to replicate the modulus strain rate sensitivity within *MAT_058, as well as the ductile fracture (induced by a constant m value) led to the over prediction of failure strain and therefore fracture energy when model the rate sensitivity in tension. At maximum experimental strain rate of 7.6×10^{1} s^{-1}, 27 % more strain energy was predicted in the model than observed experimentally. Modelling of the shear strain rate sensitive phenomena was also inhibited by the inability to model the effect of changing stiffness. However, the greater challenge was when attempting to terminate the element, since element erosion can not be manipulated with strain rate the bi-linear response strained to constant longitudinal strain of 0.22. As a result the induced strain energy was found to be 36.9 % greater than the experiment at a longitudinal strain rate of 1.0×10^{2} s^{-1}. Adjusting the material card to model a parabola instead of the bi-linear response *(TAU1 = SC and GAMMA1 = GMS)* enables the user to fail the model at the correct ultimate shear strength and strain location, thereby inducing approximately the correct strain energy density, however, it is compensated by having a significantly reduced stiffness.

The effect of increasing strain rate a multi-axial quasi-isotropic laminate was experimentally reviewed and modelled. Due to the tensile dominated failure mode

modelling the strain rate effect with either the bi-linear or parabolic method yielded little difference. At quasi-static strain rates the model was able to replicate the performance of the experimental laminate to within 0.8 %, however, dynamic modelling of the structure proved challenging. A difference of 12.7 % and 10.9 % was determined for the failure strain at 1.1 s^{-1} and 12.9 s^{-1} respectively, whilst the failure stress was 2.8 % and 4.7 % respectively. This is perceived to be a result of the inability to correctly predict the tensile brittle fracture.

Chapter 7

Conclusions and further work

7.1 Conclusions

This thesis has experimentally assessed the strain rate sensitivity of an automotive specific 12K 2 x 2 twill CFRP. It is the first time that the behaviour of such a large fabric architecture has been reported on a representative length scale at intermediate strain rates of up to 1.0×10^2 s^{-1}which are relevant to automotive crash environments. Since fabric architectures of this length scale have not previously been considered it required the development of high capacity test equipment and the proposal of a new coupon geometry. In order to achieve these objectives the work presented in this thesis can be divided into 3 main sections;

1. Development of an experimental method for characterising the in-plane tensile and shear behaviour of a 12K 2 x 2 twill CFRP laminate between nominal longitudinal strain rates of 2.2×10^{-4} $s^{-1}$and 1.0×10^2 s^{-1} (Chapters 3 and 4).
   (a) Quasi-static material characterisation according ASTM standards for tension and in-plane shear utilising non-contact optical surface strain measurement.
   (b) Establishment of a novel coupon sizing methodology in order to minimise the inertial load induced by the specimen, yet maintain the macroscopic global mechanical behaviour observed in standardised experiments.
   (c) Assessment of the current *state of the art* Instron fast jaw tensile dynamic characterisation methodology for reviewing continuous composite laminates.
   (d) Development of a new high capacity loading system capable of providing repeatable and robust experimental results.
2. Characterisation of the mechanical behaviour of 12K 2 x 2 twill CFRP laminate between nominal longitudinal strain rates of 2.2×10^{-4} $s^{-1}$and 1.0×10^2 s^{-1} (Chapter 5).

(a) Tensile characterisation using intermediate speed tensile specimen (ISTS) novel coupons.

(b) In-plane shear characterisation conducted using intermediate speed shear specimen (ISSS) novel specimen geometries.

3. Review of current FE strain rate modelling methodology within LS-DYNA (Chapter 6).

(a) Assessment of the composite specific *MAT_058 material card under quasi-static loading conditions.

(b) Building block correlation of the tensile strain rate behaviour using longitudinal $[0]_4$, shear $[45]_8$ and quasi-isotropic $[0/45]_s$ coupon length scale models.

7.1.1 Experimental methodology

The main conclusions generated during the development of experimental methods are drawn from Chapters 3, 4 and 5;

1. Quasi-static characterisation of the 12K 2 × 2 twill CFRP laminate was conducted according to ASTM D3039-14 (tension) and ASTM D3518-13 (in-plane shear) standards.

(a) DIC full field non-contact strain instrumentation was shown to be suitable for characterising the 12K 2 × 2 twill CFRP laminate as it defined the heterogeneous deformation of the woven structure on a full field length scale.

(b) Tension initially deformed in linear manner, as the specimen strained further brittle fracture occurred as a result of global transverse cracking, extensive weft cracking and splaying observed as the material approached ultimate strain. In comparison the in-plane shear response was bi-linear, the initial stiffness decayed as result of the initiation and propagation of shear matrix cracking, upon coalescence of these cracks the material stiffness was significantly reduced and strain hardening occurred as the fabric sheared until rupture.

2. A *state-of-the-art* fast jaw lost motion device (LMD) produced by Instron was reviewed and found to provide limited experimental repeatability and an inability to achieve the desired strain rates as a result of the requirement to use straight-sided composite specimens.

3. A novel composite specific high capacity LMD was developed on a prototype Instron platform. Fulcrum damping reduced premature excitement of the load cell ringing that was shown to affect the measured elastic properties. The lower jaw of the VHS was also re-designed so as to increase the acceleration length enabling strain rates of 320 s^{-1} to be achieved when using an ISTS specimen.

4. To overcome the size effects that are induced through the use of classical small dynamic specimen geometries employed in literature, novel specimens were developed that were capable of defining the heterogeneous 12K 2 x 2 twill CFRP laminate on a global representative length scale.

   (a) To minimise the inertial load of the specimen and reduce the input velocity to achieve a prescribed strain rate, a systematic specimen reduction technique was employed. Quadrangular windowing of the DIC surface strain measurement was used to determine the representative surface element (RSE) of the woven material system under both tensile and shear stress states. This defines the specimen geometry limit at which the heterogeneous strains represent the global laminate response.

      i. Under tensile elastic loading the strain field converged to a solution of 99.5 % of the global material response at approximately 1 unit $cell^2$, however, in order to capture the ultimate strength and strain of the laminate 2.81 unit $cells^2$ were required.

      ii. The shear RSE converged at 2.27 unit $cells^2$ at full fracture. However, at large deformations free edge effects in the specimen induced erroneous shear strains when measuring over a reduced ROI. As a result the shear specimen was widened to reduce the risk of free edge distortion of the global measurements over the reduced RSE.

   (b) The experimental response at quasi-static strain rates of two proposed tensile (ISTS) and shear (ISSS) specimens were statistically validated against the ASTM standard coupon data using *T-tests*, the subsequent P values greater than 0.05 demonstrated that the two specimen geometries yielded results that were not statistically different from one another at a 95 % confidence interval.

   (c) Ply drop off specimens were considered based on previous use in intermediate strain rate characterisation of UD laminates in literature. External and internal ply drop off samples were experimentally reviewed. Both variants failed prematurely as a result of inter-laminar damage initiating in the vicinity of the ply drop off. It was hypothesised that the 400 gsm fabric weight drop off created a large resin rich pocket from which the

damage propagated. As a result it was concluded that ply drop off specimens are not suitable for the characterisation of the considered 12K 2 x 2 twill CFRP laminate.

5. The large specimen that was required to produce a representative volume of the 12K 2 x 2 twill CFRP laminate resulted in high capacity specimens that induced the inertial effect of the high capacity specimen retarded the actuator causing non-constant experimental strain rates.

   (a) The lack of yield and necking phenomena required by the metallic high rate test standard to dictate the experimental strain rate required new limits to be defined.

   (b) To remove the initial strain rate rising period and large strain rate spikes as a result of local crack growth at fracture the experimental average strain rate and strain rate range in this thesis were determined at discrete strain ranges for ISTS ($\varepsilon_{(0.9\dot{\varepsilon}_{max})}$ to 1.4 % ε_{YY}) and ISSS (γ_{yield} to 11 % γ_{XY}) specimens alike.

      i. Each ISTS experiment was able to achieve the nominal stain rate based on the prescribed actuator velocity. However, once the actuator velocity was increased beyond 1 ms^{-1} the removal of the feedback loop resulted in an increase of the experimental strain rate range beyond the ±30 % of the average experimental strain rate (recommended in the metallic intermediate strain rate characterisation standard). As the test velocity was increased the non-linearity of the strain rate increased as a result of increasing strain rate rising period, whilst the strain at strain rate decay was delayed. Thus it is hypothesised that as the velocity is further increased the strain rate decay in the test will be reduced to a negligible level due to the higher kinetic energy of the LMD, however, the large variance will still exist as result of the increased strain rising period. Therefore it is not possible to induce a constant linear strain rate over the test period due to the highly brittle response of the laminate, since each of the strain rates observed remained independent of each other, it is considered acceptable to consider the generated data dependent upon the experimental response. However, the exposed non-linearity shows the importance of analysing the experimental strain rate (particuarlly when characterising mateirals in the longitudinal axis) rather than depending upon the nominal rates as observed in literature.

      ii. The ISSS specimen has a lower capacity relative to the ISTS coupon and therefore the difference between experimental and nominal strain

rate is significantly reduced. The experimental response derived at a nominal strain rate of 10 s^{-1} was the initial in-plane shear experiment to be run in open loop. Due to the low kinetic energy the experimental strain rate was found to be on the ±30 % variance threshold. However,as the input velocity was increased the strain variance was reduced and the difference between nominal and experimental strain rates was reduced. It is clear that the definition of strain rate between yield and 11 % γ_{XY} removes the non-linear strain rate rising period for each of the experiments and was not affected by localised cracking as the test approached fracture.

7.1.2 Intermediate strain rate characterisation of the 12K 2 x 2 twill CFRP laminate

Since this is the first attempt to characterise a material system with such a heterogeneous length scale at intermediate strain rates it is not possible to draw direct conclusions against other literature, however, the following conclusions can be drawn from the experimental research in Chapter 5.

7.1.2.1 Longitudinal tension strain rate sensitivity

1. The quasi-statically observed linear elastic straining prior to brittle fracture was prevalent at all strain rates investigated in this thesis.

2. Modulus was shown to follow an exponential growth with increasing strain rate, a 13.7 % increase was observed between experimental strain rates of 2.2 x 10^{-4} $s^{-1}$and 6.4 x 10^{1} s^{-1}. The increase was observed to be significantly greater than that for UD CFRP laminates which is thought to be a result of the stiffening of the large resin-rich pockets within the material created at interstitial sites and tow boundaries.

3. Ultimate tensile strain was shown to increase by 8.8 % between experimental strain rates of 2.2 x 10^{-4} $s^{-1}$and 3.5 x 10^{-2} s^{-1}. Further discrete strain rate rises between 3.5 x 10^{-2} $s^{-1}$and 6.4 x 10^{1} s^{-1} showed that at a 95 % confidence level, the ultimate strain was not statistically strain rate dependent. As a result of the lack of a growth, Cowper-Symonds and Johnson-Cook phenomenological scaling is unable to model the behaviour with a desirable R^2 value. The lack of an inherent viscoelastic behaviour for carbon fibres suggests that the increase

in ultimate strain with strain rate is a result of the delayed rate of damage coalescence as the loading period reduces.

4. Ultimate tensile strength was shown to increase with strain rate. Since the specimens continued to exhibit elastic brittle failure, the increased strength with strain rate is related to effect of increasing modulus. A 12.4 % increase in ultimate strength occurred between 2.2×10^{-4} $s^{-1}$and 3.5×10^{-2} s^{-1}, considering the only slight increase in modulus over this regime, the increased strength is a result of the large change in ultimate strain that was observed over the same strain rate regime. Between 3.5×10^{-2} $s^{-1}$and 6.4×10^{1} s^{-1} the strength was found to increase in an exponential manner by a further 11.9 % as a result of the increased modulus since the ultimate strain was shown to not increase above 3.5×10^{-2} s^{-1}.

5. Poissons ratio was shown to be insensitive to strain rate within the experimental error. The damage propagation visible on the DIC surface strain maps demonstrated extensive matrix cracking within and surrounding the weft tows and each specimen failed as a result of a transverse crack irrespective of the experimental strain rate. It is suggested that the global failure mechanism was not dependent upon strain rate.

7.1.2.2 In-plane shear strain rate sensitivity

1. The bi-linear in-plane shear response with strain hardening observed between yield and fracture that was observed at quasi-static strain rates was replicated at longitudinal experimental strain rates up to 1.04×10^{2} s^{-1}. In general literature highlighted that the rate sensitivity of the matrix dominated properties to be greater than those in tension. Strain rate dependency for the 12K 2 x 2 twill CFRP was observed in the shear modulus, shear stress and shear strain at yield and the shear stress and shear strain at fracture.

2. Shear modulus was shown to be highly sensitive to the longitudinal strain rate applied, increasing exponentially by 37.7 % between longitudinal experimental strain rates of 1.6×10^{-4} $s^{-1}$and 1.04×10^{2} s^{-1}.

3. The yield point of the shear experiment occurs at coalescence of matrix cracking prior to strain hardening induced by the rotation of the warp and weft fibres to the direction of the fibres.

   (a) Yield shear stress was shown to increase 65.7 % between 1.6×10^{-4} $s^{-1}$and 1.04×10^{2} s^{-1}, the increase was statistically different at each of the discrete strain rates evaluated.

(b) Yield shear strain increased 62.5 % between 1.6×10^{-4} s^{-1} and 1.04×10^{2} s^{-1}. The yield shear strain measured at 6.7×10^{-2} s^{-1} decreased, this was in opposition of the trend and the increasing yield shear stress at 6.7×10^{-2} s^{-1}. As a result, this yield shear strain was considered to be a result of the strain smoothing induced by the optical measurement settings required to conduct the experiment at such a low strain rate on the Instron VHS. The difference between 4.7×10^{1} s^{-1} and 1.04×10^{2} s^{-1} was not statistically different and suggests a plateauing of the shear strain at yield as the strain rate may increase further.

4. Ultimate failure of the specimen was found to occur at higher shear stress yet lower shear strain as the strain rate was increased.

   (a) Ultimate shear stress was statistically independent at each characterised longitudinal strain rate. An increase of 18.8 % was observed between 1.6×10^{-4} $s^{-1}$and 8.2×10^{0} s^{-1}, this was similar to the sensitivity of a 3K 2 x 2 twill CFRP in literature that was investigated up to 2.0×10^{1} s^{-1}, potentially highlighting an insensitivity of the fabric architecture when loaded in shear when considering ultimate shear stress. Further increasing the strain rate between 8.2×10^{0} s^{-1} and 1.04×10^{2} s^{-1} yielded an additional 7.5 % increase in ultimate strength.

   (b) Ultimate shear strain was shown to decrease by 20.4 % as the strain rate was increased between 1.6×10^{-4} $s^{-1}$and 1.04×10^{2} s^{-1}.

7.1.3 Finite element analysis

In order for automotive OEM's to incorporate intermediate strain rate data into their CAE models, a review of the appropriate finite element modelling methodologies was required. LS-DYNA composite material card *MAT_058 simulated the behaviour of the ISTS, ISSS and quasi-isotropic ISTS (ISTS-QI) coupons at different experimental strain rates. The key findings expressed in Chapter 6 were;

1. *MAT_058 is capable of replicating the bi-linear shear behaviour of the laminate succinctly at quasi-static strain rates. However, tensile behaviour was too ductile as a result of the damage constant m within the exponential damage parameter ω_{ij}, m was found to have a predetermined maximum value that was incapable of modelling the true brittle fracture.

2. Strain rate phenomena were introduced to the ISTS and ISSS coupon models using a linear interpolation phenomenological model.

(a) Inability to model the modulus rate sensitivity (observed experimentally in Chapter 5) combined with the increased ductility (a result of a pre-determined maximum m value) resulted in an increase of 37 % in the modelled strain energy of the ISTS coupon at 6.4×10^{1} s^{-1} .

(b) Modelling of the ISSS specimen induced inaccuracies as a result of;

i. Inability to increase the shear modulus prior to yield reduced the strain energy relative to the experiment, however, due to the ductility induced in the experiment as matrix cracking the model was able to accurately define the yield point as the stain rate was increased.

ii. Bi-linear modelling of the material required ERODS to eliminate the element; since this is insensitive to strain rate the ultimate strain energy was found to be over predicted by 39 % at a longitudinal strain rate of 1.04×10^{2} s^{-1}.

iii. Parabolic modelling of the material card employing the exponential decay of the elements stiffness to replicate the bi-linear response was shown to be able to generate a better prediction of the total strain energy of the element, predicting between - 2.4 % and 5.2 % of the experimental strain energy density between 1.6×10^{-4} $s^{-1}$and 1.04×10^{2} s^{-1}. However, this approach lacked significant stiffness early on in the element loading cycle.

3. An experimental study on the strain rate sensitivity of ISTS-QI specimens showed similar behaviour to the ISTS longitudinal specimen with increasing stiffness, strength and ultimate strain with increasing strain rate. As a result of the tensile based behaviour, the modelled errors were also consistent with the ISTS response;

(a) Quasi-static strain rate modelling was matched to the experimental coupon response, with errors of 0.8 % and 1.5 % observed using the shear bi-linear and parabolic modelling methodologies respectively.

(b) Modelling at intermediate experimental strain rates of 1.1×10^{0} s^{-1} and 1.3×10^{1} s^{-1} was unable to predict the engineering stress-strain response. The modelled peak longitudinal strain was over-predicted by 12.7 % and 10.9 % at 1.1×10^{0} s^{-1} and 1.3×10^{1} s^{-1} respectively, at the same strain rates, peak stress was observed to be 3.1 % and 4.9 % greater than observed experimental. The over prediction in tensile strain was a result of the inability to model the true brittle fracture of the elements due to the damage constant m.

4. This thesis has advanced the understanding of the automotive specific woven

laminates at intermediate strain rates. Significant changes to the laminates mechanical performance have been captured using a novel loading mechanism; that enables specimens to be evaluated at representative length scales for their heterogeneous nature, at a range of strain rates that are representative of loading in an automotive crash environment. However, the current material cards commercially available within LS-DYNA require further development in order to represent these strain rate sensitivities succinctly. It is recommended by the author that attention must be made by automotive OEM's to improve the material cards with which they model composite data to improve the virtual development of composite vehicles.

7.2 Limitations of this research

1. A limitation of this work is that due to the requirement of the VHS to travel the full distance of the actuator, the final fracture surfaces of the specimens cannot be reviewed for a detailed comparison of the damage mechanisms induced with increasing strain rate. A detailed understanding of the damage mechanisms would enable the author to discuss the effect of microscopic changes in the behaviour of the fibre and matrix constituents as well as the interface with increasing strain rate. Thus further improving the authors understanding of the macroscopic rate sensitivity.

2. In order to induce nominal longitudinal strain rates of 6.7×10^{-2} s^{-1} in the tension and shear specimens the VHS had to be used in conjunction with ASTM sized specimens (150 mm free length). The requirement to use the 1 MP Photron SA-X2 cameras to achieve a sampling frequency of 500 Hz resulted in a spatial resolution of 2.41 mm, significantly lower than those used at other strain rates. To compensate for the low spatial resolution the facet size was reduced until the strain resolution induced a 1 % measurement error (124.7 $\mu\varepsilon$), however, the spatial resolution induced a level of smoothing.

   (a) Strain smoothing was most prevalent when reviewing the large scale deformations of the shear specimens. The shear strain at yield was seen to initially decrease before increasing as the strain rate was increased, likewise, the reduced ultimate shear strain is thought to have been exaggerated.

   (b) Use of the Photron SA-X2 cameras in tandem with the ISTS and ISSS specimen geometries and a LMD fitted low speed servo-hydraulic machine or electro-mechanical machine would enable the user to prescribe the

desired strain rates whilst maintaining a comparable spatial resolution with the remainder of the study (~1.2 mm).

3. In order to account for the variable resin volumes, Chapter 5 normalised all data to a 52 % FVF. However, the relationship between FVF and strain rate is unknown therefore this scaling may be found to be inappropriate in the future. However, as shown in this thesis it provided a consistent methodology to attempt to compare components produced with an inherent variability.

4. Due to the inability to use dog boned specimens, the strain gauged secondary load measurement conventionally employed within metallic intermediate strain rate testing could not be applied. Piezoelectric load cells have been identified in literature as suitable for use up to 100 s^{-1} and therefore no secondary measurement was sought for this thesis. However, the lack of a secondary load measurement required the filtering of load data at the upper strain rates achieved in this research. As a result, the increases in strength at maximum strain rate for both the ISTS and ISSS specimens could be affected by noise of the load cell.

   (a) Future work using the high capacity slack adaptor should implement a secondary load measurement, especially when characterising materials above the strain rates applied in this thesis.

   (b) Mass reduction of the high capacity slack adaptor will also increase the natural frequency, thereby reducing the ringing observed in the load cell. However, this will also reduce the ability of the VHS to overcome the inertia induced by the specimen. Thus it must be considered with care.

5. The large scale specimens required to produce representative material data induced retardation of the experimental strain rate. It was shown that as the strain rate was increased the decay of strain rate was reduced, this was particularly prevalent in the ISSS shear experiments. However, within the tensile experiments the experimental range of strain rates was larger than desirable based on the metallic standard (± 30 % of $\dot{\varepsilon}_{exp}$). It is unclear the effect of such non-linearity of the strain rate on the quality of the mechanical data.

7.3 Further work

The research conducted throughout this Ph.D. raises questions which require further work in order to ensure that the characterisation of composite laminates at interme-

diate strain rates are properly understood in order to better predict the crashworthy response of automotive components.

7.3.1 Materials

This thesis has focused on the experimental analysis of a previously uninvestigated architecture consisting of a large unit cell twill weave CFRP laminate which is typical within the automotive industry. To gain a more detailed understanding of the response the following key areas of research is required;

1. Analysis of the fabric architecture involving the same fibre and matrix constituents with different tow sizes and weave patterns. This will provide an understanding of the effect of fabric architecture on the strain rate sensitivity.

2. Establishment of the change in damage propagation that occurs in a longitudinal tensile specimen between longitudinal experimental strain rates of 2.2 $\times 10^{-4}$ $s^{-1}$and 3.5 $\times 10^{-2}$ s^{-1}. This thesis showed that a significant change in the tensile behaviour occurred between these two strain rates with the ultimate strain increasing by 8.8 %, whilst the ultimate strength increased by 12.4 %. Further analysis with a low speed servo-hydraulic frame with a feedback loop will enable the user to conduct interrupted testing enabling them to review the damage hysteresis and understand whether the strain rate has a significant effect on the damage mechanisms occurring in this critical regime.

3. Real world automotive structures rarely contain perpendicular warp and weft fibres, either due to distortion during weaving and pre-pregging or the forming of complex drawn components. Since off-axis loading has been shown in this research and literature to be more sensitive to strain rate further research is required to establish the effect of real world weave angles and induced shear states with strain rate.

4. Composite structures are often produced with variable thickness and as a result variable FVF. No prior research has been conducted reviewing the effect of FVF on strain rate for a common laminate, since matrix sensitivity is greater than that of the fibre it is highly unlikely to follow the linear relationship as assumed in this thesis.

7.3.2 Experimental methodology

The novel experimental methodology employed in this thesis has provided greater experimental repeatability and thus has enabled the author to conducted experiments and obtain statistically significant results which was not possible with the Instron fast jaw system. However, the following recommendations would further enhance the collected data;

1. Damage propagation during intermediate tests should be reviewed to enable the user to attempt to observe fracture surfaces. However, previous attempts have either required the pre-straining of specimens [107], or post shear pin induced buckling [108].
2. The large range of experimental strain rate experienced as a result of the high inertial load of the specimen may be reduced by controlling the velocity drive input file. Open loop control of the VHS does not allow live feedback to the VHS. The new upper and lower jaw mechanisms of the high capacity slack adaptor developed in this thesis provides the user with a highly experimentally repeatable loading methodology. As a result the valve drive could be heuristically developed based on previous experiments in order to induce a variable velocity experiment that may overcome the inertial load of the specimen. This would enable the user to review if the variable strain rate induced in this thesis is potentially reducing the quality of the generated mechanical data.
3. The longitudinal strain rate can be further increased to 320 s^{-1} for the ISTS specimen developed in this thesis. However, this will require secondary strain and load instrumentation.
    (a) Secondary strain instrumentation must provide a higher temporal resolution since increasing the strain rate further will induce smoothing errors based on the reduced spatial resolution when maintaining the full-field measurement of the Photron SA-X2 based DIC. Continued measurement of the surface strain using 3D DIC with a higher spatial resolution and lower temporal resolution will still enable the user to review the heterogeneous strain development on the surface of the specimen. Therefore dual sided analysis using DIC and a high rate optical extensometer would be ideal in order provide greater temporal resolution of the strain at such strain rates.
    (b) Secondary load measurement must be applied to the fixturing in order to remove the ringing of the load cell that became prevalent during the upper strain rates achieved in this thesis.

4. The research conducted in this thesis has built upon knowledge that has been presented over decades of experimental composite characterisation. The author recommends that this knowledge be captured as a characterisation standard. This would provide both academia and industry with a mechanism for generating comparable data, an initial starting point for the determination of this standard is a round robin testing project; reviewing the use of the multiple fixturing solutions to determine their effect on a constant set of materials.

7.3.3 Finite element methods

This thesis has shown that the current *MAT_058 composite specific material card is unsuitable for use with strain rate dependent data. As a result the following recommendations for further research are made;

1. Despite initial reluctance due to additional costs a review of *MAT_162, which enables the user to model the strain rate sensitivity of tensile and shear modulus, is required.

2. Pending the outcome of the *MAT_162 material card review a custom user defined (VUMAT) material card may should be reviewed, the world wide failure exercise has shown that composite failure criterion are suitable for use [200]. However, it is the integration of the strain rate data and in particular the inclusion of shear and tensile modulus that must be reviewed. Control of the bi-linear shear response requires further review in order to dictate the correct stiffness and erosion of the elements.

References

[1] Department for Transport. Transport statistics Great Britain. https://www.gov.uk/government/statistics/transport-statistics-great-britain-2014 (17/2/2015), December 2014.

[2] Department for Transport. Greenhouse gas emissions (env02). https://www.gov.uk/government/statistical-data-sets/env02-greenhouse-gas-emissions (17/2/2015), December 2013.

[3] European Parliment and the Council of the European Union. Regulation (ec) no 443/2009 - setting emission performance standards for new passenger cars as part of the community's integrated approach to reduce co2 emissions from light-duty vehicles. https://eur-lex.europa.eu/legal-content/EN/TXT/PDF/?uri=CELEX:32009R0443&from=EN (20/2/2015), April 2009.

[4] UK. Automotive Council. Passenger car low carbon technology roadmap. https://www.automotivecouncil.co.uk/2013/09/automotive-technology-roadmaps/ (13/11/2014), September 2013.

[5] D Crolla, D.A. Cao. The impact of hybrid and electric powertrains on vehicle dynamics, control systems and energy regeneration. *Vehicle System Dynamics*, 50:95–109, 2012.

[6] IHS Automotive. The weight reduction in automotive design report. http://supplierinsight.ihsmarkit.com/_assets/sampledownloads/ihs-automotive-weightreduction-2016report-sample_1453384273.pdf (22/2/15), 2016.

[7] L. Genta, G. Morello. *The Automotive Chassis*, volume 1: Components Design. Springer, 2009.

[8] G. Davies. Chapter 2 - design and material utilization. In G Davies, editor, *Materials for Automobile Bodies*, pages 17 – 91. Butterworth-Heinemann, Oxford, 2012HSarw.

[9] M. Traverso. Jaguar unveils the xe midsize sedan. http://www.carbodydesign.com/gallery/2014/09/jaguar-unveils-the-xe-midsize-sedan/4/ (25/2/2015), September 2014.

[10] R. Heuss, N. Muller, W van. Sintern, A. Starke, and A. Tschiesner. Lightweight, heavy impact. https://www.mckinsey.com/ /media/mckinsey/dotcom/client_service/automotive(26/10/2014), February 2012.

[11] M. White. Lightweight vehicle technology. Castle Bromwich UK: Jaguar Land Rover Ltd, 2012 (02/05/2012).

[12] N. Warrior. Lightweighting. In *Cenex LCV*, pages 1–28, (05/12/14); Millbrook, Bedfordshire, September 2014. LCV2014.

[13] McLaren Cars. Mclaren p1 design and innovation. http://cars.mclaren.com/ultimate-series/p1/design-and-innovation (03/11/2014), 2014.

[14] P. Malnati. Prepreg compression molding makes its commercial debut. www.compositesworld.com/articles/prepreg-compression-molding-makes-its-commercial-debut (03/05/2016), January 2015.

[15] BMW. The future of urban mobility. www.bmw.com/com/en/insights/corporation/bmwi/concept.html (05/03/2015).

[16] J. Sloan. BMW Leipzig: The epicenter of i3 production. http://www.compositesworld.com/articles/bmw-leipzig-the-epicenter-of-i3-production (08/10/2014), 2014.

[17] G. Savage. Formula 1 composites engineering. *Engineering Failure Analysis*, 17(1):92–115, 2010.

[18] J. Hill. Ashesively bonded structural composites for aston martin vehicles. techreport, Ford Motor Company, Research and Advanced Engineering, PO BOX 2053, MD3135, Dearborn, MI 48104-2053, USA, 2003.

[19] European Aluminium Association. The aluminium automotive manual. https://www.european-aluminium.eu/media/1543/1_aam_body-structures.pdf (22/04/2018), 2013.

[20] C. Bisagni, G. Di Pietro, L. Fraschini, and D. Terletti. Progressive crushing of fiber-reinforced composite structural components of a formula one racing car. *Composite Structures*, 68(4):491–503, May 2005.

[21] C. Bisagni. Experimental investigation of the collapse modes and energy absorption characteristics of composite tubes. *International Journal of Crashworthiness*, 14(4):365–378, July 2009.

[22] P. Feraboli, C. Norris, and D. McLarty. Design and certification of a composite thin-walled structure for energy absorption. *International Journal of Vehicle Design*, 44(3-4):247–267, 2007.

[23] P. Feraboli, B. Wade, F. Deleo, and M. Rassaian. Crush energy absorption of composite channel section specimens. *Composites Part: A*, 40(8):1248–1256, August 2009.

[24] G. Belingardi, G. Chiandussi. Vehicle crashworthiness design - general principles and potentialities of composite material structures. In Serge Abrate, editor, *Impact Engineering of Composite Structures*, pages 193 – 264. Springer, USA, 2011.

[25] D. Hull. A unified approach to progressive crushing of fibre-reinforced composite tubes, 1990.

[26] A Mamalis, D.E. Manolakos, George Demosthenous, and M.B. Ioannidis. *Crashworthiness of Composite Thin-Walled Structural Components*. 1998.

[27] A. G. Mamalis and D. P. Papapostolou. Experimental investigation of strain rate effects on the crushing characteristics of composite sandwich panels. *International Journal of Crashworthiness*, 15(6):581–603, 2010.

[28] A. G. Mamalis, K. N. Spentzas, D. E. Manolakos, M. B. Ioannidis, and D. P. Papapostolou. Experimental investigation of the collapse modes and the main crushing characteristics of composite sandwich panels subjected to flexural loading. *International Journal of Crashworthiness*, 1(4):349–362, 2008.

[29] A. G. Mamalis, D. E. Manolakos, M. B. Ioannidis, and D. P. Papapostolou. On the response of thin-walled cfrp composite tubular components subjected to static and dynamic axial compressive loading: experimental. *Composite Structures*, 69(4):407–420, 2005.

[30] A. G. Mamalis, D. E. Manolakos, M. B. Ioannidis, and D. P. Papapostolou. The static and dynamic axial collapse of cfrp square tubes: Finite element modelling. *Composite Structures*, 74:213–225, 2005.

[31] W.C. Hwang, C.S. Cha, and I.Y. Yang. Optimal crashworthiness design of cfrp hat shaped section member under axial impact. *Materials Research Innovations*, 15(sup1):324–327, 2011.

[32] H. Hamada, S. Ramakrishna, and H. Sato. Effect of fiber orientation on the energy absorption capability of carbonÂ fiber / PEEK composite tubes. *Journal of Composite Materials*, Composite Materials, 1996.

[33] D. Hull and T. W. Clyne. *Introduction to composite materials*. Cambridge Solid State Science Series. Cambridge University Press, 1 edition, August 1996.

[34] N. Tucker and K. Lindsey. *An Introduction to Automotive Composites*. Rapra Technology Limited, Shrewsbury, SY4 4NR, 2002.

[35] P.K. Mallick. Thermoset matrix composites for lightweight automotive structures. In P.K. Mallick, editor, *Materials, Design and Manufacturing for Lightweight Vehicles*, Woodhead Publishing Series in Composites Science and Engineering, pages 208 – 231. Woodhead Publishing, 2010.

[36] R. Hillermeier, T. Hasson, L. Friedrich, and C. Ball. Advanced thermosetting resin matrix technology for next generation high volume manufacture of automotive composite structures. *SAE Technical Paper*, 2013.

[37] M. Arnold. Technical specialist, penso consulting. Automotive OEM composite material requirements, Personal Communication (28/04/2017), 2017.

[38] Z. Zong G. Sun Q. Li Q. Liu, Y. Lin. Lightweight design of carbon twill weave fabric composite body structure for electric vehicle. *Composite Structures*, 97(Supplement C):231 – 238, 2013.

[39] F.C. Campbell. Chapter 1 - introduction to composite materials and processes: Unique materials that require unique processes. In F.C. Campbell, editor, *Manufacturing Processes for Advanced Composites*, pages 1 – 37. Elsevier Science, Amsterdam, 2004.

[40] D.H.J.A. Lukazewicz. Automotive composite structures for crashworthiness. In Ahmedd Elmarakbi, editor, *Advanced Composite Materials for Automotive Applications*, pages 99 – 125. John Wiley & Sons Ltd, United Kingdom, 2014.

[41] Gurit. *Guide to composites*. www.Gurit.com, Isle of Wight, 2012.

[42] E.J. Barbero. *Introduction to Composite Materials Design*. Taylor and Francis Group, USA, 2011.

[43] T. Araki. CAE current status and future plan in nissan motor. https://altairatc.com/europe/Presentations_2010/Keynotes_Friday/Nissan_ARAKI/101029EHPC

[44] V. Cannillo and A. R. Boccaccini. Finite element modelling of brittle matrix composites. In C. Soutis and P. W. R. Beaumont, editors, *Multi-scale modelling of composite material systems*, pages 356–373. Woodhead Publishing Ltd, Cambridge England, 2005.

[45] R. Rolfes, G. Ernst, M. Vogler, and C. Huhne. *Mechanical Response of Composites*, volume 10, chapter Material and Failure Models for Textile Composites, pages 27–56. Springer, International Center for Numerical Methods in Engineering (CIMNE) Technical University of Catalunya (UPC) Edificio C-1, Campus Norte UPC Gran CapitÃ¡n, s/n 08034 Barcelona, Spain, 2008.

[46] N. V. Carvalho, S. T. Pinho, and P. Robinson. Numerical modelling of woven composites: biaxial loading. *Composites Part A: Applied Science and Manufacturing*, 43(8):1326–1337, August 2012.

[47] K. Woo and J.D. Whitcomb. A post-processor approach for stress analysis of woven textile composites. *Composites Science and Technology*, 60(5):693 – 704, 2000.

[48] O. Cousigne, D. Moncayo, D. Coutellier, P. Camanho, and H. Naceur. Numerical modeling of nonlinearity, plsticity and damage in cfrp-woven composites for crash simulations. 115:14, 2014.

[49] E.J. Barbero. *Finite Element Analysis of Composite Materials*. Taylor and Francis Group, USA, 2008.

[50] M. W. Hyer. *Stress analysis of fiber-reinforced composite materials*. WCB McGraw-Hill, 2009.

[51] P. L. Kollar and G. S. Springer. *Mechanics of Composite Structures*. Cambridge University Press, 2003.

[52] S. T. Pinho, L. Iannucci, and P. Robinson. Physically based failure models and criteria for laminated fibre-reinforced compsites with emphasis on fibre kinking. part ii: Fe implementation. *Composites Part A: Applied Science and Manufacturing*, 37(5):766–777, May 2006.

[53] M. J. Soden P. D. Kaddour, K.S. Hinton. A comparison of the predictive capabilities of current failure theories for composite laminates: additional contributions. *Composite Science and Technology*, 64(3-4):449–476, March 2004.

[54] I. M. Daniel, B. T. Werner, and J. S. Fenner. Strain-rate-dependent failure criteria for composites. *Composite Science and Technology*, 71(3):357–364, February 2011.

[55] D R Ray, B C. Rathore. A review on mechanical behavoir of frp composites at different loading speeds. *Critical Reviews in Solid State and Materials Sciences*, 40(2):119–135, 2015.

[56] I. M. Daniel and O. Ishai. *Engineering mechanics of composite materials*. Oxford University Press, New York, 1994.

[57] J.E. Bailey, P.T. Curtis, and A. Parvizi. On the transverse crack and longtitudinal splitting behaviour of glass and carbon fibre reinforced epoxy cross-ply laminates and the effect of poisson and thermal generated strain. *Proceedings of the Royal Society of London. Series A, Mathematical and Physical Sciences*, 366(1727):599–623, July 1971.

[58] P.D. Soden, M.J. Hinton, and A.S. Kaddour. Lamina properties, lay-up configurations and loading conditions for a range of fibre-reinforced composite laminates. *Composites Science and Technology*, 58(7):1011 – 1022, 1998.

[59] R. Talreja. Damage analysis for structural integrity and durability of composite materials. *Fatigue & Fracture of Engineering Materials & Structures*, 29(7):481–506, 2006.

[60] R. Talreja. Matrix and fiberâmatrix interface cracking in composite materials. In Ramesh Talreja, , and Janis Varna, editors, *Modeling Damage, Fatigue and Failure of Composite Materials*, Woodhead Publishing Series in Composites Science and Engineering, pages 87 – 96. Woodhead Publishing, 2016.

[61] P.A. Carraro and M. Quaresimin. A damage based model for crack initiation in unidirectional composites under multiaxial cyclic loading. *Composites Science and Technology*, 99:154 – 163, 2014.

[62] W.C. Hwang, K.S. Lee, Y.J. Yang, J.H. Choi, J.A. Jung, C.S. Cha, and I.Y. Yang. A study on collapse behavior and energy absorption capability of al/cfrp hybrid structural member. In *3rd International Conference on Smart Materials and Nanotechnology in Engineering*, volume 8409 of *Proceedings of SPIE-Int Soc Optical Engineering*, 2011.

[63] M. R. Wisnom. Size effects in the testing of fibre-composite materials. *Composite Science and Technology*, 59(13):1937–1957, 1999.

[64] L. Gorbatikh and S.V. Lomov. *Modeling Damage, Fatigue and Failure of Composite Materials*, chapter 3 - Damage accumulation in textile composites, pages 41 – 59. Woodhead Publishing Series in Composites Science and Engineering. Woodhead Publishing, 2016.

[65] U.A. Khashaba and M.A. Seif. Effect of different loading conditions on the mechanical behavoir of [0/_pm45/90]s woven composites. *Composite Structures*, 74(4):440–448, 2006.

[66] A. Nosier and M. Maleki. Free-edge stresses in general composite lamiantes. *International Journal of Mechanical Sciences*, 50:1435–1447, 2008.

[67] P. Lecomte-Grosbras, B. Paluch, and M. Brieu. Free edge effects study in laminated composites using digital image correlation: effect of mateiral and geometrical singularities. In *ICEM 14 - 14th International Conference on Experimental Mechanics*, pages 1435–1447, Poitiers, France, 2010. EPJ Web of Conferences.

[68] F. C. Campbell. *Structural Composite Materials*. ASM International, Materials Park, Ohio, USA, 2010.

[69] G. Nicoletto and E. Riva. Failure mechanisms in twill-weave laminates: Fem predictions vs. experiments. *Composites Part A: Applied Science and Manufacturing*, 35(7):787 – 795, 2004.

[70] T. Osada, A. Nakai, and H. Hamada. Initial fracture behavior of satin woven fabric composites. *Composite Structures*, 61(4):333 – 339, 2003. Selected Papers from the Symposium on Design and Manufacturing of Composites.

[71] U. Himayat A R. Harland V V. Silberschmidt. Characterisation of mechanical behaviour and damage analysis of 2D woven composites under bending. *Composites Part B: Engineering*, 75(Supplement C):156 – 166, 2015.

[72] L. Li, S.V. Lomov, and X. Yan. Correlation of acoustic emission with optically observed damage in a glass/epoxy woven laminate under tensile loading. *Composite Structures*, 123:45 – 53, 2015.

[73] N. De Greef, L. Gorbatikh, A. Godara, L. Mezzo, S.V. Lomov, and I. Verpoest. The effect of carbon nanotubes on the damage development in carbon fiber/epoxy composites. *Carbon*, 49(14):4650 – 4664, 2011.

[74] M.S. Kiasat and M.R. Sangtabi. Effects of fiber bundle size and weave density on stiffness degradation and final failure of fabric laminates. *Composites Science and Technology*, 111(Supplement C):23 – 31, 2015.

[75] MY Matveev, AC Long, LP Brown, and IA Jones. Effects of layer shift and yarn path variability on mechanical properties of a twill weave composite. *Journal of Composite Materials*, 51(7):913–925, 2017.

[76] J.L. Abot, R.D. Gabbai, and K. Harsley. Effect of woven fabric architechture on interlaminar mechanical response of composite materials: an experimental study. *Journal of Reinforced Plastics and Composites*, 30(24):2003–2014, 2011.

[77] J. L. Abot, A. Yasmin, A. J. Jacobsen, and I. M. Daniel. In-plane mechanical, thermal and viscoelastic properties of a satin fabric carbon/epoxy composite. *Composites Science and Technology*, 64(2):263–268, 2004.

[78] X. Tang and J.D. Whitcomb. Progressive failure behaviors of 2d woven composites. *Journal of Composite Materials*, 37(14):1239–1259, 2003.

[79] D. Cai, G. Zhou, X. Wang, C. Li, and J. Deng. Experimental investigation on mechanical properties of unidirectional and woven fabric glass/epoxy composites under off-axis tensile loading. *Polymer Testing*, 58(Supplement C):142 – 152, 2017.

[80] D. Cai, J. Tang, G. Zhou, X. Wang, C. Li, and V.V. Silberschmidt. Failure analysis of plain woven glass/epoxy laminates: Comparison of off-axis and biaxial tension loadings. *Polymer Testing*, 60(Supplement C):307 – 320, 2017.

[81] T. Lisle, C. Bouvet, M. L. Pastor, T. Rouault, and P. Marguerès. Damage of woven composite under tensile and shear stress using infrared thermography and micrographic cuts. *Journal of Materials Science*, 50(18):6154–6170, Sep 2015.

[82] E.S. Greenhalgh. The influence of fibre architecture in the failure of polymer composites. In *Failure Analysis and Fractography of Polymer Composites*, Woodhead Publishing Series in Composites Science and Engineering, pages 279 – 355. Woodhead Publishing, 2009.

[83] N. De Greef, L. Gorbatikh, S.V. Lomov, and I. Verpoest. Damage development in woven carbon fiber/epoxy composites modified with carbon nanotubes under tension in the bias direction. *Composites Part A: Applied Science and Manufacturing*, 42(11):1635 – 1644, 2011.

[84] L. Wang, B. Zhao, J. Wu, C. Chen, and K. Zhou. Experimental and numerical investigation on mechanical behaviors of woven fabric composites under off-axial loading. *International Journal of Mechanical Sciences*, 141:157 – 167, 2018.

[85] Y. Liang, H. Wang, and X. Gu. In-plane shear response of unidirectional fiber reinforced and fabric reinforced carbon/epoxy composites. *Polymer Testing*, 32(3):594–601, 2013.

[86] K. Mehmet. Investigation of damage initiation and propagation in 2 Ã 2 twill woven carbon/epoxy multi-layer composites. *Textile Research Journal*, 81(4):412–428, 2011.

[87] C. Park, C. Kan, and W. Hollowell. Investigation of crashworthiness of structural composite components in frontal and side ncap tests. *SAE Technical Papers*, 2013.

[88] P.K.C. Wood, C.A. Schley, M. Buckley, and J. Smith. An improved test procedure for measurement of dynamic tensile mechanical properties of automotive sheet steels, 2007.

[89] C. Hopmann and J. Klein. Determination of strain rate dependent material data for fea crash simulation of polymers using digital image correlation. *Computational Materials Science*, 100:181 – 190, 2015. Special Issue on Advanced Simulation Methods.

[90] A.M.S. Hamouda and M.S.J. Hashmi. Testing of composite materials at high rates of strain: advances and challenges. *Journal of Materials Processing Technology*, 77(1-3):327–336, 1998.

[91] International Organisation for Standardisation. (2010). iso 26203-1:2010 metallic materials – tensile testing at high strain rates – part 1: Elastic-bar-type systems. Geneva, Switzerland: ISO.

[92] International Organisation for Standardisation. (2011). iso 26203-2:2011. metallic materials – tensile testing at high strain rates – part 2: Servo-hydraulic and other test systems. Geneva, Switzerland: ISO, 2011.

[93] International Organisation for Standardisation. (2007). BSI ISO 18872:2007: Plastics - determination of tensile properties at high strain rates. Geneva, Switzerland: ISO, 2007.

[94] D. Kuriyama Y. Uenishi A. Yan B. Borsutzki, M. Cornette. Recommendations for dynamic tensile testing of sheet steels. Technical report, International Iron and Steels Institute, 2005.

[95] K.A. Brown, R. Brooks, and Warrior N.A. The static and high strain rate behavior of a commingled e-glass/polypropylene woven fabric composite. *Composite Science and Technology*, 70(2):272–283, 2010.

[96] S. Barré, T. Chotard, and M.L. Benzeggagh. Comparative study of strain rate effects on mechanical properties of glass fibre-reinforced thermoset matrix composite. *Composites Part A: Applied Science and Manufacturing*, 27(12):1169 – 1181, 1996.

[97] H. Kolsky. An investigation of the mechanical properties of materials at very high rates of loading. *Proceedings of the Physical Society. Section B*, 62(11):676, 1949.

[98] J. Harding, E.O. Wood, and J.D. Campbell. Tensile testing of materials at impact rates of strain. *Journal of Mechanical Engineering Science*, 2(2):88–96, 1960.

[99] G.H. Staab and A. Gilat. High strain rate response of angle-ply glass/epoxy laminates. *Journal of Composite Materials*, 29:1308–1320, 1995.

[100] P. Paul, N. Ledford, R. Mohrmann, and M. May. Testing of cfrp at high strain rates with the split hopkinson tension bar - evaluation of testing quality. *17th European Conference on Composite Materials, ECCM 2016*.

[101] A. Gilat, R.K. Goldberg, and G.D. Roberts. Experimental study of strain-rate behaviour of carbon/epoxy composite. *Composites Science and Technology*, 62(10-11):1469–1476, 2002.

[102] E.J Lang and T.W. Chou. The effect of strain gage size on measurement errors in textile composite materials. *Composites Science and Technology*, 58(3):539 – 548, 1998.

[103] B. Koohbor, S. Ravindran, and A. Kidane. Experimental determination of representative volume element (rve) size in woven composites. *Optics and Lasers in Engineering*, 90:59–71, 2017.

[104] C. Schley P. Wood. *Strain Rate Testing of Metallic Materials and their Modelling for use in CAE based Automotive Crash Simulation Tools (Recommendations and Procedures)*. Smithers, 2009.

[105] Weighing Panel and Force Measurement. Guide to the measurement of force, 2013.

[106] D. Zhu, S. D. Rajan, B. Mobasher, A. Peled, and M. Mignolet. Modal analysis of a servo-hydraulic high speed machine and its application to dynamic tensile testing at an intermediate strain rate. *Experimental Mechanics*, 51(8):1347–1363, Oct 2011.

[107] G. Battams. *The use of optical techniques to assess the damage tolerance of composite mateirals*. PhD thesis, University of Southampton, 2014.

[108] J. Fitoussi, F. Meraghni, Z. Jendli, G. Hug, and D. Baptiste. Experimental methodology for high strain rate tensile behaviour analysis of polymer matrix composites. 65:15, 2005.

[109] M. Pinnell, S. Hill, and A. Minch. Special concerns in high strain rate tensile testing of polymers. In *SAE 2006 World Congress & Exhibition*. SAE International, apr 2006.

[110] M.L. Longana. *Intermediate strain rate testing methodologies and full-field optical strain measurement techniques for composite materials characterisation*. PhD thesis, University of Southampton, 2014.

[111] Instron. Instron high strain rate vhs system.

[112] G.C. Jacob, J.M. Starbuck, J.F. Fellers, S. Simunovic, and R.G. Boeman. Strain rate effects on the mechanical properties of polymer composite materials. *Journal of Applied Polymer Science*, 94(1):296–301, 2004.

[113] D. Rathore B C. Ray. A review on mechanical behavior of frp composites at different loading speeds. *Critical Reviews in Solid State and Materials Sciences*, 40(2):119–135, 2015.

[114] X. Xiao. Dynamic tensile testing of plastic mateirals. 27:15, 2008.

[115] XL. Al-Mihaidi R. AL-Zubaidy, H. Zhao. Mechanical behaviour of normal modulus carbon fibre reinforced polymer (cfrp) and epoxy under impact tensile loads. *Procedia Engineering*, 10:2453–2458, 2011.

[116] M.M. Shokrieh and M.J. Omidi. Investigating the transverse behavior of glassâepoxy composites under intermediate strain rates. *Composite Structures*, 93(2):690 – 696, 2011.

[117] J. Berthe, E. Deletombe, M. Brieu, G. Portemont, and P. Paulmier. Dynamic characterization of cfrp composite materials â toward a pre-normative testing protocol â application to t700gc/m21 material. *Procedia Engineering*, 80(Supplement C):165 – 182, 2014. 3rd International Symposium on Aircraft Airworthiness (ISAA 2013).

[118] H Cui, D. Thomson, A. Pellegrino, J. Wiegand, and N Petrinic. Effect of strain rate and fibre rotation on the in-plane shear response of ±45Â° laminates in tension and compression tests. *Composites Science and Technology*, 135(Supplement C):106 – 115, 2016.

[119] M.M. Shokrieh and M.J. Omidi. Investigation of strain rate effects on in-plane shear properties of glass/epoxy composites. *Composite Structures*, 91(1):95–102, 2009.

[120] I.M. Daniel and T. Liber. Testing of fiber composites at high strain rates. *Civil and Environmental Engineering*, pages 1003–1018, 02 1978.

[121] M.M. Shokrieh and M.J. Omidi. Tension behavior of unidirectional glass/epoxy composites under different strain rates. *Composite Structures*, 88(4):595–601, 2009.

[122] W. Wang, G. Makarov, and R. A. Shenoi. An analytical model for assessing strain rate sensitivity of unidirectional composite laminates. *Composite Structures*, 69:45–54, 2005.

[123] M. L. Longana, J. M. Dulieu-Barton, and S. Syngellakis. Application of optical measurement techniques to high strain rate deformations in composite materials. *7th Asian-Australasian Conference on Composite Materials 2010, ACCM 2010*, pages 76–79.

[124] M.V. Hosur, J. Alexander, U.K. Vaidya, and S. Jeelani. High strain rate compression response of carbon/epoxy laminate composites. *Composite Structures*, 52(3-4):405–417, 2001.

[125] H.M. Hsiao and I.M. Daniel. Strain rate behaviour of composite materials. *Composites Part B: Engineering*, 29(5):521–533, 1998.

[126] H. Koerber, J. Xavier, and P. P. Camanho. High strain rate characterisation of unidirectional carbonepoxy im78552 in transverse compression and in-plane shear using digital image correlation. *Mechanics of Materials*, 42(11):1004–1019, 2010.

[127] L. Welsh and J. Harding. Effect of strain rate on the tensile failure of woven reinforced polyester resin composites. *Journal de Physique Colloques,*, 45 (C5):405–414., 1985.

[128] K. Kawata, M. Itabashi, and H. Kimura. *Mechanical Characterization of Solids in High Strain Rate Tension*, pages 1–16. Springer Japan, Tokyo, 1996.

[129] R. Gerlach, C. R. Siviour, N. Petrinic, and J. Wiegandm. Experimental characterisation of the strain rate dependent failure and damage behaviour of 3d composites. *DYMAT 2009*, pages 219–225, 2009.

[130] R. Foroutan, J. Nemes, H. Ghiasi, and P. Hubert. Experimental investigation of high strain-rate behaviour of fabric composites. *Composite Structures*, 106:264–269, 2013.

[131] R. Foroutan. *High Strain Rate Behavior of Woven Composite Materials*. PhD thesis, Department of Mechanical Engineering McGill University, Montreal, 2009.

[132] X. Chen, Y. Li, Z. Zhi, Y. Guo, and N. Ouyang. The compressive and tensile behavior of a 0/90 c fiber woven composite at high strain rates. *Carbon*, 61(Supplement C):97 – 104, 2013.

[133] N. K. Naik, N. M. Yernamma, R. Thoram, R. Gadipatri, and V. R. Kavala. High strain rate tensile behavior of woven fabric e-glass/epoxy composite. 29:9, 2010.

[134] T. Bergmann, S. Heimbs, and M. Maier. Mechanical properties and energy absorption capability of woven fabric composites under ±45Â° off-axis tension. *Composite Structures*, 125(Supplement C):362 – 373, 2015.

[135] X. Li, Ying. Yan, L. Guo, and C. Xu. Effect of strain rate on the mechanical properties of carbon/epoxy composites under quasi-static and dynamic loadings. *Polymer Testing*, 52(Supplement C):254 – 264, 2016.

[136] K. Naresh, K. Shankar, B.S. Rao, and R. Velmurugan. Effect of high strain rate on glass/carbon/hybrid fiber reinforced epoxy laminated composites. *Composites Part B: Engineering*, 100(Supplement C):125 – 135, 2016.

[137] D.G. Lee, S.T. Lim, and S.S. Cheon. Impact energy absorption characteristics of composite structures. *Composite Structures*, 50(4):381–390, 2000.

[138] O.I. Okoli. The effects of strain rate and failure modes on the failure energy of fibre reinforced composites. *Composite Structures*, 54:299–303, 2001.

[139] H.L. Gowtham, Jayaram R. Pothnis, G. Ravikumar, and N.K. Naik. High strain rate in-plane shear behavior of composites. *Polymer Testing*, 32(8):1334 – 1341, 2013.

[140] N. Taniguchi, T. Nishiwaki, and H. Kawada. Experimental characterization of dynamic tensile strength in unidirectional carbon/epoxy composites. *Advanced Composite Materials*, 17(2):139–156, 2008.

[141] Q. Northfield. Jaguar land rover,. Volume fraction requirements for automotive, motorsport and aerospace industries. Personal Communication (12/9/17), September 2017.

[142] M Arnold. Technical specialist, penso consulting. Personal Communication, 2017.

[143] Cytec Industrial Materials (Derby) Ltd Solvalite710-1-38400-1250 datasheet, July 10.

[144] K. Akiyama. Development of PCM* technology. In *SPEA Automotive*. Mitsubishi Rayon Co Ltd, 2011.

[145] Instron. 5980 floor model systems for high-capacity universal testing.

[146] International Organisation for Standardisation. (2012). BSI ISO 527-1:2012: Plastics – determination of tensile properties – part 1: General principles. Geneva, Switzerland: ISO.

[147] American Society for Testing Materials. (2013). ASTM D3518/D3518M-13: In plane shear response of polymer matrix composite materials by tensile test of aÂ ±45 $laminate.Pennsylvania, USA : ASTM.$

[148] D.O. Adams and D.F. Adams. Tabbing guide for composite test specimens, October 2002.

[149] Cytec Industrial Materials. Vta260.

[150] American Society for Testing Materials. (2011). ASTM ASTM D4762-11A: Standard guide for testing polymer matrix composite materials. Pennsylvania, USA: ASTM.

[151] American Society for Testing Materials. (2012). ASTM D3579/D3579M-12: ASTM standard for the Shear Properties of Composite Materials by V-Notched beam method. Pennsylvania, USA: ASTM.

[152] American Society for Testing Materials. (2007). ASTM D4255/D4255M-01: Standard test method for In-plane shear polymer matrix composite materials by rail shear method. Pennsylvania, USA: ASTM.

[153] American Society for Testing Materials. (2013). ASTM D7078-12: ASTM standard for the Shear Properties of Composite Materials by V-Notched Rail Shear Method. Pennsylvania, USA: ASTM.

[154] S. Lee and M. Munro. Evaluation of in-plane shear test methods for advanced composite materials by the decision analysis technique, 1986.

[155] American Society for Testing Materials. (2013). ASTM D3518/D3518M-13: In plane shear response of polymer matrix composite materials by tensile test of aÂ ± 45 $laminate.Pennsylvania, USA : ASTM, 2013$.

[156] W. Chen, H. Hao, D. Hughes, Y. Shi, J. Cui, and Z.-X. Li. Static and dynamic mechanical properties of expanded polystyrene. *Materials and Design*, 69:170–180, 2015.

[157] M. L. Longana, J. M. Dulieu-Barton, F. Pierron, and S. Syngellakis. Identification of constitutive properties of composite materials under high strain rate loading using optical strain measurement techniques. In *7th International Conference on Composites Testing and Model Identification*, 2015.

[158] American Society for Testing Materials. (2011). ASTM ASTM D4762-11A: Standard guide for testing polymer matrix composite materials. Pennsylvania, USA: ASTM.

[159] D.R. Hufner and M.L. Accorsi. A progressive failure theory for woven polymer-based composites subjected to dynamic loading. *Composite Structures*, 89(2):177 – 185, 2009.

[160] B. Pan, K. Qian, H. Xie, and A Asundi. Two-dimensional digital image correlation for in-plane displacement and strain measurement: a review. *Measurement Science and Technology*, 2009.

[161] A. Michael, JJ. Orteu, and H.W. Schreier. Two-dimensional and three-dimensional computer vision. In *Image Correlation for Shape, Motion and Deformation Measurements: Basic Concepts,Theory and Applications*, pages 1–16. Springer US, Boston, MA, 2009.

[162] GOM. Aramis user manual - software (v6.3 and higher), 2013.

[163] G Crammond, S W Boyd, and J M Dulieu-Barton. Dynamic analysis of composite marine structures using full-field measurement techniques. *Journal of Marine Engineering and Technology*, 13(1):23–35, 2014.

[164] GOM. Aramis user information - hardware, 2013.

[165] Albert J. P. Theuwissen. Cmos image sensors: State-of-the-art. *Solid-State Electronics*, 52:5, 2008.

[166] P. L. Reu and T. J. Miller. The application of high-speed digital image correlation, 2008.

[167] Photron. Fastcam sa-x2 fastcam sa-x2 rv hardware manual.

[168] D. Lee, H. Tippur, and P. Bogert. Quasi-static and dynamic fracture of graphite/epoxy composites: An optical study of loading-rate effects. *Composites Part B: Engineering*, 41(6):462 – 474, 2010.

[169] D. Lee, H. Tippur, and P. Bogert. Dynamic fracture of graphite/epoxy composites stiffened by buffer strips: An experimental study. *Composite Structures*, 94(12):3538 – 3545, 2012.

[170] H Koerber and P.P. Camanho. High strain rate characterisation of unidirectional carbonepoxy im7-8552 in longitudinal compression. *Composites Part A: Applied Science and Manufacturing*, 42(5):462 – 470, 2011.

[171] H. Koerber, J. Xavier, P.P. Camanho, Y.E. Essa, and F. MartÃn de la Escalera. High strain rate behaviour of 5-harness-satin weave fabric carbonâepoxy composite under compression and combined compressionâshear loading. *International Journal of Solids and Structures*, 54:172 – 182, 2015.

[172] M. Flores, D. Mollenhauer, V. Runatunga, T Beberniss, D. Rapking, and M. Pankow. High-speed 3d digital image correlation of low-velocity impacts on composite plates. *Composites Part B: Engineering*, 131:153 – 164, 2017.

[173] M. Pankow, B. Justusson, A. Salvi, A.M. Waas, Chian-Fong Yen, and Seth Ghiorse. Shock response of 3d woven composites: An experimental investigation. *Composite Structures*, 93(5):1337 – 1346, 2011.

[174] F. Coussa, J. Renard, S. Joannes, JC. Teissedre, R. Bompoint, and N. Feld. A consistent experimental protocol for the strain rate characterization of thermoplastic fabrics. *Strain*, 53(3):1475–1305, 2017.

[175] M. A. Sutton, J.-J. Orteu, and H. W. Schreier. *Image Correlation for Shape, Motion and Deformation Measurements*, chapter Practical Considerations for Accurate Measurements with DIC, pages 229–252. Springer, Boston, MA, 2009.

[176] American Society for Testing Materials. (2014). ASTM D3039/D3039M-14 Standard test method for tensile properties of polymer matrix composite materials. Pennsylvania, USA: ASTM.

[177] GOM. Photron product information, 2017.

[178] H. Haddadi and S. Belhabib. Use of rigid-body motion for the investigation and estimation of the measurement errors related to digital image correlation technique. *Optics and lasers in Engineering*, 46(2):185–196, 2008.

[179] G. Crammond, S. W. Boyd, and J. M. Dulieu-Barton. Speckle pattern quality assessment for digital image correlation. *Optics and lasers in Engineering*, 51:11, 2013.

[180] D. Lecompte, A. Smits, S. Bossuyt, H. Sol, J. Vantomme, D. Van Hemelrijck, and A. M. Habraken. Quality assessment of speckle patterns for digital image correlation. *Optics and lasers in Engineering*, 44(11):1132–1145, 2006.

[181] Y. Barranger, P. Doumalin, J. C. Dupre, and A. Germaneau. Digital image correlation accuracy: influence of kind of speckle and recording setup. *ICEM 14 â 14th International Conference on Experimental Mechanics*, 2010.

[182] M.V. d'Agostino, I. Giorgio, L. Greco, A. Madeo, and P. Boisseui. Continuum and discrete models for structures including (quasi-) inextensible elasticae with a view to the design and modeling of composite reinforcements. *International Journal of Solids and Structures*, 59:1 – 17, 2015.

[183] K. Saka and J. Harding. The deformation and fracture of hybrid reinforced composites undertensile impact. *Macro- and Micro-Mechanics of High Velocity Deformation and Fracture.*, pages 97–111, 1987.

[184] J. Solvay Hackett. Correspondence about the potential to use an autoclave moulding as alternative to compression moulding for solvalite 710-1-38Personal communication, October 2017.

[185] J. Solvay Hackett. Autoclave parameters for solvalite710-1-38Personal communication.

[186] K He, S.V Hoa, and R Ganesan. The study of tapered laminated composite structures: a review. *Composites Science and Technology*, 60(14):2643 – 2657, 2000.

[187] Livermore Software Technology Corporation. *LS-DYNA Keyword User's Manual Volume II Material models*, 2014.

[188] R.A. Beaumont. *Determining the effect of strain rate on the fracture of sheet steel*. PhD thesis, University of Warwick, 2012.

[189] J.O. Hallquist. *LS-Dyna Theory Manual*. Livermore Software Technology Corporation, 2006.

[190] C.T. Mottram, J.T. Shaw. *Using finite elements in mechanical design*. McGraw-Hill, 1996.

[191] N.D. Raath. *Failure prediction of spot welded boron steel*. PhD thesis, University of Warwick, 2014.

[192] A. Tabiei. *Composite materials in LS-DYNA*. Livermore Software Technology Corporation, 2012.

[193] B.Z. Haque. *A progressive composite damage model for unidirectional and woven fabric composites*. University of Delaware for Composite Materials, 2017.

[194] J. Kopp G. Friedrich H.E. Krishnamoorthy, S.K. Hoptner. Prediction of structural response of frp composites for conceptual design of vehicles under impact loading. In *8th European LS-DYNA Users Conference, Strasbourg*, 2011.

[195] P. Jaguar Land Rover Bristo. Composite modelling matieral card selection and training course selection. Personal communication, 2014.

[196] R. O. Ochola, K. Marcus, G. N. Nurick, and T. Franz. Mechanical behaviour of glass and carbon fibre reinforced composites at varying strain rates. *Composite Structures*, 63(3-4):455–467, 2004.

[197] J. Coulton. Improvements to material 58 (woven composite) (addition of strain rate effects). In *LS-DYNA Anwender Forum*, Stuttgart, 2013. Hyundai Motor European Technical Center GmbH.

[198] M.M. Shokrieh and M.J. Omidi. Compressive response of glass-fiber reinforced polymeric composites to increasing compressive strain rates. *Composite Structures*, 89(4):517–523, 2009.

[199] Ls-dyna keyword user's manual volume ii material models, 2014.

[200] P. D. Soden, A. S. Kaddour, and M. J. Hinton. Recommendations for designers and researchers resulting from the world-wide failure exercise. *Composites Science and Technology*, 64(3-4):589–604, 2004.

Appendix A

Slack adaptor upper jaw engineering drawings

A.1 High capacity slack adaptor impactor - with fulcrum dampers

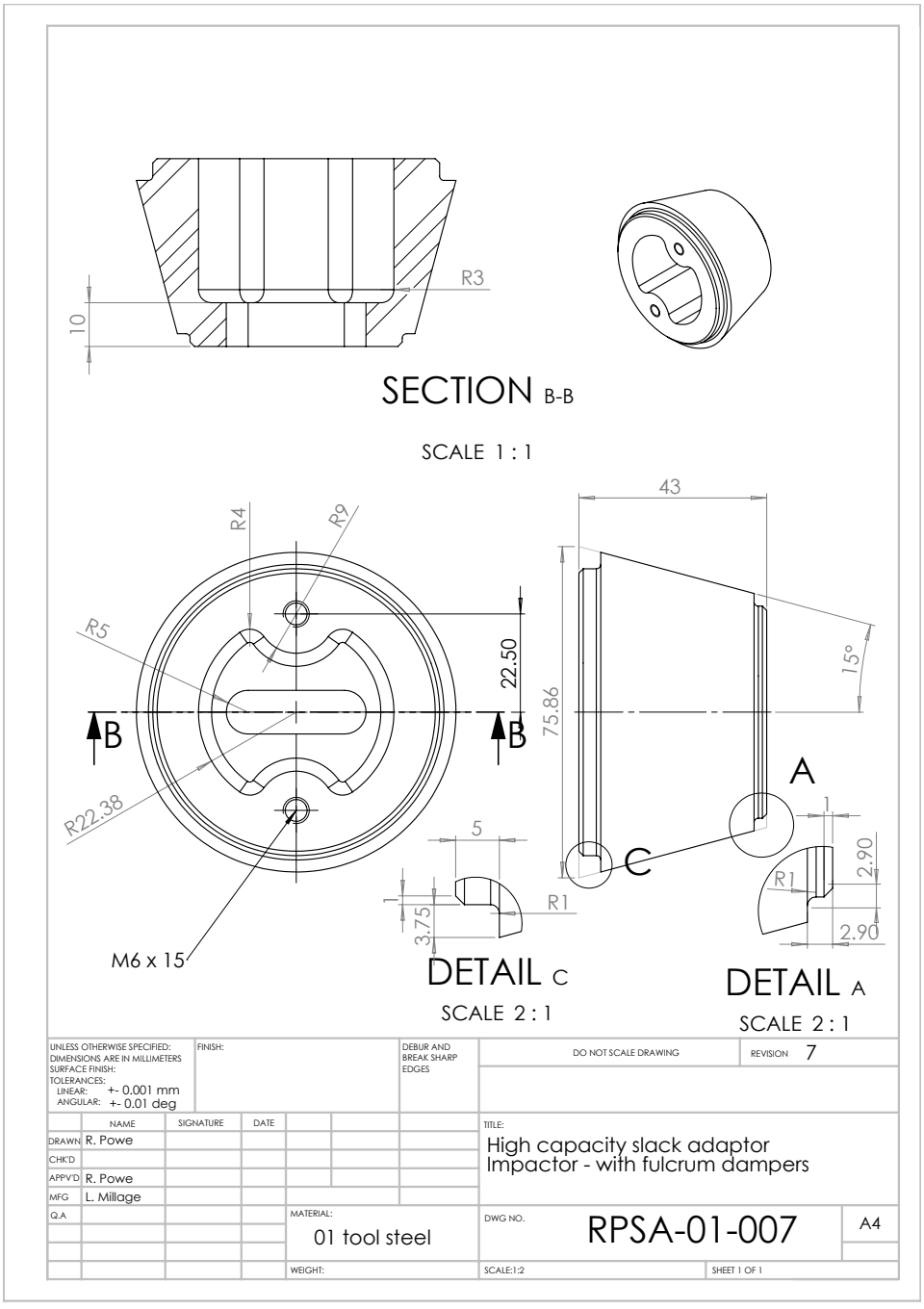

A.2 High capacity slack adaptor impactor guide

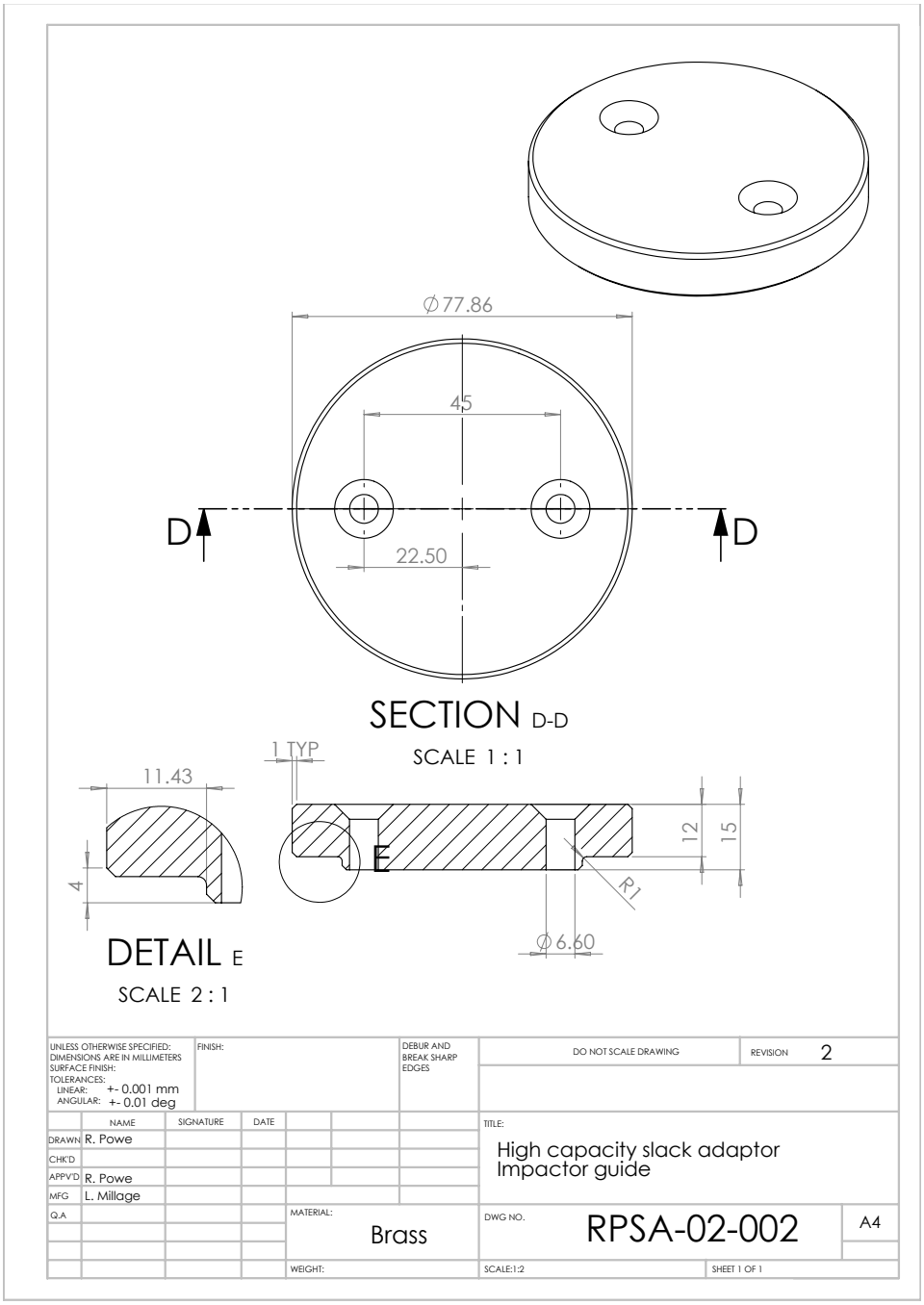

A.3 High capacity slack adaptor serrated jaw

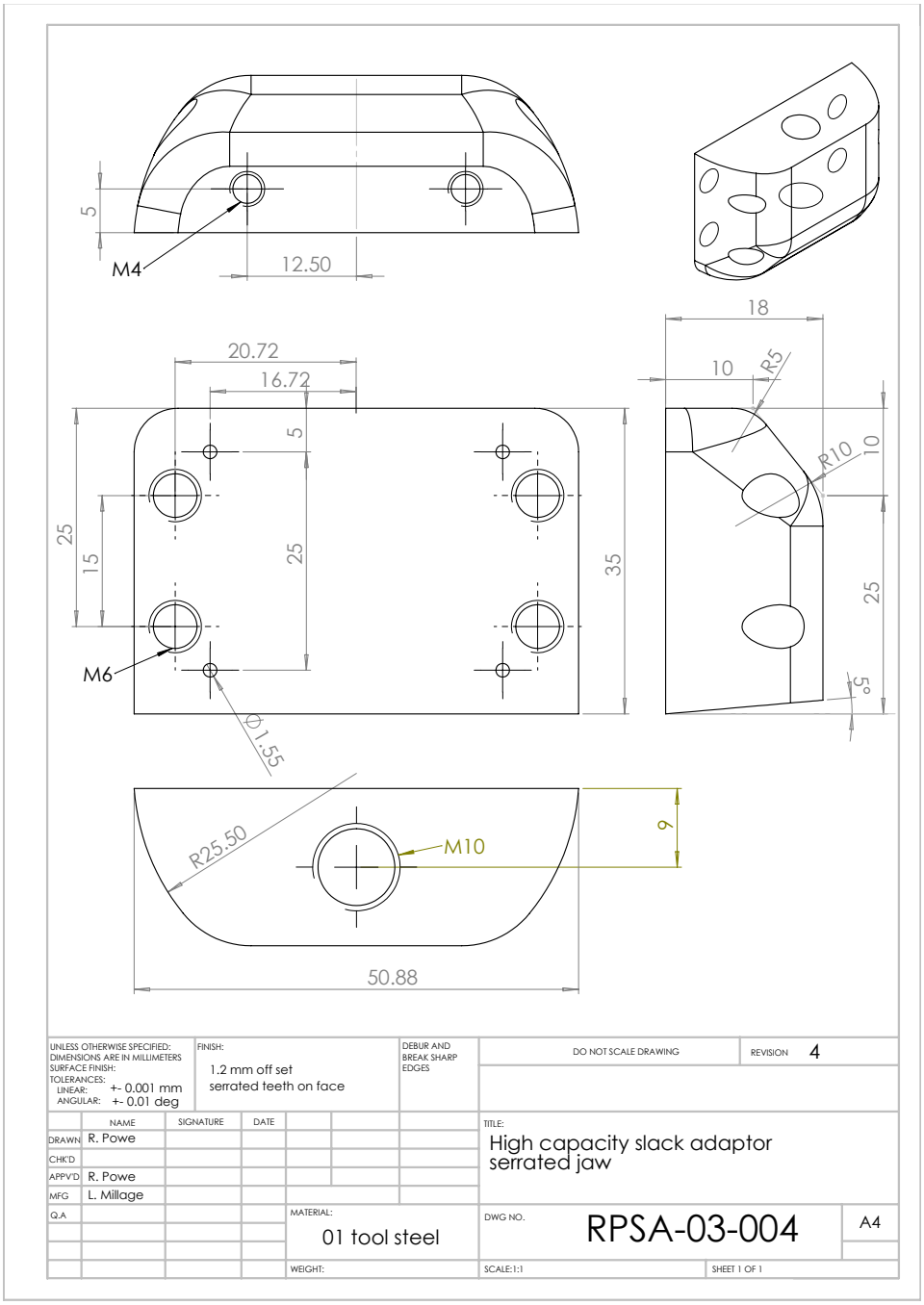

A.4 High capacity slack adaptor lower fulcrum damper

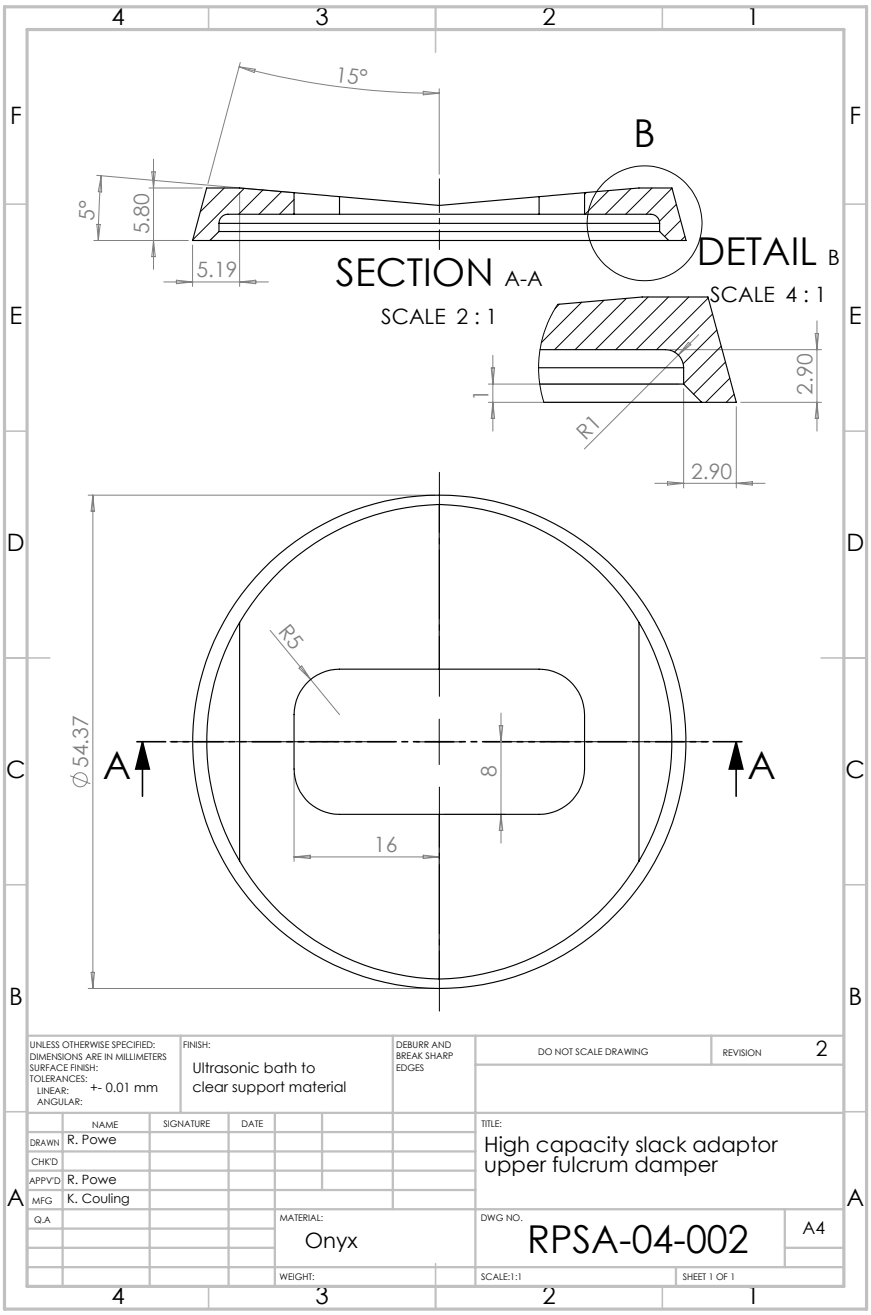

A.5 High capacity slack adaptor upper fulcrum damper

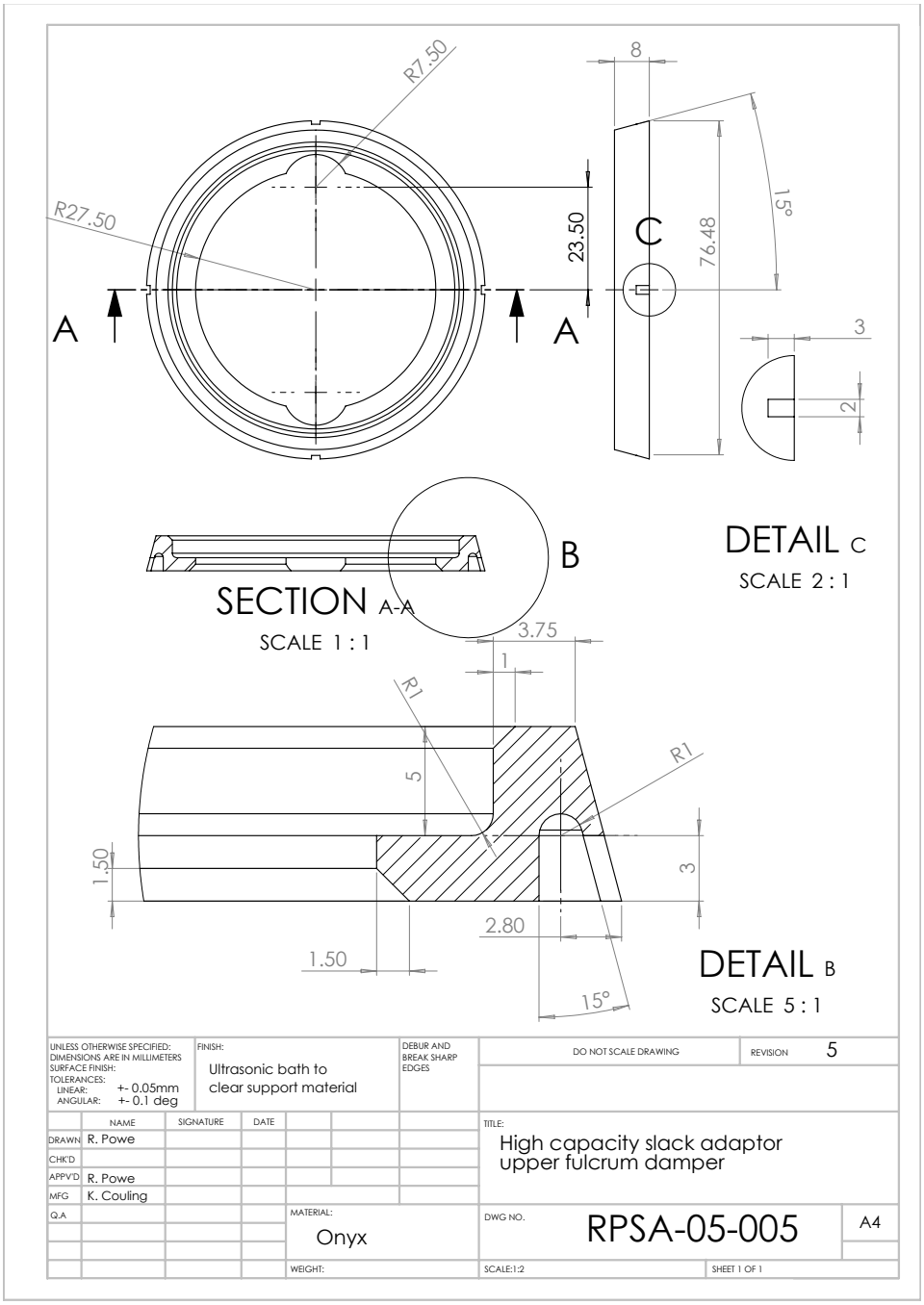

A.6 High capacity slack adaptor lower jaw mounting plate

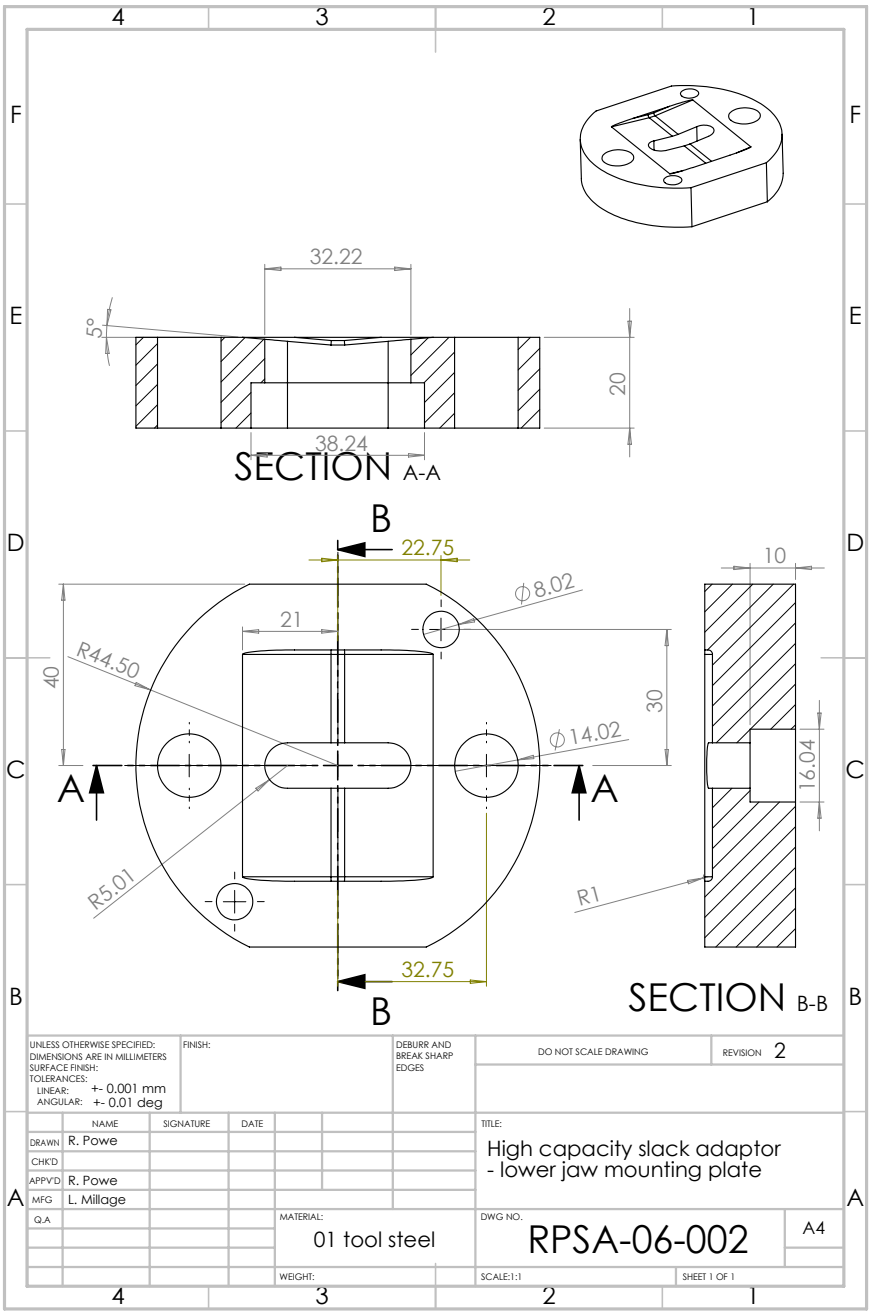

Appendix B

Input file for single element model

```
*KEYWORD
$>
$> Primer12.0 created on: Sun Aug 19 17:08:24 2018
$>
$$ HM_OUTPUT_DECK created 13:41:30 11-16-2015 by HyperMesh Version
13.0.110.31
$$ Ls-dyna Input Deck Generated by HyperMesh Version  : 13.0.110.31
$$ Generated usi
$> end_saved_comments
$
$
$
$ =============
$ CONTROL cards
$ =============
$
*CONTROL_ACCURACY
         1         4         0
*CONTROL_BULK_VISCOSITY
       1.5    6.0E-2        -2         0
*CONTROL_ENERGY
         2         2         2         1
*CONTROL_HOURGLASS
         8       0.1
*CONTROL_SHELL
      20.0         1        -1         3        16         2         1
0
       1.0         0         3         1         0
         0         0         0         0         0       0.0       0.0
         2         2         0         1         0         0       1.0
0
*CONTROL_TERMINATION
       3.0         0       0.0       0.0       0.0         0
*CONTROL_TIMESTEP
       0.0       0.9         0       0.0   -2.5E-7         0         1
0
$
$
$ ==============
$ DATABASE cards
$ ==============
$
*DATABASE_BNDOUT
    3.0E-5         1         0         1
*DATABASE_ELOUT
    3.0E-5         1         0         1
*DATABASE_GLSTAT
    3.0E-5         1         0         1
*DATABASE_NODOUT
    3.0E-5         1         0         1       0.0         0
*DATABASE_SECFORC
    3.0E-5         1         0         1
*DATABASE_SPCFORC
    3.0E-5         1         0         1
```

```
*DATABASE_SSSTAT
    3.0E-5         1
*DATABASE_BINARY_D3PLOT
    1.0E-5         0         0         0         0
*DATABASE_EXTENT_BINARY
        22        22         0         1         0         0         0
0
         0         0         0         0         0         0         0
0
         0         0       0.0         0         0         0
         0         0         0
$
*DATABASE_HISTORY_NODE
         1         2         3         4
$
*DATABASE_HISTORY_SHELL
         1
*DATABASE_CROSS_SECTION_PLANE_ID
         1Long1
         0       0.0     -10.0      -9.5      10.0     -10.0      -9.5
       0.0       0.0      -9.5      20.0      20.0         0         0
         2Long2
         0      10.0     -10.0      -9.5      20.0     -10.0      -9.5
      10.0       0.0      -9.5      20.0      20.0         0         0
         3Trans1
         0     -15.0       0.0      10.5     -15.0      10.0      10.5
      -5.0       0.0      10.5      30.0      20.0         0         0
         4Trans2
         0     -15.0      10.0      10.5     -15.0      20.0      10.5
      -5.0      10.0      10.5      30.0      20.0         0         0
$
$
$ ====================
$ MAT (Material) cards
$ ====================
$
*MAT_SPRING_ELASTIC_TITLE
spring
         2  100000.0
$
*MAT_LAMINATED_COMPOSITE_FABRIC_TITLE
T7002x2TMTM710-1_400gsm
$#     mid        ro        ea        eb      (ec)      prba      tau1
gamma1
         3  1.507E-9   61210.0   61210.0   61210.0    6.0E-2     71.06
3.949E-2
$#     gab       gbc       gca    slimt1    slimc1    slimt2    slimc2
slims
    3737.0    3737.0    3737.0    1.0E-4    1.0E-4    1.0E-4    1.0E-4
1.0
$#    aopt     tsize     erods      soft        fs
       0.0       0.0     0.218       0.0      -1.0       0.0       0.0
0.0
$#      xp        yp        zp        a1        a2        a3
```

```
       0.0       0.0       0.0       0.0       0.0       0.0
$#      v1        v2        v3        d1        d2        d3      beta
       0.0       0.0       0.0       0.0       0.0       0.0       0.0
$#    e11c      e11t      e22c      e22t       gms
   1.03E-2   1.45E-2   1.03E-2   1.45E-2    0.1709
$#      xc        xt        yc        yt        sc
     557.0    879.32     557.0    879.32    118.34
         0         0         0         0         0         0         0
0.0
         0         0         0         0         0
$
$
$
$ =============
$ SECTION cards
$ =============
$
*SECTION_DISCRETE
         1         0       0.0       0.0       0.0       0.0
       0.0       0.0
$
         2         0       0.0       0.0       0.0       0.0
       0.0       0.0
$
$
$
$ ===============
$ HOURGLASS cards
$ ===============
$
*HOURGLASS_TITLE
JLR-best-practice:Elform16
         1         8       0.1         1       1.5    6.0E-2       0.1
0.1
$
$
$ ==========
$ PART cards
$ ==========
$
*PART_COMPOSITE
test_element
         2        16       0.0       0.0       0.0         0         0
0
         3      0.63      45.0         0
$
*PART

         3         1         2         0         0         0         0
0
$
*PART
```

```
         4         2         2         0         0         0         0
0
$
$
$
$ ==========
$ NODE cards
$ ==========
$
*NODE
       1             0.0       10.000000       0.50000000       0       0
       2       10.000000       10.000000       0.50000000       3       0
       3       10.000000             0.0       0.50000000       5       0
       4             0.0             0.0       0.50000000       0       0
$
$
$ =============
$ ELEMENT cards
$ =============
$
*ELEMENT_SHELL
       1       2       1       2       3       4
$
$
$ ============
$ DEFINE cards
$ ============
$
$
*DEFINE_CURVE
$
$: Cross-reference summary for Load-curve 1
$: ---------------------------------------------
$
$: Boundary Prescribed Motion <No label>: Velocity vs time
$: X axis : Time                        (Units: Time)
$: Y axis : Prescribed velocity         (Units: Velocity)
$: (To a total of 2 unlabelled Boundary Prescribed Motion entries)
$
$: Usage: Transient analysis
$
         1         0       0.0       0.0       0.0       0.0         0
                 0.0           10.379000
           100.00000           10.379000
$
$
$
$
$ =============
$ DAMPING cards
$ =============
$
*DAMPING_PART_STIFFNESS
         2      0.25
```

```
$
$
$ ==============
$ BOUNDARY cards
$ ==============
$
*BOUNDARY_PRESCRIBED_MOTION_NODE
         2         1         0         1       0.0         0       0.0
0.0
         3         1         0         1       0.0         0       0.0
0.0
*BOUNDARY_SPC_NODE
         1         0         1         0         1         0         0
0
         4         0         1         1         1         0         0
0
$
$
$ ==============
$ INITIAL cards
$ ==============
$
*INITIAL_VELOCITY_NODE
         2    10.379       0.0       0.0       0.0       0.0       0.0
0
         3    10.379       0.0       0.0       0.0       0.0       0.0
0
$
*END
```

[A thesis is never finished, merely abandoned]